A N N U A L R E P O R T

2014

and list of publications

Bayerisches Forschungsinstitut
für Experimentelle Geochemie und Geophysik
Universität Bayreuth

Bayerisches Geoinstitut
Universität Bayreuth
D-95440 Bayreuth
Germany

Telephone: +49-(0)921-55-3700
Telefax: +49-(0)921-55-3769
e-mail: bayerisches.geoinstitut@uni-bayreuth.de
www: http://www.bgi.uni-bayreuth.de

Editorial compilation by: Stefan Keyssner and Petra Buchert
Section editors: Andreas Audétat, Tiziana Boffa Ballaran, Leonid Dubrovinsky,
Dan Frost, Tomoo Katsura, Takaaki Kawazoe, Hans Keppler
Katharina Marquardt, Catherine McCammon, Nobuyoshi Miyajima
Dave Rubie, Gerd Steinle-Neumann

Staff and guests of the Bayerisches Geoinstitut in **July 2014**:

Die Mitarbeiter und Gäste des Bayerischen Geoinstituts im **Juli 2014**:

First row, from left (1. Reihe, v. links) Riko Iizuka, Lanlan Shi, Stella Chariton, Xochilt Gutiérrez, Natalia Solopova, Leyla Ismailova, Martha Pamato, Ahmed El Goresy, Michelle Wenz, Ana Cernok, Nicki Siersch, Zsanett Pintér, Wanting Li

Second row, from left (2. Reihe, v. links) Petra Buchert, Yana Fedortchouk, Jellie de Vries, Vera Laurenz, Antje Vogel, Fabian Wagle, Mattia Giannini, Gertrud Gollner, Catherine McCammon, Lydia Kison-Herzing, Ulrike Trenz, Florian Heidelbach

Third row, from left (3. Reihe, v. links) Stefan Keyssner, Tomoo Katsura, Katharina Marquardt, Anja Rosenthal, Ryosuke Sinmyo, Takaaki Kawazoe, Raphael Njul, Dan Frost, Hauke Marquardt, Johannes Buchen, Alok Chaudhari

Fourth row, from left (4. Reihe, v. links) Nico Walte, Hubert Schulze, Sven Linhardt, Takayuki Ishii, Christopher Beyer, Nobuyoshi Miyajima, Takahiro Yoshioka, Alexander Kurnosov, Davide Novella

Fifth row, from left (5. Reihe, v. links) Steven Jacobsen, Detlef Krauße, Andrej Bobrov, Heinz Fischer, Kurt Klasinski, Matteo Masotta, Hans Keppler, Dave Rubie, Svyatoslav Shcheka, Lin Wang

Sixth row, from left (6. Reihe v. links) Thomas Chust, Sakin Jabarov, Sergey Ovsyannikov, Robert Farla, Haihao Guo, Andreas Audétat, Leonid Dubrovinsky, Gerd Steinle-Neumann, Mickaël Laumonier

Absent (Es fehlten) Stephan Blaha, Ulrich Böhm, Tiziana Boffa Ballaran, Elena Bykova, Valerio Cerantola, David Dobson, Nicole Fischer, Holger Kriegl, Robert Myhill, Anna Pakhomova, Sylvain Petitgirard, Esther Posner, Gerd Ramming, Oliver Rausch, Fanny Sorbadere, Stefan Übelhack, Vojtech Vlcek

Contents

Foreword/Vorwort 9/I

1. Advisory Board and Directorship 11
   1.1 Advisory Board 11
   1.2 Leadership 11

2. Staff, Funding and Facilities 13
   2.1 Staff 13
   2.2 Funding 13
   2.3 Laboratory and office facilities 19
   2.4 Experimental and analytical equipment 19

3. Forschungsprojekte – Zusammenfassung in deutscher Sprache III
3. Research Projects 21
   3.1 *Earth and Planetary Structure and Dynamics* 21
      a. Development of an early density stratification in the Earth's metallic core (D.C. Rubie, S.A. Jacobson, D.J. Frost, J. de Vries, in collaboration with J. Hernlund/Tokyo and A. Morbidelli/Nice) 22
      b. Melting and crystallisation during and after planetary collisions (J. de Vries, D.C. Rubie and S.A. Jacobson; F. Nimmo/Santa Cruz, H.J. Melosh/ West Lafayette and A. Morbidelli/Nice) 23
      c. Crystallizing a magma ocean on Mars (T. Chust and G. Steinle-Neumann) ... 26
      d. Mafic rocks as lower mantle water reservoirs (M.G. Pamato, R. Myhill, D.J. Frost, T. Boffa Ballaran, F. Heidelbach and N. Miyajima) 29

   3.2 *Geochemistry* 31
      a. NWA7325: A highly reduced differentiated meteorite from an unknown parental planet (T. Nakamura/Sendai, M. Miyahara/Hiroshima, A. El Goresy, Ph. Gillet/Lausanne; E. Ohtani, K. Yogo and M.H. Ishida/Sendai; Y. Lin/Beijing and H. Schulze) 33
      b. Are current models for the giant impact hypothesis of Moon formation sufficient to explain the oxygen isotoptic similarities between Earth and the Moon? (S.A. Jacobson and D.C. Rubie, in collaboration with A. Morbidelli/Nice, E.D. Young/Los Angeles and J. Hernlund/Tokyo) 34
      c. Metal-silicate partitioning of highly siderophile elements in sulfur-bearing systems – Implications for Earth’s accretion and core formation history (V. Laurenz, D.C. Rubie and D.J. Frost) 37
      d. Oxidation state of the lower mantle: *In situ* observations of the iron electronic configuration in magnesium silicate bridgmanite at extreme conditions (I. Kupenko, C.A. McCammon, R. Sinmyo, V. Cerantola, V. Potapkin/Jülich, A.I. Chumakov/Grenoble, A. Kantor, R. Rüffer/ Grenoble and L.S. Dubrovinsky) 39

e. Melting and subsolidus phase relations in the MgO-SiO_2-Fe_2O_3 system under lower mantle conditions (R. Sinmyo, Y. Nakajima, C.A. McCammon, R. Myhill and D.J. Frost) 41
f. The behaviour of ferric iron (Fe^{3+}) during MORB petrogenesis (F. Sorbadere, D.J. Frost, M. Wenz, A. Rosenthal, V. Laurenz and C.A. McCammon) 42
g. The oxygen fugacity of diamond formation in carbonated eclogite rocks (H. Mohseni and D.J. Frost) 45
h. Syngenesis of diamonds and minerals of the Earth's lower mantle (D. Simonova and A. Spivak/Chernogolovka, L.S. Dubrovinsky, Y. Litvin/Chernogolovka) 46
i. Evolution of the Earth's lower-mantle: The stishovite paradox (experiments at 24 GPa) (A. Spivak/Chernogolovka, L.S. Dubrovinsky, Y. Litvin/ Chernogolovka) 47
j. Fluorine partitioning between garnet, clinopyroxene, and silicate melt under upper mantle conditions (C. Beyer and D.J. Frost; S. Klemme and T. Grützner/Münster; C. Magee and T.R. Ireland/Canberra) 49
k. High-pressure melting relations in the water-rich system $Mg(OH)_2$-SiO_2-H_2O (R. Myhill and D.J. Frost) 51
l. High-pressure experimental study of eclogite with varying H_2O contents (A. Rosenthal, D.J. Frost, S. Petitgirard and Zs. Pintér; G.M. Yaxley and A. Berry/Canberra) 52
m. Crude oil properties under upper mantle conditions (A. Serovaysky and A. Kolesnikov/Moscow; C.A. McCammon, D. Vasiukov/Moscow; I. Kupenko and L.S. Dubrovinsky; V. Kutcherov/Stockholm) 54
n. Compositional evolution and formation conditions of magmas (melts, fluids and minerals) related to porphyry molybdenum mineralization at Climax, Colorado (A. Audétat) 55
o. Role of evaporites in the formation of magnetite-apatite deposits along the Middle and Lower Yangtze River, China: Evidence from LA-ICP-MS analysis of fluid inclusions (W. Li and J. Zhang/Wuhan, A. Audétat) 58

3.3 *Mineralogy, Crystal Chemistry and Phase Transformations* 61
a. Phase relations and chemical stability of Fe_2O_3 and Fe_3O_4 (E. Bykova, N.A. Dubrovinskaia, L.S. Dubrovinsky, M. Bykov, C.A. McCammon and S.V. Ovsyannikov; M. Hanfland, I. Kupenko, A.I. Chumakov and R. Rüffer/Grenoble; H.-P. Liermann/Hamburg; V.B. Prakapenka/Argonne) .. 62
b. Phase relations of $MgFe_2O_4$ and the stability of $Mg_2Fe_2O_5$ (L. Uenver-Thiele and A.B. Woodland/Frankfurt; T. Boffa Ballaran and D.J Frost) 65
c. Substitution of Fe^{2+} by Mg in Fe_4O_5 compounds: Crystal chemistry of the $Mg_2Fe_2O_5$ end-member (T. Boffa Ballaran, in collaboration with L. Uenver-Thiele and A.B. Woodland/Frankfurt) 66
d. New high-pressure polymorph of $(Mg,Fe^{2+})_3Fe^{3+}{}_4O_9$ (R. Sinmyo, E. Bykova, C.A. McCammon, L.S. Ismailova, S.V. Ovsyannikov and L.S. Dubrovinsky) 68

e. Synthesis of skiagite garnet at high pressure and temperature and investigation of its crystal structure (L.S. Ismailova; A.V. Bobrov/Moscow; M. Bykov and E. Bykova/Bayreuth; V. Cerantola; I. Kantor and I. Kupenko/Grenoble; C.A. McCammon; N.A. Dubrovinskaia/Bayreuth; L.S. Dubrovinsky) 69
f. Phase relations of skiagite $Fe^{2+}_3Fe^{3+}_2Si_3O_{12}$ at transition zone pressures and temperatures (L.S. Ismailova, A.V. Bobrov/Moscow and L.S. Dubrovinsky) 71
g. Siderite ($FeCO_3$) stability in the Earth's lower mantle (V. Cerantola, I. Kupenko/Grenoble, C.A. McCammon, L.S. Ismailova/Bayreuth, I. Kantor/Grenoble and L.S. Dubrovinsky) 73
h. Influence of oxygen fugacity on iron oxidation state in chromite (Zs. Pintér and C.A. McCammon) 74
i. The effect of temperature on the $P2_1/c$ to $C2/c$ transition in H_2O-bearing $Mg_2Si_2O_6$ clinoenstatite (N. Siersch, A. Kurnosov and T. Boffa Ballaran; S.D. Jacobsen/Evanston) 76
j. Lonsdaleite is a phantom mineral (N.A. Dubrovinskaia/Bayreuth; L.S. Dubrovinsky; P. Németh/Budapest; L.A.J. Garvie, T. Aoki and P.R. Buseck/Tempe) 78
k. Monoclinic baddeleyite in the Shergotty Martian meteorite: Investigations of orthogonal twin lamellae induced during a natural dynamic event (S. Ozawa/Sendai, K. Marquardt, M. Miyahara/Hiroshima, A. El Goresy, E. Ohtani/Hiroshima, N. Miyajima, P. Gillet/Lausanne and A. Bouvier/London) 79
l. High-pressure polymorphs of coesite (A. Černok, E. Bykova and T. Boffa Ballaran; H.-P. Liermann/Hamburg, M. Hanfland/Grenoble and L.S. Dubrovinsky) 82
m. High-pressure synthesis of single-crystal $(Mg_{0.9},Fe_{0.1})_2SiO_4$ wadsleyite (T. Kawazoe) 84
n. Hydrogen positions of hydrous wadsleyite from single-crystal neutron diffraction (S.D. Jacobsen/Evanston, J.R. Smyth/Boulder, M. Gutmann/Oxfordshire and D.J. Frost) 85
o. Characterization of a natural quartz crystal as reference material for microanalytical determination of Ti, Al, Li, Fe, Mn, Ga and Ge (A. Audétat, D. Garbe-Schönberg/Kiel, A. Kronz/Göttingen, T. Pettke/Bern, B. Rusk/Bellingham, J.J. Donovan/Eugene and H.A. Lowers/Denver) 86

3.4 *Physical Properties of Minerals* 89
a. Single-crystal elasticity of wadsleyite, β-$(Mg_{0.9}Fe_{0.1})_2SiO_4$, at combined high pressure and high temperature (J. Buchen, H. Marquardt, T. Kawazoe, A. Kurnosov and T. Boffa Ballaran) 90
b. High-pressure/high-temperature measurements of the elastic properties of single-crystal ringwoodite (K. Schulze, H. Marquardt, A. Kurnosov, T. Kawazoe and T. Boffa Ballaran) 92

c. Elasticity of Al,Fe-bearing bridgmanite at high pressures and high temperatures (A. Kurnosov, H. Marquardt, T. Boffa Ballaran and D.J. Frost) 93
d. P-V-Vp-Vs-T measurements of complex clinopyroxene solid solutions up to 1323 K and 12 GPa (C. Beyer and D.J. Frost, in collaboration with J. Chantel, W. Crichton and J. Guignard/Grenoble) 95
e. Single-crystal elasticity of majoritic garnets: stagnant slabs and thermal anomalies at the base of the transition zone (M.G. Pamato, A. Kurnosov, T. Boffa Ballaran, D.J. Frost, L. Ziberna/Bristol, M. Giannini and D.M. Trots, in collaboration with S.N. Tkachev, K.K. Zhuravlev and V.B. Prakapenka/Chicago, S. Speziale/Potsdam) 96
f. Elastic properties of single crystal iron carbonate and implications for the deep Earth (C.A. McCammon, L.S. Dubrovinsky, V. Cerantola, I. Kupenko and R. Sinmyo; L.S. Ismailova/Bayreuth; A. Kantor and A.I. Chumakov/ Grenoble) 97
g. Density of amorphous $MgSiO_3$ to lowermost mantle pressures (S. Petitgirard, R. Sinmyo, I. Kupenko and D.C. Rubie; W. Malfait/Zurich, L. Hennet/Orleans, D. Harries/Jena and M. Burghammer/Grenoble) 99
h. Change of electrical and elastic properties of metals upon melting (F. Wagle, G. Steinle-Neumann and V. Vlček) 100
i. Valence state of Ti in natural hibonite: Implications for the oxygen fugacity in the Solar Nebula (M. Giannini and T. Boffa Ballaran, in collaboration with F. Langenhorst/Jena) 102
j. The most frequent interfaces in olivine aggregates (K. Marquardt, in collaboration with G.S. Rohrer and B. Lin/Pittsburgh; L. Morales and E. Rybacki/Potsdam) 104

3.5 *Fluids, Melts and their Interaction with Minerals* 106
a. The adsorption of HCl on volcanic ashes (X. Gutierrez and H. Keppler) 107
b. Volatile budget of the on-going Bárðarbunga fissure eruption on Iceland (E. Bali/Reykjavík and Bayreuth) 109
c. Anhydrite solubility in differentiated arc magmas (M. Masotta and H. Keppler) 110
d. The speciation of carbon monoxide in silicate melts and glasses (T. Yoshioka, C.A. McCammon, S. Shcheka, and H. Keppler) 112
e. Electrical conductivity of hydrous rhyolitic melt (X. Guo and L. Zhang/Hefei, H. Keppler, H. Behrens/Hannover and H. Ni/Hefei) 113
f. The effect of water content, pressure and temperature on the electrical conductivity of silicate melts: implication for the Uturuncu magmatic system (South Bolivia) and magnetotelluric imaging in subduction areas (M. Laumonier; F. Gaillard and D. Sifré/Orleans) 114
g. Diffusion in liquid iron and silicate melt at high pressure (E.S. Posner, D.C. Rubie, D.J. Frost, B. Schmickler, V. Vlček and G. Steinle-Neumann) ... 117

h. The solubility of molecular hydrogen in olivine and pyroxene (X. Yang/Nanjing and H. Keppler) 120
i. Water solubility in lower mantle phases (R. Myhill, L. Ziberna, D.J. Frost, T. Boffa Ballaran, H. Bureau/Paris, C. Raepsaet/Paris) 121

3.6 *Rheology and Metamorphism* 123
a. Microstructural contrasts between a dunite and a two-phase harzburgite: Rock deformation at different temperatures, pressures, compositions and strain magnitudes (R.J.M. Farla) 124
b. Correlation between strain rates and reaction rates at the transition from spinel to garnet lherzolite in the CMAS system (F. Heidelbach) 126
c. Texture development of olivine at high pressure and low strain rates (N. Walte, F. Heidelbach and D. Frost) 128
d. Deformation mechanism of lawsonite in deep subducting slabs from high-pressure and high-temperature experiments (R. Iizuka/Matsuyama, N. Miyajima, V. Soustelle/Providence and D.J. Frost) 131
e. Deformation fabrics of high-pressure subduction channel rocks from the Eclogite Zone of the Tauern Window (Austria) (R. Keppler and M. Stipp/Kiel, F. Heidelbach) 132
f. Deformation of (Mg,Fe)O ferropericlase at lower mantle pressures (H. Marquardt, in collaboration with L. Miyagi/Salt Lake City) 135
g. The influence of the elastic properties of ices on the early differentiation of ice satellites (A.S. Pakhomova, T. Boffa Ballaran, A. Kurnosov and D.J. Frost, in collaboration with M. Leoni/Trento) 137
h. Pressure dependence of [100](010) and [001](010) dislocation mobility in natural olivine (L. Wang, Zs. Pintér, S. Blaha, R.J.M. Farla, T, Kawazoe and T. Katsura) 138
i. Dislocation mobility of olivine as a function of water content (S. Blaha and T. Katsura) 140

3.7 *Materials Science* 143
a. Improved description of the DFT eigenstates and dielectric constants with a semi-local exchange functional (V. Vlček and G. Steinle-Neumann; L. Leppert and S. Kümmel/Bayreuth; R. Armiento/Linköping) 144
b. Structure of aluminium at high temperature comparing molecular dynamics and self-consistent ab initio lattice dynamics results (L. Wang, G. Steinle-Neumann and V. Vlček) 146
c. Bulk silicon crystals with high boron content, $Si_{1-x}B_x$, and their metallic conductivity (S.V. Ovsyannikov, H. Gou, Y. Nakajima and L.S. Dubrovinsky; A.E. Karkin and V.V. Shchennikov/Yekaterinburg, R. Wirth/Potsdam, V. Dmitriev/Grenoble, N.A. Dubrovinskaia/Bayreuth) 148
d. Synthesis of nanocrystalline diamond from glassy carbon balls (N.A. Solopova and L.S. Dubrovinsky, N.A. Dubrovinskaia/Bayreuth) 151

e. A new hard oxide semiconductor with a direct and narrow band gap (S.V. Ovsyannikov, E. Bykova and L.S. Dubrovinsky; A.E. Karkin, N.V. Morozova and V.V. Shchennikov/Yekaterinburg, A.M. Abakumov/ Antwerp, A.A. Tsirlin/Tallin and K.V. Glazyrin/Hamburg) 153
f. High-pressure/high-temperature synthesis of In_2O_3 (B. García-Domene/ Valencia; S.V. Ovsyannikov and L.S. Dubrovinsky) 155
g. A structural phase transition in multiferroic YMn_2O_5 at high pressure (D.P. Kozlenko, S.H. Jabarov, E.V. Lukin and S.E. Kichanov/Dubna, L.S. Dubrovinsky) 157
h. Structural studies of the P-T phase diagram of $BiMnO_3$ (S.H. Jabarov, D.P. Kozlenko, N.T. Dang, S.E. Kichanov, A.I. Mammadov, E.V. Lukin and B.N. Savenko/Dubna, L.S. Dubrovinsky) 158

3.8 *Methodological Developments* 160
a. Adjustment of the high-pressure volume in the new DIA-type multianvil apparatus 'IRIS-15' (L.-L. Shi, T. Katsura, T. Kawazoe and R.J.M. Farla, in collaboration with M. Petri/Mainleus) 161
b. Calibration of the ruby pressure scale up to 800 K and 46 GPa under quasi-hydrostatic conditions (N. Siersch, A. Kurnosov and T. Boffa Ballaran) 163
c. Calibration of a Sm-STB fluorescence pressure sensor using Sm-YAG absolute pressure scale (S. Rashchenko/Novosibirsk, A. Kurnosov and L.S. Dubrovinsky) 165
d. Gated laser heating in diamond anvil cells for studies of nuclear resonance processes (I. Kupenko, C. Strohm, C.A. McCammon, V. Cerantola, S. Petitgirard and L.S. Dubrovinsky, in collaboration with K. Glazyrin/ Hamburg; A.I. Chumakov and R. Rüffer/Grenoble) 167
e. Use of piezoelectric sensors for *in situ* stress determinations at high pressure and temperature (M.A.G.M. Manthilake/Clermont-Ferrand, D.J. Frost and N. Walte) 168
f. Development of a new cell to investigate the effect of water on the rheology of olivine single crystals in the D-DIA multianvil apparatus coupled to synchrotron radiation (C. Bollinger, in collaboration with J. Chen/Miami) 170
g. Calibration of metal-alloy sliding redox sensors (H. Mohseni and D.J. Frost) 172
h. Quantitative chemical analysis of carbon and oxygen in molten Fe-rich alloy by analytical transmission electron microscopy (N. Miyajima; R.A. Fischer and A.J. Campbell/Chicago; D.J. Frost; D. Harries, F. Langenhorst and K. Pollok/Jena; S. Petitgirard and D.C. Rubie) 174
i. Synthesis of large stishovite single crystals (A. Černok, S. Blaha and T. Boffa Ballaran; N.A. Dubrovinskaia/Bayreuth; L.S. Dubrovinsky) 176
j. First systematic study of synthetic fluid inclusions in opaque ore minerals: Method development (V. Casanova, K. Kouzmanov, N. Ubrig and L. Fontboté/Geneva; A. Audétat) 178

k. Ionizing finite systems – the role of electrostatics (V. Vlček and G. Steinle-Neumann, in collaboration with H.R. Eisenberg and R. Baer/Jerusalem) 180

4. Publications, Conference Presentations, Seminars 183
4.1 Publications (published) 183
a) Refereed international journals 183
b) Popular scientific magazines 189
4.2 Publications (submitted, in press) 189
4.3 Presentations at scientific institutions and at congresses 193
4.4 Lectures and seminars at Bayerisches Geoinstitut 204
4.5 Conference organization 206

5. Visiting scientists 209
5.1 Visiting scientists funded by the Bayerisches Geoinstitut 209
5.2 Visiting scientists supported by other externally funded BGI projects 210
5.3 Visiting scientists supported by the DFG Core Facility programme 211
5.4 Visitors (externally funded) 212

6. Additional scientific activities 215
6.1 Theses 215
6.2 Honours and awards 215
6.3 Editorship of scientific journals 216
6.4 Membership of scientific advisory bodies 216

7. Scientific and Technical Personnel 219

Index 223

Foreword

The fundamental research goals of the Bayerisches Geoinstitut are to investigate the structure, composition, and dynamics of Earth and planetary interiors through experimental and computational methods and through the study of terrestrial and extraterrestrial samples. Although the Geoinstitut's focus is generally on experiments at high pressures and temperatures, the application of such results to interpret geophysical and geological observations requires increasingly sophisticated modelling in order to accurately reproduce the complexity of natural processes. For this reason, the Geoinstitut widened its research portfolio in 2007 by establishing a junior professorship in geodynamic modelling. Thanks to the support of the late University President Prof. Dr. Rüdiger Bormann this position was readvertised in 2013 as a W2 professorship. In 2014, the professorship was offered to Dr. Gregor Golabek of the Swiss Federal Institute of Technology in Zurich. It is a pleasure to report that he subsequently accepted this offer and will start his position at the Geoinstitut in March 2015.

Two new pieces of major equipment were installed at the institute in the past year: a new multi-anvil press and a focused ion beam instrument (FIB). Although the Geoinstitut already possesses seven multi-anvil presses, their pressure ranges are limited to 27 GPa. This is an invaluable pressure range for investigating processes in the interior down to the top of the lower mantle, at ~800 km depth; however, recent geophysical studies imply that the upper part of the lower mantle down to ~1000 km may be chemically different to the underlying layers. The new multi-anvil press employs sintered diamond anvils to allow the routine generation of pressures up to 60 GPa, which corresponds to a depth of 1500 km. The FIB was introduced principally to prepare tiny samples for transmission electron microscopy (TEM) analysis. The volumes of products from ultrahigh-pressure experiments produced using either diamond anvil cells (DAC) or a multi-anvil press equipped with sintered diamond anvils, are extremely small, e.g. < 0.01 mm in diameter. The FIB can cut and recover samples with a sub-micron precision, allowing specific parts of a sample to be exposed for analysis without loss or damage. It can also be used to prepare optimally sized samples for DAC experiments. The FIB compliments, therefore, the new 200 kV Titan TEM installed in the previous year and together these tools will allow new methods and frontiers to be addressed in ultrahigh-pressure research.

As in previous years, and also on the behalf of my colleagues, I would like to thank the *Free State of Bavaria* as represented by the *Bavarian State Ministry of Science, Research and Art* as well as the *Commission for High-Pressure Research in Geoscience* for their continuing support and strong commitment to the Bayerisches Geoinstitut. We also gratefully acknowledge generous support from external funding agencies, in particular the *Alexander von Humboldt Foundation*, the *European Union*, the *German Science Foundation*, and the

Federal Ministry of Education and Research, which continue to contribute greatly to the further development and success of the Geoinstitut.

Bayreuth, March 2015 Tomoo Katsura

Vorwort

Das Bayerische Geoinstitut erforscht die Struktur, Zusammensetzung und Dynamik der Erde und der Planeten mit experimentellen und numerischen Methoden, sowie durch die Untersuchung terrestrischer und extraterrestrischer Proben. Obwohl der Schwerpunkt des Geoinstituts auf Experimenten bei hohem Druck und hoher Temperatur liegt, erfordert die Anwendung dieser Resultate auf geologische und geophysikalische Probleme zunehmend komplexe Modelle. Aus diesem Grund hat das Geoinstitut im Jahr 2007 sein Forschungs-Portfolio durch eine Junior-Professur in Geodynamischer Modellierung erweitert. Dank der Unterstützung durch den verstorbenen Universitätspräsidenten Prof. Dr. Rüdiger Bormann konnte diese Stelle 2013 als W2-Professur neu ausgeschrieben werden. In 2014 wurde die Professur Herrn Dr. Gregor Golabek von der ETH Zürich angeboten. Es ist uns eine große Freude, dass Herr Golabek diesen Ruf angenommen hat und ab März 2015 am Geoinstitut tätig sein wird.

Zwei neue Großgeräte sind im vergangenen Jahr am Geoinstitut installiert worden: eine neue Multi-Anvil-Presse und ein "Focused Ion Beam"-Instrument (FIB). Obwohl das Geoinstitut bereits sieben Multi-Anvil-Pressen besitzt, ist ihr Druckbereich begrenzt auf 27 GPa. Dies ist ein sehr wichtiger Druckbereich, der die Untersuchung von Prozessen bis in den obersten Teil des unteren Mantels in einer Tiefe von ~ 800 km erlaubt. Neuere geophysikalische Studien legen aber die Vermutung nahe, dass der obere Teil des unteren Mantels bis zu einer Tiefe von ~ 1000 km möglicherweise chemisch verschieden ist von tieferen Lagen. Die neue Presse verwendet Stempel aus gesintertem Diamant, um routinemäßig Drücke bis zu 60 GPa zu erzeugen, was einer Tiefe von 1500 km entspricht. Das FIB-Gerät wurde angeschafft, um extrem kleine Proben für das Transmissions-Elektronenmikroskop (TEM) zu bearbeiten. Die Versuchsprodukte von Ultrahochdruck-Experimenten, sowohl aus Diamantzellen als auch aus Multi-Anvil-Experimenten mit gesinterten Diamant-Stempeln sind extrem klein, typischerweise < 0,01 mm im Durchmesser. Das FIB kann derartige Proben mit einer Genauigkeit im sub-Mikrometer-Bereich bearbeiten. Dadurch können interessierende Teile der Probe gezielt freigelegt und untersucht werden. Das Gerät kann auch zur Herstellung von Proben für Experimente in Diamantstempel-Zellen benutzt werden. Das FIB ergänzt daher in idealer Weise das im vorigen Jahr beschaffte 200 kV Titan-TEM, und beide Geräte zusammen werden es erlauben, mit neuen Methoden grundlegende Fortschritte in der Ultrahochdruck-Forschung zu erzielen.

Meine Kollegen und ich möchten dem *Freistaat Bayern,* vertreten durch das *Bayerische Staatsministerium für Wissenschaft, Forschung und Kunst*, und der *Kommission für Geowissenschaftliche Hochdruckforschung der Bayerischen Akademie der Wissenschaften* unseren Dank für ihre fortwährende Unterstützung des Bayerischen Geoinstituts aussprechen. Wir sind auch für die großzügige Förderung durch externe Geldgeber dankbar, insbesondere der *Alexander-von-Humboldt-Stiftung,* der *Europäischen Union,* der *Deutschen Forschungsgemeinschaft* und dem *Bundesministerium für Bildung und Forschung,* die

ebenfalls wesentlich zur Entwicklung und zum Erfolg des Bayerischen Geoinstituts beigetragen haben.

Bayreuth, im März 2015 Tomoo Katsura

1. Advisory Board and Directorship

1.1 Advisory Board

The *Kommission für Geowissenschaftliche Hochdruckforschung der Bayerischen Akademie der Wissenschaften* advises on the organisation and scientific activities of the institute. Members of this board are:

Prof. Dr. G. BREY	Institut für Geowissenschaften der Johann Wolfgang Goethe-Universität, Frankfurt am Main
Prof. Dr. U. CHRISTENSEN	Max-Planck-Institut für Sonnensystemforschung, Katlenburg-Lindau
Prof. Dr. R. KNIEP	Institut für Chemische Physik fester Stoffe der Max-Planck-Gesellschaft, Dresden
Prof. Dr. H. PALME	Emeritus, Institut für Mineralogie und Geochemie der Universität zu Köln – Senckenberg Forschungsinstitut und Naturmuseum Frankfurt/M.
Prof. Dr. M. RIEDERER (Chairman)	Julius-von-Sachs-Institut für Biowissenschaften, Würzburg
Prof. Dr. R. RUMMEL (Vice Chairman)	Institut für Astronomische und Physikalische Geodäsie der TU München
Prof. Dr. E. SALJE, FRS, FRSA	Department of Earth Sciences, University of Cambridge
Prof. Dr. H. SOFFEL	Emeritus, Institut für Allgemeine und Angewandte Geophysik der Universität München

The Advisory Board held a meeting in Bayreuth (16.05.2014).

1.2 Leadership

Prof. Dr. Tomoo KATSURA (Director)
Prof. Dr. Dan FROST (Deputy Director)
Prof. Dr. Hans KEPPLER

Fissure eruption at the Bárðarbunga volcanic system in Iceland in September 2014 (courtesy H. Gunnarsson/Reykjavik). Melt inclusions in olivine phenocrysts from the erupted lava (bottom) were studied by Raman and FTIR to understand the volatile budget and the origin of the magma. See the article by E. Bali on page 109.

Spalteneruption des Bárðarbunga-Vulkans auf Island im September 2014 (Photo H. Gunnarsson/Reykjavik). Schmelzeinschlüsse in Olivin-Kristallen aus der geförderten Lava (unten) wurden mit Raman- und FTIR-Spektroskopie untersucht, um den Gasgehalt und den Ursprung des Magmas zu verstehen. Siehe den Artikel von E. Bali auf Seite 109.

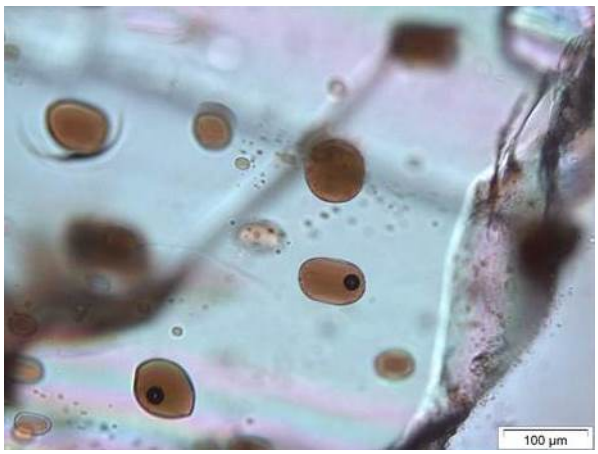

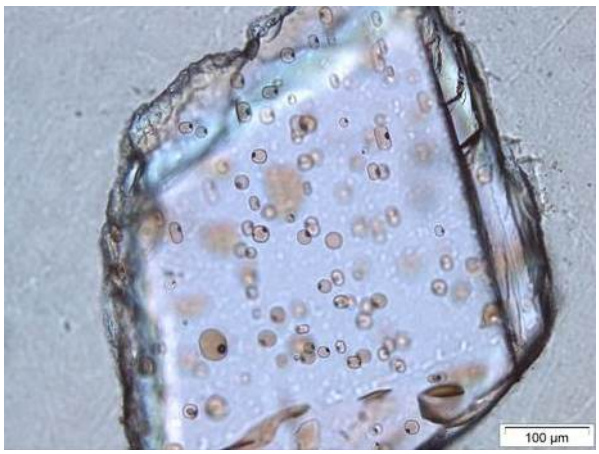

2. Staff, Funding and Facilities

2.1 Staff

At the end of 2014 the following staff positions existed in the Institute:

- Scientific staff: **12**
- Technical staff: **14**
- Administrative staff: **3**
- Administrative officer: **1**

During 2014, 40 scientific positions (313 months) were funded by grants raised externally by staff members of the institute. In addition 8 long-term scientific positions (46 months) were funded by the resources of the BGI Visiting Scientists' Programme (see Sect. 7) which also supported short-term visits for discussing future projects or presenting research results (see Sect. 5). 18 scientists (114 months) were supported by personal grants (stipends).

2.2 Funding

In 2014, the following financial resources were available from the Free State of Bavaria:

- Visiting Scientists' Programme: 218.000 €
- Consumables: 587.000 €
- Investment funding: 833.000 €
- Additional funds from the University of Bayreuth: 15.000 €

The total amount of national/international external funding (*"Drittmittel"*) used for ongoing research projects in 2014 was 2.824.000 € (Positions: 1.634.000 €; equipment, consumables and travel grants: 1.190.000 €).

	positions	**equipment, consumables, travel grants**	**total**
• AvH	177.000 €	57.000 €	234.000 €
• BMBF	250.000 €	463.000 €	713.000 €
• DFG	788.000 €	898.000 €	1.686.000 €
• EU	369.000 €	75.000 €	444.000 €
• Stifterverband	16.000 €	7.000 €	23.000 €
• Others	104.000 €	40.000 €	144.000 €
			3.244.000 €

(AvH = Alexander von Humboldt Foundation; BMBF = Federal Ministry of Education and Research; DFG = German Science Foundation; EU = European Union; Stifterverband = Stifterverband für die Deutsche Wissenschaft; Others: DAAD/PROCOPE, University of Bayreuth, Universität Bayern e.V., Chinese Science Council, Azerbaijan National Academy of Science, Industry)

In the following list only the BGI part of the funding is listed in cases where joint projects involved other research institutions. Principal investigators and duration of the grants are listed in brackets. Total project funding refers to the funding over the entire duration of this project.

Funding institution	Project, Funding	Total Project Funding
BMBF	05K12WC1 (L.S. Dubrovinsky – 8.12 – 7.15) "Single crystal crystallography at extreme pressures and variable temperatures" Total funding:	448.000 €
BMBF	056K13WC4 (L.S. Dubrovinsky – 7.13 – 6.16) "NANORES: Nanofokussierende Röntgenoptiken und Probenumgebungen für die resonante Kernstreuung zum Studium von schnellen Prozessen in Chemie, Biologie und in Materie unter extremen Bedingungen" Total funding:	475.300 €
BMBF	KEI0500009612 (T. Katsura – 7.13 – 6.16) "Aufbau einer experimentellen Station mit einer großvolumigen Hochdruckapparatur an der Damping-Wiggler-Beamline des Deutschen Elektronen Synchrotron (DESY)" Total funding:	1.186.000 €
BMBF	05K13WC1 (H. Keppler – 7.13 – 6.16) "Aufbau einer Hochdruckpresse vom Multi-Anvil-Typ an der Forschungs-Neutronenquelle FRM II in Garching" Total funding:	3.499.590 €
DAAD	Projektbezogener Personenaustausch mit Frankreich (PROCOPE) (C.A. McCammon – 1.13. – 12.14) "Element partitioning in the magma ocean" Travel funding:	6.045 €
DAAD	L.S. Dubrovinsky "Calibration of Sm-borate sensor for high-P,T studies"	3.000 €
DAAD	L.S. Dubrovinsky "Studies of stability of hydrocarbons at Earth mantle conditions"	3.000 €
DCO	Diamonds and the Mantle Geodynamics of Carbon (DMGC) programme of the Deep Carbon Observatory (D.J. Frost – 1.14 – 10.14) "The nature of diamond forming liquids" Positions:	17.500 €

DFG	AU 314/5-1 (A. Audétat – 10.14 – 9.17) "Development of new oxybarometers for silicic magmas" Position: E13/2, 36 months 90.300 € student assistant 5.000 € Consumables: 35.000 € Overhead: 26.100 €	156.400 €
DFG	BO 2550/7-1 (T. Boffa Ballaran, A. Woodland – 8.13 – 7.16) "Crystal chemistry of ferric iron in the deep upper mantle and transition zone" Position: student assistant 5.000 € Consumables and travel funding: 9.500 € Overhead: 2.900 €	17.400 €
DFG	BO 2550/8-1 (T. Boffa Ballaran – 9.14 – 8.16) DFG SPP 'The first 10 Million Years of the Solar System – a Planetary Materials Approach' "Der Einfluss von Mantel Rheologie auf die frühe Differenzierung eisiger Satelliten" Position: E 13, 24 months 127.200 € student assistant 10.000 € Consumables: 12.285 € Equipment: 27.216 € Overhead: 35.300 €	212.001 €
DFG	GO 315/21-1 (A. El Goresy, L. Dubrovinsky – 11.12 – 10.14) "Mineralogical, REE and ^{146}Sm-^{142Nd} isotopic systematics of the earliest solar condensates in unequilibrated enstatite chondrites" Consumables and travel funding: 3.000 € Publication costs: 1.500 € Overhead: 900 €	5.400 €
DFG	HE 3285/2-1 (F. Heidelbach – 4.13 – 3.16) "Reaction kinetics and plastic deformation in mantle rocks" 1 position: 36 months 188.900 € Consumables and travel funding: 21.500 € Overhead: 42.100 €	252.500 €
DFG	KA 3434/3 (T. Katsura – 4.13 – 3.16) "Dislocation recovery experiment of hydrous olivine as a function of water content and crystallographic orientation" 1 position: E 13, 36 months 186.300 € Consumables and travel funding: 20.000 € Overhead: 43.000 €	249.300 €
DFG	Forschungsgroßgeräte (T. Katsura) INST 91/291 "Ultrahochdruck-Vielstempelapparatur"	371.000 €
DFG	Forschungsgroßgeräte (T. Katsura) INST 91/302 "Fräsmaschine für Keramikteile"	241.000 €

DFG	Forschungsgroßgeräte (D.J. Frost) INST 91/315 "Focused Ion Beam Scanning Electron Microscope"	400.000 €
DFG	KE 501/10-1 (H. Keppler – 7.13 - 6.16) "DFG Core Facility: High-pressure laboratories of Bayerisches Geoinstitut" Total funding:	544.600 €
DFG	KE 501/11-1 (H. Keppler – 2013 - 2016) "Electrical conductivity and dissociation of fluids in crust and mantle" Total funding:	267.800 €
DFG	KE 501/8-2 (H. Keppler – 2014 - 2017) "In-situ observation of the crystallization kinetics and texture evolution of basalts" Total funding:	174.000 €
DFG	KO 3958/2-1 (N. de Koker, G. Steinle-Neumann – 2.11 - 3.16) "Thermal and electrical conductivity of iron at planetary core conditions from ab initio computations" Positions: E 13, 36 months 186.300 € student assistant (79 h/month) 12 months 7.965 € Consumables and travel funding: 9.000 € Publication costs: 2.250 € Overhead: 41.100 €	246.615 €
DFG	MA 6287/2-1 (K. Marquardt – 11.14 - 10.15) Travel funding: 7.800 € Overhead: 1.600 €	9.400 €
DFG	MC 3/18-1 (C.A. McCammon, L.S. Dubrovinsky, D.J. Frost – 7.13 - 6.16) "The effect of pressure, temperature and oxygen fugacity on the stability of subducted carbonates and implications for the deep carbon cycle" Positions: E 13/2, 36 months 88.000 € student assistant 5.000 € Equipment, consumables and travel funding: 31.650 € Overhead: 24.900 €	149.550 €
DFG	MC 3/19-2 (C.A. McCammon, S. Gilder – 9.13 - 8.16) DFG SPP 1488 (PlanetMag) "How pressure influences the magnetic properties of titanomagnetite and iron with implications for magnetic anomalies and core fields" Equipment, consumables and travel funding: 6.400 € Overhead: 1.300 €	7.700 €

DFG	OV 110/1-2 (S.V. Ovsyannikov – 9.13 - 8.15) "Structural and electronic properties of sesquioxides at high pressures and temperatures: new forms, new insights and new possible applications" Positions: E 13, 24 months 124.200 € Consumables and travel funding: 20.000 € Overhead: 29.200 €	173.400 €
DFG	RU 1323/2-2 (D.C. Rubie, D.J. Frost, H. Palme – 6.12 - 5.14) "Conditions, timescales and cosmochemical evolution during the early accretion of terrestrial planets" Positions: E 13/2, 24 months 57.300 € Consumables and travel funding: 40.000 € Publication costs: 1.500 € Overhead: 19.600 €	118.400 €
DFG	STE 1105/8-1 (S. Gilder/LMU München, G. Steinle-Neumann, R. Egli and N. Petersen/LMU München – 2.11 - 1.14) DFG SPP 1488 (PlanetMag) "How pressure influences the magnetic properties of titanomagnetite and iron with implications for magnetic anomalies and core fields" Budget (G. Steinle-Neumann): Positions: ¾ E13, 36 months 128.925 € Travel funding: 9.250 €	BGI funding: 138.175 €
DFG	STE 1105/10-1 (G. Steinle-Neumann – 4.14 - 3.17) DFG SPP 1488 (PlanetMag) "Structure and electronic transport properties of metallic liquids at conditions of planetary cores" Positions: E 13, 24 months 125.500 € student assistant 18.798 € Consumables: 9.820 € Overhead: 30.800 €	184.918 €
DFG	Emmy Noether-Programm (H. Marquardt – 2014 - 2019) "Structure and Elasticity of GeoMaterials at Extreme Conditions (GeoMaX)" Positions: group leader, E14/E15, 60 months: 375.400 € post doc, E13, 60 months: 317.200 € 2 PhD students, 2/3 E13, 36 months: 264.400 € student assistant: 11.904 € Consumables, travel funding: 222.550 € Investments: 127.714 € Overhead: 184.400 €	1.503.568 €

DGG	H. Marquardt Reisekostenzuschuss der Deutschen Gesellschaft für Geowissenschaften (Hermann Credner-Stipendium)	2.500 €
EU	European Research Council (ERC) Advanced Grant No. 227893 (D.J. Frost – 2.09 - 6.14) "Deep Earth elastic properties and a universal pressure scale DEEP" Positions, equipment, consumables and travel funding maximum EU contribution:	2.079.888 €
EU	European Research Council (ERC) Advanced Grant No. 290568 (D.C. Rubie – 5.12 - 4.17) "Accretion and Early Differentiation of the Earth and Terrestrial Planets" ("ACCRETE") Positions, consumables and travel funding:	1.826.200 €
EU	Marie Curie – International Incoming Fellowship Grant No. 302637 (A. Rosenthal – 10.12 - 10.14) FATEMANTLE Fellowship, consumables and travel funding	167.370 €
MF	Minerva Foundation (Vojtěch Vlček – 7.14 - 12.14) Short-term research grant for collaboration with Prof. Baer at the Hebrew University of Jerusalem, Israel	1.500 €

2.3 Laboratory and office facilities

The institute occupies an area of

ca. 1350 m^2	laboratory space
ca. 480 m^2	infrastructural areas (machine shops, computer facilities, seminar room, library)
ca. 460 m^2	office space

in a building which was completed in 1994.

2.4 Experimental and analytical equipment

The following major equipment is available at the Bayerisches Geoinstitut:

I. High-pressure apparatus
- 15 MN/1500 tonne Kawai-type multianvil high-pressure apparatus (32 GPa, 2000 K)
- 6 x 8 MN/6x800 tonne independently acting-anvil press (25 GPa, 3000 K)
- 50 MN/5000 tonne multianvil press (25 GPa, 3000 K)
- 15 MN/1500 tonne multianvil press (60 GPa, 3000 K)
- 12 MN/1200 tonne multianvil press (25 GPa, 3000 K)
- 10 MN/1000 tonne multianvil press (25 GPa, 3000 K)
- 5 MN/500 tonne multianvil press (20 GPa, 3000 K)
- 5 MN/500 tonne press with a deformation DIA apparatus
- 4 piston-cylinder presses (4 GPa, 2100 K)
- Cold-seal vessels (700 MPa, 1100 K, H2O), TZM vessels (300 MPa, 1400 K, gas), rapid-quench device
- Internally-heated autoclave (1 GPa, 1600 K)
- High-pressure gas loading apparatus for DAC

II. Structural and chemical analysis
- 1 X-ray powder diffractometer
- 1 X-ray powder micro-diffractometer
- 1 X-ray powder diffractometer with furnace and cryostat
- 2 automated single-crystal X-ray diffractometers
- High-brilliance X-ray system
- Single crystal X-ray diffraction with super-bright source
- 1 Mössbauer spectrometer (1.5 - 1300 K)
- 3 Mössbauer microspectrometers
- 2 FTIR spectrometers with IR microscope
- FEG transmission electron microscope (TEM), 200 kV analytical, with EDS and PEELS
- FEG scanning TEM, 80-200 kV analytical, with 4-SDDs EDS and post-column energy filter (EFTEM/EELS)
- FEG scanning electron microscope (SEM) with BSE detector, EDS, EBSD and CL
- Dual beam device, focused ion beam (FIB) and FEG SEM. In situ easy-lift manipulator, STEM and EDS detector, and beam deceleration option

3 Micro-Raman spectrometers with ultraviolet and visible lasers
Tandem-multipass Fabry-Perot interferometer for Brillouin scattering spectroscopy
JEOL JXA-8200 electron microprobe; fully-automated with 14 crystals, 5 spectrometer configuration, EDX, capability for light elements
193 nm Excimer Laser-Ablation ICP-MS
ICP-AES sequential spectrometer
Water content determination by Karl-Fischer titration
GC/MS-MS for organic analyses
Confocal 3D surface measurement system

III. *In situ* determination of properties

Diamond anvil cells for powder and single crystal X-ray diffraction, Mössbauer, IR, Raman, optical spectroscopy, electrical resistivity measurements up to at least 100 GPa
Facility for in situ hydrothermal studies in DAC
Externally heated DACs for in situ studies at pressures to 100 GPa and 1200 K
1-atm furnaces to 1950 K, gas mixing to 1600 K, zirconia fO2 probes
1-atm high-temperature creep apparatus
Gigahertz ultrasonic interferometer with interface to resistance-heated diamond-anvil cells
Heating stage for fluid inclusion studies
Impedance/gain-phase analyser for electrical conductivity studies
Apparatus for in situ measurements of thermal diffusivity at high P and T
Laser-heating facility for DAC
Portable laser heating system for DAC

IV. Computational facilities

9 node linux cluster (2x3.0 GHz Xeon Woodcrest Dual Core, 8 Gb memory), InfiniBand
8 node linux cluster (16x2.83 GHz Xeon 5440 Quad Core, 64 Gb memory), InfiniBand
32 TB mass storage

The Geoinstitut is provided with well equipped machine shops, an electronic workshop and sample preparation laboratories. It has also access to the university computer centre.

3. Forschungsprojekte

3.1 Struktur und Dynamik der Erde und Planeten

Die inneren Planeten in unserem Sonnensystem ähneln sich in Zusammensetzung und Struktur in dem Sinne, dass sie aus einem metallischen Kern und einer ihn umgebenden Silikatschicht bestehen. Diese Struktur ist eine direkte Folge ihrer Entstehungsgeschichte, die von einem Wachstum durch Zusammenstöße (Akkretion) und einem Absinken von flüssigem Eisen zum Mittelpunkt (Differentiation) geprägt ist. Die Differentiation wird direkt durch Kollisionen und Einschläge begünstigt, da diese Energie freisetzen und den Planeten – zumindest teilweise – aufschmelzen. Durch die weitere Freisetzung von Gravitationsenergie beim Absinken des flüssigen Eisens müssen die terrestrischen Planeten sich zeitweise in einem Magmaozean-Zustand befunden haben, der unter Umständen den gesamten Planeten aufgeschmolzen hat.

Die ersten drei Beiträge in diesem Kapitel behandeln verschiedene Aspekte der Entwicklung von terrestrischen Planeten im frühen Sonnensystem. Im ersten Beitrag wird die Wechselwirkung von Akkretion und Differentiation betrachtet. Dabei wird aufgezeigt, dass Material aus größerer Entfernung im Sonnensystem später als Material aus geringerer Entfernung zu den Planeten hinzugefügt wurde. Da der Sauerstoffgehalt von Material, das aus größerem Abstand zur Sonne stammt, höher ist, kann ein solches Akkretionsszenario zu einer stabilen Dichteschichtung im Erdkern führen. Der Umfang des Aufschmelzprozesses infolge von massiven Kollisionen und die Geschwindigkeit der folgenden Kristallisation wird im folgenden Beitrag untersucht. Dabei ist der Vergleich der Kristallisationsdauer sowie der zeitliche Abstand zwischen Kollisionen von zentraler Wichtigkeit: Wenn der Einschlag in einen Magmaozean erfolgt, stellt der metallische Teil des Impaktors ein chemisches Gleichgewicht mit der Silikatschmelze des Magmaozeans bei hohem Druck her, ansonsten geschieht dies bei Oberflächendruck. Die Zeitskala für die Kristallisation wird dabei nachhaltig durch die Gegenwart einer dichten Dampfatmosphäre bestimmt, die die Kristallisationszeit um mehrere Größenordnungen verlängern kann. Ein anderer Aspekt der Verfestigung des Magmaozeans ist die Sequenz von kristallisierenden Mineralen und das daraus resultierende anfängliche Dichteprofil eines Planeten. Dieser Vorgang wird im dritten Beitrag des Kapitels für den Mars untersucht, mit einer Modellzusammensetzung im FeO-MgO-SiO_2 System: die Kristallisation verläuft von unten nach oben und beginnt mit Ferroperiklas (Mg,Fe)O, was zu einer dichten Schicht im tiefen Mantel von Mars führt. Da im Verlauf der Kristallisation die Schmelze mit FeO angereichert wird und die Minerale relativ FeO-arm kristallisieren, haben die Kristallite ab einer gewissen Tiefe Auftrieb und steigen an die Oberfläche.

Der letzte Beitrag verlässt die frühe Zeit der Planetenentstehung und behandelt eine geochemische Fragestellung der modernen Erde: Basalte von Ozeaninseln sind wasserhaltiger als Gesteine des oberen Erdmantels. In Experimenten und thermodynamischen Modellen wird die Dehydrierung von Mineralen im System Al_2O_3-SiO_2-H_2O bei Bedingungen des tiefen

Erdmantels untersucht, als Näherung für das basische Gestein in einer subduzierenden Platte. In diesem System treten Mineralphasen auf, die als Wasser-Puffer dienen können: Bei Erhöhung des Drucks in Folge von Subduktion wird von ultrabasischen Mineralen Wasser freigesetzt, das in Al-reiche Minerale eingebunden werden kann. Bei Manteldiapiren, die als Ursache für Ozeaninseln betrachtet werden, wird das Wasser wieder in die Minerale des ultrabasischen Mantelgesteins verteilt.

3.2 Geochemie

Meteorite können als Überreste des Baumaterials des inneren Sonnensystems angesehen werden; sie stellen eine Momentaufnahme der Entwicklungsgeschichte und der Prozesse während der ersten 10 Millionen Jahre unseres Sonnensystems dar. Meteorite werden als „differenziert“ bzw. „undifferenziert“ klassifiziert, je nachdem, ob es nach der Akkretion zur Aufschmelzung der Silikate, zur Abtrennung von Metallen und zur Ausbildung magmatischer Texturen gekommen ist. Im ersten Artikel dieses Kapitels wird die Mineralogie eines kürzlich aufgefundenen differenzierten Meteoriten beschrieben, der früher einmal bereits einer anerkannten Meteoritenfamilie zugeordnet worden war. Dieser Interpretation wird hier widersprochen. Überraschend war der Befund, dass es sich hier um einen stark reduzierten Meteoriten handelt, d. h. dass die Silikatminerale nur geringe Eisenoxidanteile aufweisen. Als plausibler Mutterplanet dieses Meteoriten könnte der Planet Merkur in Frage kommen.

Das finale Stadium im Planetenzuwachs (Akkretion) sollte massive Einschläge von planetengroßen Körpern beinhalten. Die bevorzugte Erklärung für die Entstehung des Mondes beruht auf einem derartigen Impakt, jedoch haben große Gemeinsamkeiten in der Zusammensetzung von Erde und Mond stets Zweifel an dieser Hypothese geweckt. Gemäß der gängigen Ansicht sollte der Mond überwiegend aus Material des Impaktors bestehen und im Vergleich zur Erde unterschiedliche Sauerstoff-Isotopien aufweisen, da er sich in einem unterschiedlichen heliozentrischen Abstand bildete. Der zweite Beitrag befasst sich mit Simulationen zum Planetenwachstum, ausgehend von einer Scheibe aus Materie des inneren Sonnensystems mit einem realistischen Gradienten bezüglich der Sauerstoffisotope. Er kommt zu dem Schluss, dass sich die Zusammensetzungen der Erde und des Riesenimpaktors wahrscheinlich nur gering unterschieden haben. Diese Erkenntnis würde Diskussionen darüber obsolet machen, ob die Materie, aus der Erde und Mond entstanden sind, während des Impaktes eine chemische Homogenisierung auf bisher unbekannte Art erfahren hat.

Auch nach dem Riesenimpakt muss sich weiter Material an der Erde akkretiert haben; ein Hauptstreitpunkt ist jedoch, inwieweit dieses spät akkretierte Material in die Bildung des Erdkerns einbezogen wurde. Der Erdmantel weist nämlich ein Überangebot an sogenannten hoch-siderophilen (Eisen-liebenden) Elementen auf, die bei der Kernbildung stark in den Erdkern fraktionierten. Diese Elemente konnten nur dann im Erdmantel verbleiben, wenn bei ihrer Akkretion die Kernbildung bereits abgeschlossen war. Die folgende Studie hat zum Ziel, die Menge der zuletzt akkretierten Materie dadurch zu bestimmen, indem sie untersucht, ob

hoch-siderophile Elemente auch mittels Sulfidschmelzen in den Erdkern abgeführt werden konnten. Genauere Kenntnisse darüber sind sehr wichtig, weil flüchtige Bestandteile wie Wasser und Kohlendioxid wahrscheinlich ebenfalls in einem späten Akkretionsstadium der Erde zugeführt wurden.

Drei weitere Artikel befassen sich mit der Speziation und dem Einfluss von dreiwertigem Eisen (Fe^{3+}, Fe_2O_3) im Erdmantel. Über Bridgmanit, das Hauptmineral des unteren Erdmantels, wird berichtet, dass er sehr große Anteile von Eisen(III) enthält. Mit einer neu entwickelten Methodik wurde in der ersten dieser drei Studien untersucht, wo Eisen(III) in der Bridgmanit-Struktur bei hohem Druck und Temperatur eingebaut ist. Es wird gezeigt, dass sich die Position und der Gehalt von Eisen(III) unter extremen Bedingungen wenig verändern. Ergebnisse der zweiten Studie lassen erkennen, dass Bridgmanit unter Eisen(III)-reichen Bedingungen eine sehr viel niedrigere Schmelztemperatur aufweist als erwartet. Dieser Effekt könnte für die Basis des unteren Mantels eine Rolle spielen, wo sehr geringe seismische Wellengeschwindigkeiten das Vorhandensein von Schmelze anzudeuten scheinen. Der sich anschließende Bericht befasst sich mit dem Verhalten von Eisen(III) während Aufschmelzprozessen unterhalb mittelozeanischer Rücken. Es wurde beobachtet, dass Eisen(III) bei hohen Sauerstofffugazitäten bevorzugt in die Schmelzphasen fraktioniert, während es bei niedrigen Sauerstofffugazitäten bevorzugt in die Mineralphasen fraktioniert. Diese Verhaltensänderung könnte erklären, weshalb Magmen von mittelozeanischen Rücken relativ konstante Eisen(III)-Gehalte aufweisen, während viele andere Neben- und Spurenelemente vom Grad der Aufschmelzung im Mantel beeinflusst sind.

Die nächsten drei Studien widmen sich der Entstehung von Diamanten im oberen und unteren Erdmantel. Der erste Beitrag untersucht das Stabilitätsfeld von Diamant in karbonathaltigen Schmelzen, um die Bedingungen einzugrenzen, unter denen sich Diamanten in subduzierter, karbonatführender ozeanischer Kruste bilden können. Kenntnisse darüber sind von Bedeutung, da Karbonatschmelzen mobil sind und Kohlenstoff schnell an die Erdoberfläche zurückliefern können. Diamanten hingegen sind refraktär, weshalb ihre Bildung eine Fixierung von Kohlenstoff in subduzierten Platten erlauben würde und somit Kohlenstoff sehr weit in das Erdinnere transportiert werden könnte. Eine andere Studie befasst sich mit dem Wachstumsmedium von Diamanten aus der Übergangszone oder dem unteren Mantel; dazu soll experimentell dieselbe Mineralparagenese reproduziert werden, die als Einschlüsse in den Diamanten auftritt. Es wurde festgestellt, dass die charakteristische Mineralparagenese von Diamant-Magnesiowüstit-Bridgmanit-Stishovit-Karbonatmineralen unter Bedingungen stabil ist, die dem obersten Bereich des unteren Erdmantels entsprechen, wo sie mit Silikatschmelzen koexistiert, die $\geq$ 30 Gew. % gelöstes Karbonat enthalten. Die letzte der Diamantstudien hat das sogenannte „Stishovit-Paradoxon“ im Fokus; d. h. die augenscheinliche Koexistenz von Stishovit, der Hochdruckmodifikation von SiO_2, mit dem Mineral Ferroperiklas, (Fe,Mg)O, in Diamanteinschlüssen. Diese Mineralparagenese sollte nirgendwo im Erdmantel stabil sein, da die Phasen miteinander reagieren und intermediäre

Silikatminerale ausbilden sollten. Es konnte jedoch gezeigt werden, dass sich diese Mineralparagenese dennoch ausbilden kann, und zwar durch eine sogenannte peritektische Schmelzreaktion im System SiO_2-MgO-FeO.

Die nachfolgenden vier Artikel dieses Kapitels handeln von Phasenbeziehungen und Elementverteilungen im oberen Erdmantel. Im ersten wird die Verteilung von Fluor zwischen Granat, Klinopyroxen und Silikatschmelze unter Bedingungen untersucht, die für in große Tiefen subduzierte Ozeankruste repräsentativ sind. Es wurde festgestellt, dass Klinopyroxen wesentlich mehr Fluor einbauen kann als andere verbreitete Mantelminerale und somit einen Großteil des Fluors in die Übergangszone transportieren kann; dort kann es entweder in geringgradige Teilschmelzen wie Lamproite fraktionieren, oder von Hochdruckmineralen wie Ringwoodit oder Wadsleyit aufgenommen werden. In Fortsetzung einer systematischen Untersuchung H_2O-reicher Teile im MgO-SiO_2-H_2O-System, beschreibt der nächste Beitrag Experimente unter Bedingungen entsprechend der Basis des oberen Erdmantels. Sie sollen unsere Kenntnisse zur Zusammensetzung wassergesättigter Schmelzen vergrößern, die eventuell unter diesen Bedingungen gebildet werden. Das danach beschriebene Projekt erforscht die Stabilität wasserhaltiger und nominell wasserfreier Minerale in eklogitischen Gesteinen. Ziel ist, die Wasseranteile zu quantifizieren, die von nominell wasserfreien Mineralen aufgenommen werden, wenn wasserführende Minerale wie Phlogopit zerfallen. Mit dieser Methode kann die Wassermenge bestimmt werden, die in den tiefen Erdmantel hinab subduziert werden könnte.

Auf Phasenbeziehungen von Kohlenwasserstoffen und ihre Wechselbeziehung mit Eisenkomponenten in Mineralen des Erdmantels zielt der sich anschließende Beitrag. Redox-Reaktionen zwischen Kohlenwasserstoffen und Mineralphasen wurden als temperaturabhängig erkannt. Letztlich können diese Untersuchungen bei der Klärung des Schicksals von subduziertem organischem Material helfen.

Die beiden letzten Beiträge dieses Kapitels befassen sich mit der Bildung von Erzlagerstätten. Durch Untersuchungen von Fluid- und Schmelzeinschlüssen in Proben aus der porphyrischen Molybdänlagerstätte Climax (USA) werden in der ersten Studie physiko-chemische Eigenschaften der erzbringenden Magmen und Fluide rekonstruiert. Die mineralisierenden Schmelzen und Fluide weisen keine ungewöhnlich hohen Mo-Gehalte auf, was annehmen lässt, dass der Schlüssel für die wirtschaftliche Anreicherung des Molybdäns in einer ungewöhnlich effizienten Auslaugung der Restschmelzen zu finden ist. In der letzten Studie stehen Fluideinschlüsse im Fokus. Hier wird die Genese von Magnetit (-Apatit)-Lagerstätten entlang des Yangtse-Flusses in China untersucht. Auf der Basis der Haupt- und Spurenelement-Zusammensetzung von salzreichen Fluideinschlüssen sowie der Isotopensignatur von Schwefel aus Sulfidmineralen dieser Erzvorkommen wird gezeigt, dass Assimilation evaporitischer Ablagerungen durch aufsteigende Magmen eine wichtige Rolle bei der Bildung dieser Lagerstätten gespielt hat.

3.3 Mineralogie, Kristallchemie und Phasenübergänge

Zu erkennen, wie Kristalle auf Veränderungen von Druck, Temperatur und chemischer Zusammensetzung reagieren, ist für das Verständnis ihrer physikalischen und chemischen Eigenschaften von fundamentaler Bedeutung. Eine der dramatischsten Reaktionen auf derartige Veränderungen sind Phasenübergänge. Nahezu alle Minerale sind unter den hohen Drücken und Temperaturen, wie sie im Innern von Planeten herrschen, in sehr starkem Maß von solchen Umwandlungsprozessen betroffen. In diesem Kapitel wird dargestellt, wie das Bayerische Geoinstitut versucht, dem Einsetzen von Phasenübergängen auf die Spur zu kommen, um die Reaktionen so verschiedenartiger Minerale wie Eisenoxiden, Silikaten und Karbonaten auf erhöhte Drücke, Temperaturen und unterschiedliche Sauerstofffugazitäten zu identfizieren.

Das Kapitel beginnt mit Untersuchungen zu Phasenstabilitäten und -beziehungen mit Hilfe von Hochdruckexperimenten, entweder durch Messungen an von hoher Temperatur abgeschreckten Versuchsprodukten nach der Synthese oder durch *in situ* Messungen in Diamantstempelzellen. Eisen ist das wichtigste Übergangselement in der Erde, so dass die Entdeckung eines neuen Eisenoxids, Fe_4O_5, einen neuen Impuls ausgelöst hat, Eisenoxide bei hohen Drücken zu untersuchen. Untersuchungen an einfachen Eisenoxiden wie Fe_2O_3 und Fe_3O_4 liefern Einblicke in die Phasenübergänge, die gebänderte Eisenformationen bei der Subduktion in den tiefen Erdmantel erfahren. Das gut untersuchte Endglied mit der Zusammensetzung $MgFe_2O_4$ zerfällt zugunsten eines neuen Mg-Endglieds der Fe_4O_5-Phase, für das durch Einkristall-Strukturverfeinerung mit Röntgenstrahlung eine komplette Beschreibung der Kristallstruktur möglich wurde. Die neue Entdeckung eines weiteren Hochdruck-Polymorphs mit $(Mg,Fe^{2+})_3Fe^{3+}{}_4O_9$ führt zu der Annahme, dass weitere stöchiometrisch zusammengesetzte Eisenoxide mit unterschiedlichen Fe^{2+}/Fe^{3+}-Verhältnissen ebenfalls bei hohen Drücken und Temperaturen stabil sind. Untersuchungen zu Eisen-Granat mit der Zusammensetzung $Fe^{2+}{}_3Fe^{3+}{}_2Si_3O_{12}$ mit gemischten Valenzen sind für Modelle zur Sauerstofffugazität für granatführende Gesteinskomplexe wichtig, besonders seit bekannt ist, dass das Vorhandensein von Fe^{3+} in Granat Temperatur- und Druckabschätzungen beeinflussen kann; das gilt insbesondere für Abschätzungen, die auf Gleichgewichten aus dem Mg/Fe-Austausch beruhen. Stabilitätsuntersuchungen an Fe-Karbonaten wie Siderit ($FeCO_3$) ermöglichen Einblicke in den tiefen Kohlenstoff-Kreislauf; Ergebnisse entsprechender Experimente deuten darauf hin, dass Fe-reiche Karbonate in Regionen mit oxidierenden Verhältnissen bis hinunter zur Mantel/Kern-Grenze bestehen können. Die Sauerstofffugazität beeinflusst das $Fe^{3+}/\Sigma Fe$-Verhältnis in Chromiten stark, der bestimmende Faktor für das exakte Verhältnis wird dabei durch die Phasenvergesellschaftung bestimmt. Der Temperatureinfluss auf den Phasenübergang in H_2O-führendem $MgSiO_3$-Klinoenstatit zeigt sich stärker in *in situ*-Experimenten als bei experimentell abgeschreckten Proben, woraus sich Konsequenzen für die Erforschung der Ursache der X-Diskontinuität ergeben.

Der anschließende Beitrag thematisiert die Anwendung kristallchemischer Parameter in der Planetologie. Untersuchungen eines Eisenmeteoriten ergaben, dass sogenannter hexagonaler Diamant („Lonsdaleit“) möglicherweise keine individuelle Phase darstellt, sondern

stattdessen der normalen kubischen Phase zugehört, jedoch extensiv Stapelfehler und Zwillinge im Nanometermaßstab aufweist. Orthogonale Zwillingslamellen in monoklinem Baddeleyit aus dem Marsmeteoriten Shergotty bieten eindeutige Hinweise auf eine Entstehung in Verbindung mit mehrfachen Phasenübergängen aus dichteren Polymorphen. Andere Untersuchungen an Hochdruck-Polymorphen des Coesit liefern genauere Abgrenzungen in dem Phasendiagramm für metastabilen Quarz, die als potentielle Indikatoren für kurzzeitige Extremdrücke bei Ereignissen wie Impakten oder Brüchen in geschockten Meteoriten dienen können.

Die abschließenden Beiträge dieses Kapitels zielen auf den Einsatz von Einkristallen zur Messung physikalischer und chemischer Eigenschaften. Aufgrund eines methodischen Durchbruchs in der Kristallzüchtung unter hohem Druck konnten große Einkristalle von Wadsleyit dazu verwendet werden, die Elastizität dieses Minerals bei hohen Drücken zu bestimmen sowie die Gitterposition von Wasserstoff-Atomen in wasserführendem Wadsleyit zu ermitteln. Der Spurenelementgehalt von Quarz ist ein bedeutender petrogenetischer Indikator bei der Titan-in-Quarz (TitaniQ)-Thermobarometrie für die Rekonstruktion von Temperatur und Druck während der Quarzkristallisation. Die Bestimmung eines optisch homogenen, natürlichen Rauchquarzes auf 24 Spuren- und Ultraspurenelemente wurde dadurch ermöglicht.

3.4 Physikalische Eigenschaften von Mineralen

Kompressions- und Scherwellen in Mineralen des Erdmantels unter hohen Drücken und Temperaturen im Labor zu bestimmen ist notwendig, um seismische Geschwindigkeiten zu interpretieren und dadurch die chemische Zusammensetzung des Erdinneren einzugrenzen. Experimentell gewonnene Daten über elastische Mineraleigenschaften dienen dazu, die Parameter für thermo-elastische Zustandsgleichungen genauer zu bestimmen, die für die Aufstellung seismischer Modelle zum Vergleich mit beobachteten seismischen Laufzeiten von wesentlicher Bedeutung sind. Eine akzeptierte Methode zur Bestimmung druckabhängiger Veränderungen von elastischen Eigenschaften unterschiedlicher Materialien stellt die Brillouin-Spektroskopie dar; jedoch ist deren Anwendung bei gleichzeitigem hohem Druck und hoher Temperatur immer noch begrenzt. In den ersten drei Beiträgen dieses Kapitels wird eine verbesserte Methodik vorgestellt, die es ermöglicht, mit Hilfe der neu am BGI installierten fokussierten Ionensonde (FIB) Einkristalle für Hochdruck-Hochtemperaturexperimente zu präparieren. Kleiner als 100 µm große Scheiben und Scheiben in Halbkreisform wurden mit der FIB aus orientierten, doppelseitig polierten Einkristallen von Wadsleyit, Ringwoodit und Bridgmanit herausgearbeitet und in Diamantstempelzellen, die mit am BGI entworfenen und weiter entwickelten Heizelementen kombiniert sind, eingebracht. Der Vorteil dieses Verfahrens kommt besonders für Proben mit einer niedrigen Symmetrie wie Wadsleyit und Bridgmanit zum Tragen, da zur genaueren Bestimmung des vollständigen elastischen Tensors stets mindestens zwei Kristalle mit zueinander rechtwinkligen Orientierungen unter gleichen Druck-und Temperaturbedingungen gehalten werden müssen. Mit den Halbscheiben besitzen die Proben eine perfekte Form für eine

gemeinsame Einpassung in die kreisförmige Öffnung der Dichtungsscheibe der Diamantstempelpresse.

Die Minerale des Erdmantels stellen häufig komplexe Mischkristallreihen zwischen mehreren Endgliedern dar. Um präzise mineralogische Modelle zu konstruieren, muss daher der Einfluss bestimmt werden, den verschiedene Kationensubstitutionen auf die thermoelastischen Parameter der Zustandsgleichungen ausüben. Die Beiträge vier und fünf behandeln omphazitische Klinopyroxene, die auch *Ca-Eskola-* und *Ca-Tschermak-*Komponenten enthalten, sowie Majorit-Granat im System Pyrop-Majorit-Almandin. Die Wellengeschwindigkeiten für diese Proben wurden an Synchtrotron-Einrichtungen bestimmt. Für Messungen an Klinopyroxen kam eine Multianvil-Presse zum Einsatz, für die Granatmessungen die Brillouin-Spektroskopie. Bei beiden Verfahren wurde gleichzeitig die Dichte mit Hilfe von Röntgenbeugungsanalysen bestimmt. Mit den erzielten Ergebnissen lassen sich die seismischen Eigenschaften des oberen Erdmantels und der Übergangszone eingrenzen. Ein Hauptergebnis ist, dass wegen der Anteile von Granat die seismischen Wellengeschwindigkeiten an der Basis der Übergangszone niedriger zu sein scheinen, als aus Referenzmodellen entlang der 1673 K Adiabate abzulesen ist; es scheinen also in dieser Region große Temperaturanomalien zu bestehen, die durch das Vorhandensein von stagnierenden Krustenplatten verursacht sein könnten.

Weitere Experimente an Synchrotron-Einrichtungen zur Messung von Debye-Schallgeschwindigkeiten in Siderit ($FeCO_3$) mithilfe inelastischer Kernstreuung (NIS) sowie Dichtebestimmungen von amorphem $MgSiO_3$ durch Röntgenabsorption werden in den zwei folgenden Artikeln beschrieben. Wesentliche Veränderungen zeigen sich in den Debye-Schallgeschwindigkeiten in Verbindung mit dem Übergang von *high-spin* nach low-*spin* im Eisen des Siderits bei hohen Temperaturen; dies scheint ein vielversprechender Ansatz zu sein, um das Vorhandensein von Karbonat in Krustenplatten, die in den unteren Mantel subduziert werden, nachzuweisen. Zwischen amorphem und kristallinem $MgSiO_3$ ließ sich bei 130 GPa ein kleiner Dichteunterschied feststellen, was im Gegensatz zu bisher veröffentlichten Ergebnissen steht. Die Ergebnisse liefern wichtige Hinweise für die Interpretation des Dichtekontrasts zwischen festen und schmelzflüssigen Silikaten an der Basis des unteren Erdmantels.

Will man Genaueres über Wärmediffusion im Erdinneren und ihren Einfluss auf den Geodynamo wissen, muss man sowohl die thermische als auch die elektrische Leitfähigkeit von Eisen unter den extremen Druck- und Temperaturbedingungen des Erdkerns kennen. Diese Eigenschaften sind aber wegen der sehr anspruchsvollen experimentellen Erfordernisse bisher kaum bekannt. Untersuchungen zu Veränderungen des elektrischen Widerstands und der isothermischen Kompressibilität für unterschiedliche Metalle entsprechend der Ziman-Theorie werden im achten Artikel vorgestellt. Die Ergebnisse zeigen, dass sich ein derartiger Ansatz dazu verwenden lässt, die Druck/Temperatur-Abhängigkeit des elektrischen Widerstands entlang der Schmelzkurve von Eisen zu bestimmen, um daraus den Widerstand schmelzflüssiger und fester Anteile von planetaren Eisenkernen abzuleiten.

Physikalische Eigenschaften der Minerale werden durch ihre Kristallstruktur kontrolliert, die eine Hauptrolle bei der Festlegung von Größe und Ladung des Atombestands spielt. Der vorletzte Beitrag verdeutlicht, wie stark die Kristallchemie des in Meteoriten aufgefundenen Minerals Hibonit eine Stabilisierung von Ti^{4+} - Mg^{2+}-Paaren auch unter sehr reduzierenden Bedingungen des solaren Nebels beeinflusst. Andererseits werden die Eigenschaften der Gesteine nicht nur durch die Eigenschaften ihres Mineralbestands beeinflusst, sondern auch durch die Flächenverteilung von Korngrenzen zwischen den Mineralkörnern. Zum Schluss wird die anisotrope Flächenverteilung von Korngrenzen in einem isostatisch komprimierten Forsteritaggregat beschrieben.

3.5 Fluide, Schmelzen und ihre Wechselwirkung mit Mineralen

Bei Vulkanausbrüchen werden große Mengen an Wasser, Kohlendioxid, Chlorwasserstoff und Schwefeldioxid in die Atmosphäre freigesetzt. Der gesamte HCl-Ausstoß durch Vulkane ist so groß, dass er die Ozonschicht in der Stratosphäre erheblich schädigen könnte. Es ist jedoch ungeklärt, welcher Anteil des von Vulkanen freigesetzten HCl letztlich die Stratosphäre erreicht. Der erste Beitrag dieses Kapitels zeigt, dass durch Adsorption an der Oberfläche von Aschen unter bestimmten Bedingungen der größte Teil des HCl aus der Eruptionssäule entfernt werden kann. Interessanterweise nimmt die HCl-Adsorption mit der Temperatur zu, während frühere Untersuchungen gezeigt hatten, dass die Adsorption von SO_2 mit der Temperatur abnimmt. Dies bedeutet, dass HCl und SO_2 bei der Adsorption fraktioniert werden und dass sich der Fraktionierungsfaktor über einen Temperaturbereich von nur 300 K um fünf Größenordnungen ändert. Dieser Effekt muss berücksichtigt werden wenn man die Zusammensetzung vulkanischer Gase aus Analysen vulkanischer Aschen ableitet. Im Jahr 2014 erfuhr die Spalteneruption des Bárðarbunga auf Island eine erhebliche Resonanz in den Medien. Ein kurzer Beitrag in diesem Jahresbericht beschreibt erste Messungen des H_2O- und CO_2-Gehalts des Magmas vor und nach der Entgasung. Ergebnisse der Untersuchungen von Flüssigkeitseinschlüssen zeigen, dass die Entgasung des Magmas in einer Tiefe von ca. 9 km begonnen haben muss und dass das Magma daher nicht, wie diskutiert wurde, aus einer flachen Magmakammer in der Oberkruste stammen kann. Ein dritter Beitrag versucht die Schwefelmenge zu quantifizieren, die durch Magmen in Subduktionszonen freigesetzt wird. Hier könnte Anhydrit ($CaSO_4$) den größten Teil des Schwefels binden und ihn damit für eine schnelle Entgasung nicht mehr verfügbar machen. Ein neues quantitatives Modell der Anhydrit-Löslichkeit in Magmen ermöglicht nun eine vollständige Quantifizierung dieses Effekts. Modellrechnungen für die Pinatubo-Eruption im Jahr 1991 ergeben, dass die Entgasung von Schwefel durch eine leichte Depolymerisation der Schmelze gefördert wird, weil hierdurch Anhydrit destabilisiert wird. Kohlenmonoxid ist ein Bestandteil vulkanischer Gase der bisher wenig Aufmerksamkeit erfahren hat, da CO normalerweise nur als Spurenkomponente auftritt. Jedoch könnte Kohlenmonoxid eine bedeutende Rolle bei der Entgasung von Planeten unter reduzierten Bedingungen spielen, wie z. B. bei dem Mond. Ein Beitrag betrachtet daher im Detail die Speziation von

Kohlenmonoxid in Silikatschmelzen und Gläsern. Es konnte gezeigt werden, dass keine starke Wechselwirkung von Kohlenmonoxid mit Eisen in der Schmelze besteht, wie früher vorgeschlagen wurde.

Zur Vorhersage von Vulkanausbrüchen sind genaue Erkenntnisse über Volumen, Lage und Wasseranteil eines Magmas in seinem unterirdischen Reservoir erforderlich. Weil Silikatschmelzen relative gute elektrische Leiter darstellen und weil ihre Leitfähigkeit mit dem Wassergehalt sehr stark zunimmt, werden magneto-tellurische Methoden, mit der die elektrische Leitfähigkeit in der Erdkruste und im oberen Mantel bestimmt wird, bei der Erforschung aktiver Vulkane routinemäßig eingesetzt. Diese Methoden setzten voraus, dass die Leitfähigkeit der Schmelze als Funktion von Druck, Temperatur und Wassergehalt experimentell kalibriert wird. Zwei Beiträge dieses Kapitels stellen daher neue Leitfähigkeitsdaten für rhyolithische und dazitische Schmelzen vor. Die Daten werden angewandt, um die Zustände in den Magmenkammern unterhalb dreier Vulkane einzugrenzen, dem Uturuncu in Bolivien, Usu in Japan und Mt. St. Helens in den USA.

Diffusion in Silikatschmelzen kontrolliert die Zeitskalen zahlreicher geologischer Prozesse. Ein weiterer Artikel in diesem Jahresbericht beschreibt Untersuchungen zur Druckabhängigkeit von Diffusionskoeffizienten in Silikatschmelzen und in geschmolzenem Eisen; dadurch sollen die Zeitskalen und Prozesse der Kernbildung innerhalb von Planeten besser verstanden werden. Eine komplexe Abhängigkeit des Eigendiffusionskoeffizienten von Si vom Druck wurde beobachtet; dies wird mit Veränderungen der Koordination in der Schmelze um 10 GPa in Zusammenhang gebracht.

Die beiden abschließenden Beiträge dieses Kapitels behandeln die Speicherung von Wasser und Wasserstoff im Erdmantel. Gewöhnlich liegt Wasserstoff in gelöster Form als OH-Gruppen in Mineralen des Erdmantels vor. Unter sehr reduzierenden Bedingungen ist dies jedoch nicht mehr möglich und molekularer Wasserstoff (H_2) könnte als eine bedeutende Spezies in Mineralen auftreten. Tatsächlich scheint H_2 eine messbare Löslichkeit in Olivin und Pyroxen zu haben, die jedoch um Größenordnungen kleiner ist als die Wasser/OH-Löslichkeit bei oxidierenderen Bedingungen. Diese Daten zeigen, dass Wasserstoff nur im Silikatanteil eines Planeten verbleibt, falls während der Akkretion oxidierende Bedingungen vorherrschten. Der letzte Beitrag in diesem Kapitel liefert neue Daten zur Wasserlöslichkeit in Granat, Stishovit sowie in Bridgmanit, dem wichtigsten Mineral des unteren Erdmantels.

3.6 Rheologie

Einsichten in die Dynamik und die Entstehung der Erde sind nur möglich, wenn die rheologischen Eigenschaften des Mineralbestands und der Mineralvergesellschaftung bekannt sind. Mineralphasen und ihre Eigenschaften verändern sich bei zunehmendem Druck und Temperatur im tiefen Erdinneren. Das BGI verwendet und optimiert Methoden, um

rheologische Eigenschaften der Erdmaterie unter diesen Bedingungen zu erfassen und zu quantifizieren. Die Ergebnisse erlauben die Interpretationen geophysikalischer und geochemischer Daten und liefern wertvolle Eingangsparameter für geodynamische Modellierungen. Obwohl im Labor Verformungsraten üblicherweise 10^{-4}~$10^{-4\text{-}5}s^{-1}$ betragen und damit 7-8 Größenordnungen über natürlichen Verformungsraten von 10^{-12} s^{-1} liegen, werden Verformungsprozesse durch verschiedene Defektvarianten (Punkt-, Linienfehler, planare Defekte) kontrolliert. Defekt-Eigenschaften sind gut bekannt, so dass deren experimentelle Identifizierung und Quantifizierung genutzt werden können, um Deformation auch in geologischen Zeitskalen zu erklären. Die Mehrzahl der in diesem Kapitel beschriebenen Projekte führt Verformungsexperimente an relevanten Mineralen und Gesteinen über einen breiten *P-T*-Bereich mit Multianvil-Pressen (6-achsige Anordnung) und Diamantstempelzellen durch.

Der erste Beitrag des Kapitels zielt darauf, Mechanismen zu identifizieren, die die Festigkeit der Lithosphäre herabsetzen und Plattentektonik in Modellen zulassen. Aktuelle Untersuchungen zeigen, dass im Vergleich zu Aggregaten aus reinem Olivin ein Gemenge aus Enstatit und Olivin zu einer Herabsetzung der rheologischen Festigkeit führt. Verformung in mehrphasiger Materie ruft Änderungen in der Reaktionsgeschwindigkeit hervor. Der zweite Beitrag zeigt, dass bei der Reaktion von Spinell-Peridotit zu Granat-Peridotit bei gleichzeitiger Verformung weiterer Granat gebildet wird.

Das BGI betreibt an der Neutronen-Forschungseinrichtung des Heinz Maier-Leibnitz Zentrums (MLZ) in Garching eine großvolumige 6-Stempel-Hochdruckpresse für Neutronenstreuung und -radiographie. Der dritte Beitrag informiert darüber, wie diese „SAPHiR“-Apparatur Untersuchungen kristallographischer Vorzugsorientierungen („CPO“) in Olivin bei niedrigeren Verformungsraten von circa 10^{-7} s^{-1} dient. Aus den Ergebnissen ist kein eindeutiger Erhalt von Texturen des A-Typs zu erkennen; CPOs vom B-Typ aus früheren Untersuchungen können auch bei niedrigeren Verformungsgeschwindigkeiten beobachtet werden. Niedrige seismische Geschwindigkeiten im oberen Bereichen subduzierter Platten werden teils als hydratisierte, mafische Gesteinskomplexe interpretiert, die Lawsonit enthalten. Untersuchungen zur Bildung kristallographischer Vorzugsorientierungen in Lawsonitaggregaten beobachten lediglich eine schwache CPO-Bildung. Der fünfte Artikel informiert über Studien zu Verformungsmechanismen in Subduktionskanälen bei hohem Druck; es hat sich gezeigt, dass im Verlauf der Subduktion ein Übergang von oblater zu prolater Verformung auftritt. Der sechste Beitrag präsentiert Untersuchungen, bei der durch radiale Röntgenbeugungsmethoden gezeigt werden konnte, dass die Festigkeit von Ferroperiklas bei Drücken, die dem unteren Erdmantel entsprechen, steigt. Eine sich daraus ergebende Viskositätszunahme in Arealen mit hohen Spannungen kann eventuell zur Stagnation abtauchender Schollen führen.

Verformungsmechanismen unter extremen Druck- und Temperaturbedingungen, wie sie extrasolaren Planeten entsprechen, wurden mit einem neuen Ansatz der Einkristall-

Röntgendiffraktometrie bei hohen Drücken untersucht, um Spannungs-Verformungs-Beziehungen in Eis-VI zu bestimmen. Für die in Erdtiefen zwischen 200 und 300 km beobachtete Abnahme der seismischen Wellengeschwindigkeiten wird eine Umordnung der CPO in Olivin verantwortlich gemacht. Jedoch ist ein druckinduzierter Übergang vom [100](010)-Gleitsystem zum [001](010)-Gleiten unwahrscheinlich, da beide eine ähnliche Druckabhängigkeit aufweisen, wie im achten Artikel dieses Kapitels gezeigt wird. Untersuchungen zur Versetzungsmobilität sind Thema des abschließenden Beitrags. Bei 1500K und 3 GPa ist die Versetzungsmobilität proportional zum Wassergehalt potenziert mit 1.2, was bisherige Ergebnisse aus Deformationsstudien unterstützt.

3.7 Materialwissenschaften

Historisch betrachtet wurden Methoden für Hochdruckexperimente zuerst entwickelt, um den Zustand und Prozesse im tiefen Erdinneren zu verstehen. In einem beachtlichen Umfang haben die Interpretation solcher Experimente und die darauf aufbauende Simulation von Prozessen im Innern von Planeten auch zur Entwicklungen von theoretischen Methoden und Simulationstechniken beigetragen, einschließlich solcher, die *ab-initio* Berechnungen von Materialeigenschaften erlauben, d. h. ohne Information aus Experimenten auskommen. Auf diese Entwicklungen aufbauend haben Physiker, Chemiker und Materialwissenschaftler die Methoden aus den Geowissenschaften übernommen und begonnen, das Verhalten von Materialien unter hohem Druck zu untersuchen. Am Bayerischen Geoinstitut steht eine Kombination von theoretischen Methoden, Hochdruck-Geräten und Analysemethoden, sowohl *in-* als auch *ex situ*, zur Verfügung, die es erlaubt, komplexe und herausfordernde wissenschaftliche Fragestellungen zu bearbeiten. In diesem Kapitel des Jahresberichts werden Ergebnisse aus Untersuchungen an verschiedenen Materialklassen vorgestellt: elementare Metalle, Halbleiter und Isolatoren sowie Oxide und Manganite.

In den ersten beiden Beiträgen des Kapitels werden Elektronenstruktur-Berechnungen präsentiert, beide bei Normaldruck. Im ersten Artikel wird ein neuentwickeltes Potential für elektronischen Austausch innerhalb der Dichtefunktionaltheorie für die Berechnung der Elektronenstruktur von Festkörpern benutzt, die in ihren Eigenschaften von Mott-Isolatoren bis zu Isolatoren mit großer Bandlücke reichen. Das Potential führt zu einer deutlich verbesserten Beschreibung der Elektronenstruktur und der dielektrischen Konstanten, insbesondere bei Mott-Isolatoren: Für Ge, α-Sn und CdO wird im Gegensatz zu anderen (halb-)lokalen Potentialen eine Bandlücke geöffnet. Im zweiten Beitrag werden die Gitterschwingungen in festem Aluminium bei hohen Temperaturen untersucht, indem die Bewegungslinien der Atome aus Molekulardynamik-Simulationen mit deren Auslenkungen in einer selbstkonsistenten Formulierung der Gitterschwingungen, die anharmonische Anteile berücksichtigt (SCAILD Methode), verglichen. Während die SCAILD Methode über die übliche quasi-harmonische Näherung hinausgeht, bleiben die Auslenkungen inhärent harmonisch und SCAILD erreicht eine deutlich geringere Anzahl von Konfigurationen als Molekulardynamik.

Kontrollierte Dotierung ist nach wie vor eine der wichtigsten Methoden, die elektronischen Eigenschaften von Materialien zu verändern. Dies gilt auch für Silizium, das wahrscheinlich das wichtigste Material in der Halbleitertechnologie ist. Die Entwicklung von Bor-dotiertem Silizum könnte neue technologische Möglichkeiten eröffnen. Verschiedene Untersuchungen haben bisher eine niedrige Löslichkeit von 0.5 at. % von Bor in Silizium in der Diamantstruktur ergeben. Dotierung von B in Si bei hohem Druck und hoher Temperatur führt zu einer stark erhöhten Löslichkeit von bis zu 2.4 at. %, wie im dritten Beitrag des Kapitels beschrieben wird. Von ähnlicher Wichtigkeit bei der Synthese von Hochdruck-Phasen ist der Zustand des Ausgangsmaterials, wie z. B. die Synthese von Diamant aus verschiedenen Kohlenstoff- Allotropen gezeigt hat. Im vierten Beitrag wird die Bildung von Nano-Diamanten aus amorphen Kohlenstoffkugeln untersucht und ideale Synthesebedingungen bestimmt. Weitere Hochdruck-Synthesen für die Sesquioxide Mn_2O_3 und In_2O_3 werden in den beiden folgenden Artikeln vorgestellt. Die dabei entstehenden Hochdruckphasen zeichnen sich durch eine hohe Härte und weitere elektronische und optische Eigenschaften aus, die für eine technologische Anwendung interessant sind.

Multiferroische Materialen stehen seit einigen Jahren im Fokus intensiver wissenschaftlicher Untersuchungen in der Festköperphysik und der Chemie. Sie zeichnen sich durch eine Kopplung von magnetischen und elektrischen Phänomenen aus und sind für die Entwicklung neuer elektrischer Geräte von Wichtigkeit, in denen optische und magnetische Eigenschaften von einem elektrischen Feld kontrolliert werden. Innerhalb der Multiferroika sind die Manganate eine wichtige Materialklasse; in den abschließenden zwei Beiträgen des Kapitels werden Phasenstabilität sowie Phasenübergänge von YMn_2O_5 und $BiMnO_3$ bei hohem Druck untersucht.

3.8 Methodische Entwicklungen

Experimentelle und computergestützte Untersuchungen haben sowohl in den Erd- als auch Materialwissenschaften stets unverzichtbare Ziele: Verbesserung der verwendeten Methodik und Erarbeitung neuer Lösungsansätze. Neue Entwicklungen dienen zum Beispiel der Erzeugung zunehmend höherer Drücke und Temperaturen, wodurch ein besseres Verständnis des tiefen Erdinneren erreicht wird, der Erzeugung kontrollierter, nicht-hydrostatischer Spannung als Notwendigkeit für rheologische Untersuchungen sowie genaueren Bestimmungen der chemischen Zusammensetzung experimentell erzeugter Proben. Stetig wird danach gestrebt, einflussreiche experimentelle Parameter mit zunehmender Genauigkeit zu bestimmen, so zum Beispiel Temperatur, Druck, Spannungsunterschiede und Sauerstofffugazität. Die Beiträge dieses Kapitels behandeln zahlreiche Aspekte dieser methodischen Entwicklungen.

Eine neue Vielstempelpresse („IRIS-15“), mit der sich Drücke von 60 Gigapascal (GPa) oder mehr erzeugen lassen, wurde 2014 im Geoinstitut installiert. Bei dieser Apparatur

komprimieren sechs äußere Druckstempel die kubisch angeordneten inneren Stempel. Um extrem hohe Drücke zu generieren und dabei die inneren Würfel nicht zu zerstören, muss diese exakte kubische Geometrie der äußeren Würfel unbedingt bewahrt bleiben. Die neuesten Entwicklungen auf dem Weg zu diesem Ziel werden in dem ersten Artikel beschrieben.

Drei folgende Beiträge präsentieren Neuentwicklungen bei Experimenten mit Diamantstempelzellen (DAC). Zwei dieser Artikel erklären, wie die in diesen Hochdruckzellen eingestellten experimentellen Bedingungen mithilfe von Fluoreszenz-Sensoren bestimmt werden. Im ersten Beitrag werden zwei verschiedene Eichmedien (Rubin und ein mit Samarium gedopter Yttrium-Aluminium-Granat-Einkristall – Sm-YAG) gleichzeitig eingesetzt, um sowohl Druck als auch Temperatur zu bestimmen. Der zweite dieser Artikel stellt mit Sm-gedoptem Strontiumtetraborat (Sm-STB) einen neuartigen Drucksensor vor, der bis zu einem Druck von 60 GPa geeicht wurde und wie auch Sm-YAG nicht Temperatur-beeinflusst ist. Der dritte Beitrag in dieser Reihe beschreibt Neuentwicklungen zur Erzielung stabiler Temperaturen beim Aufheizen von DACs mit Lasern für Untersuchungen, die mit Kernresonanz-Prozessen verknüpft sind.

Für rheologische Untersuchungen bei hohen Drücken mit Multianvil-Pressen liegt ein Hauptproblem darin, Spannungsunterschiede zu bestimmen. Konventionelle Methoden erlauben Bestimmungen oft nur, wenn die Spannungen sehr hoch sind. Der folgende Artikel präsentiert eine wichtige Neuentwicklung, bei der ein piezoelektrischer Sensor in Form eines Einkristalls entweder aus Quarz oder aus $GaPO_4$ eingesetzt wird. Die Bestimmung des elektrischen Signals, das ein derartiger Sensor erzeugt, ermöglicht Spannungsmessungen im Bereich 0-1 GPa bei Temperaturen bis zu 600 K. Der H_2O-Einfluss auf die Rheologie stellt bei Verformungsstudien einen weiteren Unsicherheitsfaktor dar; zum Beispiel hat in Olivin gelöstes OH einen deutlichen Abschwächungseffekt hinsichtlich der Rheologie. Um Proben bei hohen Drücken und Temperaturen verformen zu können und danach den Einfluss von gelöstem OH auf die Rheologie und aktive Gleitsysteme zu quantifizieren, muss die Probe in einer Metallkapsel eingeschlossen werden, die den Verlust oder die Aufnahme von Wasserstoff verhindert. Problematisch dabei ist, dass derartige Verformungsexperimente zu Spannungsbestimmungen mit *in-situ*-Röntgenbeugungsmessungen durchgeführt werden müssen. Daher ist eine für Röntgenstrahlen transparente Probenkapsel erforderlich, eine Metallkapsel erfüllt diese Bedingung nicht. Erste Annäherungen an eine Lösung dieser Problematik werden im Folgenden beschrieben.

Bei zahlreichen Hochdruckexperimenten soll zusätzlich zu Temperatur und Druck die Sauerstofffugazität quantitativ bestimmt werden. Als am besten geeignete Methode dafür hat sich die Verwendung eines aus einer Metalllegierung bestehenden Redoxsensors erwiesen. Das heißt zum Beispiel, dass die genaue Zusammensetzung einer Fe-Pt-Legierung, die während des Experiments in einer Probe eingeschlossen ist, durch die Sauerstofffugazität kontrolliert wird. Anschließend werden Ergebnisse aus Versuchen, in denen drei Sensoren aus

verschiedenen Legierungen über einen weiten Bereich von Sauerstofffugazitäten verglichen wurden, vorgestellt.

Bei Experimenten mit laserbeheizten DACs können chemische Reaktionen mit den Druckstempeln zu einer Anreicherung von Kohlenstoff in der Probe führen. Diese Problematik ist in Experimenten zur Metall/Silikat-Verteilung in Schmelzen signifikant, da gelöster Kohlenstoff in einer aus Fe-Legierung bestehenden Schmelze einen wesentlichen Einfluss auf die Verteilung siderophiler Elemente haben kann. Um diesen Effekt auszugleichen, muss der Kohlenstoffgehalt in abgeschreckter Eisenschmelze bestimmt werden. Wie im Folgenden beschrieben, sind diese Messungen eine große Herausforderung und zahlreiche Vorsichtsmaßnahmen müssen getroffen werden, um die korrekte Konzentration zu messen.

Häufig ist es wünschenswert, dass die zu untersuchenden Proben zur Bestimmung ihrer physikalischer Eigenschaften als Einkristalle vorliegen. In einem Artikel wird die Synthese großer Einkristalle von Stishovit, einer Hochdruckmodifikation von SiO_2 beschrieben. Kristalle mit einer Kantenlänge bis 1,7 × 1,5 × 1,0 mm wurden in einer Multianvil-Presse synthetisiert; sie dienen Bestimmungen von Zustandsgleichung und elektrischer Leitfähigkeit bei Drücken und Temperaturen bis 500 GPa und 8000 K.

Die Untersuchung von Fluideinschlüssen führt zu Erkenntnissen über die Zusammensetzung erzbildender Fluide. Da viele Erzminerale lichtundurchlässig (opak) sind, waren Fluid-Bestimmungen in diesen Mineralen bisher sehr schwer bis gar nicht möglich. Eine hier vorgestellte, wesentlich weiterentwickelte Methode arbeitet mit der Nah-Infrarot (NIR)-Mikroskopie zur Untersuchung von Flüssigkeitseinschlüssen in Opakmineralen.

Der das Kapitel abschließende Beitrag stellt Fortschritte dar, die hinsichtlich des Verständnisses theoretischer Aspekte in der computergestützten Chemie gemacht wurden. In der Dichtefunktional-Theorie wird das Ionisierungspotential, d. h. die Energiedifferenz zwischen einem neutralen Molekül und seinem einfach geladenen Kation, zutreffend beschrieben; mit zunehmender Anzahl von Atomen in dem Cluster verschlechtert sich aber diese Übereinstimmung aus bisher unbekannten Gründen. Wenn man allerdings die elektrostatische Energie in einem derartigen System betrachtet, lässt sich dieses Verhalten erklären.

3. Research Projects

3.1 Earth and Planetary Structure and Dynamics

The inner planets in our solar system are characterized by a similar structure and composition, *i.e.*, a silicate envelope overlying a metallic core. This structure is a direct consequence of accretion from planetesimals and planetary embryos and the simultaneous differentiation of their dense iron portions that sink to the center. Differentiation is directly aided by collisions and impacts that release energy and melt parts of the planet. With further release of gravitational energy as a result of the sinking metallic bodies the terrestrial planets must have experienced episodes of global melting, resulting in a magma ocean of variable depth, and possibly melting entire planets. The subsequent solidification is the starting point of the dynamic evolution of the planets over geological time.

The first three contributions in this section look at different aspects of the early evolution of terrestrial planets. The first contribution deals with the accretion and simultaneous differentiation of the Earth's core and shows that material from greater heliocentric distances accretes later in planetary history. As the oxygen content increases with heliocentric distance the differentiation of material richer in oxygen at late stages of core formation can cause stable stratification in the core of the Earth. The extent to which large accretionary collisions melt a planetary body and how fast the melt recrystallizes is examined in the following contribution. A particularly important question in that context is the comparison of time scales for crystallization of the melt and for the recurrence rate of collisions: if the impact occurs into a magma ocean, the equilibration of the impactor material occurs at conditions at the bottom of the magma ocean. The importance of a dense steam atmosphere is emphasized for the duration of crystallization, increasing the crystallization time by three orders of magnitude. A different aspect of magma ocean crystallization is considered in the third contribution. Here, the crystallization sequence, *i.e.*, the phases that crystallize as the molten body cools, is computed for Mars. In the FeO-MgO-SiO_2 system a dense basal layer consisting of ferro-periclase builds up initially, but due to FeO-enrichment in the melt the crystallizing minerals become buoyant at intermediate depths, floating to the surface.

The final contribution looks at the modern Earth, addressing the question of why ocean island basalts are richer in water than upper mantle rocks. The dehydration of minerals in the Al_2O_3-SiO_2-H_2O system at lower mantle pressure is studied, as a proxy for mafic rocks as they occur in a subducting slab. Minerals in that system, including the high-pressure Al-rich phase D, can store H_2O at lower mantle conditions. Dehydration of ultramafic rocks can transfer water to the Al-rich phase D, and in mantle upwellings water can then be redistributed into nominally anhydrous phases.

a. *Development of an early density stratification in the Earth's metallic core (D.C. Rubie, S.A. Jacobson, D.J. Frost, J. de Vries, in collaboration with J. Hernlund/Tokyo and A. Morbidelli/Nice)*

Formation of the Earth's core was a multistage process that involved Fe-rich metal equilibrating with silicate liquid at pressure-temperature conditions that progressively increased with time. Because the partitioning of silicon and oxygen between metal and silicate liquids depends strongly on temperature, the concentrations of these light elements in core-forming liquids must also have evolved during accretion. If the final liquids added to the core were enriched in such light elements relative to earlier liquids because of increasing temperatures, stable density stratification could have resulted that would inhibit the onset of core convection. In fact, a relic of such stratification may still be present today in the form of a low density layer at the top of the outer core and/or a high density layer (F-region) above the inner core boundary. We have modelled the evolving compositions of core-forming liquids by combining a multistage core formation model with N-body accretion simulations of terrestrial planet formation. We focus especially on Grand Tack simulations because of their success in producing bodies that closely resemble the terrestrial planets of the Solar System. These simulations typically start with a few tens of embryos (Moon to Mars size) that are embedded in a proto-planetary disk of several thousand much smaller planetesimals. The starting bodies, which are typically distributed over heliocentric distances from 0.7 to 12 AU, collide and accrete to form larger bodies. Due to the high energies involved, impacts result in extensive melting and magma ocean formation that facilitate metal-silicate segregation and thus episodes of core formation. In order to model each core formation event, we combine rigorous mass balance with metal-silicate element partitioning data for the major elements Fe, Si, Ni, and O in order to determine the compositions of equilibrated silicate and metal liquids. The mass balance requires the bulk compositions of all starting embryos and planetesimals to be defined as a function of their heliocentric distances of origin. To do this, we assume that non-volatile elements are present mostly in Solar System (CI) relative abundances in all bodies and that oxygen content is the main compositional variable. The primary constraint on the combined model is the calculated mantle composition of an Earth-like planet (*i.e.*, located at ~1 AU and of 1 Earth mass) with secondary constraints being the mantle compositions of Mercury and Mars. The model is refined by least squares minimization using five fitting parameters that consist of the metal-silicate equilibrium pressure and four parameters that define the starting compositions of primitive bodies. Results are highly sensitive to the compositional model for starting bodies and acceptable fits are only obtained when bodies that originated close the Sun (< 1-1.5 AU) are highly reduced and those at greater distances are increasingly oxidized.

The models predict that the Earth's core contains 8-9 wt. % silicon and 3-4 wt. % oxygen. However, batches of metallic core-forming liquids show a progressive increase in light element concentrations as accretion proceeds. This is especially the case for oxygen which is essentially absent during early stages of accretion but is present at concentrations of up to 14

wt. % in core-forming liquids during the final 20 % of accretion. Thus, stable density stratification in the early core is highly likely and may be ubiquitous in Earth-mass planets towards the end of accretion (Fig. 3.1-1).

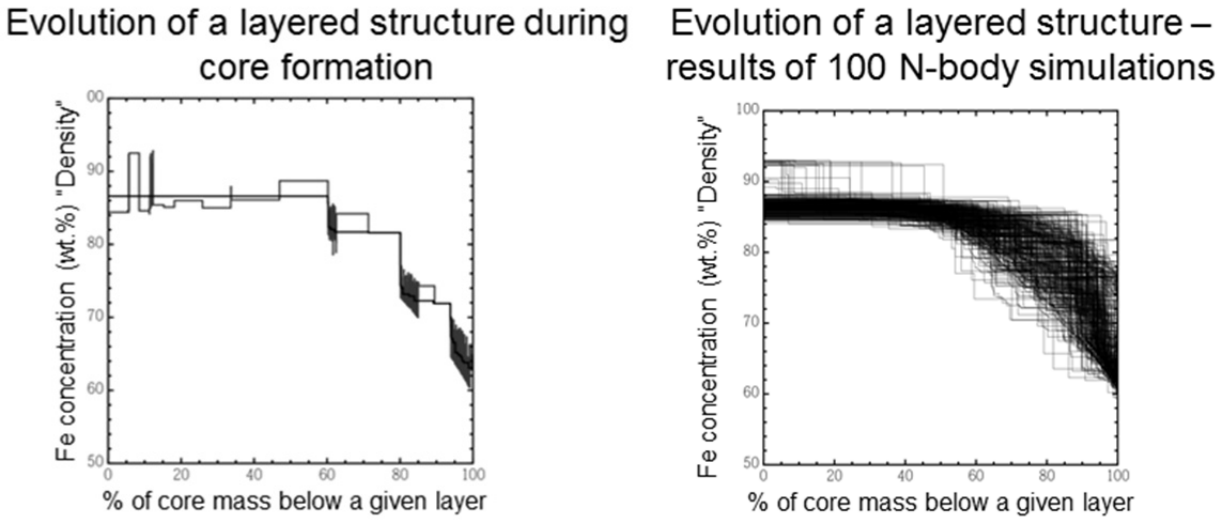

Fig. 3.1-1: Density stratification predicted by a combined N-body accretion/core formation model for an Earth-like planet (left). The grey line shows density (as approximated by Fe concentration) of the successive layers that have been added to the core during accretion. When a high density layer overlies one that has a lower density, the two layers are merged which leads to a stable density profile as shown by the black line. Results for one hundread N-body simulations – which show a strong density stratification in all cases (right).

Only a giant impact involving a major core-merging event is likely to provide sufficient energy to mix the core to the extent necessary for convection and action of a geodynamo. The kinetic energy of the impact needs to exceed the gravitational potential energy of the stratified region. In the case of the Earth, the core of an impactor with a mass similar to that of the Earth's core and descending at 1 km/s would have sufficient energy to destroy density stratification. The absence of a magnetic field on Venus may be due to density stratification that has survived due to the absence of a late giant impact

b. *Melting and crystallisation during and after planetary collisions (J. de Vries, D.C. Rubie and S.A. Jacobson; F. Nimmo/Santa Cruz, H.J. Melosh/West Lafayette and A. Morbidelli/ Nice)*

The terrestrial planets in our solar system were formed by a series of collisions between smaller bodies - a process that is modelled numerically using N-body accretion simulations. Planetary embryos grow by accreting smaller bodies from their so called 'feeding zone' and

collide with one another when they enter each other's feeding zones. The energy involved in each collision causes large-scale melting, which allows metal-silicate segregation to occur, thus resulting in an episode of core formation. To develop a model of the compositional evolution of our rocky planets, based on a collisional history predicted by N-body accretion models, estimates of the equilibration conditions (pressure and temperature) are required. Assuming that equilibration takes place at the bottom of a magma ocean, the amount of melting and the pressure and temperature conditions at the base of the magma ocean are required. To determine the amount of melting for each of the several hundred to several thousands of collisions, as calculated from N-body models, a reliable and efficient formulation of shock related melting is needed. Models of the compositional evolution of the inner solar system can be used as an additional constraint on the outcome of N-body accretion simulations. If the compositional evolution does not result in a reasonable present-day composition for the Earth, the collision history is unlikely to represent a realistic scenario.

Full three-dimensional models for planetary collisions are computationally too time consuming for the large number of impacts calculated from N-body accretion models. Two-dimensional models cannot be used for non-vertical impacts due to their assumed symmetry in the third dimension. Therefore, a parameterised model is used which describes the amount and depth of melting based on the energy needed to melt a dunite mantle (and in the case of deep melting an iron core) and the energy available from the impact. The energy set free depends on the impact angle and velocity as well as on the impactor size and the material properties of both the impactor and the target.

The result of a collision between similar sized bodies is a deep melt pool with equilibration and core formation at high pressures. On slightly longer time scales these melt pools will spread over the surface due to isostatic adjustment to form a global magma ocean. Depending on the crystallisation time of this magma ocean, a next impact may or may not occur on a molten surface. Small impacts by themselves will not cause core formation events as they cause very little melting (Fig. 3.1-2a). In such a scenario there is only very little equilibration between target and impactor material. However, if such a small impactor sinks into a pre-existing magma ocean, equilibration with a significant fraction of target material may take place at the bottom of this magma ocean (Fig. 3.1-2b). Initial estimates from calculations with a simple linear crystallisation model have shown that core equilibration of planetesimals in a pre-existing magma ocean may be an important factor, especially if there was an insulating atmosphere around the target which slows magma ocean crystallisation (Fig. 3.1-3). A dense steam atmosphere, created by degassing of the magma ocean has likely surrounded the growing embryos. However, giant impacts may have blown (parts of) these atmospheres away, increasing the crystallisation rate of the magma ocean.

Current work focuses on determining the pressure and temperature at the bottom of magma ocean left over from a giant impact when the next impact occurs. Two endmember models are studied, with a dense steam atmosphere or no atmosphere at all. Preliminary results show that

without an atmosphere most magma oceans crystallise before the next impact. This means that smaller impactors equilibrate at low pressure with a very small fraction of the target. This is inconsistent with geochemical constraints on core formation conditions, indicating that an insulating atmosphere must have been present during most of planetary history. Currently, a constant cooling rate is used for a first estimate of the depth of the magma oceans. However, in future work we plan to improve this model and incorporate the removal of atmosphere by giant impacts.

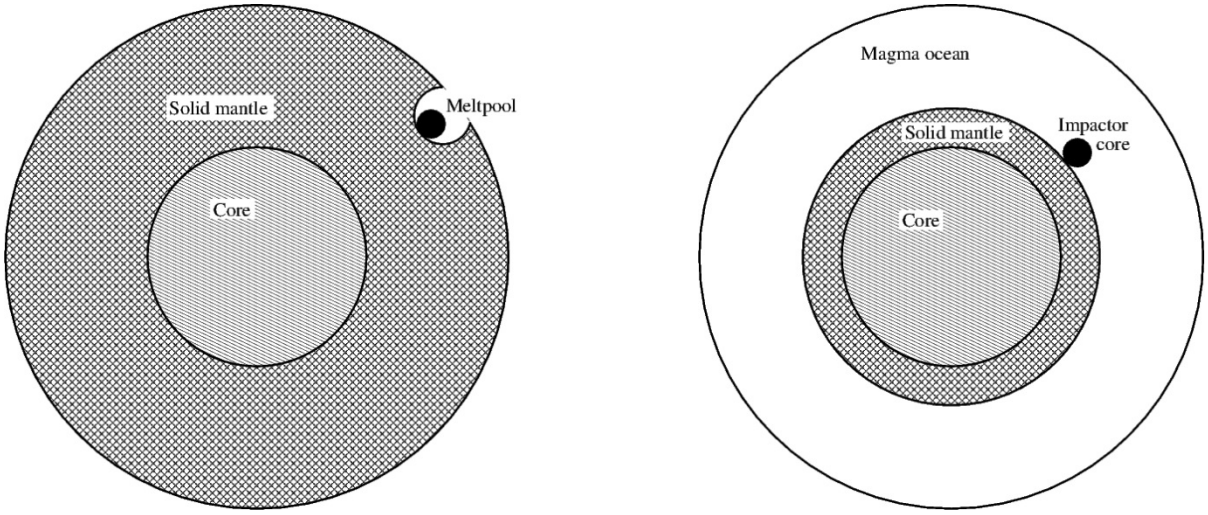

(a) (b)

Fig. 3.1-2: The impactor core (black) equilibrates with the target mantle on its way through the molten material. In the case of an impact on a solid surface (a) equilibration takes place with a small amount of material at low pressures. In the case of an impact in a pre-existing magma ocean (b), equilibration takes place at larger depth and therefore higher pressures.

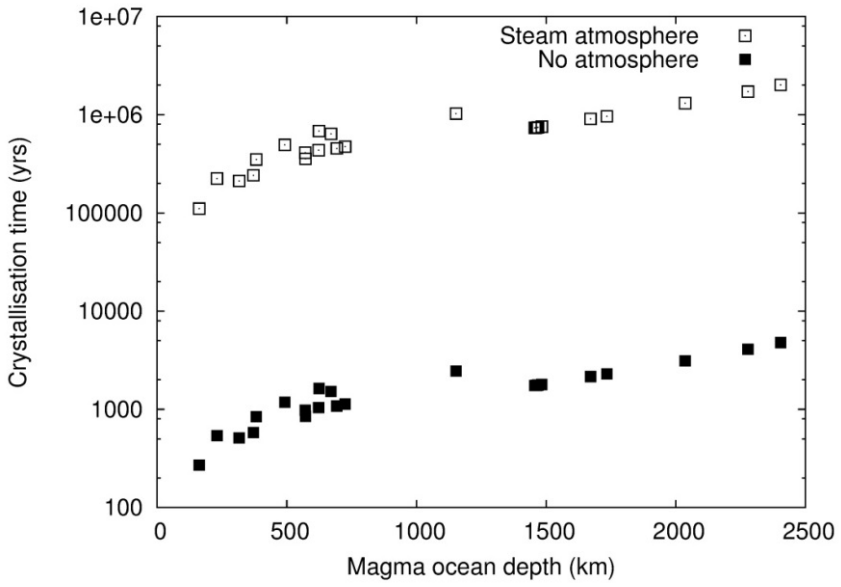

Fig. 3.1-3: The crystallization time of magma oceans created by embryo-embryo collisions. The presence of a dense steam atmosphere increases the crystallization time by several orders of magnitude.

c. *Crystallizing a magma ocean on Mars (T. Chust and G. Steinle-Neumann)*

The structure of terrestrial planets with a mantle consisting of solid rock may have evolved from a largely molten stage through fractional crystallization. After solidification with unstable density stratification, the structure of the planet may have undergone further changes governed by the mechanics of mantle convection, possibly including a catastrophic overturn of the entire mantle. We are looking at a possible scenario for the crystallization of the Martian mantle from a magma ocean and compute geodynamically significant parameters of the resulting layers of rock, such as density profile, total radius and moment of inertia. Using recent experimental data to constrain the crystallization sequence of minerals and partitioning of elements we are revisiting previous results with surprising density profiles. For that purpose we have developed a Mars Crystallizer which models fractional crystallization of a large volume spherical shell of silicate melt around a sphere of solid material and is based on our EoS simulation software library for mineralogical thermodynamics.

Since an adiabatic temperature profile for a Martian magma ocean intersects the melting curve at the bottom of the mantle, crystallization proceeds from the bottom of the magma ocean to the top. The program simulates fractional crystallization of the magma reservoir in steps, tracking the mass budget of the different chemical elements available in the melt shell and in each thin spherical layer of crystallizing solid.

We employ thermodynamic models to determine the density of the solid phases and the silicate melt; the pressure at the advancing bottom of the magma ocean can then be calculated at every step. The crystallization sequence of minerals in the Martian mantle is constrained using experimental phase stability data, so the code can consult a lookup table at every step to map the pressure at the liquid-solid interface and the bulk silica content of the melt to a liquidus temperature and a set of crystallizing phases. Furthermore, the partitioning of elements between the melt and the crystallizing phases is determined based on experimental results; distribution coefficients for various pairs of elements between the solid and the melt are used to derive the composition of solid solutions from that of the liquid (For Fe/Mg see Fig. 3.1-4). Finally, the relative amounts of multiple possible solid solutions are determined by minimizing the Gibbs free energy of the assemblage at fixed pressure, temperature and solution composition with the additional constraint that no more material can be used than is present in a small fraction of melt. The resulting masses of crystallized components are then removed from the melt reservoir and added to the accumulated solid. While simulating the crystallization of one thin layer of minerals after another, the software accumulates information about the density structure of the solidified body.

The thermodynamic model for the melt is defined in the MgO-SiO_2 (MS) system, so in a first step we renormalize the Martian composition to the MS system and compute the crystallization sequence and density profile in that system (Fig. 3.1-5). In the absence of FeO both the liquid and solid densities are smaller than those in previous models and the melt is

always buoyant compared to the coexisting solid. Crystallization starts with periclase, enters the stability field of anhydrous phase B at 13.1 GPa (which is replaced by a stoichoimetrically equivalent combination of ferropericlase and wadsleyite in our model), proceeds to forsterite at 12.3 GPa and eventually reaches the eutectic point at 7.1 GPa. At lower pressure the simulation code always crystallizes an energetically favorable combination of olivine polymorphs, pyroxenes and garnets and keeps the silica content of the melt close to the eutectic composition.

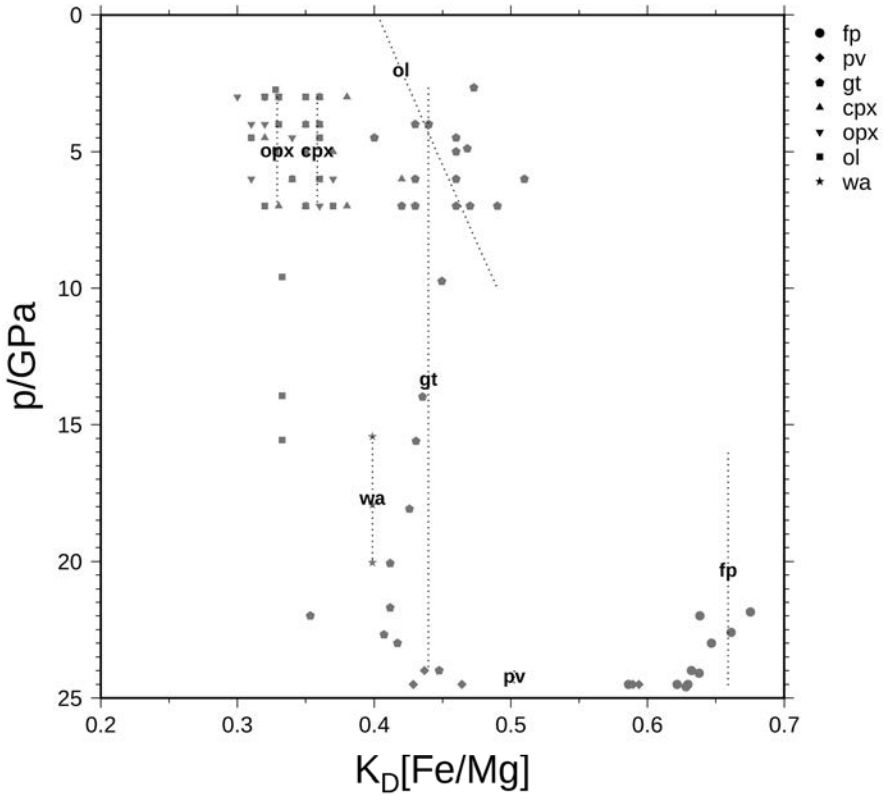

Fig. 3.1-4: Distribution coefficients for Fe/Mg between peridotite melt and different minerals. Experimental data are compiled from the literature for olivine, wadsleyite, garnet, ortho- and clino-pyroxene, ferro-periclase and bridgmanite (silicate perovskite).

The addition of other chemical components requires an adaptation of the melt model: we assume that for given silica content the volume per atom is that of the MS system and change the molar mass according to the composition. The model for solids can handle solid solutions with various additional chemical components; however, the solution compositions in equilibrium with the melt need to be determined. This computation is guided by the element distribution data (Fig. 3.1-4) and is performed conceptually independently by the determination of potentially stable phases and subsequent energetic optimization. The selection of energetically optimal phases among a set of solid solutions with known compositions under composition constraints can be modeled as a linear optimization problem and solved by the existing infrastructure.

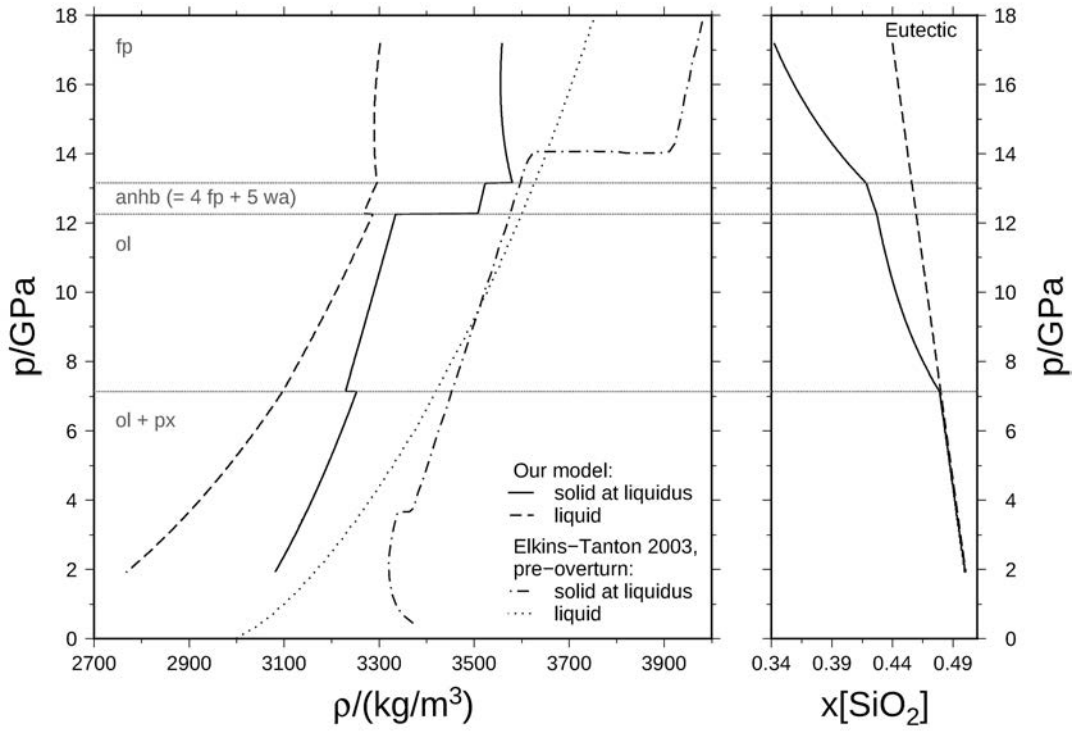

Fig. 3.1-5: Density and molar silica content of a crystallizing Martian magma ocean in the MS system, with an initial composition of 56 wt. % MgO and 46 wt. % SiO_2. Boundaries between different crystallizing assemblages are marked by horizontal lines. The left panel shows the density of the crystallizing solid and the melt at the interface. For comparison the density profile of a crystallizing magma ocean and the coexisting melt from Elkins-Tanton *et al.* [Meteoritic & Planet. Sci. 38, 1753, (2003)] is shown. The right panel shows the molar SiO_2 content of the melt and the SiO_2 content at the eutectic.

Figure 3.1-6 shows results of a calculation in the FeO-bearing FMS system. The pressure at the initial interface between liquid and solid is higher than in the MS system, due to the high density of the FeO component in the melt; the simulation follows the same crystallization sequence and the silica content of the melt behaves very similarly. Changes on crystallization occur at 16.7 GPa from ferropericlase to the anhydrous B proxy, at 15.5 GPa to olivine, and at 9.7 GPa the eutectic point is reached. There the phase assemblage is again selected from the olivine polymorphs, pyroxenes and garnets. Since the distribution coefficients for the iron magnesium ratio between the solid and the melt are all well below unity, relatively little iron is incorporated into the crystallizing solids and as a consequence the FeO-content of the melt gradually increases towards lower pressures.

The iron magnesium distribution coefficient is also about 1.5 times higher for ferropericlase than for olivine and wadsleyite. As a consequence the density is always larger than for the pure MgO-SiO_2 case and closer to the previous studies, but it exhibits a large drop once periclase is no longer the crystallizing phase – so large that the crystallized material becomes less dense than the liquid that is enriched in FeO, creating buoyant crystalline material.

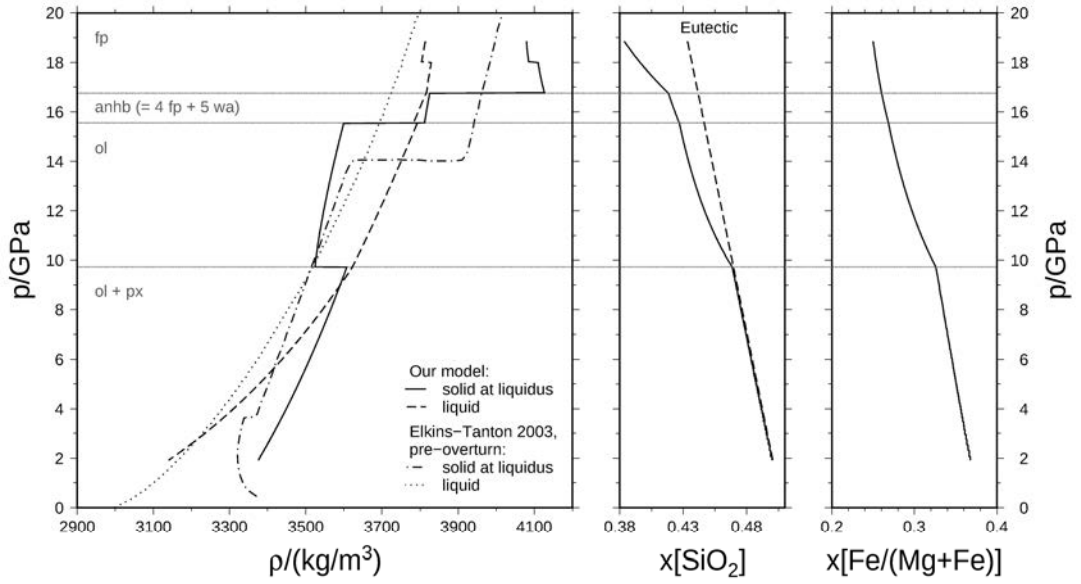

Fig. 3.1-6: Density, molar silica and FeO content of a crystallizing Martian magma ocean is shown with a composition of 35 wt. % MgO, 21 wt. % FeO and 44 wt. % SiO_2. The two panels on the left are setup as in Fig. 3.1-5, the right panel shows the development of the molar Fe / (Mg + Fe) ratio in the melt with crystallization.

d. *Mafic rocks as lower mantle water reservoirs (M.G. Pamato, R. Myhill, D.J. Frost, T. Boffa Ballaran, F. Heidelbach and N. Miyajima)*

The source rocks for basaltic lavas that form ocean islands are often inferred to have risen as part of a thermal plume from the lower mantle. These rocks are water-rich compared with average upper-mantle rocks. However, experiments indicate that the solubility of water in ultramafic rocks in the lower mantle is very low, prompting suggestions that plumes may be sourced from as-yet unidentified reservoirs of water-rich primordial material in the deep mantle.

In this study, we have investigated the possibility that mafic rocks are important water reservoirs in the lower mantle. Mafic rocks are relatively rich in alumina, which is known to stabilise dense hydrous phases. Schreinemakers analysis (Fig. 3.1-7) reveals the sequence of reactions that can occur in the Al_2O_3–SiO_2–H_2O system based on a series of multianvil experiments conducted at the BGI. $Al_2SiO_4(OH)_2$ – the aluminium-rich endmember of dense, hydrous magnesium silicate phase D – is stable at temperatures extending to over 2000 °C at 26 GPa. These temperatures exceed those within the majority of the uppermost mantle. Further experiments indicate that Al-rich phase D is stable within mafic rocks, which implies that subducted oceanic crust could be a significant long-term water reservoir in the convecting lower mantle.

We suggest that melts formed in the lower mantle by the dehydration of hydrous minerals in dense ultramafic rocks will migrate into mafic lithologies and crystallize to form Al-rich

phase D. When mantle rocks upwell, water will be locally redistributed into nominally anhydrous minerals. This upwelling material provides a potential source for ocean-island basalts without requiring reservoirs of water-rich primordial material in the deep mantle.

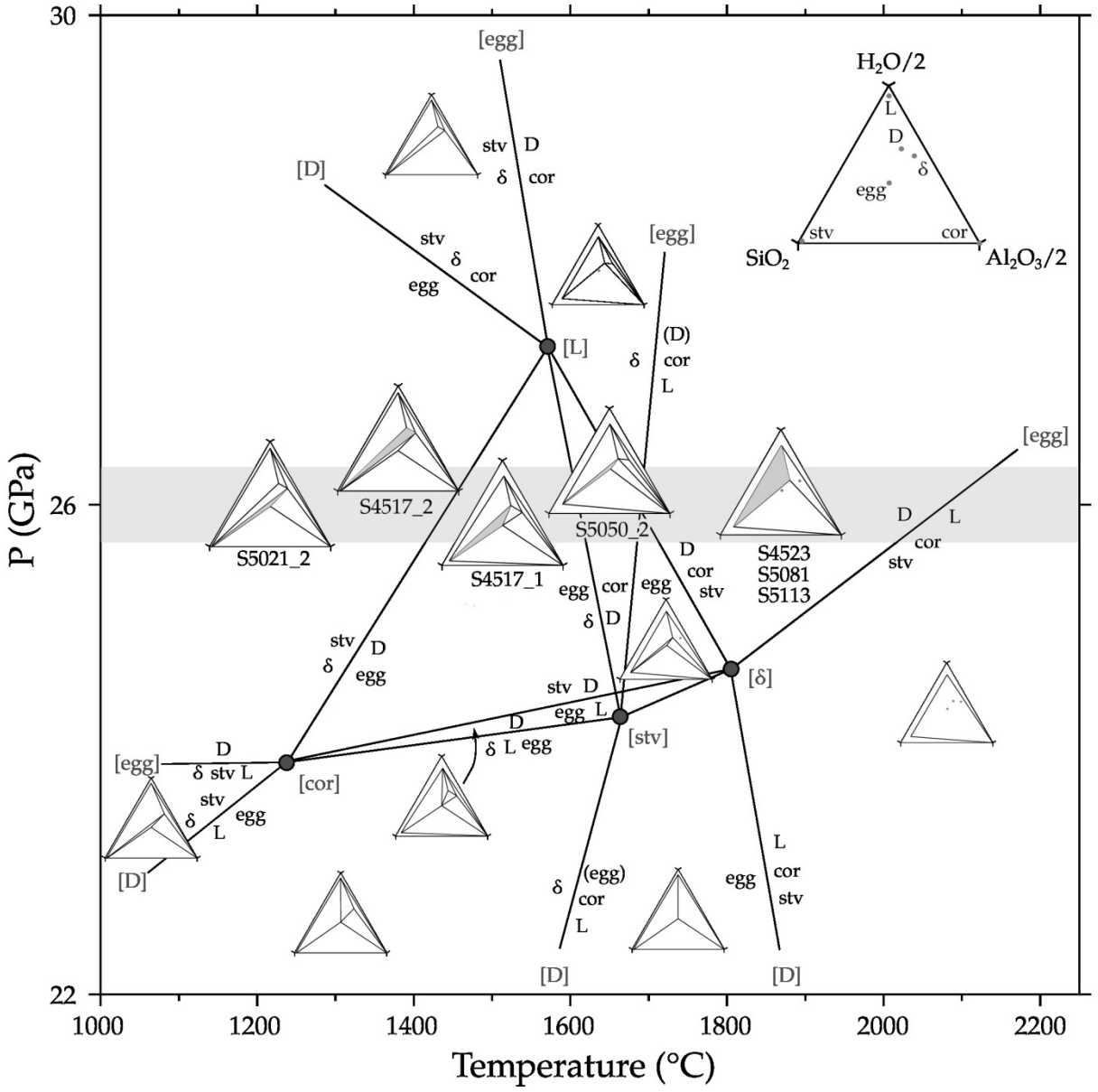

Fig. 3.1-7: Schreinemakers analysis of phase relations in the system Al_2O_3–SiO_2–H_2O, based on experiments performed between 22 and 26 GPa. Shaded regions show phase assemblages observed in this study at 26 GPa. The other phase relations are deduced from this and previous studies. Phase abbreviations are as follows: δ, δ-AlOOH; stv, stishovite; D, Al-phase D; egg, phase Egg; cor, corundum; L, hydrous liquid/melt.

3.2 Geochemistry

Meteorites represent leftover building material of the inner solar system and preserve a snapshot of the processes occurring in the first 10 million years of solar system history. They are classified as either differentiated or undifferentiated depending on whether heating after formation has led to silicate melting, separation of metal and the development of igneous textures. The first report in this section describes the mineralogy of a recently discovered differentiated meteorite, which previous studies had suggested may belong to an already recognised family of meteorites. This is found not to be the case and an intriguing aspect is that as the meteorite is relatively reduced, *i.e.*, the silicate minerals contain little iron oxide, a plausible parent body might be the planet Mercury.

Planetary accretion in its final stages should involve collisions between planet sized bodies. The favoured explanation for the formation of the Moon is by such an impact, but the similarity in composition between the Earth and Moon has always raised problems for this hypothesis. The Moon should be composed mainly of material from the impactor, which should have a different oxygen isotope ratio to the Earth as it formed at a different heliocentric distance. In the second study of this section, simulations of planetary growth from an initial disk of inner solar system material with a realistic oxygen isotope gradient are described. It is demonstrated that the difference in composition between the Earth and the giant impactor would have likely been very small. This removes the necessity to argue that Earth and Moon-forming material were somehow chemically homogenised during the impact.

After the giant impact accretion must have continued but a major question is how much of this late accreted material underwent core formation. The mantle has an overabundance of elements that would normally be expected to partition very strongly into the core, so called highly siderophile elements. These elements could only have remained in the mantle if no core formation occurred after they were accreted. The next study in this section attempts to put very tight constraints on the amount of late accreted material by examining whether sulphide melts could have also separated highly siderophile elements to the core. Such constraints are very important because volatiles such as water and carbon were likely also added to the Earth during late accretion.

The next three contributions examine the speciation and influence of ferric iron (Fe^{3+}, Fe_2O_3) in the mantle. The dominant lower mantle mineral bridgmanite (formally known as magnesium silicate perovskite) has been reported to contain very large proportions of ferric iron. Using a newly developed technique the first of these studies examines where ferric iron is located in the bridgmanite structure at high pressure and temperature, and finds that the position and amount of ferric iron changes very little at these extreme conditions. The second study finds that under ferric iron-rich conditions bridgmanite melts at much lower temperature than expected. Such an effect may be important at the base of the mantle where very low seismic wave velocities seem to implicate the existence of melt. The next study examines the

partitioning of ferric iron during melting beneath mid-ocean ridges. Ferric iron is found to prefer the melt phase under high oxygen fugacities but to partition more favourably into the mineral phases at low oxygen fugacities. This change in behaviour may help to explain why mid-ocean ridge magmas maintain relatively constant ferric iron contents compared to many other minor or trace elements that are affected by the degree to which the mantle melts.

The following three studies seek to examine the conditions and consequences of diamond formation in both the upper and lower mantle. The first looks at the stability field of diamond with respect to carbonate-bearing melts in order to understand the conditions at which diamonds might form within subducted carbonate-bearing oceanic crust. This is important because carbonate melts are mobile and can strip carbon from the subducting slab and return it to the surface. Diamonds on the other hand are refractory and their formation would allow carbon to remain fixed in subducting slabs that can then take carbon deep into the interior. The following study puts constraints on the liquid growth medium of super-deep (transition zone or lower mantle) diamonds by trying to experimentally reproduce the mineral assemblages present as inclusions within these diamonds that crystallised from the same medium. It is found that the characteristic mineral assemblage of diamond-magnesiowustite-bridgmanite-stishovite-carbonate is stable at conditions compatible with the top of the lower mantle coexisting with silicate melts containing ≥30 wt. % carbonate component. The final diamond study examines the so called "stishovite paradox", *i.e.*, the apparent coexistence of stishovite, the high-pressure form of SiO_2, with the mineral ferropericlase, (Fe,Mg)O, in diamond inclusions. This assemblage should be unstable throughout the mantle as the phases should react to form intermediate silicate minerals. It is found that this assemblage can form, however, through a so called peritectic melting reaction in the system SiO_2-MgO-FeO.

The following four contributions deal with phase relations and element partitioning in the Earth's upper mantle. The first examines the partitioning of fluorine between garnet, clinopyroxene and silicate melt at conditions representative of deeply subducted oceanic crust. It is found that clinopyroxene can incorporate significantly more F than other common mantle minerals and thus may act as a major carrier of F into the transition zone, where it may either form small-degree partial melts such as lamproites, or enter higher pressure minerals such as ringwoodite or wadsleyite. In a continuation of a systematic investigation of H_2O-rich regions of the MgO-SiO_2-H_2O system, the next study describes experiments performed at conditions compatible with the base of the upper mantle that help to understand the composition of water-saturated melts that might form at these conditions. In the following study the stability of hydrous and nominally anhydrous minerals in eclogitic rocks are examined. The objective is to quantify the amount of water that enters nominally anhydrous minerals as hydrous minerals such as phlogopite breakdown. In this way constraints can be placed on the amount of H_2O that may be being subducted into the deep mantle.

The phase relations of hydrocarbons and their interaction with iron components in minerals of the mantle is the focus of the next study. Redox reactions between the hydrocarbons and

mineral phases are found to be temperature dependent. Such studies may ultimately help to understand the fate of subducted organic material.

The last two contributions deal with the formation of ore deposits. By studying melt and fluid inclusions in samples collected near the Climax porphyry molybdenum deposit, USA, the first study reconstructs the physicochemical characteristics of the ore-forming magmas and fluids. It is found that the mineralizing melts and fluid did not contain unusually high amounts of Mo, which suggests that efficient focusing of residual melts and fluids were the key for economic mineralization. Fluid inclusions are the main focus of the final study in this section, which examines the genesis of magnetite(-apatite) deposits along the Lower Yangtze river in China. Based on the major and trace element composition of highly saline brine inclusions and the sulphur isotopic signature of ore sulphides, it is demonstrated that assimilation of evaporite sequences by ascending magmas played a major role in the formation of these deposits.

a. *NWA7325: A highly reduced differentiated meteorite from an unknown parental planet (T. Nakamura/Sendai, M. Miyahara/Hiroshima, A. El Goresy, Ph. Gillet/Lausanne; E. Ohtani, K. Yogo and M.H. Ishida/Sendai; Y. Lin/Beijing and H. Schulze)*

NWA7325 is a 345 gms green ungrouped achondrite tentatively classified as an olivine gabbro cumulate and perhaps ejected from the planet Mercury. Fragments were collected in the Moroccan desert in 2012. It was originally a differentiated meteorite but it experienced a complex evolution. NWA7325 has spatially heterogeneous mineral abundances. Constituents include: major (55 %) anorthite (An_{88}), (10-15 %) forsterite, (25-30 %) Cr-diopside, minor Ti-chromite, Co-rich (3.5 wt. % Co) kamacite, taenite, schreibersite [$(FeNi)_3P$], and considerably weathered sulphides.

NWA7325 is an extremely reduced meteorite. Early reported XANES results show evidence for Ti^{3+}, V^{2+} and Cr^{2+} in olivine and diopside, respectively suggesting fO_2 between IW-7 and IW-2. In diopside these cations seem to have apparent higher valence than in olivine, most likely as a result of crystal chemical differences. NWA7325 was subjected to a pervasive melting episode in its very early history, dated to 4562.5 ± 4.4 Ma. Oxygen isotopic compositions were believed to indicate genetic alliance with ureilites. A novel assemblage of residual melted oldhamite (CaS) with a unique REE pattern, a Ba-rich sulphide, CaS residues and chromite were also encountered. This meteorite offers a new cosmochemical venue for evaluating the effects of a second melting episode on an already differentiated meteorite.

Six sections sliced from the same fragment unexpectedly revealed heterogeneous mineral abundances. Modal abundances of metals, $(Fe,Ni)_3P$ and sulphides to total silicates and chromite vary considerably across the 6 sections. Intergrowth textures believed earlier to be

evidence for anorthite replacing diopside are more likely to be depicting a typical intersertal co-crystallization fabric also with 60 µm large troilite and metal assemblages that are characteristic of slow cooling (Fig. 3.2-1). Anorthite grains have high concentrations of Eu and Sr but are depleted in Ba. The meteorite probably did not emerge from an ureilitic parental planet. Enclaves in both FeNi and FeS with high abundances of Ca and S most likely originated as CaS with a unique REE and trace element signature. Their CI-normalized Eu, Ba and Sr are hence different from CaS in EH, EL chondrites and aubrites altogether. Chromite shows enormous CI-normalized V (1486 times CI) enrichments but unexpectedly low Ti concentrations. Remarkably, troilite contains high CI-normalized Sr concentration (> 10). The interpretation that this meteorite is related to ureilites is inconsistent with the mineralogy, fabric and CI-normalized trace element inventories of the mineral constituents. The unique REE pattern with positive Eu anomaly of the both anorthite prisms and oldhamite residues unambiguously indicates that this meteorite could not have formed by melting of an enstatite chondrite or aubrite.

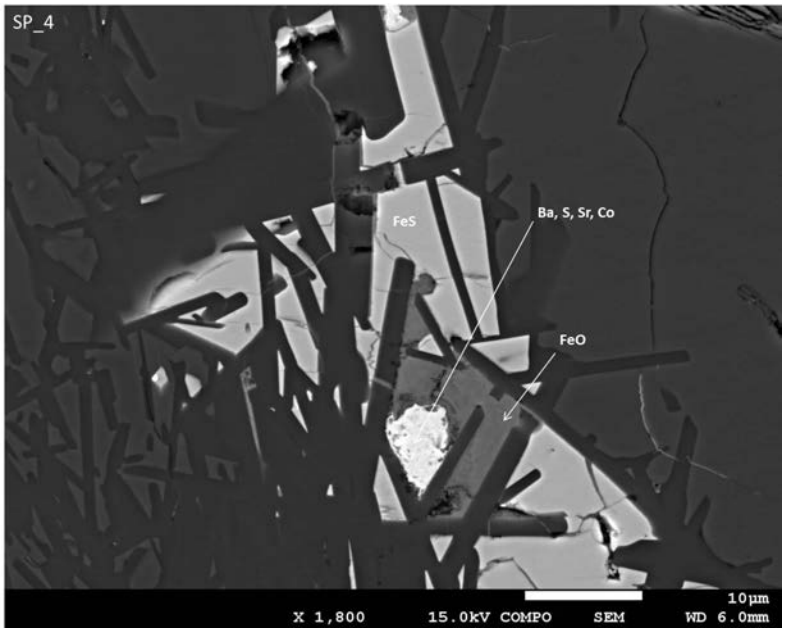

Fig. 3.2-1: A BSE-SEM photograph depicting the intimate anorthite (black prisms), diopside (dark grey), troilite (FeS) and Ba- and Sr sulphides (bright, in the centre).

b. *Are current models for the giant impact hypothesis of Moon formation sufficient to explain the oxygen isotoptic similarities between Earth and the Moon? (S.A. Jacobson and D.C. Rubie, in collaboration with A. Morbidelli/Nice, E.D. Young/Los Angeles and J. Hernlund/ Tokyo)*

There are a number of variations on the giant impact hypothesis for the formation of the Moon but in each a planetary embryo, often called Theia, strikes the proto-Earth creating a

disk of debris orbiting about Earth, and the Moon accretes out of this disk of debris. Models of this hypothesis successfully produce an Earth-Moon system with the correct masses and angular momentum, but whether the compositions are produced correctly has been an open question.

The Earth-Moon system is strikingly homogeneous in a number of different isotopic systems including oxygen, titanium, chromium, tungsten and silicon. Here, we focused on oxygen since it is the most exacting requirement; the measured $\Delta^{17}O$ difference between Earth and the Moon is 0.010 ± 0.002‰. This compositional similarity could be satisfied in two ways within the giant impact hypothesis: (1) there is significant material transport and mixing during the disk lifetime or (2) the impact dynamics naturally mixes the proto-Earth and Theia. Models of the giant impact provide estimates for the deviation percentage, *i.e.*, how compositionally different the proto-Earth and Theia can be before the impact. We constructed a model that predicts the oxygen isotopic composition of the proto-Earth and Theia, then examined whether the predicted impact scenarios could account for these deviation percentages.

We used numerical N-body simulations to model the formation of Earth and the other terrestrial planets in the Grand Tack scenario. From these N-body simulations, we have the accretion history and original locations of the planetesimals and embryos, which come together to create Earth and the Moon. We assigned each planetary building block a near CI chondrite composition and an oxidation state according to a heliocentric model. After each accretion event, accreted metal is absorbed into Earth's core including any siderophile elements according to partition equations developed from laboratory studies. The oxidation state model is a free parameter that is fitted such that the composition of the simulated Earth's mantle matches reality. From this oxidation state model and for every N-body simulation, we determine the relative abundance of oxygen as a function of heliocentric distance in three reservoirs: silicates, iron, and water. These are shown in Fig. 3.2-2.

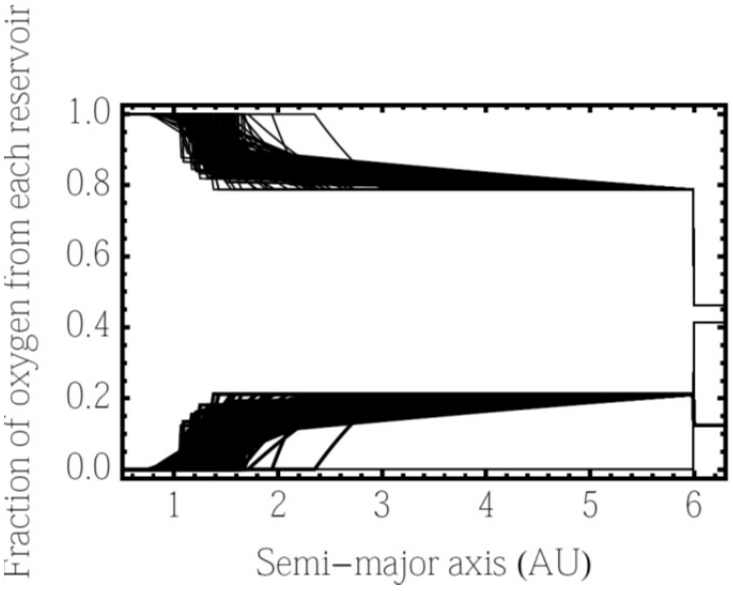

Fig. 3.2-2: The relative abundance of oxygen in three reservoirs for over 200 N-body simulations: silicates (uppermost lines), iron (lowermost lines), water (appearing only exterior to 6 AU).

Each oxygen reservoir is assigned a different isotopic composition because of different interaction profiles with the nebular gas. Silicates are expected to not interact very strongly with the gas and thus reflect a more solar composition, while iron is expected to interact more with the gas, and water is expected to interact strongly. Due to CO self-shielding, the nebular gas is expected to be strongly enriched in $\Delta^{17}O$. Since there are three reservoirs, we have three unknowns and only two measurements, the isotopic compositions of the Earth-Moon system and Mars. The $\Delta^{17}O$ composition of the silicates and the iron is then determined as a function of the $\Delta^{17}O$ of the water. These compositions are found to be mostly independent of the choice of water composition because water is such a small delivery mechanism for oxygen to Earth and Mars.

We determined the $\Delta^{17}O$ composition of the proto-Earth and Theia for each of the numerical N-body simulations assuming a $\Delta^{17}O$ water composition of 50‰. From this data, we derived probability distribution functions for the compositions of each body as shown in Fig. 3.2-3. Both of these bodies are negative compared to Earth, because late accreted mass is more enriched in water and so brings the $\Delta^{17}O$ composition more positive to zero. Remember, since we fitted the model to Earth and Mars, every simulation reproduces the $\Delta^{17}O$ composition of Earth and Mars exactly.

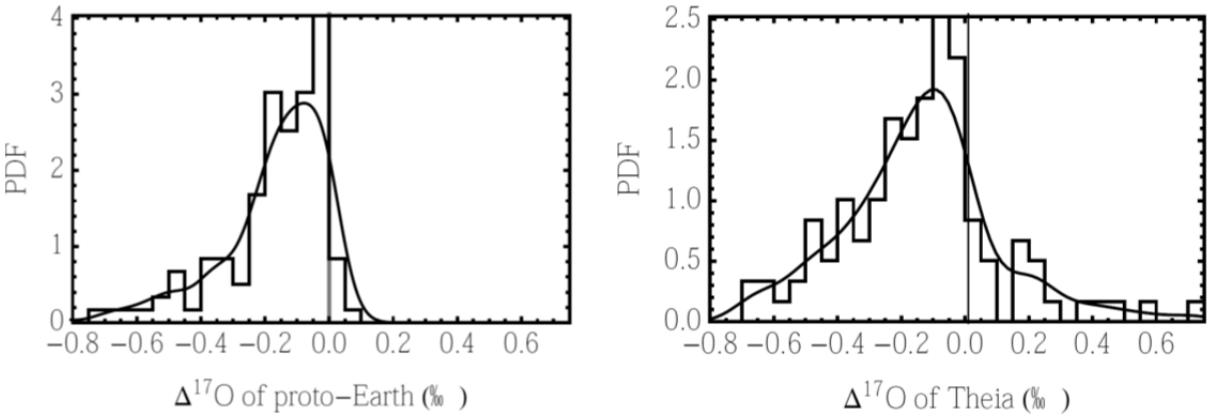

Fig. 3.2-3: Probability distribution functions of $\Delta^{17}O$ compositions for the proto-Earth and Theia.

From the compositions of the proto-Earth and Theia, we calculate the necessary deviation percentage (*i.e.*, the amount of mixing needed) to re-create the measured difference between Earth and the Moon's $\Delta^{17}O$ composition, as shown in Fig. 3.2-4. We find that ~ 10 % of numerical simulations produce proto-Earth and Theia compositions similar enough that the limited amount of mixing (small deviation percentages) found in giant impact simulations is enough. Therefore, this study supports the giant impact hypothesis in its canonical form without the need for significant disk-mantle interactions.

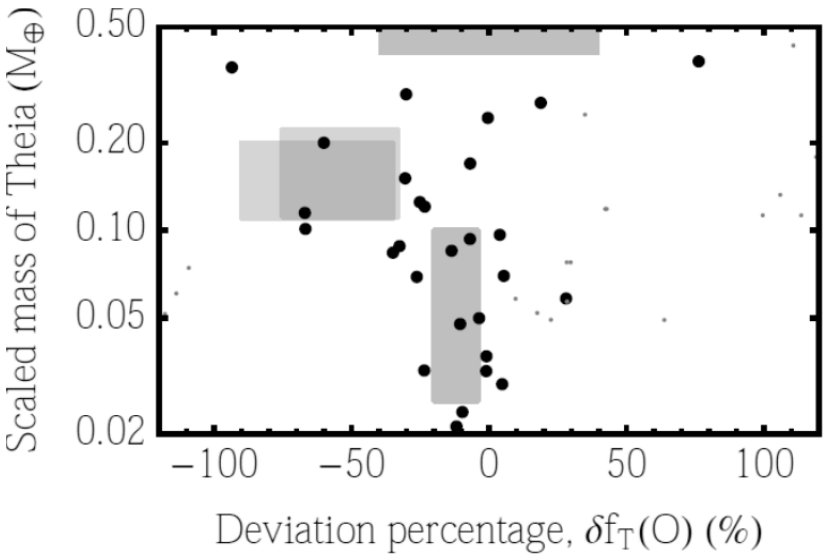

Fig. 3.2-4: The black points show deviation percentages and Theia masses for the roughly 10 % of numerical simulations that may be explained by natural mixing in the giant impact hypothesis. Different predictions for giant impact mixing are indicated by the gray rectangles; these are only representative and it is expected that families of solutions exist around these determined solutions.

c. *Metal-silicate partitioning of highly siderophile elements in sulfur-bearing systems – Implications for Earth's accretion and core formation history (V. Laurenz, D.C. Rubie and D.J. Frost)*

The highly siderophile elements (HSEs - Os, Ir, Ru, Rh, Pt, Pd, Re, Au) are useful tracers for processes involving metal-silicate equilibration, such as the formation of the Earth's core. Metal-silicate partition coefficients ($D_{HSE}^{metal\text{-}silicate}$) are not only high, but are also very variable among the HSE, so that they should become strongly fractionated during core formation. Yet, the HSEs are present in near-chondritic proportions in the mantle. The most widely accepted explanation for this apparent contradiction is the so-called "late-veneer" hypothesis. The late-veneer involves the accretion of highly oxidized, chondritic material after core formation ceased, imposing the chondritic proportions among the HSE on the Earth's mantle. The amount of material added during this period is thought to be in the range of 0.3 to 1.0 % of the final Earth mass. These estimates crucially depend on the estimated abundance of HSE in the mantle after core formation, which is based on experimentally determined $D_{HSE}^{metal\text{-}silicate}$. However, most previous experimental work on HSE metal-silicate partitioning has been carried out on S-free systems. Sulfur was likely accreted during the late stages of accretion. It was suggested that consequently a discrete sulfide melt would be stabilized which would be sequestered to the core. This could have had a strong effect on the behaviour of the HSE during the final stages of core formation, and consequently on estimates of mantle HSE abundances and the mass of late veneer.

In order to investigate the effect of S on the behaviour of the HSEs during core formation, we have studied the metal-silicate and sulfide-silicate partitioning of Pt, Pd, Ru and Ir under high-pressure/high-temperature conditions. The starting silicate was a primitive mantle composition, which was equilibrated with a range of compositions along the Fe-FeS binary (5 - 35 wt. %. S), doped with two of the HSEs at a time (1-10 wt. % each). All experiments were performed in a multianvil apparatus at 2100-2400 °C and 11-21 GPa using single crystal MgO capsules. Quenched silicate and metal or sulfide were analysed by electron microprobe for their major element concentrations while trace element abundances were determined using LA-ICPMS.

Overall, it can be seen, that all HSEs become less siderophile with increasing S-content. However, the individual effect of S on the HSEs is variable. While D_{Pd} decreases only slightly, D_{Ir} decreases by more than two orders of magnitude. As a result, D_{HSE} of Pt, Pd, Ru and Ir converge towards high S concentrations. Furthermore, our experiments indicate that $D_{HSE}^{sulfide\text{-}silicate}$ (*i.e.*, ≈ 35 wt. % S) of Pt and Ru increase with pressure, whereas those of Ir and Pd decrease. Moreover, all $D_{HSE}^{sulfide\text{-}silicate}$ increase with temperature.

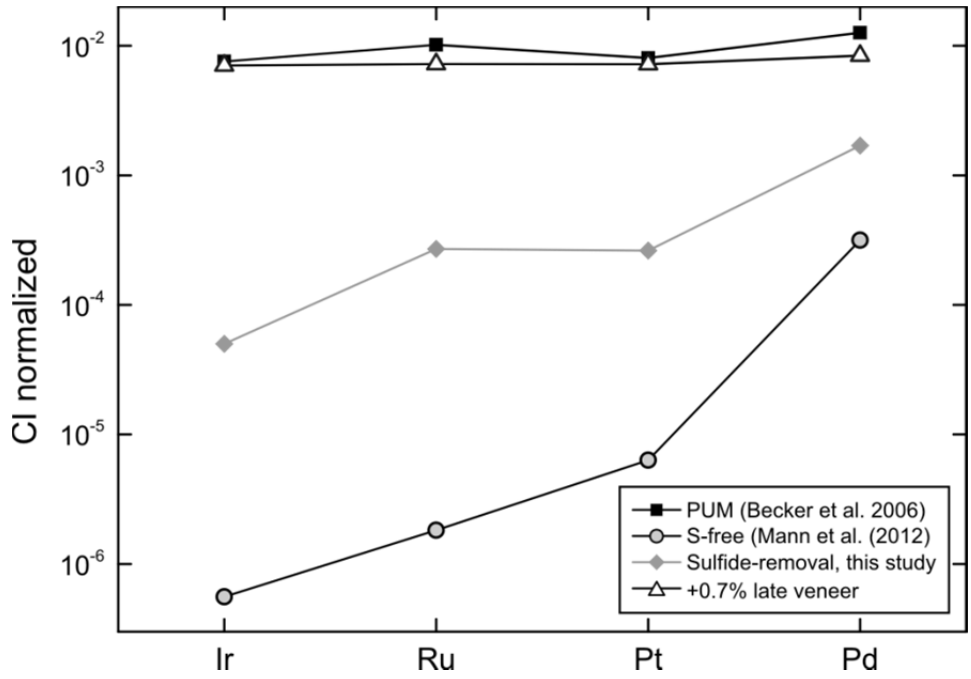

Fig. 3.2-5: Comparison of the CI-normalized abundances of the HSEs determined for the Earth's mantle (■ - Becker *et al.* 2006), compared with the results of our two-stage core formation model. Taking into account the segregation of a discrete sulfide phase (◆) during the last 10 % of accretion and core formation results in elevated, and less fractionated HSE patterns compared to the S-free scenario (○). The addition of ~ 0.7 % of late-veneer (△) then raises the HSE mantle abundances to the observed values for the primitive upper mantle (PUM - Becker *et al.* 2006; GCA 70, 4528-4550).

In order to assess the consequences of these results for the behaviour of the HSE during core formation, we have modelled the HSE in a simple two-stage core formation scenario. We assumed that Earth has a chondritic bulk composition, and that the core comprises 32 % of Earth's mass. Furthermore, we assumed that the first 90 % of Earth's mass was accreted from S-free material, so that the HSE abundances in the mantle can be modelled using metal-silicate partition coefficients determined in S-free systems. The silicate mantle becomes strongly depleted in HSEs during this phase, producing highly fractionated HSEs patterns in the Earth's mantle (Fig. 3.2-5). Assuming that sulfide melt was segregated to the core while the last 10 % of material was added to Earth, we have modelled the HSEs in the mantle using $D_{HSE}^{\text{sulfide-silicate}}$ determined in this study. The fractionation among the HSE is significantly smaller than that observed for the S-free case. However, the near-chondritic proportions of the HSE in the Earth's mantle cannot be reproduced (Fig. 3.2-5) Also, the calculated abundances of HSE are significantly smaller than the observed HSE abundances of the mantle. The amount of late-veneer necessary to raise the HSE abundances to the values of the mantle is calculated to be ~ 0.7 % of the Earth mass. This value compares well with previous estimates assuming core formation in a S-free environment, since absolute differences between the two scenarios are small.

d. *Oxidation state of the lower mantle:* In situ *observations of the iron electronic configuration in magnesium silicate bridgmanite at extreme conditions (I. Kupenko, C.A. McCammon, R. Sinmyo, V. Cerantola, V. Potapkin/Jülich, A.I. Chumakov/Grenoble, A. Kantor, R. Rüffer/Grenoble and L.S. Dubrovinsky)*

$MgSiO_3$ bridgmanite that contains Fe and Al (hereafter FeAlBg) is considered to be the most abundant phase in the Earth and to constitute roughly 75 % of the lower mantle. Iron can occur in both ferrous (Fe^{2+}) and ferric (Fe^{3+}) forms in FeAlBg. In contrast to phases in the upper mantle, the amount of ferric iron in FeAlBg is expected to be high, but until now all estimations of $Fe^{3+}/\Sigma Fe$ in the lower mantle have been based on measurements at room temperature from quenched samples.

The spin state of iron in FeAlBg in different valence states may affect the thermodynamic properties, electrical and thermal conductivities, and other properties of the Earth's interior. Many studies have been performed to determine the spin state of Fe in FeAlBg, but the conclusions reached are not uniform. Moreover the majority of previous reports describing the spin state behaviour in FeAlBg at lower mantle conditions are based on analysis of temperature-quenched samples. Recent progress has been made by probing the spin state of FeAlBg at lower mantle temperatures based on Nuclear Forward Scattering (NFS) data. However, NFS is not well suited to materials with a large number of components arising from multiple sites, valence states, and spin states (which is the case for FeAlBg), which leads to spectral complexity and non-uniqueness of fitting models. Energy-domain Mössbauer spectroscopy (MS) is better suited for the analysis of iron distribution between individual

structural sites in FeAlBg, and its oxidation and electronic states. However, studies of lower mantle phases at the relevant high-pressure and -temperature conditions are not possible using conventional MS with a radioactive source due to the challenge of focusing gamma rays in the laboratory. The recently developed Synchrotron Mössbauer Source (SMS) allows measurements of high quality and well resolved energy-domain spectra on timescales of only a few hours, combining the advantages of synchrotron radiation and the MS technique.

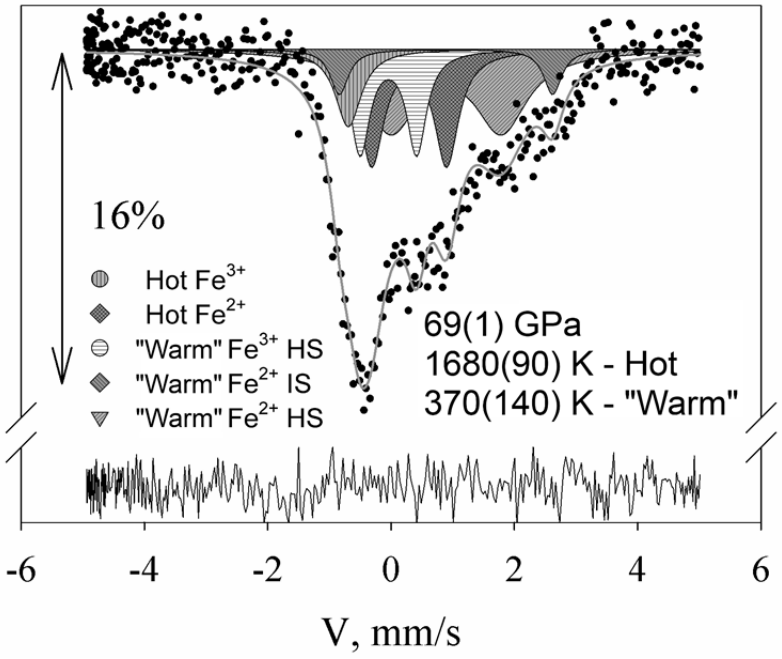

Fig. 3.2-6: High-pressure SMS spectrum of $Mg_{0.83}Fe_{0.21}Al_{0.06}Si_{0.92}O_3$ bridgmanite at high temperature. The solid line shows the theoretical fit, the arrow shows the amount of absorption, and the residual is indicated below the spectrum. Due to nonhomogeneous heating the spectrum shows a superposition of absorption arising from hotter and cooler (referred to as "warm") material. Temperatures were determined from the shift of the centre shift values. HS: high-spin; IS: intermediate-spin.

We have investigated the electronic configuration of iron in Fe-, Al-containing magnesium silicate bridgmanite, the main component of the lower mantle, at conditions of the deep Earth's interior using the energy domain SMS technique. We show that the high ferric iron content observed previously in quenched samples is preserved at high temperatures and high pressures (Fig. 3.2-6). Our data are consistent with high-spin to intermediate-spin (HS-IS) crossover in Fe^{2+} at high pressures and ambient temperature. We see no evidence of spin crossover in Fe^{3+} occupying the A-position of bridgmanite. On laser heating at pressures above ~ 40 GPa we observe a new doublet with relative area below 5 % which likely corresponds to Fe^{3+} in the octahedral (B-site) position in bridgmanite (Fig. 3.2-7). We conclude that at lower mantle conditions Fe^{3+} remains predominantly in the HS state, while Fe^{2+} occurs solely in the IS state.

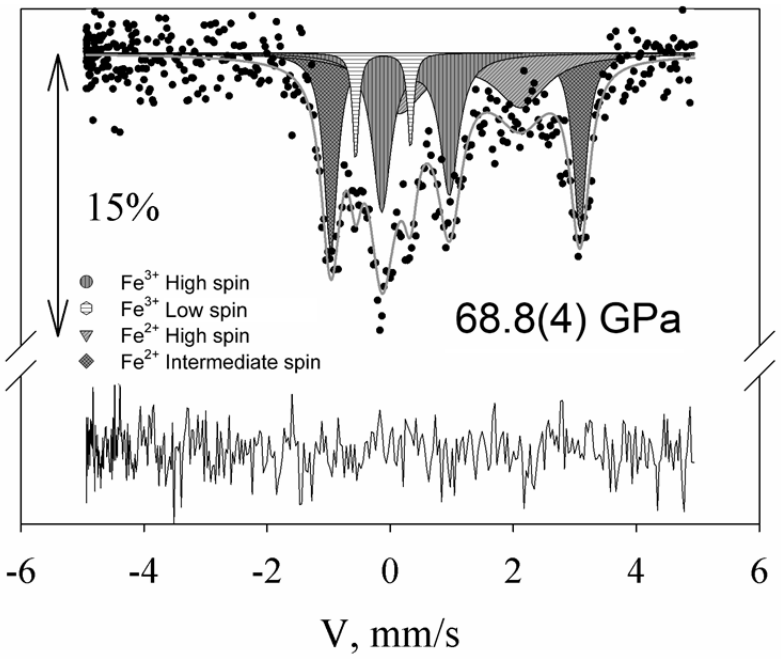

Fig. 3.2-7: High-pressure SMS spectrum of $Mg_{0.83}Fe_{0.21}Al_{0.06}Si_{0.92}O_3$ bridgmanite at room temperature. The solid line shows the theoretical fit, the arrow shows the amount of absorption, and the residual is indicated below the spectrum.

e. *Melting and subsolidus phase relations in the MgO-SiO_2-Fe_2O_3 system under lower mantle conditions (R. Sinmyo, Y. Nakajima, C.A. McCammon, R. Myhill and D.J. Frost)*

It is known that bridgmanite, which is the most abundant mineral in the Earth, can accommodate much greater concentrations of Fe^{3+} than other mantle minerals. Moreover, many previous studies have highlighted a significant effect of Fe^{3+} on the elastic parameters, element partitioning and transport properties of bridgmanite. However, the high-pressure phase relations are poorly understood in compositions including Fe^{3+} such as in the MgO-SiO_2-Fe_2O_3 system.

We have conducted high-pressure and -temperature experiments using the multianvil apparatus to study phase relations in the MgO-SiO_2-Fe_2O_3 system under lower mantle conditions. MgO, SiO_2 and Fe_2O_3 were used as starting materials. These were mixed without reducing the ferric iron. The starting materials have compositions of $Mg_{0.95}Fe_{0.10}Si_{0.95}O_3$, $Mg_{0.75}Fe_{0.50}Si_{0.75}O_3$, $Mg_{0.80}Fe_{0.20}Si_{1.00}O_3$ and $MgFe_2O_4$. All experimental runs were conducted at 26 GPa, corresponding to the pressure at the top of the lower mantle. Recovered samples were investigated by electron probe microanalysis, Mössbauer spectroscopy and X-ray diffraction (XRD). Mössbauer spectroscopy showed that iron in the recovered samples was dominantly Fe^{3+}. At temperatures below ~ 1900 K, we observed $MgSiO_3$-rich bridgmanite, Fe^{3+}-rich oxide phase and stishovite in the recovered sample by XRD and microprobe analysis. On the contrary, quenched partial melt was observed together with bridgmanite and

stishovite in the sample above ~ 1973 K (Fig. 3.2-8). This indicates that the solidus temperature is significantly lower than that in the Fe^{3+}-free bulk composition. This is likely due to a lower eutectic point between bridgmanite and an Fe^{3+}-rich oxide phase, compared to bridgmanite and ferropericlase. Although the maximum solubility of iron in bridgmanite was significantly higher than observed in reduced bulk compositions, the coexisting liquid was still more iron-rich than bridgmanite. Current results suggest that strong anomalies in mantle oxygen fugacity could lead to partial melting and influence subsolidus phase relations of the lower mantle.

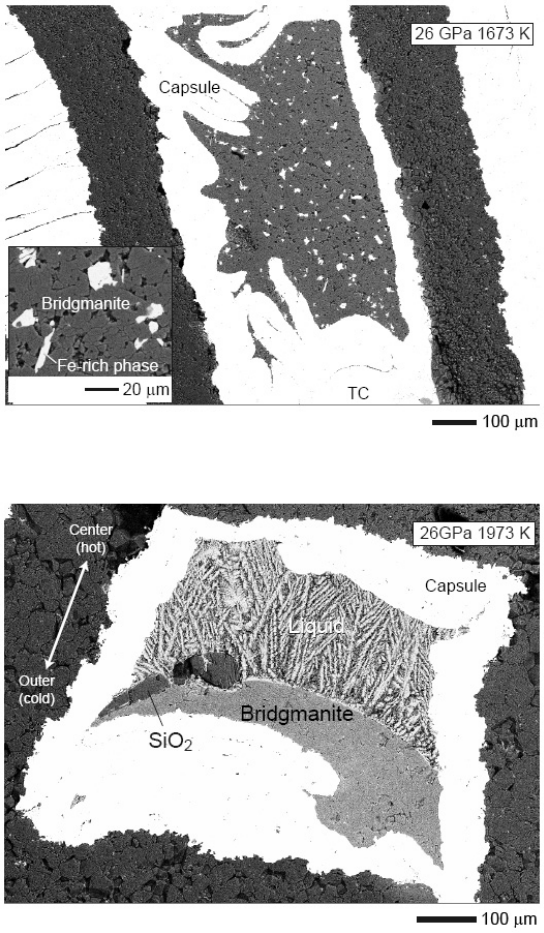

Fig. 3.2-8: Backscattered electron images of recovered samples from 26 GPa and 1673 K (upper) and 1973 K (lower).

f. *The behaviour of ferric iron (Fe^{3+}) during MORB petrogenesis (F. Sorbadere, D.J. Frost, M. Wenz, A. Rosenthal, V. Laurenz and C.A. McCammon)*

The oxidation state of iron in MORB glasses is proposed to be directly related to the oxygen fugacity (fO_2) of the upper mantle, from where it derives. Recently measured $Fe^{3+}/\Sigma Fe$ ratios in MORB show a very narrow range, from 0.15 to 0.18, with a global average of 0.16±0.01, which corresponds to an fO_2 close to the fayalite-magnetite-quartz (FMQ) buffer. Fe^{3+} is assumed to be incompatible during partial melting. Hence, $Fe^{3+}/\Sigma Fe$ ratios in MORB are expected to correlate with degrees of partial melting and fractional crystallisation, similar to the behaviour of other incompatible elements. However, Fe_2O_3 contents of primitive MORB

do not vary with melt-fraction related parameters such as the Na_2O (Fig. 3.2-9). Although correlations between $Fe^{3+}/\Sigma Fe$ ratios and indices of low pressure fractional crystallization have been recognized in global MORB, they are not systematic. The absence of clear correlations between the $Fe^{3+}/\Sigma Fe$ ratio of MORB and the degrees of partial melting and/or fractional crystallization implies that this ratio is controlled or even buffered by some additional process.

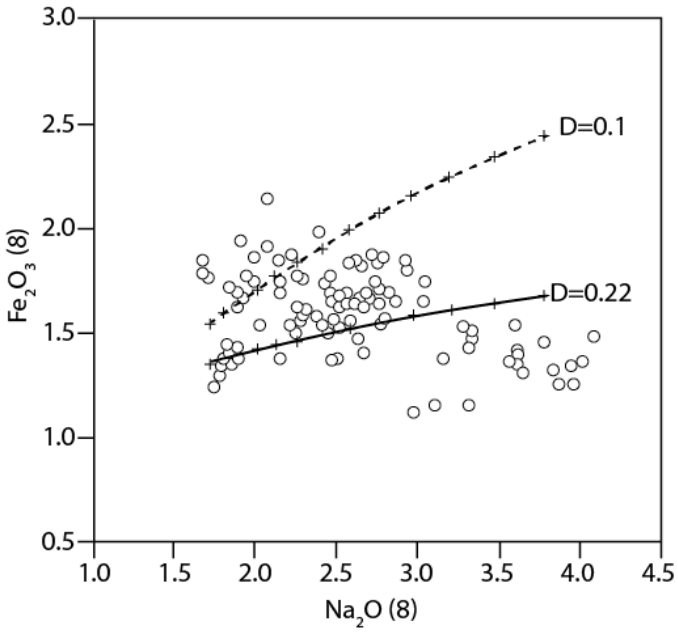

Fig. 3.2-9: Plot of Fe_2O_3 (8) as a function of Na_2O (8) for MORB (open circles) modified from Cottrell and Kelley (2011; EPSL 305, 270-282). Oxide concentrations were corrected for fractionation to 8 wt. % MgO. Curves show theoretical evolution of melts derived from a typical MORB-mantle source at between 8 and 20 % of partial melting and assuming Fe_2O_3 mineral/melt partition coefficients of 0.1 (dashed curve) and 0.22 (solid curve).

One possibility to account for this $Fe^{3+}/\Sigma Fe$ paradox might be a change in the Fe^{3+} partition coefficient between mineral and melt as a function of the degree of peridotite melting (Fig. 3.2-9). The decrease in the Fe^{3+} content of the melt expected for increasing melt extraction would have to be off-set by a process that would make Fe^{3+} more incompatible at higher degrees of melting. To determine the effect of temperature and fO_2 on the Fe^{3+} partition coefficient between spinel (*i.e.*, the main mineral which contains Fe^{3+} in a MORB-mantle source) and liquid during the partial melting of a MORB-mantle source, we have performed partial melting experiments of the peridotite MPY-90 at 1.5 GPa, between 1320 and 1450 °C, over a range of fO_2 varying from FMQ-5 to FMQ+3. Changes in oxygen fugacity were obtained using different capsule materials (*i.e.*, graphite for reduced, rhenium for intermediate and gold-palladium for oxidized conditions). Fe^{3+} contents of the spinels and melts have been obtained using X-ray Absorption Near Edge Structure (XANES) in Grenoble at the Synchrotron. Glass and spinel standards have been previously synthesized and analysed by

Mössbauer spectroscopy. Glass standards have been synthesized from a basaltic composition using a gas mixing furnace at various fO_2 conditions. For spinel synthesis, we used a sol-gel auto-combustion method to synthesize our starting material. FMQ-2, FMQ+0, and air fO_2 conditions were established using a gas mixing furnace. Piston cylinder experiments were then performed at 1.5GPa, and 1350 °C to obtain solid material for XANES measurements. To maintain distinct oxidizing conditions, we used the same three different capsules as for our experiments. To complete our Fe^{3+} range of spinel standards for XANES measurements, we also used spinels from natural peridotites from different tectonic contexts. Both glasses and spinel standards analyzed by Mössbauer spectroscopy had $Fe^{3+}/\Sigma Fe$ values which are consistent with the Fe edge position obtained using XANES (Fig. 3.2-10). The resulting calibration curves have been used to determinate the $Fe^{3+}/\Sigma Fe$ ratio of glasses and spinels of our samples.

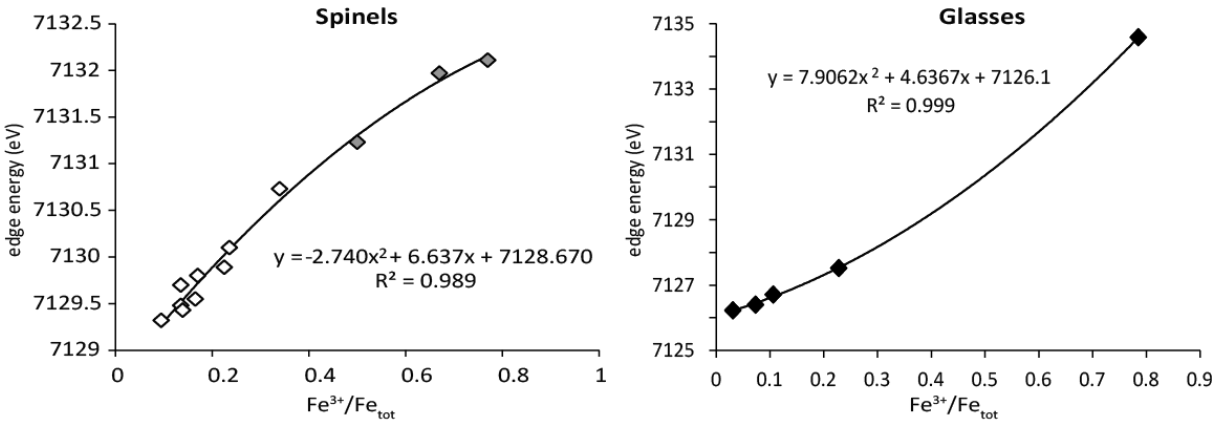

Fig. 3.2-10: Iron edge energy obtained from XANES spectra versus Fe^{3+}/Fe_{tot} ratio measured by Mössbauer spectroscopy for natural (open diamonds) and synthetic (grey diamonds) spinels and glasses used as standards. R^2 is the correlation coefficient of the curve.

$Fe^{3+}/\Sigma Fe$ values for our partial melting experiments increase with fO_2. However, there is no correlation between partial melting degree and $Fe^{3+}/\Sigma Fe$ in melts, because melt fraction is essentially controlled by the presence of H_2O (less than 1 wt. %), which is particularly concentrated in the most oxidizing experiments. This has been confirmed by Fourier Transform Infra-Red (FTIR) measurements in glasses which show H_2O increases with increasing Fe^{3+}. However, fO_2 conditions, calculated using spinel as a oxybarometer, are positively correlated with the Fe_2O_3 partition coefficient between spinel and liquid (Fig. 3.2-11). Under high fO_2 conditions, Fe^{3+} is more compatible in spinel (D^{Fe2O3}=5 at FMQ+3) than under low fO_2 conditions (D^{Fe2O3}=0.5 at FMQ-4). This result demonstrates that Fe^{3+} behaviour changes as a function of oxidation state during partial melting of a peridotite source. Considering a fractional melting process as the dominant process responsible for MORB genesis, then the fO_2 in the mantle source is expected to decrease while both melt fraction and melt extraction increase. This is due to incompatible behaviour of Fe^{3+} which is preferably

incorporated in melts, thus leaving a residue depleted in Fe^{3+}. Therefore, D^{Fe2O3} variations as a function of fO_2 (and partial melting degree) could explain the absence of a correlation between Fe^{3+} and melt-fraction related parameters, observed in primary MORB.

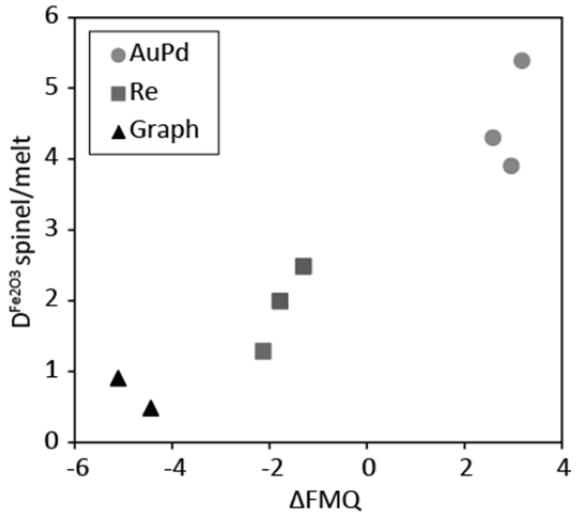

Fig. 3.2-11: Fe_2O_3 partition coefficient between spinels and melts as a function of variations of oxygen fugacity relative to the FMQ buffer for our experiments using different capsules: Graph (graphite) for reduced, Re for intermediate and AuPd for oxidizing conditions.

g. *The oxygen fugacity of diamond formation in carbonated eclogite rocks (H. Mohseni and D.J. Frost)*

The oxygen fugacity of mantle rocks can influence, or can be influenced by, the speciation of volatile elements. Carbon will vary its mobility, from immobile graphite or diamond to mobile carbon dioxide or carbonate melts, as a function of fO_2. As a consequence, in order to understand the carbon cycle within the Earth's interior, it is important to determine carbon speciation as a function of mantle redox state. At subduction zones carbon is returned to the mantle in the form of carbonate minerals in altered oceanic crust. At pressures above 1 GPa these rocks would recrystallize to form carbonated eclogite. In this study we have attempted to determine the fO_2 at which carbonate liquid components in these rocks would become immobilised by reduction to form graphite or diamond. In such a refractory form carbon would then be subducted into the deep mantle, rather than being returned to the overlying shallow mantle as a melt or fluid.

In each experiment the fO_2 was fixed by the equilibrium between graphite or diamond and CO_2 bearing melt produced within a carbonated eclogite assemblage. The fO_2 was then measured using sliding alloy redox sensors with the equilibrium:

$$\underset{\text{garnet}}{Fe_3Al_2Si_3O_{12}} = \underset{\text{kyanite}}{Al_2SiO_5} + \underset{\text{coesite}}{2SiO_2} + \underset{\text{alloy}}{3Fe} + 1.5O_2$$

Through the expression for the Gibbs free energy of the equilibrium, the fO_2 becomes sensitive to the activities of each component. If the Fe component is diluted with an alloying metal such as Ir, the composition of the alloy shifts to equilibrate with the buffered fO_2, which can then be determined from the component activities. In this study 3 different alloy redox sensors were used in a single experiment using the same carbonated eclogitic assemblage to buffer the fO_2. In this way the different alloys could be compared to ensure that they predict the same fO_2 at high pressure. Experiments were performed in the range 4-10 GPa and 1000-1500 °C using a multianvil device.

Results of the fO_2 measurements obtained from the 3 alloys at 7 GPa are shown in Fig. 3.2-12. Oxygen fugacities measured using Ir-Fe and Pt-Fe alloys are generally consistently within ~ 0.5 log units. Pt-Fe values are consistently higher than Ir-Fe, which may result from underestimating the excess volume of mixing, due to the formation of intermediate ordered alloy structures in the Pt-Fe system at 1 bar. The more scattered values calculated from the Pd-Fe alloys may be caused by the much higher carbon solubility in these alloys, which reaches ~ 2 wt. %. The more reliable values determined from Ir and Pt based alloys define a decreasing trend in fO_2. Each point separates the stability field of diamond at lower fO_2 from the stability of carbonate melt/CO_2-bearing silicate melt at higher fO_2. Melts become more silicate rich with temperature and the resulting dilution of the CO_2 component drives the fO_2 down. The EMOD curve describes the fO_2 buffered by the reaction of magnesite and enstatite to olivine and diamond, which will similarly control the diamond stability field with respect to carbonate in peridotite rocks. The results show that the diamond stability field in eclogitic assemblages actually extends to higher fO_2 than in peridotite assemblages, although this relationship reverses at higher temperatures.

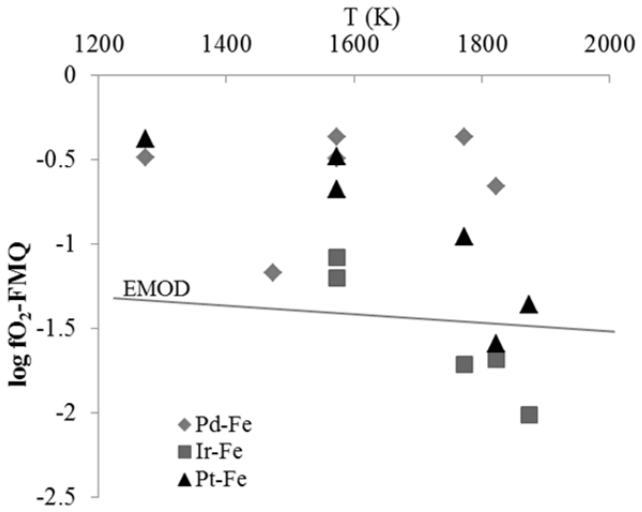

Fig. 3.2-12: Oxygen fugacities determined for the equilibrium between carbonate/CO_2-bearing silicate melts and diamond in an eclogite assemblage at 7 GPa, measured using 3 different sliding alloy sensors. The EMOD curve defines the stability field of carbonate melt and diamonds in peridotitic compositions.

h. *Syngenesis of diamonds and minerals of the Earth's lower mantle (D. Simonova and A. Spivak/Chernogolovka, L.S. Dubrovinsky, Y. Litvin/Chernogolovka)*

Primary (syngenetic) inclusions in lower mantle diamonds are fragments of the growth medium (medium in which the diamond was formed) and carry accurate and detailed

information about the phase and chemical composition of the growth medium, but cannot reveal the mechanism of diamond formation. The genesis of diamonds may be understood based on results of physicochemical experiments and on a syngenesis criterion of diamonds and inclusions

Formation of lower mantle diamonds was experimentally studied in melts of variable compositions in the system carbonate-oxide-silicate-carbon $(FeO)(MgO)(SiO_2)$-(Mg-Fe-Ca-Na-carbonate)-C at lower mantle conditions of 26 GPa and 1700 °C. It was found that diamonds crystallize paragenetically with magnesiowustite, bridgmanite, stishovite and carbonate minerals in ultrabasic and basic parental melts at these conditions (Fig. 3.2-13). Furthermore, it was demonstrated that at lower mantle conditions the nucleation concentration barrier for diamond formation in carbonate-bearing silicate melts lies at 70 wt. % silicate component, which is about twice as high as the ~ 35 wt. % determined at upper mantle conditions. Compositional data of inclusions within diamonds suggest that carbonates are one of the main components of the primary growth medium. Mg,Fe-bridgmanite, magnesiowustite, stishovite and diamonds may thus form paragenetic associations at conditions of partial carbonate-silicate-oxide melting. The experimental data are useful to interpret the paragenetic relations for lower-mantle diamonds and their primary ultrabasic and basic inclusions.

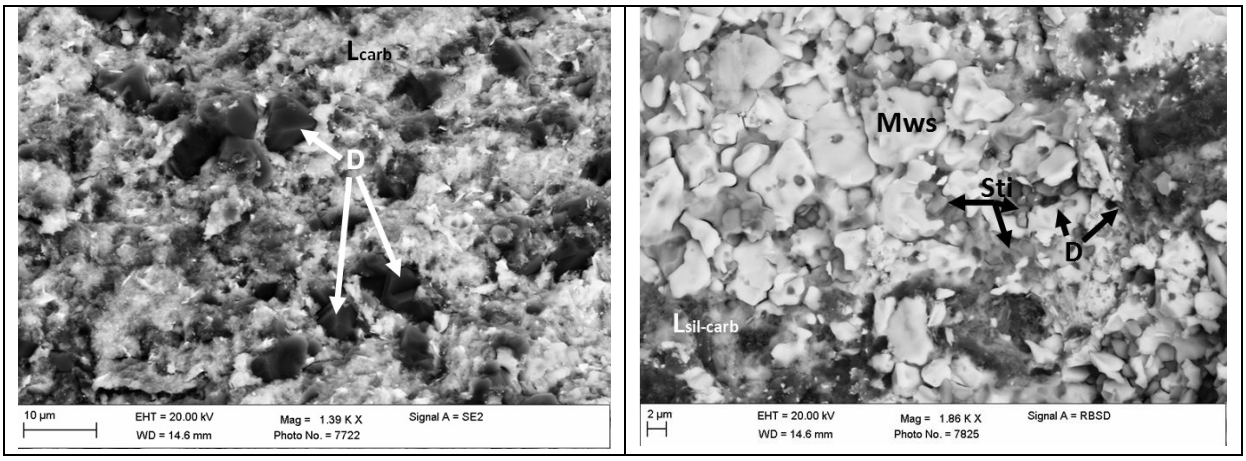

Fig. 3.2-13: SEM image of experimental samples. (left) diamond crystallization in the carbonate $(Fe\text{-}Mg\text{-}Na\text{-}Ca\text{-}Carb)_{60}\text{-}C_{40}$ system, 1700 °C, 26 GPa (#S6011-2). (right) syngenesis of diamond, magnesiowustite and stishovite in the carbonate-silicate $(((MgO)_{49}(FeO)_{30}(SiO_2)_{21})_{60}$–$(Fe\text{-}Mg\text{-}Na\text{-}Ca\text{-}Carb)_{40})_{60}\text{-}C_{40}$ system, 1650 °C, 26 GPa (#S6017-2)

i. *Evolution of the Earth's lower-mantle: The stishovite paradox (experiments at 24 GPa) (A. Spivak/Chernogolovka, L.S. Dubrovinsky, Y. Litvin/Chernogolovka)*

Ultrabasic-basic evolution of lower-mantle matter is marked by essential physicochemical events such as the "stishovite paradox" and the origin of "super-deep" diamonds. Stishovite

and ferropericlase-magnesiowustite phases (Mg,Fe)O are paradoxically found together as inclusions within lower-mantle "super-deep" diamonds. Due to formation of intermediate silicates, similar associations of these oxides should be chemically "forbidden" *i.e.*, out of equilibrium, under crustal and upper mantle conditions. Experimental and physicochemical studies of melting relations in the MgO – FeO – SiO_2 system at 24 GPa suggest that the "stishovite paradox" may be explained by the peritectic reaction $(Mg,Fe)SiO_3 + L = SiO_2 + (Mg,Fe)O$ (Fig. 3.2-14). Formation of "super-deep" diamonds associated with ultrabasic $(Mg,Fe)SiO_3 + (Mg,Fe)O$ and basic $(Mg,Fe)O + SiO_2$ minerals was experimentally determined for carbonatite-silicate-oxide-carbon melts parental for diamonds and their lower-mantle inclusions. From this it is inferred that a similar peritectic mechanism is responsible for the "stishovite paradox" in the parental media of natural diamonds.

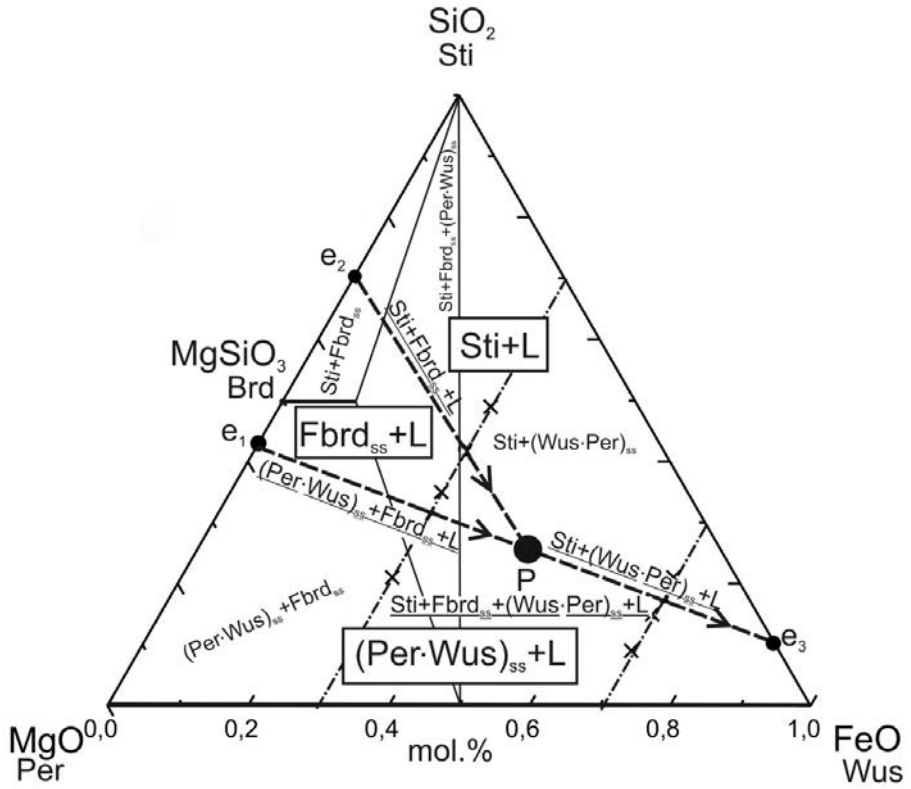

Fig. 3.2-14: Schematic melting phase diagram on the lower-mantle Per – Sti – Wus system based on experimental evidence at 24 GPa. Boundaries between subsolidus fields are marked by thin lines, univariant cotectics by dashed lines with arrows, solid solutions by thick lines. Symbols for solidus invariant points: e_1 - eutectic Per+Brd = L of the binary boundary join Per – Brd; e_2 - eutectic MgPrv+Sti = L of the binary boundary join Brd – Sti; e_3 - eutectic Sti+Wus = L of the binary boundary join Sti – Wus; *P* - peritectic $Fbrd_{ss}$ +L = Sti+$(Wus{\cdot}Per)_{ss}$ of the ternary system Per – Sti – Wus. Symbols for components: Per – periclase MgO, Sti – stishovite SiO_2, Wus – wustite FeO, Brd – bridgmanite $MgSiO_3$, $Fbrd_{ss}$ – limited solid solutions of bridgmanite $(Mg,Fe)SiO_3$, $(Wus{\cdot}Per)_{ss}$ – unlimited solid solutions of wustite FeO and periclase MgO. The position of the polythermal sections, studied experimentally, are marked by the dot-and-dashed lines.

j. *Fluorine partitioning between garnet, clinopyroxene, and silicate melt under upper mantle conditions (C. Beyer and D.J. Frost; S. Klemme and T. Grützner/Münster; C. Magee and T.R. Ireland/Canberra)*

Fluorine (F) is the most abundant element among the halogens (Cl, Br, I). Over the last couple of years there has been renewed interest in the fate and cycling of fluorine within the mantle and in its partitioning behaviour between melts and fluids and nominally fluorine-free minerals (NFFM). Formerly, it was commonly accepted that the Earth's F budget is mainly governed by nominally fluorine-bearing minerals such as apatite, clinohumite, and phlogopite. But recent experimental studies indicate that the entire F cycle within the Earth's mantle can be solely hosted within NFFMs. Due to their high modal abundance and wide range of stability, F concentrations in major rock forming mineral phases like olivine and pyroxenes are sufficient to explain Earth's F budget. Although this concept is underpinned by several measurements on natural samples and experimental partitioning studies, it is not entirely understood how F is distributed between different mantle reservoirs (*e.g.*, ocean island basalt, lamproite, kimberlite) and what mechanisms cause the various concentrations in these reservoirs. Moreover, the partitioning behaviour of F under high pressure and temperature has not been extensively studied.

In this study we have investigated the partitioning of F between garnet, omphacitic clinopyroxene, and silicate melt in a hydrous basaltic system, which is representative of deeply subducted oceanic crust. We performed partitioning experiments between 4 and 7 GPa in a 1000 ton Kawai-type multianvil using 18/11 pressure media. Experimental charges yielded homogeneous, euhedral to subhedral garnet and clinopyroxene crystals coexisting with glassy basaltic melt. Since analysis of trace amounts of fluorine is a challenging task, run products were analysed using Sensitive High Resolutions Ion Microprobe (SHRIMP) to obtain precise F concentrations.

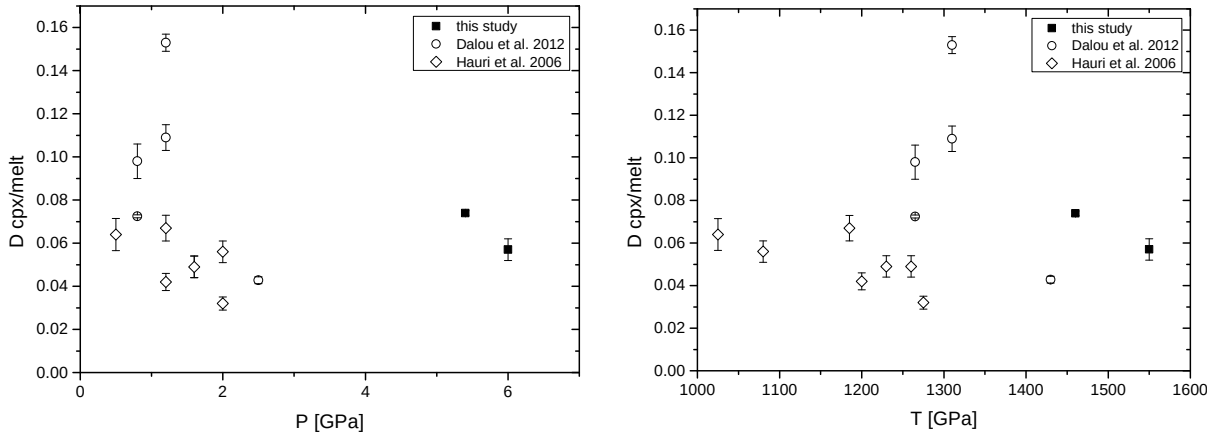

Fig. 3.2-15: $D_F^{cpx/melt}$ plotted against pressure (**left**) and temperature (**right**). Error bars represent the 1σ error. Dalou *et al.* (2012), Contrib. Mineral. Petrol. 163 (4); 591-609, Hauri *et al.* (2006), EPSL 248 (3-4):715-734

Our measurements indicate that clinopyroxene has the highest partition coefficient (av. $D_F^{cpx} = 0.065 \pm 0.010$) of all NFFMs in the Earth's upper mantle and is therefore the dominant F-host. We found that the partitioning is independent of end-member composition and independent of pressure and temperature (Fig. 3.2-15a and b). Garnet has a much smaller partition coefficient ($D_F^{grt} = 0.016 \pm 0.003$) that is slightly larger than olivine. A garnetite or dunite lithology would therefore be poor in F. Similar to cpx, garnet D's also show no distinct variation with pressure and temperature (Fig. 3.2-16a and b).

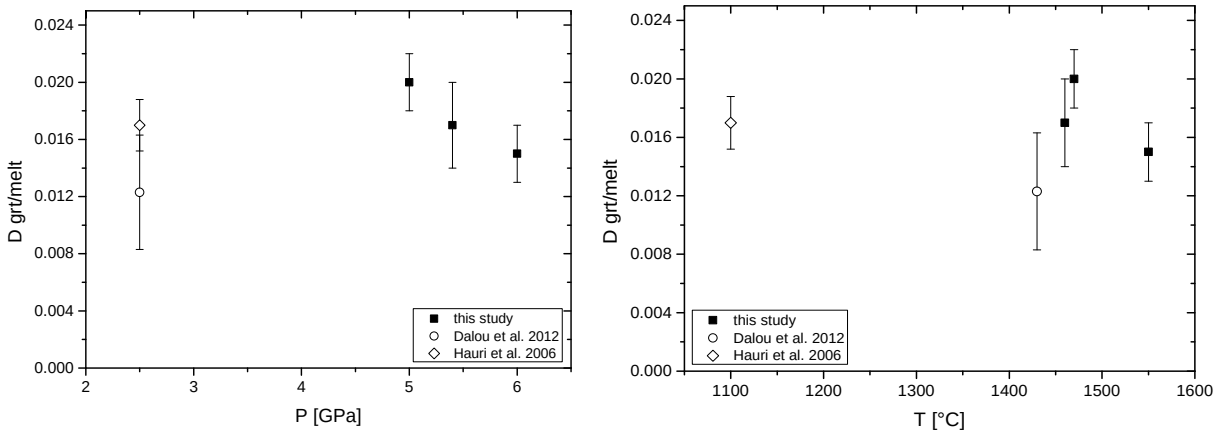

Fig. 3.2-16: $D_F^{grt/melt}$ plotted against pressure (**a**) and temperature (**b**). Error bars represent the 1σ error. Dalou *et al.* (2012), Contrib. Mineral. Petrol. 163 (4); 591-609, Hauri *et al.* (2006), EPSL 248 (3-4):715-734

F partition coefficients for major mantle minerals decrease in the order $D^{cpx} > D^{opx} >> D^{grt} > D^{ol}$. As a consequence, an eclogite assemblage dominated by clinopyroxene and garnet would likely transport proportionately more F into the deep Earth than peridotitic lithologies. The calculated bulk partition coefficient for a typical peridotite is 0.016, whereas the bulk partition coefficient for eclogitic subducted oceanic crust is ~ 0.048. Together with the finding that F partitioning does not decrease with pressure, it is possible that F will not be released during slab transport towards the Earth's transition zone. With increasing pressure, however, the transformation of eclogitic assemblages into a majoritic garnet dominated lithology, may result in the saturation of minerals with F, possibly leading to its incorporation into small degree partial melts such as lamproites, which are known to be F-rich. At transition zone conditions it is also likely that F can be incorporated into dominant minerals such as ringwoodite and wadsleyite. This seems reasonable given the large proportions of OH that are known to partition into these minerals and the fact that OH groups and F are nearly identical in ionic radii, charge, and mass.

k. *High-pressure melting relations in the water-rich system $Mg(OH)_2$-SiO_2-H_2O (R. Myhill and D.J. Frost)*

The deep hydrogen cycle is driven in part by the subduction of cold lithosphere, which carries mineral-bound water within a series of hydrous phases. As subducting slabs heat up, these phases are progressively dehydrated, releasing water-rich fluids and melts. The compositions of hydrous fluids and melts that percolate through the slab are a function of temperature, pressure and the composition of the solid residue. Movement of such liquids is affected by reaction with their surroundings, which in turn can cause large-scale metasomatism. However, the equilibrium compositions of fluids under the relatively cold conditions of subducting slabs are poorly known, as suitable starting compositions are too water-rich to be prepared from materials that are solid under room conditions.

In this study, we have conducted multianvil experiments at 13 GPa, using solid platinic acid ($H_2Pt(OH)_6$) as a novel water source. Short experimental run durations and $Pt_{90}Rh_{10}$ and Au capsules are used to limit water loss. This technique has allowed us to study melting relations in parts of the MgO-SiO_2-H_2O system which have not been covered by previous studies. This study provides much improved constraints on water-induced melting of forsterite-enstatite mixes, and also the SiO_2-H_2O liquidus curve, previously studied to only 2 GPa (Fig. 3.2-17).

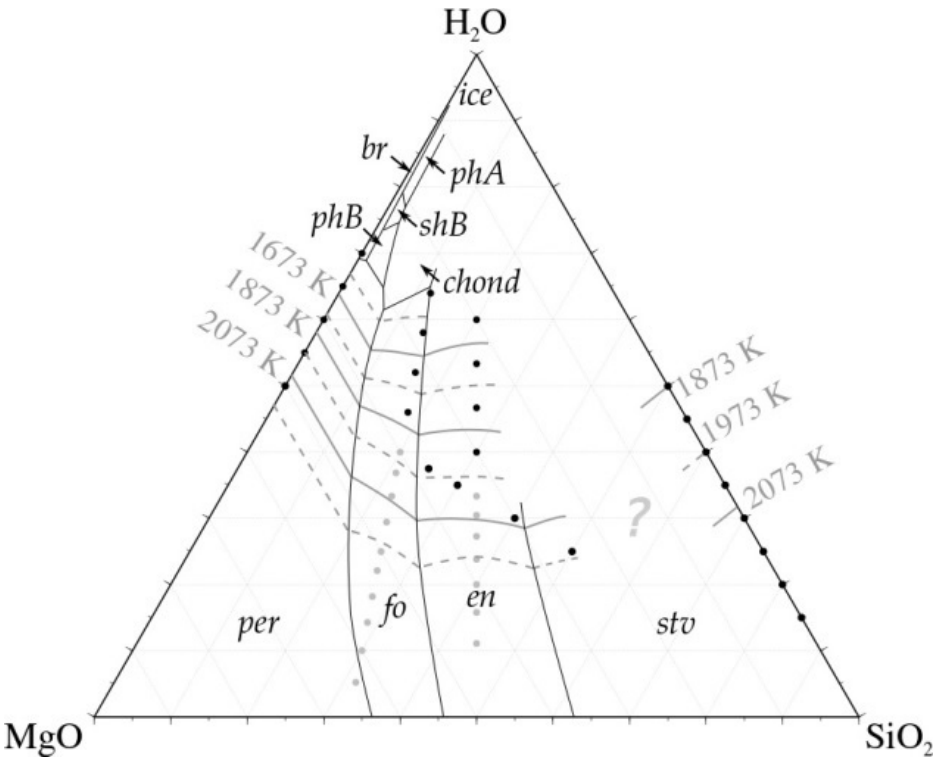

Fig. 3.2-17: MgO-SiO_2-H_2O liquidus diagram at ~ 13 GPa. Starting compositions are plotted as filled circles. Liquidus fields and their associated isotherms are constrained by the disappearance of the last solid phase in experimental run products.

l. *High-pressure experimental study of eclogite with varying H_2O contents (A. Rosenthal, D.J. Frost, S. Petitgirard and Zs. Pintér; G.M. Yaxley and A. Berry/Canberra)*

Heterogeneities in the mantle caused by the subduction of basaltic oceanic crust are unlikely to be homogenised in the mantle within a single convective cycle. It is, therefore, likely that a component of decompressive melting beneath mid ocean ridges and ocean islands is derived from such recycled basaltic units. The volatile contents of such recycled components may strongly influence the melting process. One of the only ways to determine this volatile content is to use high-pressure and temperature experimental facilities to simulate the entire volatile cycle within the basaltic material starting with the subduction process. During this initial process hydrated basaltic crust is transformed to eclogite and hydrous minerals that formed at the surface start to breakdown. As this occurs, minor but important amounts of H_2O are likely retained within nominally anhydrous minerals (NAMs) such as garnet, clinopyroxene, coesite/stishovite. The abundance and speciation of H_2O in eclogitic material is controlled by compositional variations of eclogite, which occur with increasing pressure and temperature. Changes in oxygen fugacity caused by pressure effects on ferric/ferrous component activities can also influence fluid speciation. The objective of this study is to measure H_2O contents and $Fe^{3+}/\sum Fe$ ratios of minerals formed in eclogitic assemblages at conditions followed by subducting oceanic crust.

By using synchrotron FTIR spectroscopy, and secondary ion mass spectroscopy (SIMS) the concentrations of H_2O incorporation into eclogitic minerals such as garnet, clinopyroxene, coesite/stishovite as nominally hydrous minerals such as phengite breakdown, will be determined as a function of P, T and oxygen fugacity. In addition, Micro-X-ray absorption near edge structure (XANES) analyses at the Fe K-edge will be also employed to determine garnet $Fe^{3+}/\sum Fe$ ratios.

The starting material is an average oceanic basalt (GA1) with a varying bulk H_2O content ($\leq$7 wt. %), doped with 3 wt. % Ir, which alloys with Fe during experiments and hence acts as a redox sensor. Experiments using GA1 have been performed at different pressures (6-10 GPa; *i.e.*, up to ~ 330 km depth), temperatures (850-1500 °C) and bulk H_2O contents using a multianvil apparatus. The run products at each P, T, bulk H_2O content, and fO_2 show well-equilibrated eclogitic phase assemblages of garnet ± clinopyroxene ± coesite/stishovite ± rutile ± phengite ± melt ± vapour, with average grain sizes of 10 to 20 µm. These sizes are sufficiently large for analysis by synchrotron FTIR microscopy, Nano-SIMS and Fe K-edge XANES. A subset of experimental runs will be prepared as doubly polished thin sections for analysis by synchrotron FTIR microscopy and Fe K-edge XANES. The $Fe^{3+}/\sum Fe$ ratio will be determined relative to a series of standards for which $Fe^{3+}/\sum Fe$ ratios have been determined previously by Mössbauer spectroscopy.

The solidus is determined to be at ~ 900 °C at 6 GPa, ~ 1000 °C at 8 GPa and ~ 1050 °C at 9 GPa. Above these temperatures small melt fractions can be detected (Fig. 3.2-18 and Fig. 3.2-19). Similar to previous studies, the stability of phengite varies as a function of P, T, buffering mineral paragenesis and bulk H_2O concentration. Phengite breaks down above 9 GPa (*i.e.*, ~ 300 km depth) (Fig. 3.2-18). At 6 GPa and between 950 °C and 1050 °C, phengite co-exists

with a small melt fraction for bulk H_2O contents of 0.4-1.0 wt. % before it disappears completely towards higher T (Fig. 3.2-19). Phengite also breaks down at subsolidus conditions in the presence of excess hydrous fluids. The K_2O concentration in both phengite and clinopyroxene decreases with increasing bulk H_2O content at subsolidus conditions at a given P, T, suggesting a leaching of K_2O by a vapour-rich fluid.

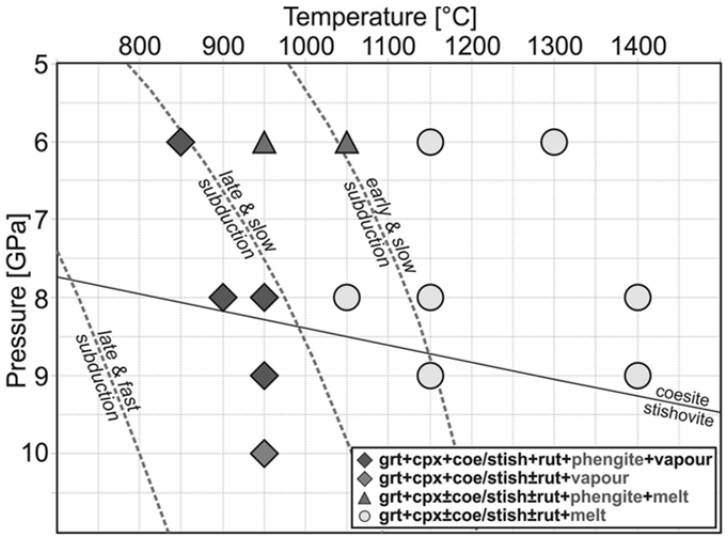

Fig. 3.2-18: P, T-grid of GA1+H_2O (0.6-1.0 wt. % H_2O) experimentally observed phase relations.

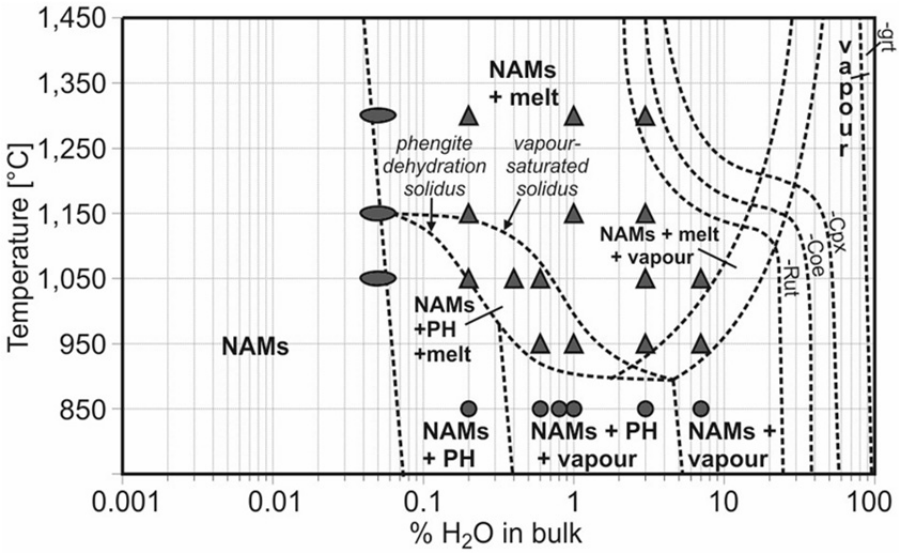

Fig. 3.2-19: Schematic phase diagram showing the phase stabilities of eclogitic minerals and phengite (hydrous phase) as a function of H_2O (wt. %) and T. If the H_2O storage limit of phengite and the eclogitic minerals is exceeded at subsolidus conditions, vapour will form in association with phengite and minerals. Strikingly, runs with 7 wt. % H_2O are phengite-free. Towards higher T instead, melt in association with phengite will appear at the phengite dehydration solidus until phengite is completely exhausted at the vapour-saturated solidus of GA1+ H_2O. Ph, phengite.

m. *Crude oil properties under upper mantle conditions (A. Serovaysky and A. Kolesnikov/ Moscow; C.A. McCammon, D. Vasiukov/Moscow; I. Kupenko and L.S. Dubrovinsky; V. Kutcherov/Stockholm)*

Formation of natural-gas-like hydrocarbon mixtures from inorganic substances or from individual hydrocarbons under conditions of the upper mantle has restarted discussion on the issue of petroleum formation and hydrocarbon properties in general. While individual hydrocarbon compounds under pressure have been studied to a certain extent, raw natural petroleum has never been loaded into diamond anvil cells or large volume presses except for studies devoted to thermal conductivity measurements. The purpose of this research is to examine the effects of temperature and pressure on vitrification and crystallization of petroleum in addition to examining possible chemical changes such as those related to cracking, dissociation or condensation.

In pilot experiments, crude oil from the Astrakhan region was loaded into a diamond anvil cell with a rhenium gasket. Raman spectra (He-Ne laser wavelength 632.8 nm) of the oil in the pressure range 1-14 GPa showed extreme fluorescence most probably due to the presence of polycondensed aromatic compounds. As a result further direct Raman measurements on the material were not possible.

As it was not possible to examine the oil breakdown products *in situ* a technique was developed to examine how petroleum-like materials may interact with iron components within minerals of the Earth's interior. As a mineral proxy ferropericlase was employed (containing 20 % ^{57}FeO). While optical microscopy made it possible to visually observe petroleum reactions with ferropericlase during heating, the iron-57 isotope made it possible to examine the redox reactions taking place by using Mössbauer spectral analysis.

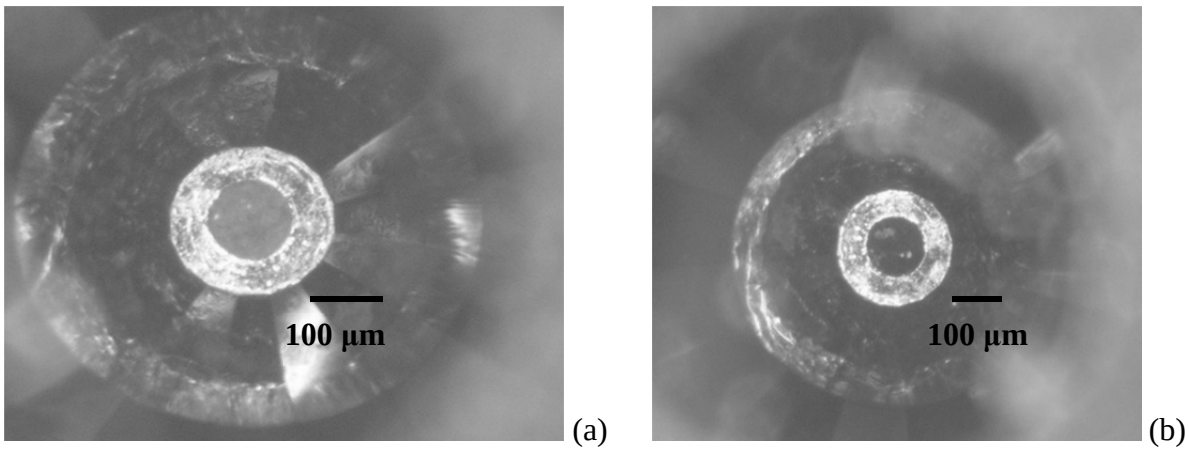

(a) (b)

Fig. 3.2-20: An optical microscope photograph of Astrakhan crude oil with ferropericlase (20 % ^{57}FeO) heated at 9.5 GPa: a) at pressure before heating; b) after heating to 1000 °C.

Laser heating of Astrakhan crude oil and ferropericlase (Fig. 3.2-20a – before heating) at 9.5 GPa up to 1000 °C led to the formation of a black opaque compound inside the gasket hole (Fig. 3.2-20b). The Mössbauer spectrum of the system heated up to 1000 °C showed no difference to the spectrum before heating (Fig. 3.2-21a), meaning that no chemical reaction with the ^{57}FeO-compound occurred. In contrast, however, heating up to 1400-1500 °C led to dramatic changes in the Mössbauer spectrum (Fig. 3.2-21b), indicating that up to 50 % of the ferropericlase FeO was transformed to more reduced phases such as iron metal and iron carbides. Though the exact nature of the reduced iron-containing compounds is still an analytical challenge, it is likely that at least light dissociation of petroleum occurred at 1000 °C, but at temperatures a few hundreds degrees higher the carbon bearing compounds started to react with the ferropericlase FeO component. A Raman spectrum indicating the presence of elemental carbon in products heating up to 1500 °C implies that it was not petroleum but rather the product carbon (or maybe hydrogen) that reacted with FeO to change the Mössbauer spectrum upon heating to this temperature.

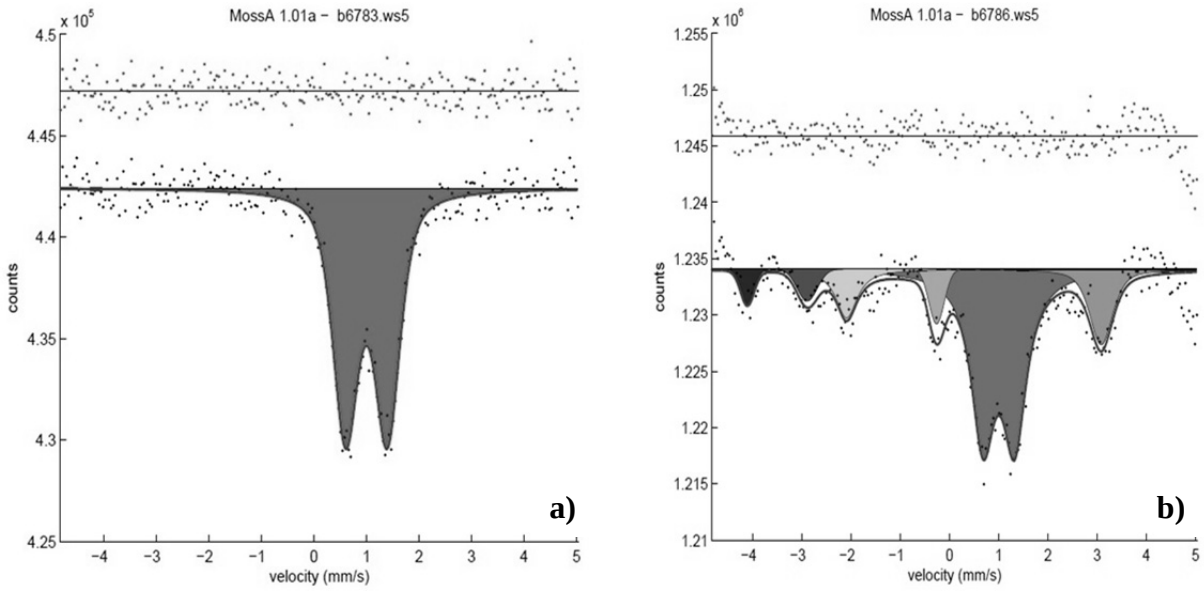

Fig. 3.2-21: Mössbauer spectra of ferropericlase (20 % ^{57}FeO) heated with Astrakhan crude oil at 9.5 GPa: a) at room temperature after heating to 1000 °C; b) after heating to 1500 °C.

n. *Compositional evolution and formation conditions of magmas (melts, fluids and minerals) related to porphyry molybdenum mineralization at Climax, Colorado (A. Audétat)*

In order to reconstruct the magmatic-hydrothermal processes leading to mineralization in the famous porphyry Mo deposit at Climax, Colorado, USA, four magma units emplaced before, during and shortly after the mineralization events were investigated: (1) a late white dike of the Alma district, (2) the syn-mineralization Chalk Mountain rhyolite, (3) a late- to post-mineralization rhyolite porphyry dyke, and (4) a mafic enclave within the productive Bartlett stock. Melt inclusions, mineral inclusions and fluid inclusions trapped in quartz phenocrysts were investigated by means of LA-ICP-MS, EPMA and microthermometry (Fig. 3.2-22).

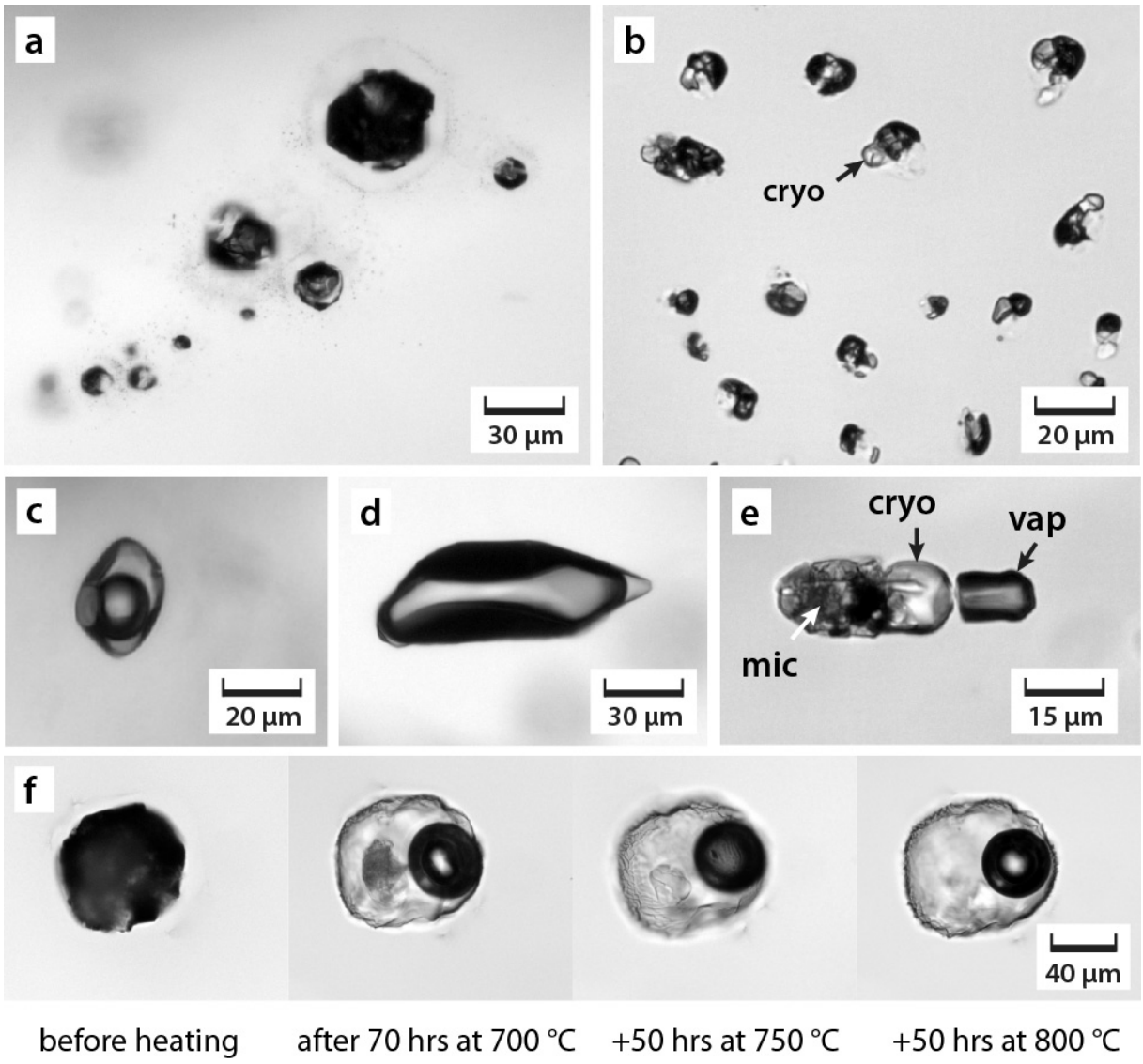

Fig. 3.2-22: Transmitted-light photomicrographs of quartz-hosted fluid and melt inclusions at Climax. (a) Primary, crystallized melt inclusions in a quartz phenocryst. (b) Highly evolved, secondary melt inclusions. (c) Intermediate-density fluid inclusion that trapped fluid in the single-phase field. (d, e) Late, vapor-rich and salt-rich fluid inclusions that trapped fluids at low pressure in the two-phase field. (f) Partial re-homogenization of a primary melt inclusion in quartz at 1.5-2.0 kbar confining pressure. cryo – cryolite (Na_3AlF_6); mic – mica; vap – vapor.

Both the Chalk Mountain rhyolite and the rhyolite porphyry magmas were ~ 10 times more fractionated than average granite (Fig. 3.2-23) and show geochemical characteristics of topaz rhyolites. They were saturated in magnetite, Mn-rich ilmenite, fluorite, aeschynite, monazite, pyrrhotite and thorite, and crystallized predominantly at 710-730 °C, 1.2-2.6 kbar and log fO_2 ≈ FMQ+2.2. The silicate melt of the Chalk Mountain rhyolite magma contained 3.5±0.4 wt. % F, 0.09±0.03 wt. % Cl, ≥1.4±0.7 wt. % H_2O, 15-90 µg/g Cs, 500-1500 µg/g Rb and 5-7 µg/g Mo, whereas that of the rhyolite porphyry contained more water (4.9±1.2 wt. % H_2O)

and less fluorine (1.1±0.3 wt. % F), but otherwise was compositionally very similar. The fluid exsolving from the latter melt had a bulk salinity of 10±2 wt. % $NaCl_{equiv}$ and contained on the order of 100 µg/g Mo. After emplacement of the Chalk Mt. rhyolite magma at subvolcanic levels, extremely fractionated silicate melts coexisting with hypersaline brines (salt melts) and low-density vapor percolated at near-solidus conditions through the rock. These silicate melts contained 6.6±0.4 wt. % F, ≥4.5±0.6 wt. % H_2O, 0.51±0.05 wt. % Cl, and up to 0.5 wt. % Cs and 100 µg/g Mo, whereas the hypersaline brines contained up to 2.0 wt. % Cs and 0.6 wt. % Mo. However, due to their negligible mass these liquids are unlikely to have played a major role in the mineralization process.

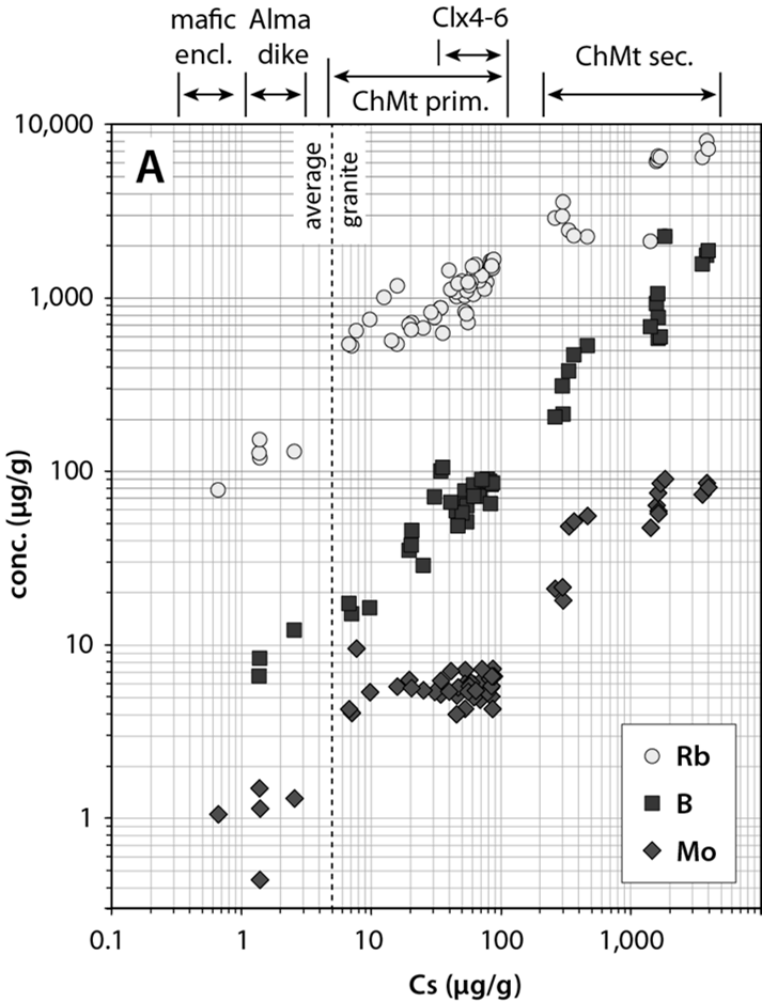

Fig. 3.2-23: Concentrations of Cs, Rb, B and Mo in melt inclusions analyzed from the Climax magma system. Cesium is the element that behaved most incompatibly during magma fractionation, thus giving an indication of the amount of crystallization associated with these trends. To increase the Cs concentration in the residual liquid from 1 µg/g to 1,000 µg/g by closed-system fractional crystallization, at least 99.9 % crystallization is required. Although the most evolved liquids contained spectacularly high Mo concentrations, they were so rare that they are unlikely to have played a major role in the mineralization process. The bulk of the Mo mineralization appears to have formed by fluids that exsolved from melts containing 5-7 µg/g Mo.

The majority of Mo in the Climax deposit seems to have been derived from melts containing 5-7 µg/g Mo, a concentration which is similar to that found in equally fractionated melts in barren and sub-economically mineralized intrusions. However, whereas melts of this fractionation degree were mostly dispersed in barren intrusions, they seem to have been present as large, coherent masses in the apical parts of Climax-type porphyry Mo-forming magma systems. Efficient segregation of fractionated melts and fluids into the top of the latter

intrusions was promoted by high fluorine concentrations in the silicate melt, which was partly a primary feature and partly a consequence of other characteristics of within-plate magmas.

o. *Role of evaporites in the formation of magnetite-apatite deposits along the Middle and Lower Yangtze River, China: Evidence from LA-ICP-MS analysis of fluid inclusions (W. Li and J. Zhang/Wuhan, A. Audétat)*

Numerous magnetite-apatite deposits occur in the Ningwu and Luzong sedimentary basins along the Middle and Lower Yangtze River, China. These deposits are located in the contact zone of (gabbro)-dioritic porphyries with surrounding volcanic or sedimentary rocks and are characterized by massive, vein and disseminated magnetite-apatite±anhydrite mineralization associated with voluminous sodic-calcic alteration. Petrologic and microthermometric studies on multiphase inclusions in pre- to syn-mineralization pyroxene and garnet from the deposits at Meishan (Ningwu basin), Luohe and Nihe (both in Luzong basin) demonstrate that they represent extremely saline brines (~ 90 wt. % $NaCl_{equiv}$) that were trapped at temperatures of about 780 °C. Laser ablation ICP-MS analyses and Raman spectroscopic studies on the natural fluid inclusions and synthetic fluid inclusions manufactured at similar P-T conditions reveal that the brines are composed mainly of Na (13-24 wt. %), K (7-11 wt. %), Ca (~ 7 wt. %), Fe (~ 2 wt. %), Cl (19-47 wt. %) and variable amounts of SO_4 (3-39 wt. %) (Fig. 3.2-24).

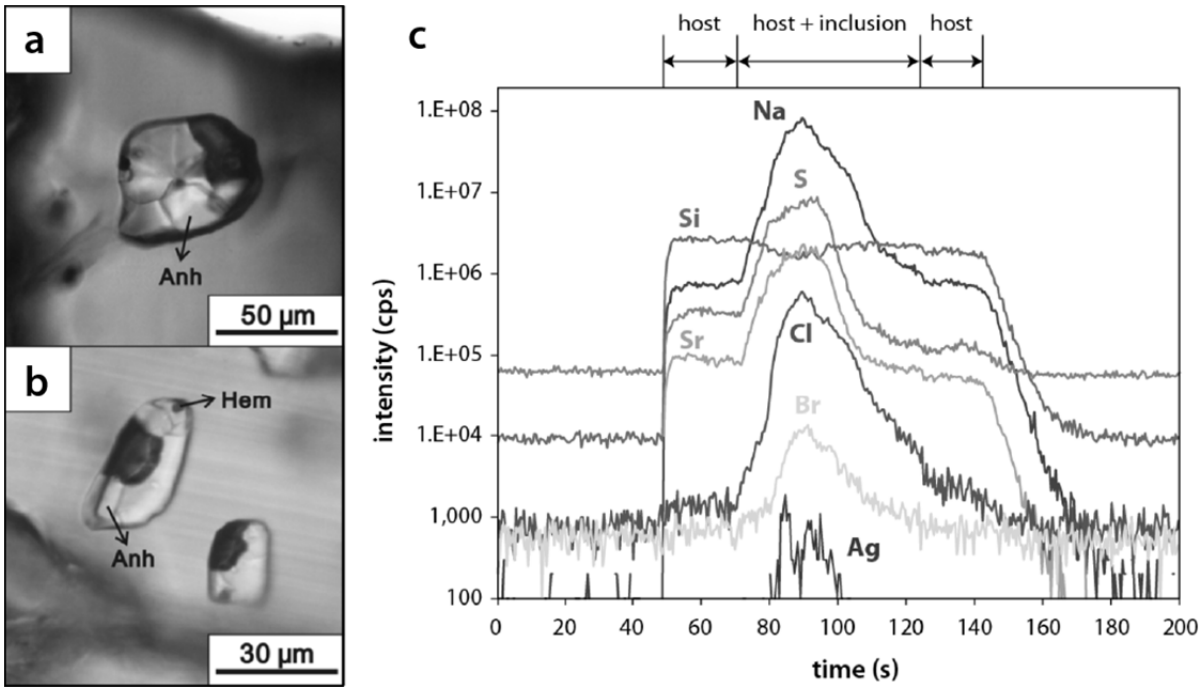

Fig. 3.2-24: (a, b) Transmitted-light photographs of hypersaline brine inclusions in garnet (a) and clinopyroxene (b). (c) LA-ICP-MS signal of a hypersaline brine inclusion in clinopyroxene. Notice the well-resolved signals of S, Cl and Br.

The Cl/Br, Na/K and Na/B ratios measured in the fluid inclusions are markedly different from those of seawater evaporation brines and lie between those of magmatic fluids and sedimentary halite, suggesting a significant contribution from halite-bearing evaporites (Fig. 3.2-25). High S/B and Ca/Na ratios in the fluid inclusions and heavy sulphur isotopic signatures of syn- to post-mineralization anhydrite ($\delta^{34}S_{Anh}$ = +15.2 to +16.9‰) and pyrite ($\delta^{34}S_{Py}$ = +4.6 ‰ to +12.1‰) further suggest a significant contribution from sedimentary anhydrite (Fig. 3.2-26). These interpretations are in line with the presence of evaporite sequences in the lower parts of the sedimentary basins.

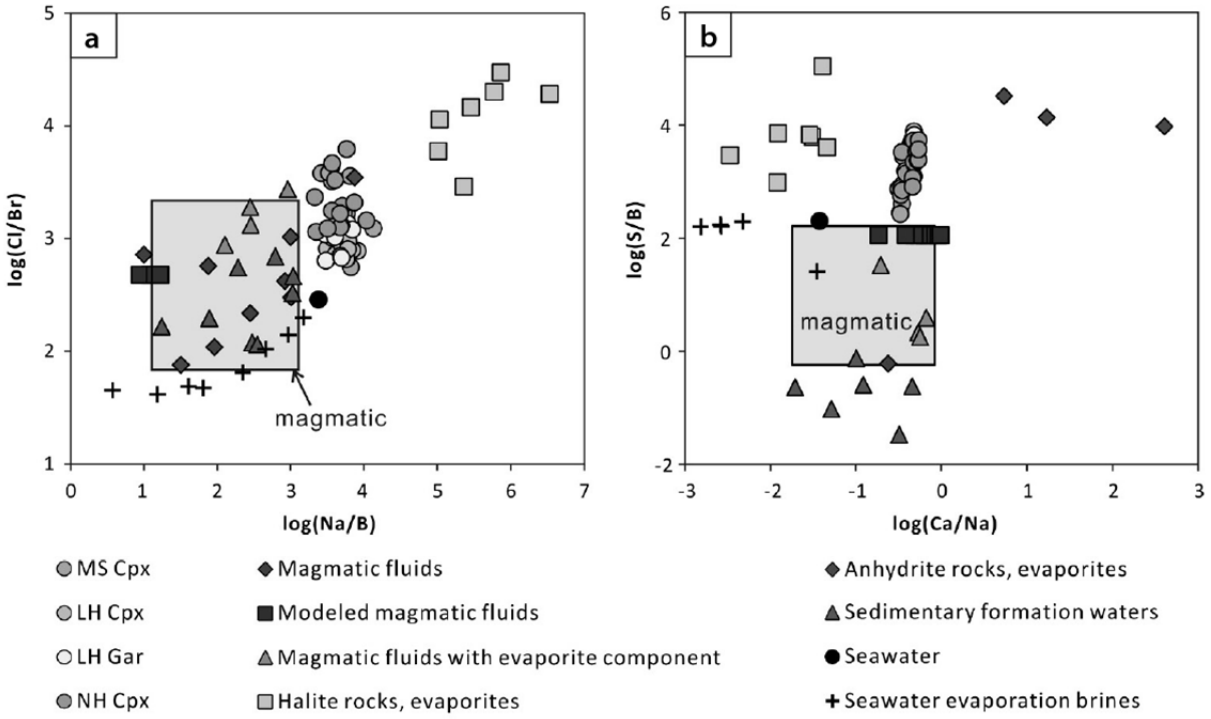

Fig. 3.2-25: Compositions of hypersaline brine inclusions analyzed in this study (MS Cpx = clinopyroxene from Meishan, LH Cpx = clinopyroxene from Luohe, LH Gar = garnet from Luohe, NH Cpx = clinopyroxene from Nihe) compared to potential source fluids and assimilants. The compositions of the hypersaline brines can be explained by magmatic fluids that assimilated significant amounts of halite- and anhydrite-bearing evaporites.

The combined evidence thus suggests that the magnetite-apatite deposits along the Middle and Lower Yangtze River formed by fluids that exsolved from magmas which assimilated substantial amounts of Triassic evaporites during their ascent. Due to the Fe-oxide-dominated mineralogy of the deposits, their association with large-scale sodic-calcic alteration and their spatial and temporal association with subvolcanic intrusions we interpret them as a special type of IOCG deposits that is characterized by unusually high contents of Na, Ca, Cl and SO_4 in the ore-forming fluids. Evaporite assimilation apparently led to the production of large

amounts of high-salinity brine and thus to an enhanced capacity to extract iron from the (gabbro)-dioritic intrusions and to concentrate it in the form of ore bodies. As a consequence, we suggest that evaporite-bearing sedimentary basins are more prospective for magnetite-apatite deposits than evaporite-free basins.

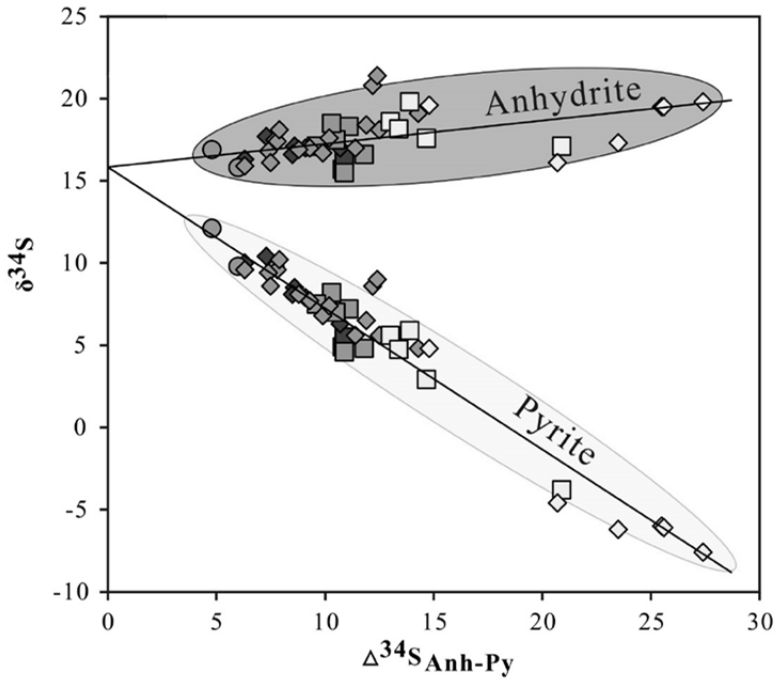

Fig. 3.2-26: Sulphur isotopic composition and -fractionation between pairs of coexisting anhydrite and pyrite. Extrapolation of the data back to zero anhydrite-pyrite fractionation suggests that the total sulphur isotopic composition of the fluids was about +16 ‰, which provides strong evidence for an involvement of sedimentary anhydrite.

3.3 Mineralogy, Crystal Chemistry and Phase Transformations

Studying the response of crystals to changes in pressure, temperature and chemical composition is fundamental to understanding their physical and chemical properties. One of the most drastic responses to such changes is a phase transformation. Nearly all materials are strongly affected by transformation processes in the pressure and temperature ranges that occur in planetary interiors. In this chapter, we highlight continuing efforts at BGI to detect the onset of phase transformations and to understand the response of different materials such as iron oxides, silicates and carbonates to high pressures, temperatures and different oxygen fugacities.

The chapter starts with studies of phase stabilities and relations from high-pressure experiments either by characterising the quenched run products after synthesis or by *in situ* measurements using diamond anvil cells. Iron is one of the most important transition elements in the Earth, so the discovery of a new iron oxide, Fe_4O_5, has provided new impetus for investigations of iron oxides at high P-T conditions. The simplest iron oxides, Fe_2O_3 and Fe_3O_4, provide insight into the fate of banded iron formations subducted deep into the mantle. The well-known spinel endmember, $MgFe_2O_4$, decomposes to produce a new Mg-endmember of the Fe_4O_5 phase, for which single crystal refinements have provided a full description of the crystal structure. Discovery of a new high-pressure polymorph of $(Mg,Fe^{2+})_3Fe^{3+}{}_4O_9$ suggests that other stoichiometric iron oxides containing different ratios of Fe^{2+} and Fe^{3+} may also be stable at high pressure and temperature. Studies of the mixed valence iron garnet, $Fe^{2+}{}_3Fe^{3+}{}_2Si_3O_{12}$, are important to oxygen fugacity models for garnet-bearing assemblages, especially since the presence of Fe^{3+} in garnet can affect temperature and pressure estimates, particularly those based on Mg/Fe exchange equilibria. Studies of the stability of Fe-carbonates such as siderite ($FeCO_3$) provide insight into the deep carbon cycle, and experiments suggest that Fe-rich carbonates could exist down to the core-mantle boundary in oxidised regions. Oxygen fugacity has a strong effect on $Fe^{3+}/\Sigma Fe$ in chromites, but the phase assemblage is a crucial factor in determining the exact relation. The effect of temperature on the phase transition of H_2O-bearing $MgSiO_3$ clinoenstatite is being investigated to better understand potential causes of the seismic X-discontinuity.

The next contributions address applications of crystal chemistry to planetary science. Studies of an iron meteorite revealed that so-called hexagonal diamond (“lonsdaleite”) is probably not an individual phase but is instead cubic diamond with extensive stacking faults and twins at the nanometre scale. Orthogonal twin lamellae in monoclinic baddeleyite from the Shergotty Martian meteorite present clear evidence for a mode of formation involving multiple phase transformations from dense polymorphs. A study of the high-pressure polymorphs of coesite provides improved constraints on the metastable phase diagram of silica, which can be used as

a potential tracer of peak transient pressures (stress) reached in processes such as impacts or faulting in a shocked meteorite.

The final contributions focus on the use of single crystals for evaluating physical and chemical properties. Large wadsleyite single crystals synthesised through a breakthrough in high-pressure crystal growth methodology have been used to study the elasticity of wadsleyite at high pressure, as well as determination of hydrogen positions in hydrous wadsleyite using neutron diffraction. The trace element content of quartz is important as a petrogenetic indicator to reconstruct the temperature and pressure of quartz crystallization via titanium-in-quartz (TitaniQ) thermobarometry, motivating the characterisation of an optically homogenous, natural smoky quartz crystal for 24 trace and ultratrace elements.

a. *Phase relations and chemical stability of Fe_2O_3 and Fe_3O_4 (E. Bykova, N.A. Dubrovinskaia, L.S. Dubrovinsky, M. Bykov, C.A. McCammon and S.V. Ovsyannikov; M. Hanfland, I. Kupenko, A.I. Chumakov and R. Rüffer/Grenoble; H.-P. Liermann/Hamburg; V.B. Prakapenka/Argonne)*

Banded Iron Formations (BIFs) and ironstones formed starting from the late Precambrian (between 2.8 and 1.8 billion years ago) until the Pliocene. Typical BIFs consist of distinctly separated alternating iron-rich (magnetite, Fe_3O_4, and hematite, α-Fe_2O_3) and amorphous silica-rich layers. Together with downwelling lithosphere, BIFs are expected to penetrate deep into the mantle. Available experimental data suggest that iron oxides melt above the geotherm in the entire mantle and thus remain solid in slabs that are colder than the surrounding mantle. Thus the fate of iron oxides, a major component of subducted BIFs, depends on the pressures and temperatures (*P*-*T*) to which they are exposed.

At ambient conditions magnetite has the cubic crystal structure of inverse spinel ($Fm\bar{3}m$). Previous powder X-ray diffraction (XRD) and Mössbauer spectroscopy experiments in diamond anvil cells showed that magnetite transforms into a high-pressure (HP) phase above 19 GPa but its crystal structure has been debated. Our recent single-crystal XRD data finally established it to have a $CaTi_2O_4$-type structure (*Bbmm*, a = 9.309(3) Å, b = 9.282(2) Å, and c = 2.6944(9) Å, R_1 (all data) = 6.91 % at 44.3(5) GPa). The crystal structure is composed of FeO_6 octahedra and trigonal prisms (Fig. 3.3-1). Laser heating of *HP*-Fe_3O_4 at 2350(100) K and pressures up to 50 GPa does not result in any chemical or structural modifications. In addition, we identified reflections belonging to *HP*-Fe_3O_4 in the products of thermal decomposition of siderite, $FeCO_3$ (70(1) GPa and 2400(100) K). Thus, our experimental results show that *HP*-Fe_3O_4 may exist to depths of at least 2000 km.

Hematite, α-Fe_2O_3, adopts the rhombohedral crystal structure of corundum, Al_2O_3 (Fig. 3.3-2a). In agreement with previous studies, our cold compression experiments of hematite single

crystals to 54(1) GPa results in a transition to the ζ-Fe_2O_3 phase manifested by a ~ 8.4 % volume discontinuity. According to single-crystal XRD data, ζ-Fe_2O_3 possesses a distorted $GdFeO_3$ perovskite structure (*Pbnm*) with monoclinic or triclinic unit cell (Fig. 3.3-2c). At 67(1) GPa a small drop in the unit cell volume (~ 1.7 %) manifests the next transformation to the novel θ-Fe_2O_3 phase (Fig. 3.3-2e) with orthorhombic symmetry (*Aba*2, a = 4.608(7) Å, b = 4.730(4) Å, c = 6.682(18) Å, R_1 (all data) = 10.55 % at 73.8(7) GPa). On compression at ambient temperature θ-Fe_2O_3 is observed to at least 100 GPa.

During *in situ* laser heating of θ-Fe_2O_3 above 1600(50) K, post-perovskite PPv type η-Fe_2O_3 is formed (Fig. 3.3-2d). Once synthesized, η-Fe_2O_3 may be preserved at ambient temperature down to at least 26 GPa. At lower pressures it transforms back to hematite. Moderate heating to ~ 2000 K at pressures of about 50 GPa results in a transition to the distorted perovskite ζ-Fe_2O_3 phase. Decompression of ζ-Fe_2O_3 or η-Fe_2O_3 to 41(1) GPa with heating at 1800(100) K results in the growth of Rh_2O_3-II-type ι-Fe_2O_3 (Fig. 3.3-2b). Interestingly, hematite was reported to transform to ι-Fe_2O_3, thus bracketing the possible *P-T* stability field of ι-Fe_2O_3.

The behaviour of η-Fe_2O_3 under heating is rather remarkable. Firstly, we observed that its unit cell volume increases by up to 1 % upon laser heating to about 2000 K at ~ 56 GPa and 64 GPa. Secondly, after heating for a few seconds to 2700-3000 K and 71 GPa we observed a novel mixed-valence iron oxide Fe_5O_7 ($FeO{\cdot}2Fe_2O_3$) crystallized in the monoclinic $C2/m$ space group (a = 9.208(7) Å, b = 2.7327(10) Å, c = 8.270(5) Å and β = 105.50(8)°, R_1 (all data) = 6.77 % at 40.7(3) GPa, Fig. 3.3-2f. Thus, we explain our observations as a continuous loss of oxygen by η-Fe_2O_3 upon heating at moderate temperatures and pressures above ~ 60 GPa, according to the reaction η-$Fe_2O_3 \rightarrow$ η-$Fe_2O_{3-\delta}$ + 0.5 $\delta{\cdot}O_2$. The reaction is accompanied by a partial reduction of Fe^{3+} to larger-sized Fe^{2+} that consequently increases the unit cell volume. Upon heating at sufficiently high temperature (above ~ 2700 K), the oxygen deficiency in η-Fe_2O_3 reaches a critical limit and results in a reconstructive phase transition to the mixed-valence iron oxide Fe_5O_7: 5 η-$Fe_2O_3 \rightarrow$ 2 Fe_5O_7 + 0.5 O_2.

Similarities in the crystal structures of η-Fe_2O_3, Fe_5O_7, *HP*-Fe_3O_4, and the recently discovered Fe_4O_5 demonstrate that iron oxide phases form a homological series nFeO·$m$$Fe_2O_3$ (with wustite, FeO and η-Fe_2O_3 as the end-members), so that potentially other mixed-valence iron oxides may be found under pressure-temperature conditions of the lower mantle (Fig. 3.3-1).

Our results demonstrate clearly the complex behaviour of iron oxides subjected to high pressures and temperatures (Fig. 3.3-3). Fe_2O_3 and Fe_3O_4 can be transferred into the deep Earth's interior by subduction of BIFs. Upon subduction into the lower mantle, hematite undergoes numerous phase transformations. At pressures above ~ 60 GPa the HP phase η-Fe_2O_3 starts to decompose, promoting reactions involving oxygen. Based on estimates of the amount of BIFs subducted into the Earth's mantle, the amount of oxygen produced by the formation of Fe_5O_7 can vary from 2 to 8 masses of oxygen in the modern atmosphere.

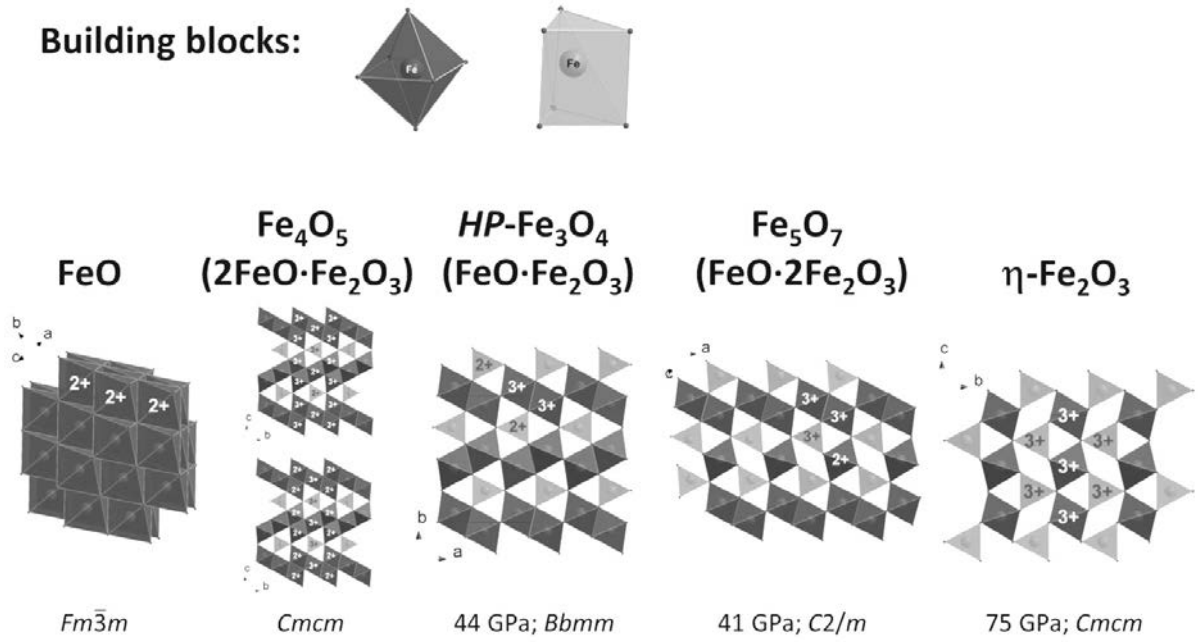

Fig. 3.3-1: Homological series of iron oxides described by the common formula nFeO·$m$$Fe_2O_3$. The structures may be described as constructed from two building blocks, FeO_6 octahedra (dark grey) and trigonal prisms (light grey). "2+" and "3+" represent the charges of iron ions.

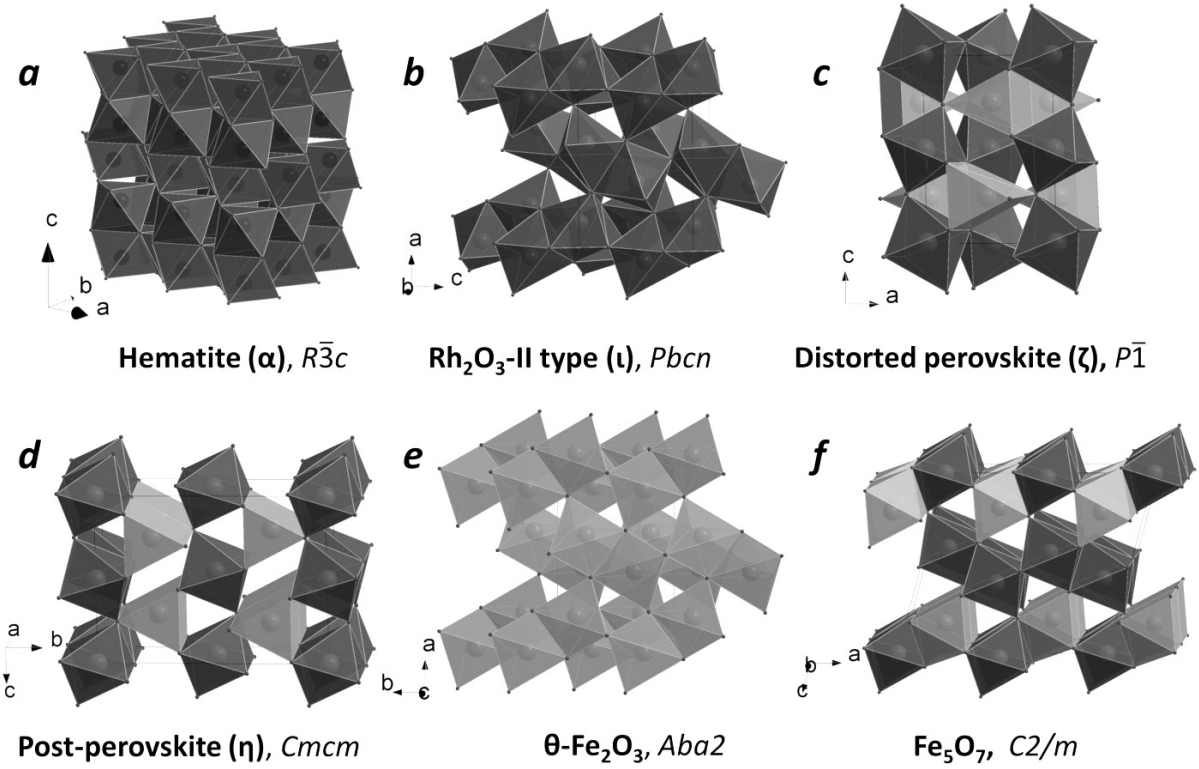

Fig. 3.3-2: Crystal structures of hematite, HP polymorphs of Fe_2O_3 and a new compound, Fe_5O_7, studied in the present work by single-crystal XRD. Building blocks are octahedra (dark grey) and trigonal prisms (light grey).

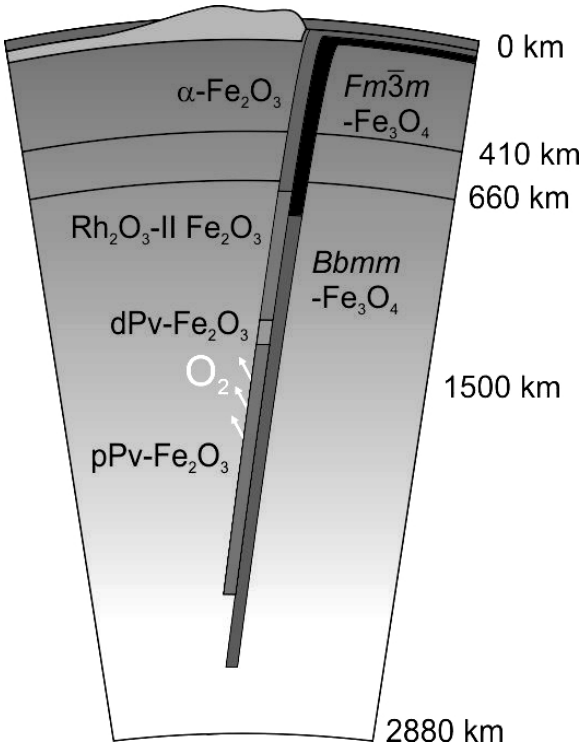

Fig. 3.3-3: Possible consequence of phase transitions of Fe_2O_3 and Fe_3O_4 in a BIF subducted to the lower mantle.

b. *Phase relations of $MgFe_2O_4$ and the stability of $Mg_2Fe_2O_5$ (L. Uenver-Thiele and A.B. Woodland/Frankfurt; T. Boffa Ballaran and D.J Frost)*

Spinel-structured minerals with formula AB_2O_4 are of particular interest under non-ambient conditions in having the ability to incorporate Fe^{3+} and Fe^{2+} into their crystal structure, which makes their stability redox sensitive. Such phases are common in mantle peridotite, which occurs in parts of the Earth's upper mantle and transition zone. Magnesioferrite ($MgFe_2O_4$) is one of the Fe^{3+}-bearing components that may be present. Previous studies have proposed a phase diagram for magnesioferrite; however the phase fields were based upon calculations rather than experimental observation. The recent discovery that Fe_3O_4 breaks down to a mixture of Fe_4O_5 and Fe_2O_3 opens the possibility that analogous behaviour may occur in magnesioferrite, which would have implications for its phase diagram. The aim of this study is therefore to explore the phase transformations of $MgFe_2O_4$ at the pressure and temperature conditions of the Earth's mantle.

Multianvil experiments were performed at pressures between 8 and 23 GPa and temperatures of 1100-1600 °C. The starting material was a stoichiometric mixture of MgO + Fe_2O_3 or pre-synthesized $MgFe_2O_4$. PtO_2 powder was added to produce a high partial pressure of oxygen to prevent reduction of Fe^{3+}. Run products were analysed by microprobe and powder X-ray diffraction.

Our experiments show that $MgFe_2O_4$ breaks down to MgO + Fe_2O_3 and that this reaction is nearly isobaric at 9-10 GPa over several hundred degrees (Fig. 3.3-4). Above 14 GPa a new phase appears, indicating a stability field of $Mg_2Fe_2O_5$ + Fe_2O_3. At high temperatures it is

likely that $MgFe_2O_4$ breaks down directly to $Mg_2Fe_2O_5$ + Fe_2O_3. Further experiments showed that the $Mg_2Fe_2O_5$ phase remains stable up to 18 GPa at 1300 °C. At higher pressures, we found indications of a high-pressure phase with $MgFe_2O_4$ stoichiometry, the structure of which remains to be confirmed. Our experiments imply that the phase relations of $MgFe_2O_4$ are more complicated than those previously proposed. This study provides further evidence that M_4O_5- structured phases can be considered as additional phases in the phase relations of many simple oxide systems at high P-T conditions.

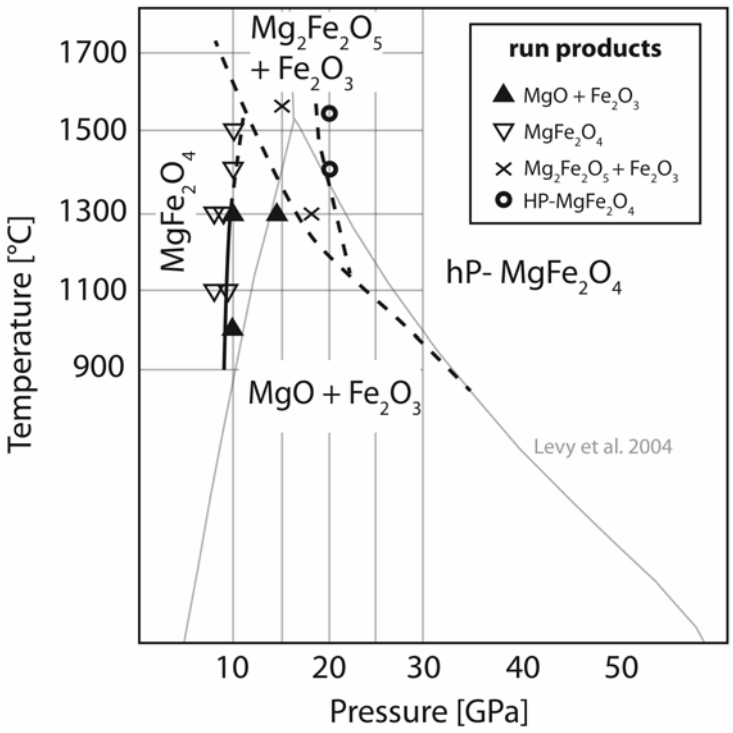

Fig. 3.3-4: Phase diagram for magnesioferrite illustrating the new phase boundaries compared to those proposed by Levy *et al.* (2004) [Phys. Chem. Min. 31: 122-129]. Note the additional phase field for $Mg_2Fe_2O_5$ + Fe_2O_3.

c. *Substitution of Fe^{2+} by Mg in Fe_4O_5 compounds: Crystal chemistry of the $Mg_2Fe_2O_5$ end-member (T. Boffa Ballaran, in collaboration with L. Uenver-Thiele and A.B. Woodland/Frankfurt)*

Since the discovery of Fe_4O_5, a mixed-valence iron oxide phase that can be synthesized at high pressures and temperatures, several studies have shown that Mg and Cr can substitute for Fe^{2+} and Fe^{3+} into the Fe_4O_5 end-member structure. The structure of the Fe_4O_5 end-member has been determined mainly by powder diffraction and DFT calculations, given that the number of observed structure factors from the only single crystal experiment conducted so far was extremely small (20 independent reflections). The data presented so far in the literature are consistent with a *Cmcm* space group and a structure similar to that of $Sr_2Tl_2O_5$ and

$CaFe_3O_5$, consisting of layers of edge-sharing FeO_6 octahedra and layers of trigonal prisms alternating along the *c*-axis. Recently it has also been reported that chromite ($FeCr_2O_4$) dissociates into $Fe_2Cr_2O_5$ and Cr_2O_3 at high pressure. However, according to powder diffraction refinements, $Fe_2Cr_2O_5$ is isostructural with $Mg_2Al_2O_5$, having space group *Pbam* in which the octahedral units form long chains surrounding the trigonal prisms. Like Cr, Mg can substitute into the Fe_4O_5 structure; however, whether complete Mg substitution in Fe_4O_5 gives rise to a change in symmetry is still unknown. In this study, part of a project aimed to investigate the phase stability of $MgFe_2O_4$, we have determined the crystal structure of $Mg_2Fe_2O_5$ based upon X-ray single-crystal diffraction. Single-crystal structural data allowed not only an accurate determination of the space group of this material as well as the oxygen positions and the displacement parameters of all atoms present in the structure, but also provided important constraints on the cation occupancies of the distinct crystallographic sites in this phase.

The sample of $Mg_2Fe_2O_5$ oxide was synthetized at 15 GPa and 1550 °C and consists of very good quality crystals with sharp diffraction profiles. Intensity data were collected for a single crystal with dimension 75 x 60 x 35 μm^3 using an Xcalibur diffractometer with MoKα radiation operated at 50 kV and 40 mA, equipped with a CCD detector and a graphite monochromator. The extinction conditions of the measured reflections are consistent with the *Cmcm* space group. The refined crystal structure of $Mg_2Fe_2O_5$ indicates that this compound is isostructural with Fe_4O_5 with layers of edge-sharing octahedra (M1 and M2 sites) alternating with layers of triangular prisms along the *c*-axis (M3 site) (Fig. 3.3-5). The unit-cell lattice

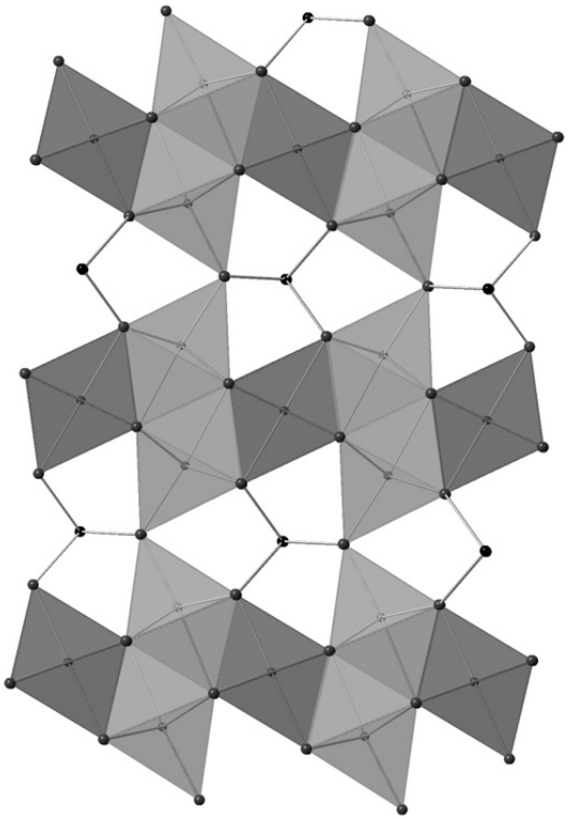

Fig. 3.3-5: Crystal structure of $Mg_2Fe_2O_5$ projected down the *a* axis.

parameters, a = 2.8889(4) Å, b = 9.7282(4) Å and c = 12.5523(7) Å, are smaller than those of Fe_4O_5 and the Mg and Fe^{3+} cations are disordered among all three crystallographic sites of the $Mg_2Fe_2O_5$ structure, although preference of Mg for the trigonal prism coordination (M3) is observed. Substitution of Mg into the Fe_4O_5 structure reduces the octahedral distortion of both the M1 and M2 sites. The substitution of Mg into the Fe_4O_5 structure appears different in detail with respect to that of Cr, given that $Fe_2Cr_2O_5$ crystallizes with a different space group. Although the $Fe_2Cr_2O_5$ structural analysis still needs to be confirmed by single crystal X-ray data, a possible explanation of such differences may reside in the different Jahn-Teller distortions in the two compounds, since in $Fe_2Cr_2O_5$ only Cr^{3+} is present while in $Mg_2Fe_2O_5$ the transition cation is exclusively Fe^{3+}.

d. *New high-pressure polymorph of $(Mg,Fe^{2+})_3Fe^{3+}{}_4O_9$ (R. Sinmyo, E. Bykova, C.A. McCammon, L.S. Ismailova, S.V. Ovsyannikov and L.S. Dubrovinsky)*

Iron oxides have a fundamental importance for geology, materials science and industry. Since iron can have multiple valence states, many minerals can accommodate both Fe^{2+} and Fe^{3+}. It is known that such minerals can have interesting physical properties (*e.g.*, optical absorbance, thermal/electrical conductivity) due to electron transfer between Fe^{2+} and Fe^{3+}. At ambient conditions, Fe_3O_4 magnetite is the only stable iron oxide phase with multiple valence states of iron (Fe^{3+}/Fe^{2+} = 2/1), except for minor amounts of Fe^{3+} in $Fe_{1-x}O$ wustite. Recently, a novel iron oxide Fe_4O_5 was discovered with Fe^{3+}/Fe^{2+} = 2/2 that is stable at high pressure above 5 GPa. Here we report a new high-pressure iron-rich oxide with a chemical composition of $(Mg,Fe^{2+})_3Fe^{3+}{}_4O_9$ that could be part of a Mg-Fe^{2+} solid solution with Fe_7O_9 (Fe^{3+}/Fe^{2+} = 4/3).

Single crystals of $(Mg,Fe^{2+})_3Fe^{3+}{}_4O_9$ were synthesized using the multianvil press, and the crystals could be recovered to ambient conditions (Fig. 3.3-6). Single-crystal X-ray diffraction

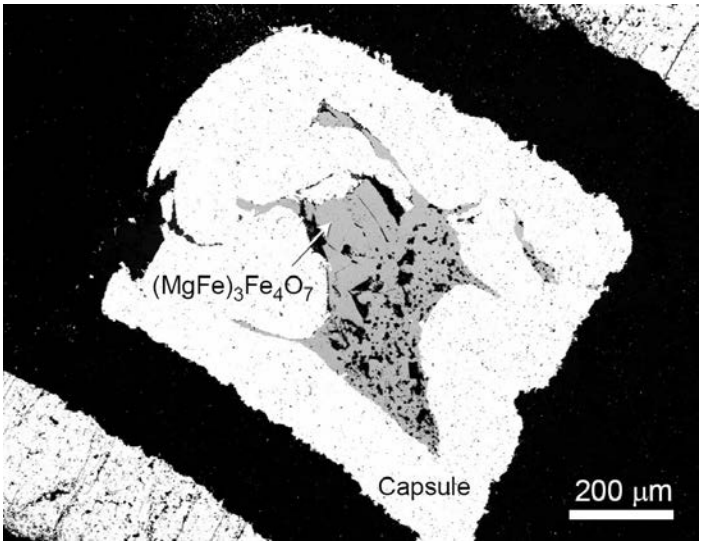

Fig. 3.3-6: Backscattered electron image of the sample recovered from the high-pressure synthesis.

(XRD) measurements revealed that the crystal structure has the monoclinic *C*2/*m* space group with 4 possible cation sites (Fig. 3.3-7). Electron microprobe analysis showed that the obtained oxide has a chemical composition of 15.1(3) at. % magnesium and 84.9(3) at. % iron. We obtained the chemical formula $Mg_{1.06}Fe^{2+}_{1.94}Fe^{3+}_{4.00}O_9$ with $Fe^{3+}/\Sigma Fe$ = 67 % to reconcile the stoichiometry inferred from single crystal XRD measurements. Mössbauer spectroscopy showed a $Fe^{3+}/\Sigma Fe$ ratio ~ 0.7, and 4 sites for iron in the sample. All of the results are in good agreement with the crystal structure obtained by single-crystal XRD measurements. The results from this newly found phase suggest that iron oxide may have a more variable mixed-valence state under high-pressure conditions than previously thought.

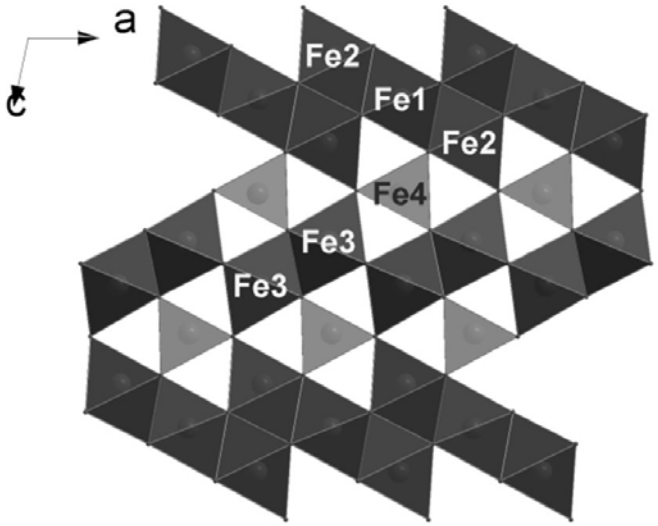

Fig. 3.3-7: Crystal structure of $(Mg,Fe^{2+})_3Fe^{3+}_4O_9$ obtained from single crystal XRD data.

e. *Synthesis of skiagite garnet at high pressure and temperature and investigation of its crystal structure (L.S. Ismailova; A.V. Bobrov/Moscow; M. Bykov and E. Bykova/Bayreuth; V. Cerantola; I. Kantor and I. Kupenko/Grenoble; C.A. McCammon; N.A. Dubrovinskaia/ Bayreuth; L.S. Dubrovinsky)*

Garnets from mantle xenoliths and inclusions in diamonds contain both ferrous (Fe^{2+}) and ferric (Fe^{3+}) iron. Thus information about properties and high-pressure behaviour of the pure iron garnet endmember skiagite, $Fe^{2+}_3Fe^{3+}_2(SiO_4)_3$, can be important. So far the pure iron-skiagite endmember has not been synthesized and investigated by current mineral physics methods. Here we report the high-pressure, high-temperature synthesis of single crystals of skiagite-rich garnet and the results of its characterization using high-resolution single-crystal synchrotron X-ray diffraction, Synchrotron Mössbauer source (SMS) spectroscopy, and nuclear forward scattering (NFS).

The starting material (corresponding to the nominal composition $Fe_3Fe_2Si_3O_{12}$) was a powdered mixture of chemically pure oxides (FeO, $^{57}Fe_2O_3$ and SiO_2). Experiments were performed on a multianvil apparatus at 9.5 GPa and 1100 °C. The composition of skiagite garnet obtained by averaging 30 microprobe analyses suggested the chemical formula $Fe^{2+}_3(Fe^{2+}_{0.276(1)}Fe^{3+}_{1.44(1)}Si_{0.276(1)})Si_3O_{12}$.). Structure refinement of single-crystal X-ray

diffraction data collected at the Swiss-Norwegian beamline (BM01A, ESRF) revealed that the octahedral site is fully occupied by Fe and Si atoms, which is in good agreement with the results of the electron microprobe analysis. According to the obtained structural formula, there is a significant amount of Si (0.234(2)) and Fe^{2+} (0.234(2)) on the octahedral position, suggesting that ~ 23 mol. % of iron-majorite ($Fe_4Si_4O_{12}$) component is accommodated in the synthesised skiagite garnet. SMS and NFS spectra were recorded at the Nuclear Resonance Beamline (ID18) at ESRF. Spectra collected from different crystals showed similar hyperfine parameters, although different relative intensities. The variation of intensities likely arises from different isotope compositions for Fe^{2+} and Fe^{3+}, since the starting mixture containing non-enriched FeO and ^{57}Fe-enriched Fe_2O_3. We therefore focus only on the values of center shift (CS) and quadrupole splitting (QS).

Mössbauer spectra of skiagite contain two doublets (Fig. 3.3-8), one with large CS (1.313(8) mm/s) and QS (3.45(2) mm/s) assigned to Fe^{2+} in the dodecahedral site, and a second doublet with small CS (0.37(1) mm/s) and QS (0.26(2) mm/s) assigned to Fe^{3+} in the octahedral position. We also collected a NFS spectrum (Fig. 3.3-9) to obtain complementary information on the Mössbauer parameters. We fixed the CS of Fe^{2+} (1.313 mm/s) since the absolute CS value cannot be obtained from NFS data. The best fit values to the NFS spectrum are QS = 3.49(5) mm/s for Fe^{2+} and CS = 0.40(5) mm/s and QS = 0.27(1) mm/s for octahedral Fe^{3+}, showing good agreement between the NFS and Mössbauer data.

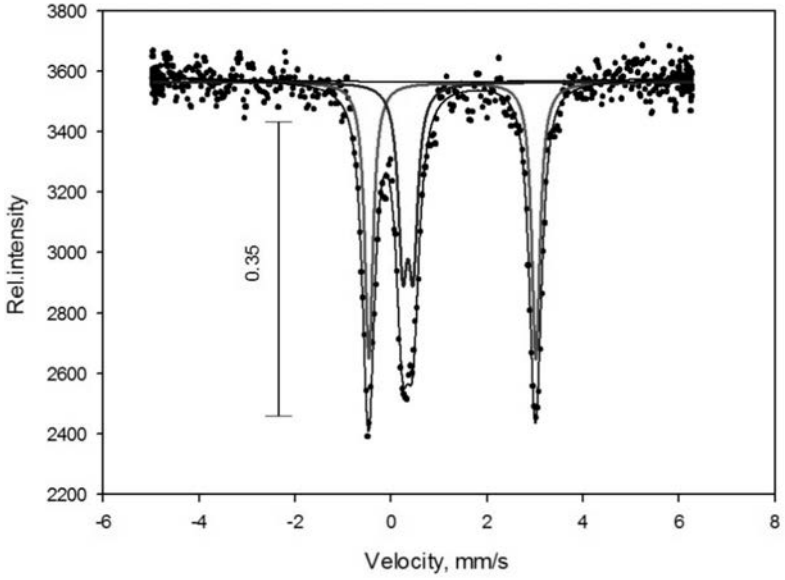

Fig. 3.3-8: SMS spectrum of skiagite garnet at ambient conditions. The doublet with large splitting represents Fe^{2+} while the doublet with small splitting represents Fe^{3+}.

The results of our study relate back to the question of solubility of the iron-majorite end-member in skiagite. We have shown the possibility to synthesize single crystals of a majorite-skiagite garnet and demonstrated based on single-crystal X-ray diffraction data that at least 23 mol. % of iron-majorite can be dissolved in skiagite at high-pressure and high-temperature conditions. Our present data should motivate further investigation of this mineralogically important system. Since the synthesized garnet contains octahedral Si, this may be an important pressure indicator for garnets of mantle assemblages.

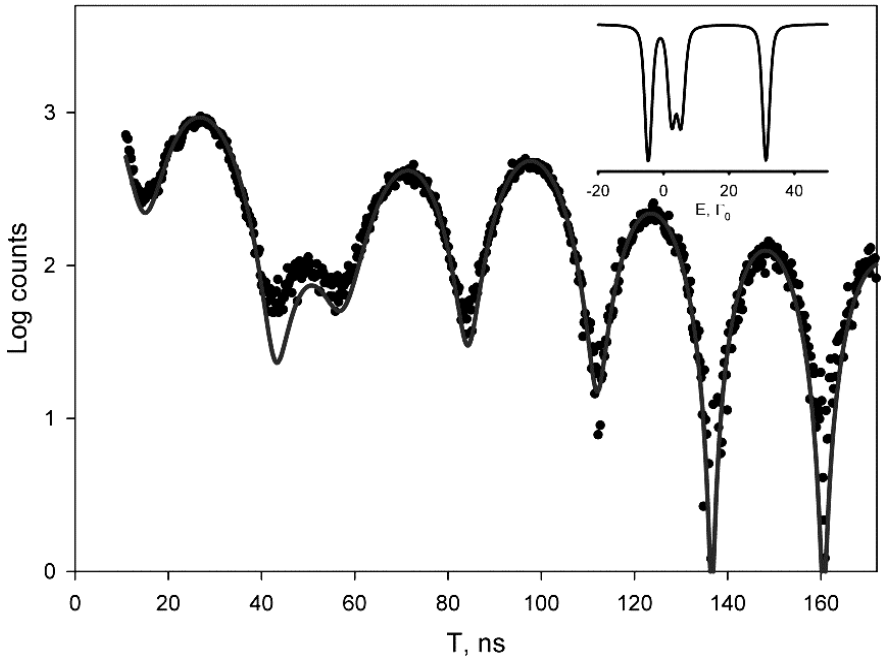

Fig. 3.3-9: NFS spectrum of skiagite garnet at ambient conditions showing the best-fit model (solid line). The inset shows the corresponding energy domain spectrum.

f. *Phase relations of skiagite $Fe^{2+}{}_3Fe^{3+}{}_2Si_3O_{12}$ at transition zone pressures and temperatures (L.S. Ismailova, A.V. Bobrov/Moscow and L.S. Dubrovinsky)*

Garnets containing both Fe^{2+} and Fe^{3+} are potentially useful monitors of oxygen fugacity in metamorphic rocks and garnet peridotites from the mantle. The presence of Fe^{3+} in garnet can also have a significant effect on temperature and pressure estimates, especially those based on Mg/Fe exchange equilibria. Thus, information about properties and high-pressure behaviour of the pure iron garnet end-member skiagite, $Fe^{2+}{}_3Fe^{3+}{}_2(SiO_4)_3$, is crucial for mineral physics and geochemistry of the Earth's upper mantle and transition zone. However, little is known about the phase relations and properties of skiagite. We have therefore studied the stability of skiagite in multianvil experiments and investigated the probable reactions controlling its formation and composition.

The starting material (corresponding to the nominal composition $Fe_3Fe_2Si_3O_{12}$) was a powdered mixture of chemically pure oxides (FeO, Fe_2O_3 and SiO_2) homogenized at room temperature using ethanol and then dried in a furnace at 100 °C for 24 hours. Multianvil experiments were performed at 7.5-11.5 GPa and 1100-1600 °C. With increasing temperature, the field of skiagite stability spread to the higher pressure region (up to 11.5 GPa at 1200-1300 °C). The recovered samples consisted of multi-phase assemblages including red subhedral garnet crystals and minor amounts of magnetite and coesite (Fig. 3.3-10), confirmed by X-ray diffraction data and microprobe analysis.

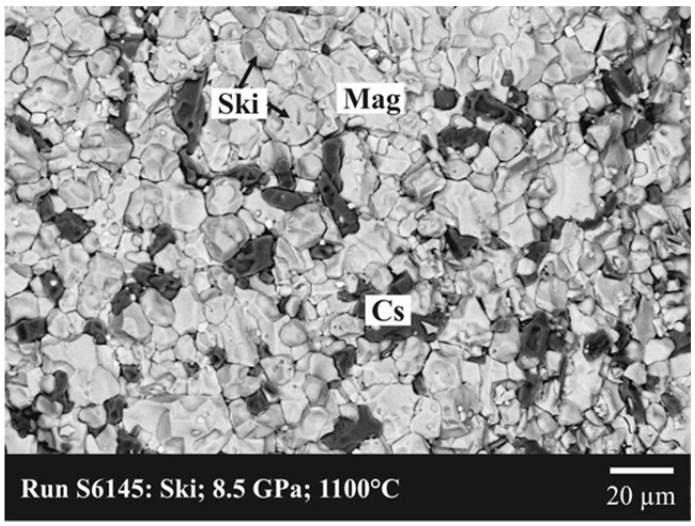

Fig. 3.3-10: Backscattered electron image of the run product (S6145) synthesized at 8.5 GPa and 1100 °C consisting of skiagite (Ski), coesite (Cs), and magnetite (Mag).

The composition of the synthesized garnet is characterized by Si excess (up to 3.4 a.f.u.), thus indicating a Fe-majorite-skiagite solid solution in the range of 15-40 mol. % $Fe_4Si_4O_{12}$ (Fig. 3.3-11). Incorporation of Fe-majorite in skiagite proceeds through the following reaction: $Fe^{2+}{}_3Fe^{3+}{}_2Si_3O_{12}$ (Ski) = $Fe^{2+}Fe^{3+}{}_2O_4$ (Mag) + SiO_2 (Cs) + 0.5 $Fe^{2+}{}_4Si_4O_{12}$ (Fe-maj). With increasing pressure (or decreasing temperature), garnet is replaced by an association of ferroringwoodite-magnetite solid solution and coesite (stishovite): $Fe^{2+}{}_3Fe^{3+}{}_2Si_3O_{12}$ (Ski) = $Fe^{2+}Fe^{3+}{}_2O_4$ + Fe_2SiO_4 (Mag_{ss}) + 2 SiO_2 (coesite/stishovite). The range of $FeFe_2O_4$–Fe_2SiO_4 solid solution expands from ~ 25 to ~ 70 mol. % Fe_2SiO_4 in magnetite. At 1400-1600 °C we observed partial melting with magnetite and coesite as liquidus phases.

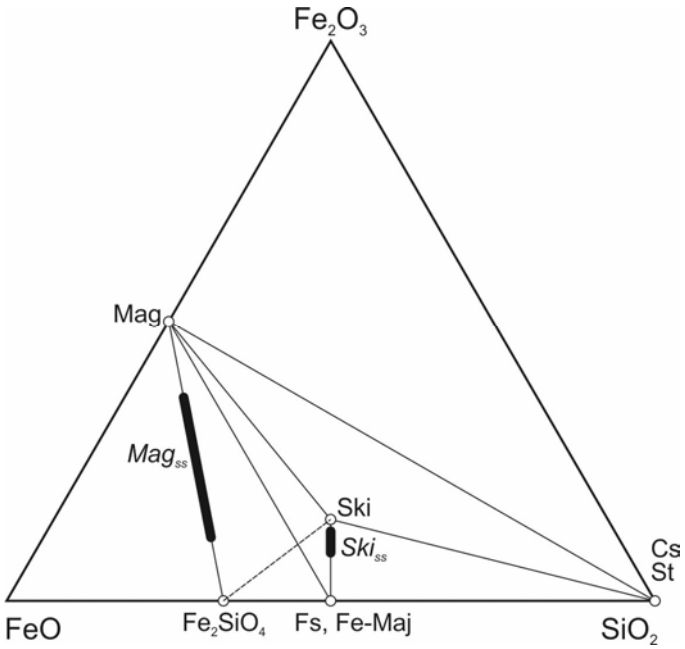

Fig. 3.3-11: Plot of the system FeO-Fe_2O_3-SiO_2 showing the phase assemblages at 7.5-11.5 GPa and 1100-1600 °C. The solid solutions of skiagite ($Fe_3Fe_2Si_3O_{12}$-$Fe_4Si_4O_{12}$) and magnetite (Fe_3O_4-Fe_2SiO_4) are indicated by thick lines.

g. *Siderite ($FeCO_3$) stability in the Earth's lower mantle (V. Cerantola, I. Kupenko/Grenoble, C.A. McCammon, L.S. Ismailova/Bayreuth, I. Kantor/Grenoble and L.S. Dubrovinsky)*

The increasing concentration of CO_2 in the atmosphere together with climate change has increasingly focused attention on the carbon cycle and its evolution at the Earth's surface, where mankind is most affected by its variations. However, the roots of the carbon cycle extend well below the Earth's surface, via subduction, which is thought to be the main mechanism that carries carbon to the deep Earth. Since current models show that subducting slabs can go through the transition zone and enter the lower mantle, the deep carbon cycle may extend as far down as the core-mantle-boundary. In this study we focus our attention on carbonate phases, the main carbon-bearing minerals in subducting slabs, and in particular on the stability of Fe-carbonates such as siderite ($FeCO_3$). Previous experimental work already demonstrated the stability of $MgCO_3$ to pressures and temperatures near the core-mantle boundary. Even though there is complete solid solution between $MgCO_3$ and $FeCO_3$ at ambient conditions, the high-pressure spin transition of iron atoms in $FeCO_3$ could affect its phase stability. We therefore performed experiments on $FeCO_3$ at high pressures and high temperatures to investigate its phase stability and the nature of its potential decomposition products.

Synthetic $FeCO_3$ crystals were subjected to pressures up to 100 GPa and temperatures up to 2500 K using double-sided laser heated diamond anvil cells. Neon was used as a pressure medium in order to preserve the single crystal nature of the samples even after short laser heating periods, roughly 5 minutes long. Single-crystal X-ray diffraction measurements and Synchrotron Mössbauer Source (SMS) spectroscopy were performed at APS and on the Nuclear Resonance beamline (ID18) at ESRF. Experiments at 100 GPa showed a complete transformation of $FeCO_3$ into two new high-pressure carbonates with Fe in different oxidation states depending on the heating temperature. Laser heating above 2000 K was inferred to induce the following reaction based on the run products: $17\ FeCO_3 \rightarrow Fe_4(CO_4)_3 + Fe_{13}O_{19} + 10\ CO_2 + 4\ C$, forming a new carbonate with C in four-fold oxygen coordination and all Fe in the 3+ valence state. Laser heating at lower temperatures (1600 K < T < 2000 K) was inferred to trigger a different redox reaction: $4\ FeCO_3 + ½\ O_2 \rightarrow Fe_2^{2+}Fe_2^{3+}C_4O_{13}$, where half of the Fe atoms are in the 2+ state and half are in the 3+ state. SMS spectra of the "high" and "low" temperature runs are consistent with these reactions (Fig. 3.3-12), where the relative area of these two components in the $Fe_2^{2+}Fe_2^{3+}C_4O_{13}$ phase are 49(7) and 51(7) %, identical within experimental uncertainty to the site occupancy refined by single crystal X-ray diffraction.

Our experiments suggest that Fe-rich carbonates could exist down to the core-mantle boundary in regions of high oxygen fugacity, for example in the proximity of subducting slabs and that high temperatures (above 2000 K) would be required to oxidise all Fe^{2+} to Fe^{3+} in the iron endmember to produce diamond. Further studies are required to establish the composition effect on the stability of carbonates in the lower mantle and their potential decomposition products.

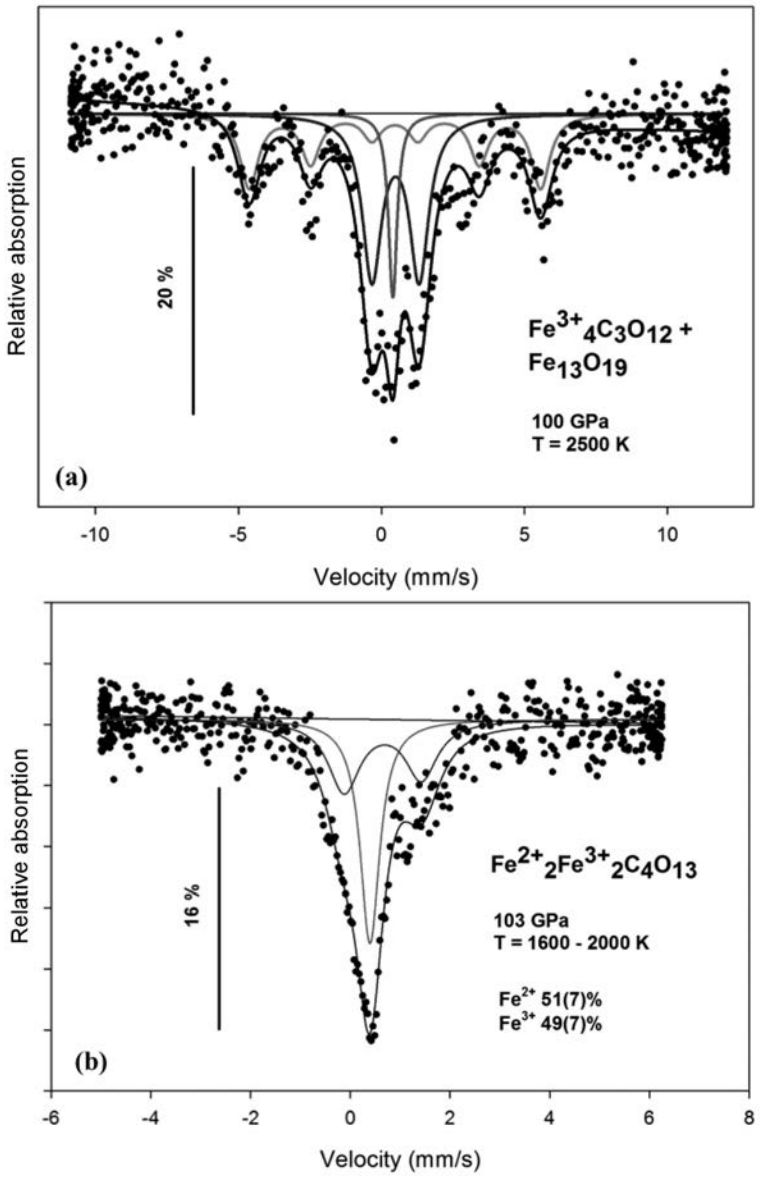

Fig. 3.3-12: Room temperature SMS spectra of $FeCO_3$ decomposition collected at the indicated pressures and after laser heating to the indicated temperatures: (a) $Fe_4(CO_4)_3$ + $Fe_{13}O_{19}$ and (b) $Fe_2{}^{2+}Fe_2{}^{3+}C_4O_{13}$. The magnetic sextet corresponds to Fe^{3+} in $Fe_{13}O_{19}$ (a) and the quadrupole doublets to Fe^{3+} in $Fe_4(CO_4)_3$ (a) and $Fe_2{}^{2+}Fe_2{}^{3+}C_4O_{13}$ (b). The singlets correspond to Fe^{2+} in the low-spin state from unconverted $FeCO_3$ (a) and $Fe_2{}^{2+}Fe_2{}^{3+}C_4O_{13}$ (b).

h. *Influence of oxygen fugacity on iron oxidation state in chromite (Zs. Pintér and C.A. McCammon)*

In spite of its low abundance, spinel is an important mantle mineral due to its flexible crystal chemistry that can be a sensitive indicator of its environment. The affinity of spinel for iron and its ability to incorporate two different oxidation states can provide a measure of oxygen fugacity according to the equilibrium conditions under which it formed. For example in spinel peridotite, spinel composition and $Fe^{3+}/\Sigma Fe$ can be used in conjunction with the compositions of co-existing olivine and orthopyroxene (opx) to determine the oxygen fugacity at which the assemblage was last in equilibrium. Spinel is also found in the form of chromite (Cr-rich spinel) in ophiolite suites, where it forms large bodies of podiform chromitites. These are considered to have been formed through melt-mantle interaction, where unusual variations in the $Fe^{3+}/\Sigma Fe$ ratio of some chromites (for example from the Luobusa ophiolite in southern

Tibet) have been used to infer a complex tectonic history. While the influence of oxygen fugacity on the $Fe^{3+}/\Sigma Fe$ ratio is well established in spinel peridotite through experimental calibration of olivine-opx-spinel oxybarometers, the variation of $Fe^{3+}/\Sigma Fe$ with oxygen fugacity in chromite from podiform chromitites is not yet known. As a preliminary step within a larger investigation, we synthesised a suite of chromites with varying composition at different conditions and measured $Fe^{3+}/\Sigma Fe$ using Mössbauer spectroscopy.

Spinel compositions were chosen based on the observed compositions of chromite in the Luobusa ophiolite. Starting materials were synthesised from oxides using the gel method and equilibrated either as pressed pellets in a gas mixing furnace overnight with different CO_2-CO gas mixtures, or run in a piston cylinder press. The latter were loaded into graphite capsules and run at 1100 °C and 20 kbar for 16-20 hours. The run products from all experiments were characterised using powder X-ray diffraction (XRD), electron microprobe analysis (EMPA), and Mössbauer spectroscopy. XRD showed all run products to consist almost entirely of spinel, but with minor amounts of MgO. Compositions determined using EMPA showed up to 10 % variation on the micron scale in samples from gas-mixing experiments, while piston-cylinder samples were more homogeneous (< 5 % variation). Mössbauer spectra showed the presence of only spinel in all run products and a large influence of oxygen fugacity on the spectral shape (Fig. 3.3-13).

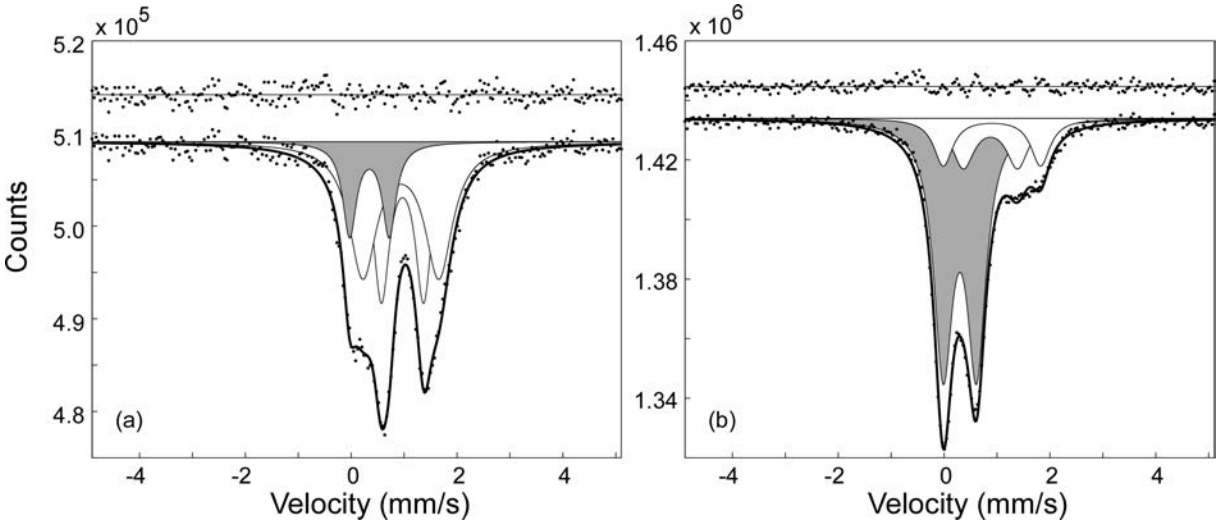

Fig. 3.3-13: Room temperature Mössbauer spectra of $MgCrAl_{0.5}Fe_{0.5}O_4$ spinel synthesised at 1100 °C and oxygen fugacities of (a) -0.7 log bar units below the iron-wustite buffer (IW-0.7) and (b) IW+4.3. Doublets corresponding to Fe^{2+} and Fe^{3+} are shaded white and grey, respectively.

Oxygen fugacity is the dominant influence on the $Fe^{3+}/\Sigma Fe$ ratio in the chromites that we studied, while variations in pressure, temperature and composition have a smaller effect (Fig. 3.3-14). Indeed $Fe^{3+}/\Sigma Fe$ values are much higher than in a chromite of similar composition in equilibrium with mantle olivine and opx, emphasising the role of the phase assemblage in

controlling the relation between $Fe^{3+}/\Sigma Fe$ and oxygen fugacity. Further experiments are underway to quantify the oxygen fugacity conditions under which natural chromite from the Luobusa ophiolite last equilibrated.

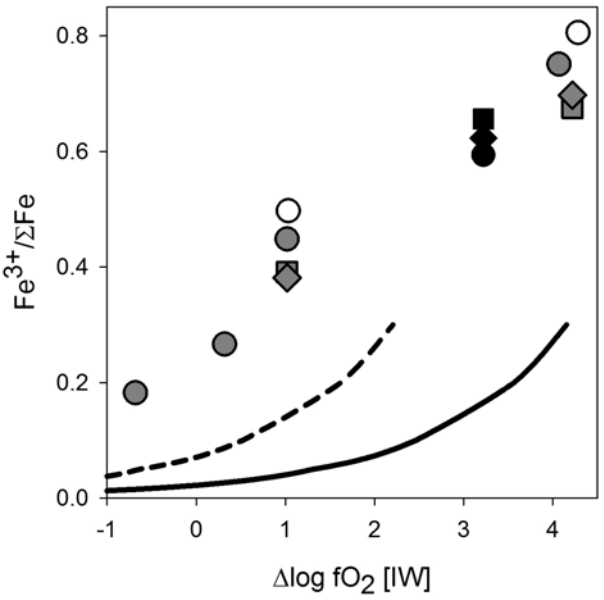

Fig. 3.3-14: Variation of $Fe^{3+}/\Sigma Fe$ in chromite with oxygen fugacity relative to the IW buffer. The symbols indicate the composition (circles: $MgCrAl_{0.5}Fe_{0.5}O_4$, squares: $Mg_{0.8}Cr_{0.6}Al_{1.2}Fe_{0.4}O_4$, diamonds: $Mg_{0.8}Cr_{0.8}AlFe_{0.4}O_4$) while the shading indicates the conditions (unshaded: 900 °C and 1 bar, grey: 1100 °C and 1 bar, black: 1100 °C and 20 kbar). The lines indicate the values calculated according to the olivine-opx-spinel oxybarometer [Wood *et al.* 1990, *J. Geophys. Res.* 95: 15845-15851] at 1100 °C and 20 kbar for $MgCrAl_{0.5}Fe_{0.5}O_4$ spinel in equilibrium with $Mg_{1.8}Fe_{0.2}Si_2O_6$ opx and $Mg_{1.8}Fe_{0.2}SiO_4$ olivine (solid line) or $Mg_{1.7}Fe_{0.3}SiO_4$ olivine (dashed line).

i. *The effect of temperature on the $P2_1/c$ to $C2/c$ transition in H_2O-bearing $Mg_2Si_2O_6$ clinoenstatite (N. Siersch, A. Kurnosov and T. Boffa Ballaran; S.D. Jacobsen/Evanston)*

A sharp velocity increase at 260-330 km depth in the Earth's mantle, known as the X discontinuity, is one of the most difficult seismic discontinuities to explain due to its regional variation, depth variability, and its broad range of observed shear wave reflection coefficients. The transition of orthoenstatite to high-clinoenstatite with *C*2/*c* symmetry is a likely candidate for the X-discontinuity since P-T conditions of the transition broadly match corresponding depths. It was recently shown that at room temperature, the low-clinoenstatite ($P2_1/c$) to high-clinoenstatite transition is strongly influenced by H_2O, and that just 1300 ppm H_2O by weight in $MgSiO_3$ can displace the $P2_1/c$ to $C2/c$ transition to lower pressures by up to 2 GPa (~ 60 km). To investigate the influence of H_2O on the $MgSiO_3$ phase diagram for pyroxenes, further *in situ* observations at higher temperatures are required. The aim of this study is to characterise by means of Raman spectroscopy and single-crystal X-ray diffraction the $P2_1/c$ to

*C*2/*c* transition of $MgSiO_3$ clinoenstatite containing different amounts of water at high pressures and temperatures using an electrically heated diamond anvil cell.

A crystal of $MgSiO_3$ clinoenstatite containing 900 ppm of water, about 100 µm in diameter and polished to 20 µm thickness, was placed in a diamond anvil cell with a 500 µm culet diamond size. A ruby chip and a Sm:YAG single crystal were placed next to the clinoenstatite for *in situ* temperature and pressure determination. The high-pressure and high-temperature experiment was conducted under quasi-hydrostatic conditions using neon as a pressure-transmitting medium. Preliminary results have been obtained so far at 190 °C and at pressures ranging between 4.7 to 9.9 GPa. The *P*2$_1$/*c* low-clinoenstatite phase is characterised by the presence of a vibrational doublet located between 650 and 750 cm^{-1}, resulting from the Si-O-Si vibrations of the two symmetrically distinct tetrahedral chains. The transition to the *C*2/*c* high-clinoenstatite can be easily observed because the tetrahedral chains rotate and become equivalent, giving rise to a single Si-O-Si vibration (Fig. 3.3-15).

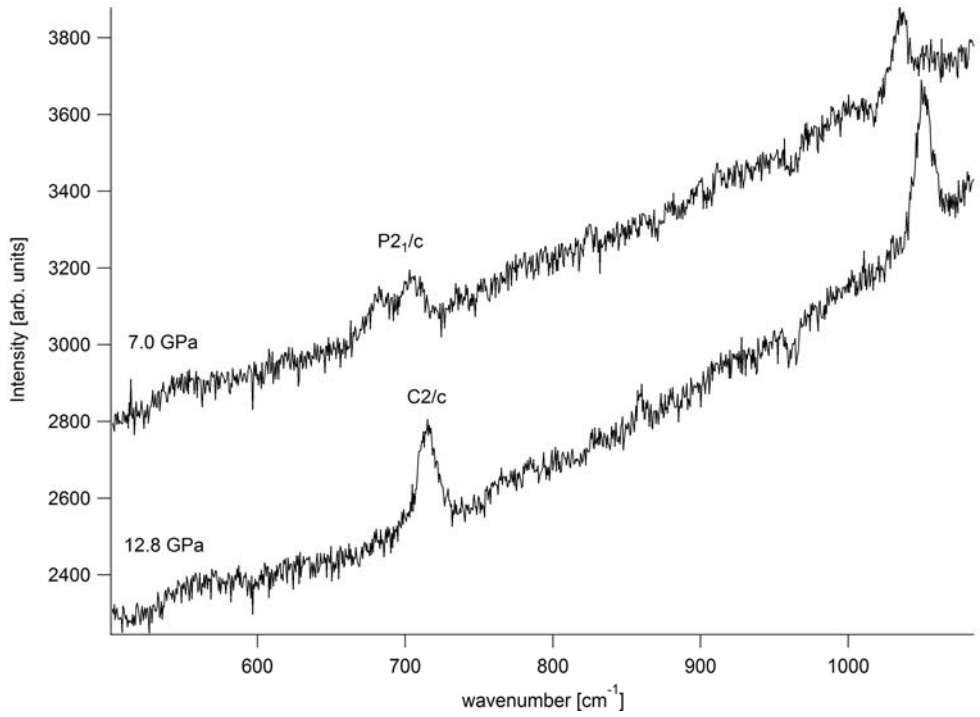

Fig. 3.3-15: The transition from the *P*2$_1$/*c* to the *C*2/*c* structure can be recognised as the point where the characteristic doublet of low-clinoenstatite become a single peak.

At 190 °C, the *P*2$_1$/*c* to *C*2/*c* transition occurs at about 9.0 GPa and no significant hysteresis was observed. The transition pressure is almost 3 GPa larger than that observed at room temperature, suggesting a much larger influence of temperature on such a transition than that observed from quenched experiments. More measurements are needed to better constrain such observations and to determine the effect of water on the transition.

j. *Lonsdaleite is a phantom mineral (N.A. Dubrovinskaia/Bayreuth; L.S. Dubrovinsky; P. Németh/Budapest; L.A.J. Garvie, T. Aoki and P.R. Buseck/Tempe)*

Diamond is reported to have a number of polytypes, of which lonsdaleite (also called hexagonal diamond) has received particularly intense attention. Lonsdaleite was first described almost 50 years ago from the Canyon Diablo iron meteorite. Its formation was attributed to shock-induced transformation of graphite within the meteorite upon impact with the Earth, and its occurrence was used as an indicator of shock. It has since been reported from several meteorites as well as from terrestrial sediments and has been attributed to asteroidal impacts, both extraterrestrial and on Earth. Lonsdaleite is thought to play a central role during the graphite-to-diamond transformation, and calculations suggest it possesses mechanical properties superior to diamond. However, despite extensive efforts, lonsdaleite has never been produced or described as a separate, pure material.

Published powder X-ray diffraction (XRD) patterns of lonsdaleite show peaks of cubic diamond plus extra, very broad and poorly resolved, maxima at 0.218, 0.193, 0.151, and 0.116 nm that have been indexed using a hexagonal unit cell. However, these maxima either occur on the shoulders of diamond peaks or match those of graphite, but well-resolved X-ray reflections for lonsdaleite have not been reported. In the course of our work we studied a sample from the Canyon Diablo meteorite, the type specimen from which "lonsdaleite" was first described, and synthetic high-pressure high-temperature microcrystalline diamond. We showed that defects in cubic diamond provide an explanation for the characteristic *d*-spacings and reflections reported for lonsdaleite (Fig. 3.3-16).Ultrahigh-resolution electron microscope

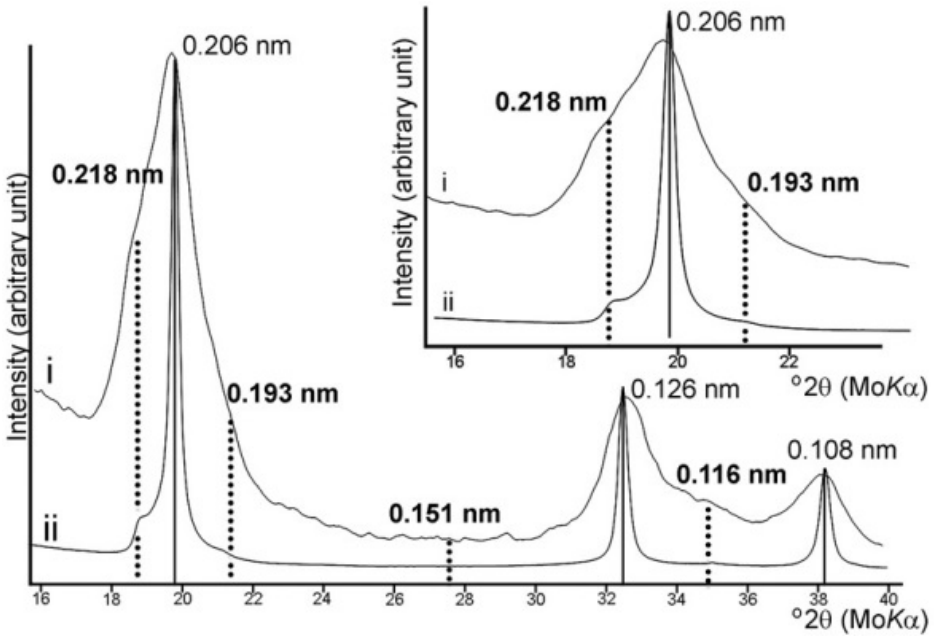

Fig. 3.3-16: XRD patterns from Canyon Diablo (i) and synthetic (ii) diamond samples. The patterns show features reported for "lonsdaleite". Cubic diamond reflections are marked with solid black lines. The positions attributed to lonsdaleite are indicated by vertical dotted lines and bold numbers.

images demonstrate that samples displaying features attributed to lonsdaleite consist of cubic diamond dominated by extensive {113} twins and {111} stacking faults. These defects give rise to nanometer-scale structural complexity. Our findings question the existence of lonsdaleite and point to the need for re-evaluating the interpretations of many lonsdaleite-related fundamental and applied studies.

k. *Monoclinic baddeleyite in the Shergotty Martian meteorite: Investigations of orthogonal twin lamellae induced during a natural dynamic event (S. Ozawa/Sendai, K. Marquardt, M. Miyahara/Hiroshima, A. El Goresy, E. Ohtani/Hiroshima, N. Miyajima, P. Gillet/Lausanne and A. Bouvier/London)*

The origin, nature and igneous crystallization ages of Martian shergottites have been the subject of extensive multidisciplinary investigations, but the results are frequently plagued with controversial interpretations from different sources. The origin of monoclinic ZrO_2 baddeleyite in Martian shergottites is controversially debated as to whether it evolved through: (1) pristine igneous crystallization in Martian basaltic flows in the young geologic history of Mars, or (2) decompression by recovery from a shock-induced dense polymorph in a young dynamic episode on Mars. This controversial debate also fostered the "*shergottite age conundrum*" that plagued shergottite chronology for more than three decades, thus hindering possibilities to explore details of igneous processes on Mars.

The sources of discrepancy are manifold relating to details of the different investigation techniques, the lack of reliable *in situ* $U^{238}/Pb^{207}*$ SIMS dating of baddeleyite due to orientation effects, negligence of kinetic effects during natural shock events, and the unrealistic assumption that the magnitude of natural dynamic deformation and the resulting radiometric resetting could be convincingly calibrated by the several orders of magnitude shorter laboratory dynamic experiments. A further source of error is the common assumption that the sole confirmation of the monoclinic nature of ZrO_2 in shergottites automatically reveals undisputable evidence for an igneous origin. ZrO_2 occurs in two distinct petrographic settings in shergottites: (1) polycrystalline longitudinal objects in shock melted and unmelted mesostasis, and (2) inclusions in titanomagnetite or ilmenite or at the rims of these phases. The temperature range of ZrO_2 crystallization in the mesostasis extends between 1250 °C and 935 °C and thus encompasses the tetragonal to monoclinic polymorph phase boundary. The tetragonal polymorph is 4 % denser than the monoclinic baddeleyite-structured polymorph and is unquenchable below 1000 °C. It inverts to the monoclinic polymorph during cooling, producing polysynthetic orthogonal twin lamellae. Here we investigated seven baddeleyite grains in their shocked assemblages in the Shergotty meteorite using SEM, EPMA, and FIB-TEM and compared their submicron structure with a natural terrestrial single untwinned monoclinic baddeleyite crystal from the Phalaborwa carbonatite.

TEM investigations on the Phalaborwa ZrO_2 reference grain show that a single untwinned monoclinic crystal (Fig. 3.3-17) crystallized as such below 1000 °C. The original nature of the magmatic ZrO_2 in Shergotty and other shergottites cannot be determined since the baddeleyite

now present resulted from overprinting by the dynamic event at ~ 22 GPa. Baddeleyite grains in the shock-melted mesostasis of Shergotty now coexist with molten and quenched maskelynite and are mostly in close association with seifertite (Fig. 3.3-18), thus indicating that they were subjected to the same P-T regime that created seifertite from the low pressure SiO_2 polymorph. Lack of melting in the titanomagnetite-baddeleyite-ilmenite lithology strongly suggests that the assemblage was shock modified below the solidus. The studied ZrO_2 grains in Shergotty are no longer single crystals. They depict a complex orthogonal twin pattern that presumably resulted from multiple phase transformations from a denser polymorph: either tetragonal, hexagonal, cubic, Ortho II, tetragonal or another unquenchable modification to monoclinic baddeleyite. Peak-shock pressures in shergottites imply a P-T residence higher than that of the Ortho II P-T stability field. Accordingly, application of only microRaman and EBSD studies could not reveal any reliable information on the origin of baddeleyite in any shergottite or the P-T path during compression and decompression.

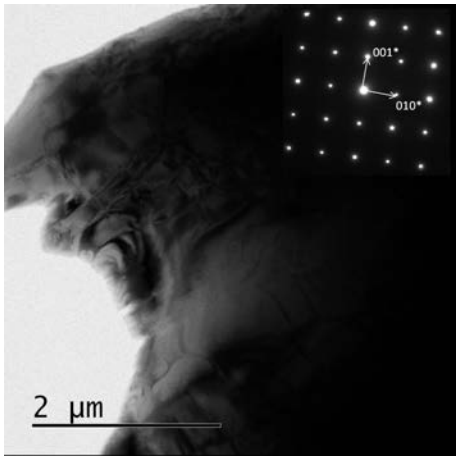

Fig. 3.3-17: TEM micrograph of a natural single monoclinic crystal of igneous baddelelyite from the Phalabora carbonatite. The electron diffraction pattern (inset) confirms the absence of twinning.

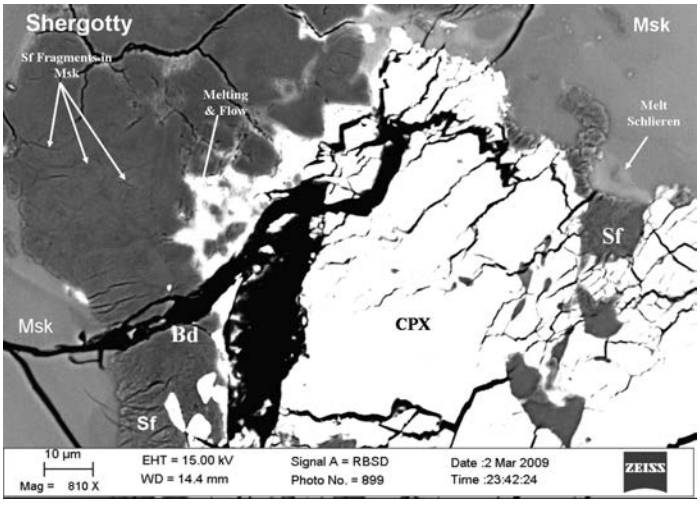

Fig. 3.3-18: BSE-SEM micrograph of a shock melted and quenched mesostasis containing seifertite (Sf) in contact with baddeleyite (Bd). The image also shows melt and plagioclase quenched to maskelynite (Msk) and heavily fractured pyroxene (cpx) as well as melt schlieren.

The fine-grained nature of the baddeleyite can be uncovered by FIB-TEM, presenting clear evidence for the mode of formation, whether it was igneous or through multiple phase transformations from dense polymorphs with the typical inversion mosaic. TEM images show that ZrO_2 in Shergotty contains submicron domains that have many grain-boundaries, implying that volume and interface diffusion effectively occurred, thus questioning the validity of U-Pb results obtained by SIMS. Interface diffusion was probably promoted by pervasive fracturing induced through the large volume coefficients of expansion in the temperature range estimated. Transition from the 4 % denser tetragonal to monoclinic ZrO_2 is martensitic, resulting in a crystallographic relationship between the tetragonal parent and monoclinic product as a result of transformation strain. It produces twinning in Shergotty daughter baddeleyite along four different crystallographic planes and fractures. Consequently, active interface and volume diffusion took place upon decompression, thus casting considerable doubt on the validity of the claimed SIMS ^{238}U-^{206}Pb dating results erroneously declared "*pristine igneous crystallization ages*"**.**

A further serious source of error from *in situ* $^{206}Pb^*/^{238}U$ dating of baddeleyite by SIMS emerges from orientation effects to the ion beam. TEM bright and dark field images reveal fine-grained twin lamellae and intragranular fractures. The twin lamellae are generally less than 200 nm in size (Fig. 3.3-19a). They are oriented parallel to (110), (1-10), (100) and (010) (Fig. 3.3-19b). During SIMS analysis $^{206}Pb^*/^{238}U$ and UO^+/ U^+ vary with crystallographic orientation to the ion beam, thus leading to significant differences in the calculated $^{206}Pb^*/^{238}U$ ages with an uncertainty between -13 % to +17 %. The orientation effect for baddeleyite in shergottites leads to unreliable results, because the ion beam will continuously extract variable $^{206}Pb^*$ and ^{238}U ions from twin lamellae with different orientations during its sputtering with depth in the grain during the investigations.

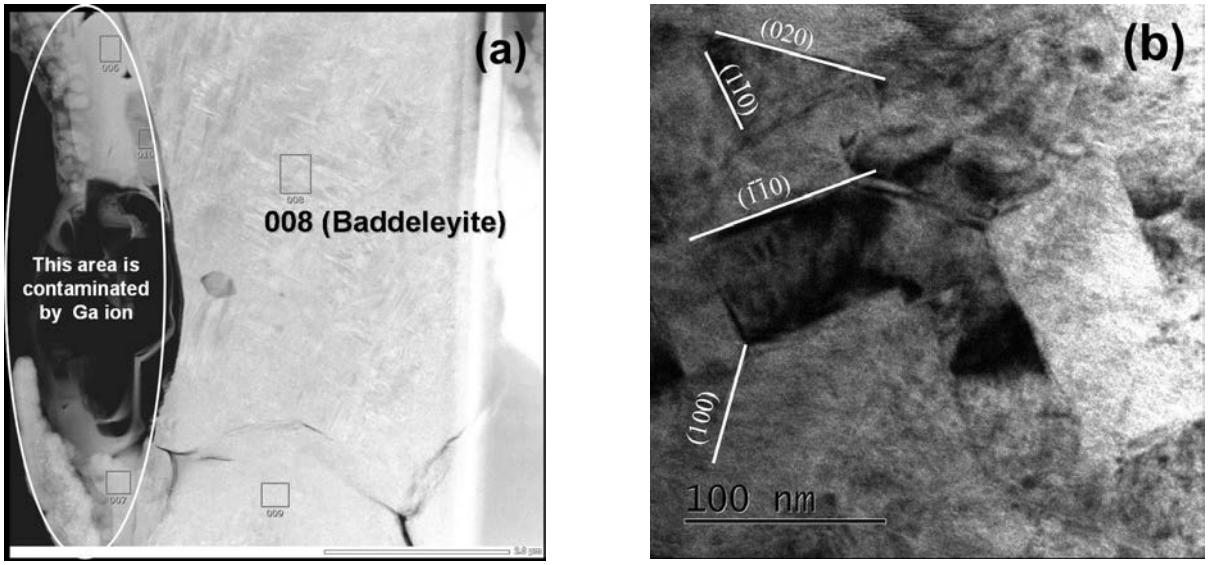

Fig. 3.3-19: (a) BSE-SEM micrograph of a baddeleyite SHE7 FIB slice depicting the orthogonal twin lamellae resulting from the phase transformation. (b) Bright-field TEM micrograph documenting the orientation of the fine-grained orthogonal twin lamellae of secondary baddeleyite.

l. *High-pressure polymorphs of coesite (A. Černok, E. Bykova and T. Boffa Ballaran; H.-P. Liermann/Hamburg, M. Hanfland/Grenoble and L.S. Dubrovinsky)*

Silica, SiO_2, exhibits a very rich polymorphism with more than 30 stable or metastable phases, most of which occur at ambient to moderate pressures (< 9 GPa). Coesite is the densest polymorph of silica that contains silicon atoms tetrahedrally coordinated to oxygen and is thermodynamically stable above ~ 2.5 GPa at temperatures in excess of 500 °C. It is a framework silicate comprised of fully polymerized corner-sharing SiO_4 tetrahedra, having nearly hexagonal symmetry at room pressure ($C2/c$, Z = 16) with almost equal a and c axes and a β angle close to 120°. Previous high-pressure studies up to ~ 10 GPa concluded that the symmetry of the unit cell appears less hexagonal with increasing pressure. However, this pressure range was too low to investigate the phase transition coesite I→II near 25 GPa, which was previously observed only by spectroscopic studies.

We studied the high-pressure behaviour of coesite on single crystals using diamond anvil cells with neon as the pressure-transmitting medium by means of *in situ* Raman spectroscopy and synchrotron single-crystal X-ray diffraction up to pressures of ~ 51 GPa. High-pressure single crystal data were collected at ID09a at ESRF and at the Extreme Conditions Beamline P02.2 at Petra III.

We found that coesite undergoes two phase transitions and does not become amorphous at least up to ~ 51 GPa (Fig. 3.3-20). The first phase transition (coesite I to coesite II) is reversible and occurs around 23 GPa. The volume-pressure data of coesite-I up to ~ 20 GPa can be described by means of a third-order Birch-Murnhagan EoS with parameters V_0 = 547.26(66) Å^3, K_{T0} = 96(4) GPa, K'_{T0} = 4.1(4). Above this pressure we witnessed the formation of a well crystallized, novel high-P polymorph coesite-II, the structure of which we solved and refined at ~ 28 and ~ 31 GPa with final R_1 indices of 8 % and 12 %, respectively. Coesite-II has $P2_1/n$ symmetry and a unit cell that is "doubled" along the b-axis with respect to that of the initial coesite-I (Z=32): a = 6.5591(10) Å, b = 23.2276(14) Å, c = 6.7953(9) Å, β = 121.062(19)° and V = 886.84(19) Å^3 at ~ 28 GPa. All Si atoms are in tetrahedral coordination. The displacive phase transition I→II is likely driven by the extreme shortening (0.05 Å or 3.2 %) of the shortest and the most compressible Si1-O1 bond, related to the stiff 180° Si1-O1-Si1 angle (Fig. 3.3-21). The second transition (coesite II to coesite III) above ~ 30 GPa is also reversible but involves a large hysteresis. The transition to the lowest-symmetry phase, coesite III, is possibly a first-order phase transition that leads to a very distinct structure. Indexing of the unit cell reflections revealed triclinic symmetry: a = 6.788(4) Å, b = 7.040(4) Å , c = 8.714(5) Å , α = 69.47(5)° , β = 82.26(5)°, and γ = 80.89(5)° at 30.94(41) GPa. Samples recovered from the highest pressure achieved, ~ 51 GPa, show Raman spectra and the unit cell parameters of the initial coesite.

It was previously widely accepted that coesite undergoes pressure-induced amorphization at significantly lower pressures (30 GPa) and the structures of the metastable high-pressure

phases of coesite had not been studied. Investigations of the high-pressure behaviour of coesite are important to better constrain the metastable phase diagram of silica. Crystalline or amorphous metastable phases derived from coesite under high-pressure conditions are of particular interest because they can be used as potential tracers of peak transient pressures (stress) reached in processes such as impacts or faulting.

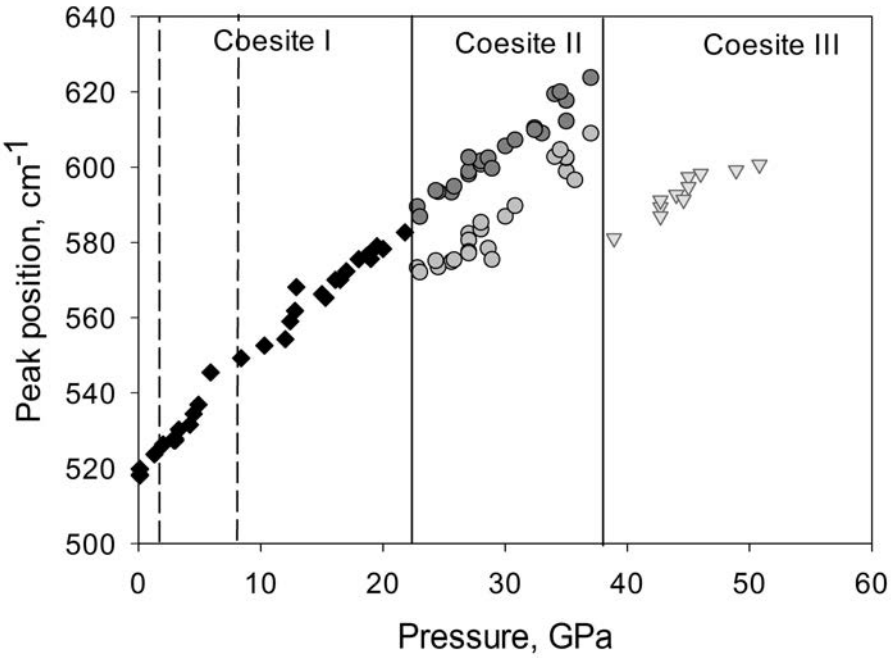

Fig. 3.3-20: Pressure dependence of the main Raman active mode obtained from several different experiments at ambient temperature. Phase transitions at ~ 23 and ~ 35 GPa are indicated by solid lines, and the thermodynamic stability field of coesite is indicated by dashed lines.

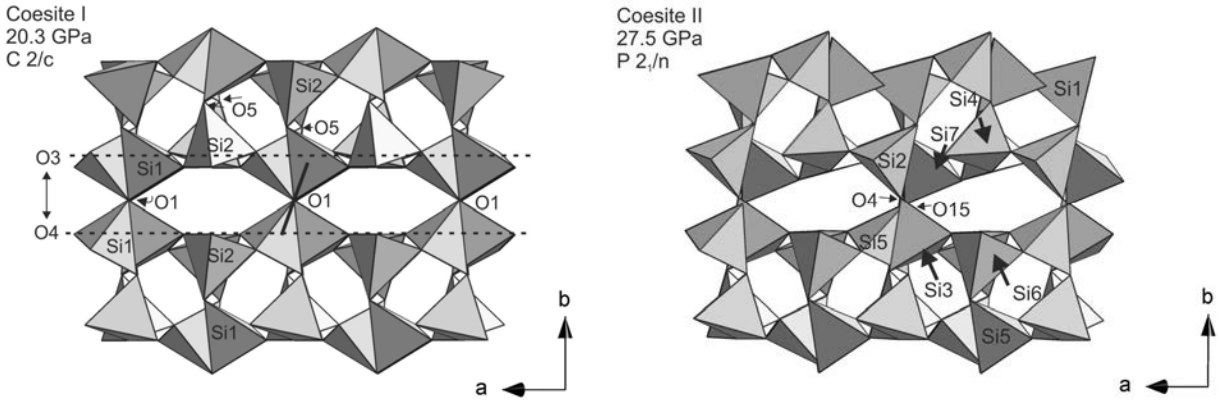

Fig. 3.3-21: Structural study of *C*2/*c* coesite-I at pressures above 20 GPa reveals a displacive phase transition to $P2_1/n$ coesite-II, driven by the extreme shortening of the shortest and the most compressible Si1-O1 bond, related to the stiff 180º Si1-O1-Si1 angle.

m. *High-pressure synthesis of single-crystal $(Mg_{0.9},Fe_{0.1})_2SiO_4$ wadsleyite (T. Kawazoe)*

Wadsleyite is the dominant mineral in the upper part of the mantle transition zone. Use of single crystals in experiments enables us to study the crystal orientation dependence of mineral properties (*e.g.*, C_{ijkl} and activities of slip systems). Thus high-pressure synthesis of single-crystal wadsleyite is useful to study dynamics in the upper mantle-transition zone region. However, wadsleyite single crystals made in previous studies may have contained a small amount of flux or ringwoodite.

Wadsleyite synthesis experiments were performed at 16 GPa, 1870 K and nominally anhydrous conditions for 1 hour with a Kawai-type multianvil apparatus. The starting material was a powder of San Carlos olivine. No flux was used. The powder was packed in foil capsules made of Re, Ni or Mo to examine the effect of oxygen fugacity on the grain size of recovered crystals. The mineral phase assemblage of run products was identified by Raman spectroscopy. Single crystals were recognized by their uniform extinction under a polarization microscope. The mineral phase of the run products was wadsleyite in all of the experiments. The diameter of wadsleyite grains increased with increasing oxygen fugacity and grew to sizes up to ~ 500 μm (Fig. 3.3-22). The wadsleyite single crystals will be used to study the elasticity of wadsleyite at high pressure by Brillouin spectroscopy using a diamond anvil cell.

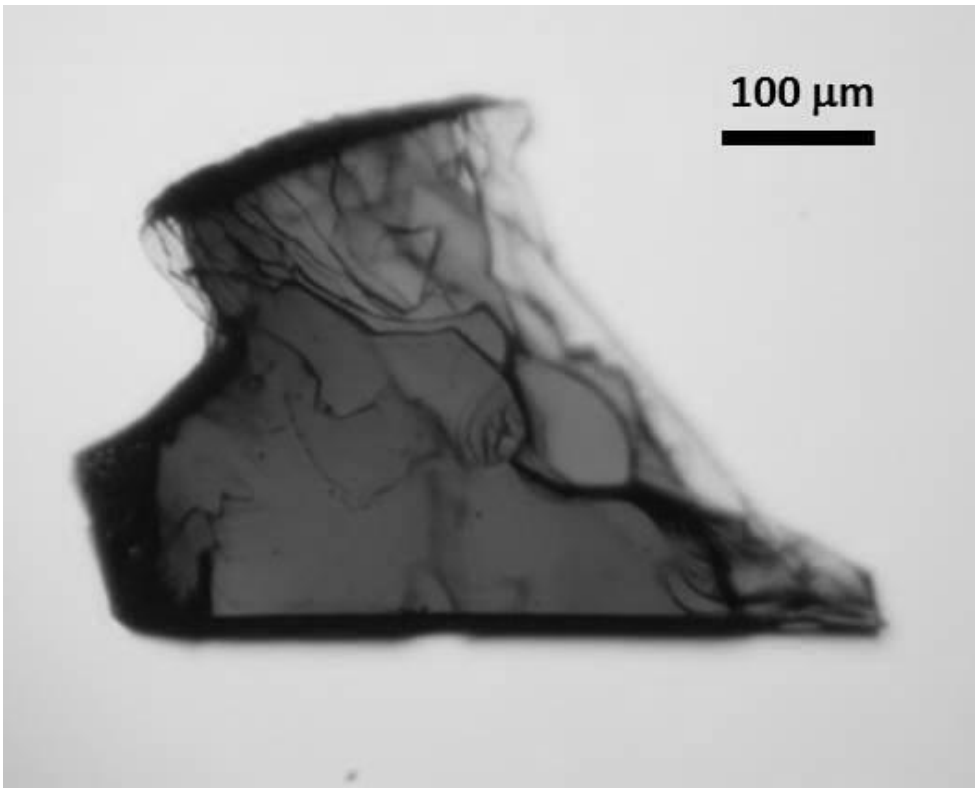

Fig. 3.3-22: Photomicrograph of a wadsleyite single crystal synthesized at 16 GPa and 1870 K for 1 hour.

n. *Hydrogen positions of hydrous wadsleyite from single-crystal neutron diffraction (S.D. Jacobsen/Evanston, J.R. Smyth/Boulder, M. Gutmann/Oxfordshire and D.J. Frost)*

Wadsleyite (β-Mg_2SiO_4) is nominally anhydrous, but incorporates hydrogen through charge-coupled chemical substitutions, β-$Mg_{2-x}H_{2x}SiO_4$. Being the major potential host for H_2O in the mantle transition zone (410-660 km depth), precise knowledge of the hydrogen positions in wadsleyite will guide theoretical calculations on how hydration influences the thermoelastic properties of wadsleyite at transition zone conditions. By tightly constraining the effects of hydration on wadsleyite physical properties, it may be possible to map the distribution of water in the transition zone from forthcoming, high-resolution regional seismic data.

Although hydrous wadsleyite has been studied for nearly three decades, the hydrogen positions of wadsleyite were not well known until recently because of the difficulty in using X-ray diffraction to locate small amounts of H. Even wadsleyite containing 2 wt. % H_2O contains on average only ~ 2.5 H atoms per unit cell. Neutron diffraction is better suited for locating H in nominally anhydrous minerals because hydrogen has a large scattering cross section for thermal neutrons. A recent study in the literature reported powder neutron diffraction data on a deuterated wadsleyite sample that was used to locate two deuterium positions on the O1 sited and associated with M3 site vacancies as predicted by an earlier work. To improve upon the model, it would be desirable to use single-crystal neutron diffraction with hydrogen in the structure. Single-crystal neutron diffraction (SCND) of hydrous wadsleyite has not been possible because of the very large samples required for neutron diffraction.

In Bayreuth, we synthesized a hydrous wadslyeite single crystal measuring about 1 mm^3 in volume, just meeting the minimum required sample size for SCND. Secondary-ion mass spectrometry was used to determine the water content of 1.2 wt. % H_2O, leading to a formula unit of β-$Mg_{1.90}H_{0.185}SiO_4$. Time-of-flight, single-crystal Laue neutron diffraction data were measured on the SXD (S3) beamline of ISIS, Rutherford Appleton Laboratory, pulsed-spallation neutron source. The S3 beamline is 8.3 m from the ambient water moderator, giving pulsed bunches with 0.2-10 Å incident wavelength and $\sin\theta/\lambda$ = 0.03-2.5 $Å^{-1}$. The SXD instrument features 11 position-sensitive, ZnS scintillating detectors surrounding the sample on all sides, each with 192 x 192 mm^2 active area. In this experiment, we collected intensity data at 60 K at three different sample orientations for 24 hours, totaling three days acquisition time.

2147 reflections were integrated to give an average $F^2/\sigma F^2$ = 24.9. Type I and type II Lorentzian extinction factors were refined in the initial model, giving fit parameters of $wR(F^2)$ = 0.117 and χ^2 = 3.275 for 45 variables, without hydrogen in the model. Difference-Fourier maps were calculated in sections throughout the structure to search for negative scattering residuals because in contrast to all other elements in this phase, hydrogen has a negative bound coherent scattering length. The largest negative residual at > 0.6 Å from a cation or

oxygen was modeled as H1 at fractional coordinates 0.401, 0.713, and 0.805. Inclusion of H1 in the model reduced the $wR(F^2)$ to 0.105 and χ^2 to 2.621 with fully anisotropic displacement parameters for H1. The H1 position corresponds to a hydrogen bond O1-H1…O4 with O1-H1 distance of 1.00 Å, H1…O4 distance of 2.11 Å, and hydrogen bond angle of 170 degrees. A second hydrogen position, H2, was found at 0.5 (fixed), 0.686, and 0.810 fractional coordinates and modeled with a fixed isotropic displacement parameter of 0.025. The H2 position forms a trifurcated hydrogen bond, O1-H2…(O4/O3), with O1-H2 = 1.05 Å, H2…O4(x2) = 2.25 Å, and H2…O3(x1) = 2.31 Å. The results correspond well to polarized infrared spectroscopy already reported by our group in the literature. Refined occupancy factors for Mg3, H1, and H2 correspond to the formula β-$Mg_{1.93}H_{0.15}SiO_4$, in very close agreement with the measured composition. The structure model of hydrous wadsleyite is illustrated in Fig. 3.3-23.

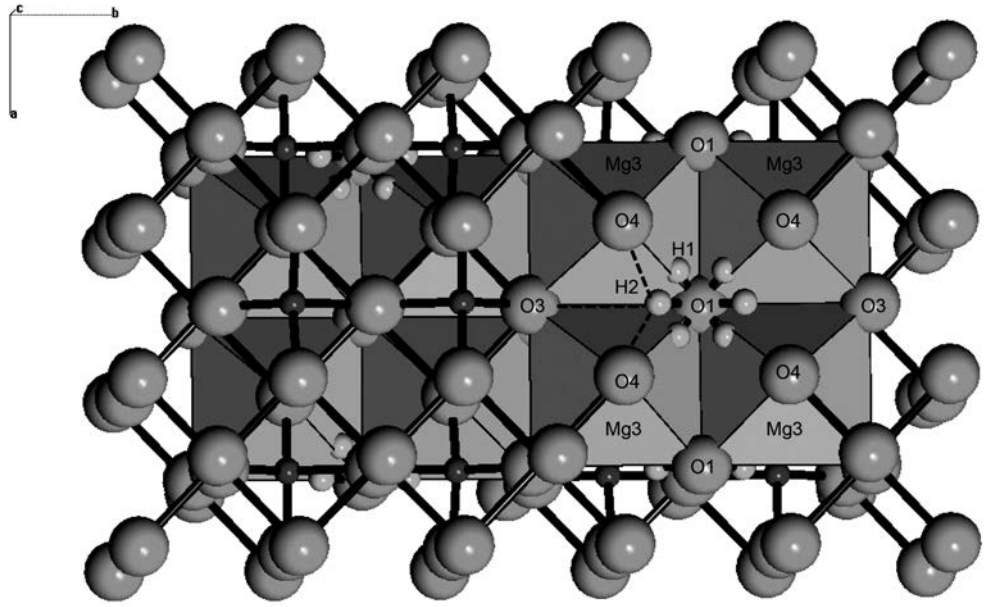

Fig. 3.3-23: Structure model of hydrous wadsleyite from single-crystal neutron diffraction.

o. *Characterization of a natural quartz crystal as reference material for microanalytical determination of Ti, Al, Li, Fe, Mn, Ga and Ge (A. Audétat, D. Garbe-Schönberg/Kiel, A. Kronz/Göttingen, T. Pettke/Bern, B. Rusk/Bellingham, J.J. Donovan/Eugene and H.A. Lowers/Denver)*

In recent years there has been growing interest in using the trace element content of quartz as a petrogenetic indicator, in particular to reconstruct the temperature and pressure of quartz crystallization via titanium-in-quartz (TitaniQ) thermobarometry. However, particularly with respect to Ti concentrations there is a lack of suitable reference materials because (i) natural samples are typically too inhomogeneous, and (ii) synthetic quartz is typically too pure

because the Ti-solubility is very low at the conditions at which large quartz crystals can be synthesized. For this reason an optically homogenous, natural smoky quartz crystal from Shandong province, China, was thoroughly characterized by laser ablation ICP-MS, electron probe microanalysis (EPMA), and solution ICP-MS to determine the concentration of 24 trace and ultratrace elements (Fig. 3.3-24). Pieces of a growth zone of 9 mm thickness within the quartz crystal were analyzed in four different LA-ICP-MS laboratories, three EPMA laboratories, and one solution-ICP-MS laboratory. Although the growth zone itself is not entirely homogeneous (Fig. 3.3-25), averages of multiple analyses across the growth zone return well-constrained, reproducible concentrations of Ti (57±4 µg g^{-1}), Al (154±15 µg g^{-1}), Li (30±2 µg g^{-1}), Fe (2.2±0.3 µg g^{-1}), Mn (0.34±0.04 µg g^{-1}), Ge (1.7±0.2 µg g^{-1}) and Ga (0.020±0.002 µg g^{-1}), and detectable, but less reproducible, concentrations of Be, B, Na, Cu, Zr, Sn and Pb (Fig. 3.3-25). Concentrations of K, Ca, Sr, Mo, Ag, Sb, Ba and Au were below the limits of detection of all three techniques. The uncertainties on the average concentration determinations by multiple techniques and laboratories for Ti, Al, Li, Fe, Mn, Ga and Ge are low; hence this quartz can serve as a reference material or a secondary standard material for microanalytical applications involving the quantification of trace elements in quartz.

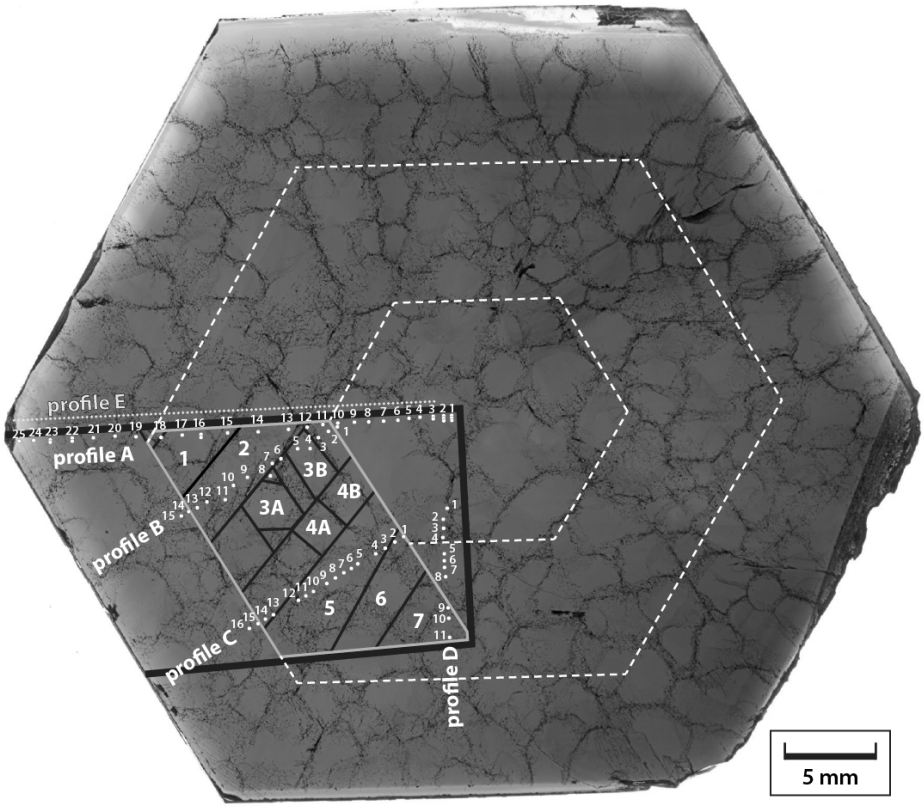

Fig. 3.3-24: Transmitted-light photograph of a polished section cut perpendicular to the *c*-axis of the quartz crystal. The reticulate structure arises from healed cracks decorated with fluid inclusions. Dashed white lines indicate the boundaries of three main growth zones. White dots and small white numbers represent the locations of the LA-ICP-MS analyses; for profile E the trace of the EPMA traverse shown in Fig. 3.3-25.

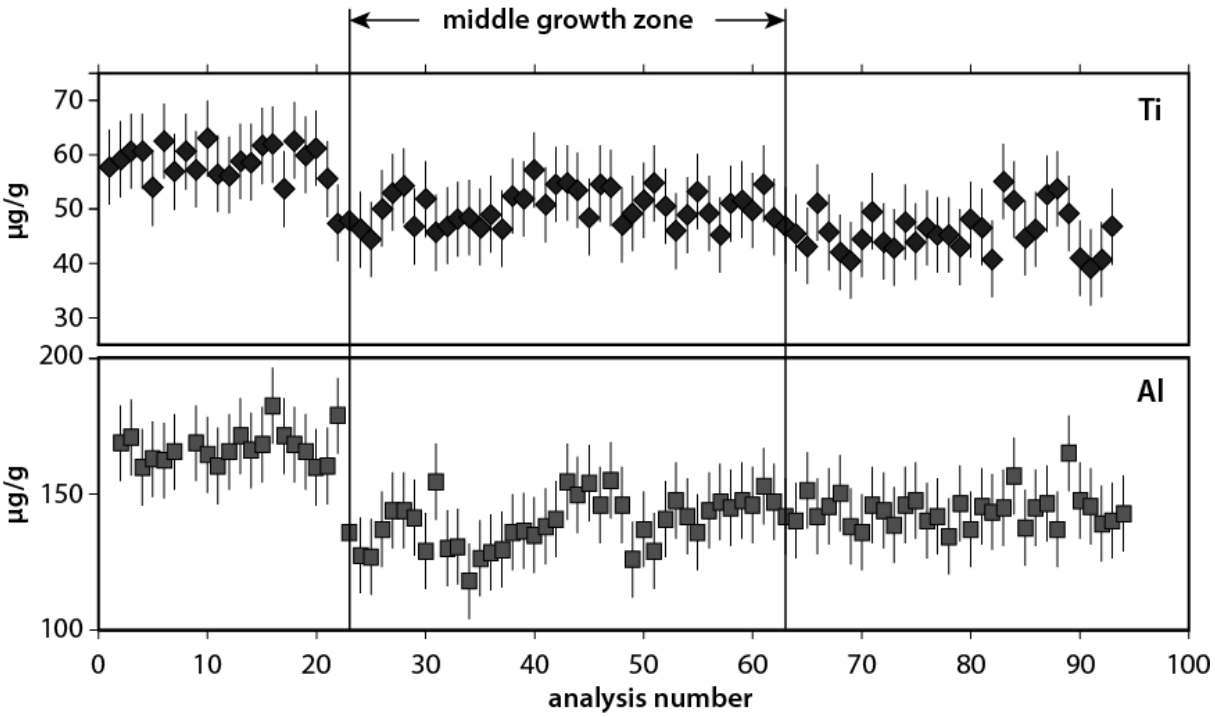

Fig. 3.3-25: Ti and Al concentrations determined by EPMA along profile E shown in Fig. 3.3-24, arranged from core (left) to rim (right).

3.4 Physical Properties of Minerals

Laboratory measurements of compressional and shear wave velocities of mantle minerals at high pressures and high temperatures are essential to interpret seismic velocities and hence to constrain the chemical composition of the Earth's interior. The elastic properties obtained experimentally are used to constrain thermo-elastic equation of state (EoS) parameters essential for constructing seismic models to compare with seismic travel time observations. Brillouin spectroscopy has been widely used to determine the variation with pressure of elastic properties of different materials, however its use at simultaneous high pressures and high temperature is still limited. The first three contributions in this section present an optimised method which makes use of the focused ion beam (FIB) instrument newly installed at BGI to prepare single crystals for high-pressure and high-temperature experiments. Disks and half disks of dimensions smaller than 100 µm have been cut from double-side polished oriented single crystals of wadsleyite, ringwoodite and bridgmanite using the FIB and loaded into diamond anvil cells equipped with heating elements designed and developed at BGI. The advantage of this method is particularly important for low-symmetry samples such as wadsleyite and bridgmanite since constraining their full elastic tensor requires one to measure at least two crystals with perpendicular orientations held at the same pressure and temperature conditions. By using half disks, the resulting samples have the perfect shape for loading together in the circular hole of the gasket.

Since mantle minerals are often complex solid solutions of a wide range of ideal end-members, determining the effect of the different cation substitutions on the thermo-elastic EoS parameters is mandatory to obtain accurate mineralogical models. The fourth and fifth contributions deal with omphacitic clinopyroxenes also containing Ca-Eskola and Ca-Tschermak components and majoritic garnets in the pyrope-majorite-almandine system. Wave velocities of these samples have been measured at synchrotron facilities using ultrasonics in a multianvil apparatus in the case of clinopyroxene, and by Brillouin spectroscopy in the case of garnets. Density was determined simultaneously in both studies by means of X-ray diffraction. The results are used to constrain the seismic properties of the Earth's upper mantle and transition zone. A major result is that, due to the presence of garnets, the seismic wave velocities at the base of the transition zone appear lower than the values obtained from reference models along a 1673 K adiabat, suggesting large temperature anomalies in this region which may be caused by the presence of stagnant slabs.

In the following two contributions, experiments were performed at synchrotron facilities to measure Debye sound velocities of siderite, $FeCO_3$, by means of nuclear inelastic scattering (NIS) and the density of amorphous $MgSiO_3$ by means of X-ray absorption. Major changes in Debye sound velocities associated with the high-spin to low-spin transition of Fe in siderite at high pressures provides a promising direction for detecting the presence of carbonate in slabs subducted into the lower mantle. A very small difference in density has been observed between amorphous and crystalline $MgSiO_3$ at 130 GPa in contrast with results reported in the literature. This result gives important constraints for assessing the density contrast between solid and liquid silicates at the base of the lower mantle.

Knowledge of the thermal and electrical conductivity of iron mixtures under the extreme pressure and temperature conditions of the Earth's core is essential to constrain heat diffusion in the Earth's interior and its influence on the geodynamo. These properties remain, however, poorly known because of the challenging experimental conditions. The analysis of the changes in electrical resistivity and isothermal compressibility for different metals upon melting according to Ziman's theory is reported in the eighth contribution. The results show that such approach can be used to determine the pressure-temperature dependence of the electrical resistivity along the melting curve of iron to infer the resistivity of liquid and solid portions of planetary iron cores.

The physical properties of minerals are controlled by their crystal structure, which plays a major role in determining the size and charge of the constituent atoms. The properties of rocks, on the other hand, depend not only on the properties of the mineral assemblages they are made up of, but also on the area distribution of grain boundaries among the mineral grains. The crystal chemistry of the mineral hibonite found in meteorites has a strong influence in stabilizing Ti^{4+} - Mg^{2+} couples even at the very reducing conditions of the solar nebula. The last contribution characterises the anisotropic area distribution of grain boundaries in an isostatically pressed forsterite, which allows to identify the most frequent grane boundaries in olivine dominated rocks.

a. *Single-crystal elasticity of wadsleyite, β-$(Mg_{0.9}Fe_{0.1})_2SiO_4$, at combined high pressure and high temperature (J. Buchen, H. Marquardt, T. Kawazoe, A. Kurnosov and T. Boffa Ballaran)*

The high-pressure polymorph of the mineral olivine, wadsleyite, β-$(Mg_{1-x}Fe_x)_2SiO_4$ with $0 < x < 0.25$, contributes as a major phase to any mineralogical model of Earth's upper mantle. In the transition zone at depths between 410 km and 520 km, wadsleyite accounts for a volume fraction of about 60 % in pyrolite. In addition, the phase transitions of olivine polymorphs cause discontinuities in seismic wave velocities. Their magnitudes and depths are sensitive probes for constraining lateral temperature or compositional variation in the Earth's transition zone. The elastic anisotropy inherent to the orthorhombic crystal symmetry of wadsleyite may further be useful for interpreting seismic anisotropy of the mantle. Knowledge of the elastic properties of wadsleyite at mantle pressures and temperatures is therefore essential for interpreting seismic observations in terms of the composition and dynamics of the Earth's mantle. Although the variation of wadsleyite elastic properties with pressure has been addressed in several previous studies, a complete set of single-crystal elastic constants for wadsleyite has not been determined at simultaneous high temperature at high pressure.

We are currently using Brillouin spectroscopy on single-crystal specimens loaded in a resistively heated diamond-anvil cell. Wadsleyite crystals with an iron content of $x \approx 0.1$ and sizes up to 500 µm have been synthesised from powdered San Carlos olivine at 16 GPa and 1600 °C in a multianvil apparatus. Single-crystal X-ray diffraction was used to select a large,

high-quality single crystal for polishing down to 22 µm. Subsequently, a circular platelet was cut from the polished crystal with a focused ion beam (FIB) and loaded in a diamond-anvil cell with neon as the pressure-transmitting medium (inset in Fig. 3.4-1). A Brillouin spectrum collected at room temperature and 0.6 GPa is presented in Fig. 3.4-1. Inelastic scattering from acoustic phonons of wadsleyite gives rise to three spectral features. Two of them can be attributed to shear waves, V_S' and V_S", and the remaining one to the compressional wave, V_P, associated with the propagation vector defined by the scattering geometry and the orientation of the specimen.

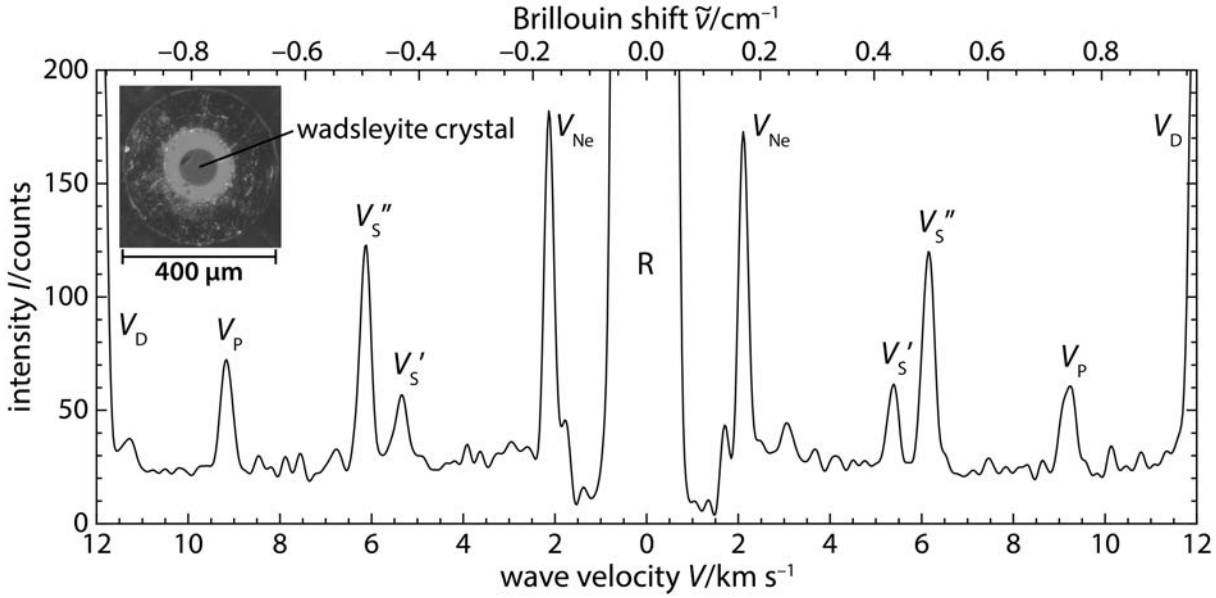

Fig. 3.4-1: Brillouin spectrum of a FIB-cut wadsleyite crystal (inset) at 0.6 GPa and room temperature; V_P, V_S', and V_S" mark the peaks arising from the compressional and the two shear waves in wadsleyite, respectively. Also visible are features due to elastic scattering (R), acoustic waves of the Ne pressure-transmitting medium (V_{Ne}), and of the diamond anvils (V_D).

To constrain all individual elastic constants, the velocities of acoustic waves travelling along several crystallographic directions are needed to be measured. For orthorhombic crystals like wadsleyite, this requires at least two platelets of different orientation to allow for a sufficient spatial dispersion of the probed propagation vectors. With the FIB, specimens of appropriate shape are currently prepared from two crystal orientations perpendicular to each other. To ensure the measurement of all elastic wave velocities at exactly the same pressure-temperature conditions, the two platelets will be loaded together in the diamond-anvil cell. The unit-cell volume and hence density will be determined at the same conditions with X-ray diffraction on the single-crystal disks. From the combination of the bulk modulus, calculated from the elastic constants, and the unit-cell volume evolution, absolute pressures can be

derived. For experiments at high temperatures, this is of primary importance since conventional pressure standards like the ruby fluorescence technique yield large uncertainties. With the double-specimen approach, the complete elastic tensor can be determined at a series of pressures along several isotherms. The accurate description of the elasticity of wadsleyite will not only allow an evaluation of discontinuities in seismic wave velocities due to its phase transitions but will also give insight into whether wadsleyite may be a source for seismic anisotropy in the upper mantle.

b. *High-pressure/high-temperature measurements of the elastic properties of single-crystal ringwoodite (K. Schulze, H. Marquardt, A. Kurnosov, T. Kawazoe and T. Boffa Ballaran)*

Ringwoodite is the major mineral of the Earth's transition zone at a depth between 520 km and 660 km. Quantitative knowledge about its single-crystal elastic properties at pressure- and temperature conditions of Earth's transition zone is needed to construct mineral physics-based models that can be compared to seismological observations, both for average seismic velocities and for seismic anisotropy. So far, experimental measurements of ringwoodite single-crystal elasticity have been mostly limited to high pressure at room temperature. The only combined high-pressure/high-temperature experiment on ringwoodite single-crystals reported in the literature has been conducted on hydrous ringwoodite. Although hydrous ringwoodite may be an important phase in hydrated regions of the transition zone, very likely it is not the most relevant phase in the bulk of the mantle between 520 km and 660 km depth, away from subducting slabs. To constrain the elasticity and seismic velocities of these regions, Brillouin Scattering experiments on anhydrous ringwoodite single-crystals at simultaneous high pressure and high temperature are underway. In addition a series of measurements with ringwoodite single-crystals with different iron- and water-percentage will be conducted to determine the influence of water and iron on its elastic properties.

The first step has been to develop a methodology for growing large single crystals of low water content ringwoodite of reasonable quality. To this end, San Carlos olivine $(Mg_{0.9}Fe_{0.1})_2SiO_4$ has been used as starting material for synthesis in a multianvil press at 21 GPa and 1900 K. We have obtained ringwoodite crystals with sizes up to 200 µm (Fig. 3.4-2a), from which we selected and oriented a single-crystal to be prepared as a double-side polished [100]-oriented slice 17 µm thick for elasticity measurements. From this slice, three samples from within a circle of 120 µm diameter have been cut using the FEI Scios focused ion beam (FIB) machine to allow for a number of high-pressure/high-temperature measurements on the same single-crystal material with the same crystallographic orientation (Fig. 3.4-2b). The anisotropic elasticity of a cubic crystal, such as ringwoodite, is characterized by three independent, non-zero elastic constants $C_{11,}$ C_{12} and C_{44}. We are measuring acoustic velocities in a resistive-heated diamond-anvil cell (Fig. 3.4-2c) along the [100] and [110] directions. Shear velocities in these two specific directions are given by

$(C_{44}/\rho)^2$ and $(C_{11}\text{-}C_{12}/2/\rho)^2$ respectively, where ρ is the density. The measured compressional velocities along these directions, therefore, will allow us to derive all three elastic constants from velocity measurements on a single specimen. Simultaneously to the acoustic velocity measurements, we are collecting X-ray diffraction data on the ringwoodite single-crystal. By combining all measurements, we will be able to determine single-crystal elasticity, density and absolute pressure.

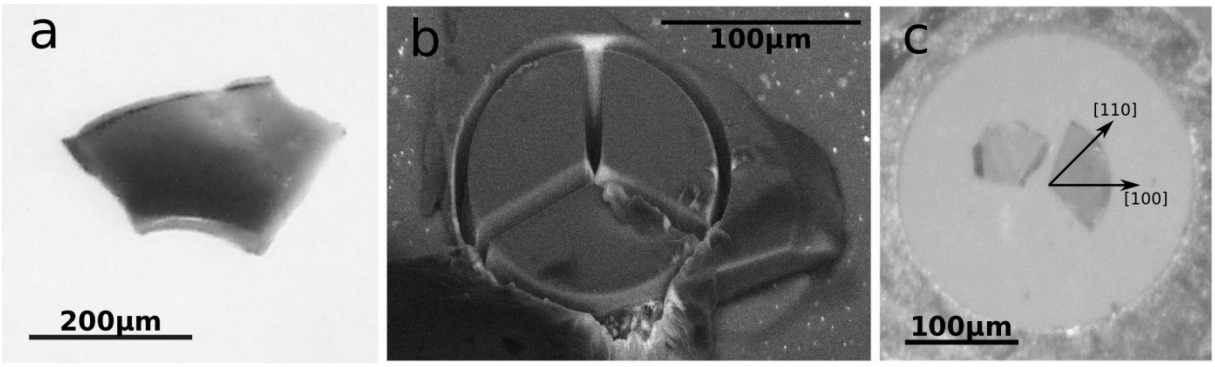

Fig. 3.4-2: (a) A large, low-water content $(Mg_{0.9}Fe_{0.1})_2SiO_4$ ringwoodite single-crystal. (b) Sample cut by the FIB method in a divided circle from the polished and oriented single-crystal. (c) Two single-crystal pieces loaded in a diamond anvil cell. The crystallographic orientations of interest also are shown.

c. *Elasticity of Al,Fe-bearing bridgmanite at high pressures and high temperatures (A. Kurnosov, H. Marquardt, T. Boffa Ballaran and D.J. Frost)*

Chemical substitutions in $MgSiO_3$ bridgmanite involving Al and Fe may contribute to seismic velocity anomalies observed in the Earth's lower mantle. The effect of these substitutions on the elastic properties of bridgmanite at high pressures and temperatures are, however, still a matter of debate and need to be better constrained experimentally in order to interpret seismic data. Simultaneous measurements of density and sound velocities have been made on different bridgmanite compositions at high pressures and room temperature using single-crystal X-ray diffraction and Brillouin spectroscopy (see annual reports 2012 and 2013) in order to obtain self-consistent data, which do not depend on a pressure scale. The same techniques can be applied to *in situ* high-pressures and high-temperature (*HP-HT*) studies. Absolute pressures can be obtained from experimental data collected along isotherms. Given the orthorhombic symmetry of bridgmanite, the density and sound velocities of at least two single crystals need to be measured. These two crystals need to have the appropriate orientations in order to constrain the full elastic tensor of the orthorhombic symmetry. Moreover, they should be double-side polished and held at exactly the same pressure and temperature for each data point. This can only be achieved when the two samples are loaded together in the same diamond anvil cell.

Two high-quality crystals of Al,Fe-bearing bridgmanite, *i.e.*, having relatively sharp reflection profiles, have been selected, oriented and mechanically double-side polished down to 15 µm. From each crystal, a circle of 100 µm in diameter has been cut using the FEI Scios focused ion beam (FIB) instrument. The two circles have then been cut in two semicircles (Fig. 3-4.3 left), which have been loaded in the diamond anvil cell (DAC) pressure chamber made of an indented Re gasket with a 240 µm hole (Fig. 3.4-3 right).

A heating element was prepared from Macor ceramic and Pt-wire. The dimensions of the heater are adjusted to fit perfectly around the diamond to provide uniform heating. The cell was loaded with Ne as the pressure-transmitting medium and density and sound wave velocities have been measured so far up to 6 GPa at room temperature for both crystals. As demonstrated in Fig. 3-4.3, the gasket hole is still large enough to ensure hydrostatic conditions. Moreover, by using the FIB we can accurately control the dimensions of the crystals, which need to be large enough to obtain high-quality data in a reasonable amount of time, yet small enough to reach pressures of the Earth's lower mantle.

Measurements at high temperatures will be performed while protecting the diamonds, gasket, and parts of the cell from oxidation with the atmosphere with a flow of inert Ar-H_2 mixture (2 % H_2).

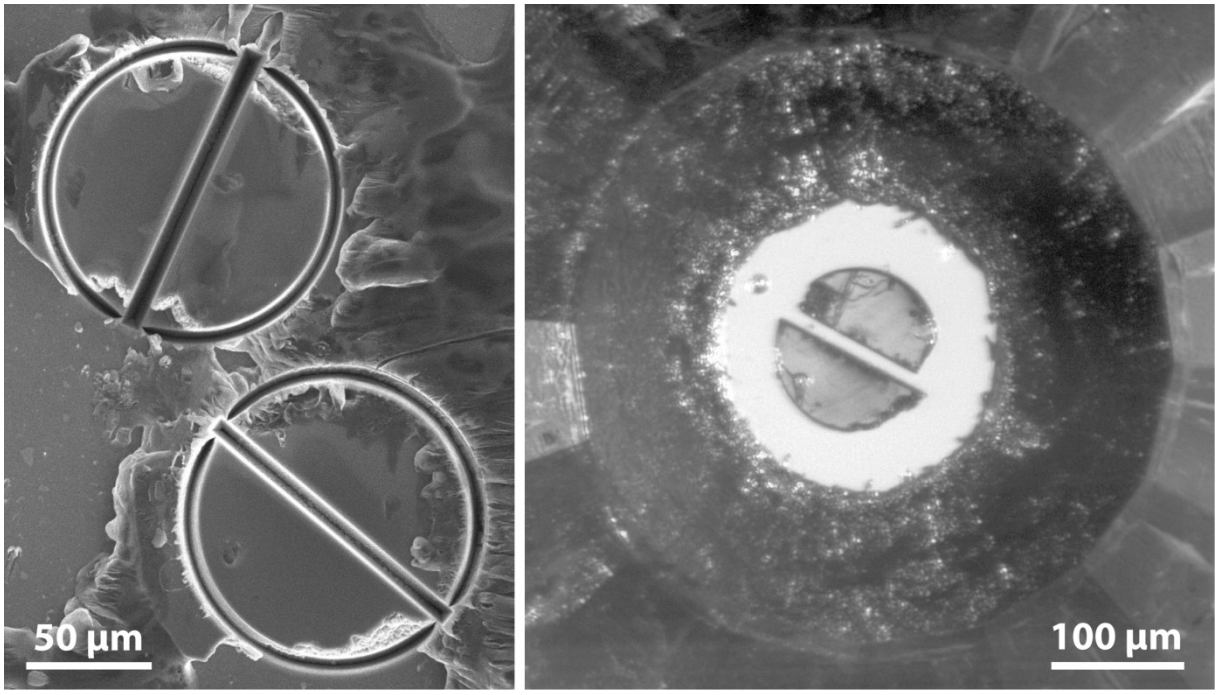

Fig. 3.4-3: FIB cut bridgmanite semicircles (left) with different orientations loaded in the DAC at P = 6 GPa (right). A ruby sphere is used as a reference for approximate pressure changes, however absolute pressure will be determined using the density and sound wave velocity measurements.

d. *P-V-Vp-Vs-T measurements of complex clinopyroxene solid solutions up to 1323 K and 12 GPa (C. Beyer and D.J. Frost, in collaboration with J. Chantel, W. Crichton and J. Guignard/Grenoble)*

Clinopyroxene (cpx) solid solutions constitute a substantial volume of the Earth's upper mantle. They are the major mineral fraction in basaltic systems and one of the most abundant phases in peridotitic systems. Over the pressure and temperature range of the upper mantle, cpx can incorporate a wide range of end-members from which diopside ($CaMgSi_2O_6$) and jadeite ($NaAlSi_2O_6$) are the most important. Currently very little is known concerning how elastic properties change within complex solid solutions. Previous studies appear to indicate that cpx elastic properties cannot be simply calculated by treating them as a diopside-jadeite binary. Possible candidates for influencing elastic properties in addition to the iron-bearing end-member include Ca-Eskola (vacancies) and Ca-Tschermak (tetrahedral Al).

One way to infer the chemical composition of the deeper mantle is to interpret seismic velocities in terms of mineral chemistry using experimentally obtained velocity data. The aim of this project, therefore, is to analyse the elastic properties of synthetic and natural omphacitic cpx with a basaltic composition. Such compositions also contain substantial proportions of the components CaEsk, CaTs, and hedenbergite. Elastic properties are determined by measuring the compressional (V_P) and shear (V_S) velocities at elevated pressures and temperatures. These properties can then be used to refine thermo-elastic equation of state parameters for describing the elastic properties of cpx as a function of pressure, temperature and composition. Ultimately, these data will be incorporated into a seismic model of the upper mantle to interpret seismic travel time observations.

Measurements have been conducted on two clinopyroxene solid solution compositions at the ESRF, Grenoble, in a multianvil apparatus using a 10/4 assembly. Both compositions contain ~ 7 mol. % CaTs and ~ 15 mol. % hedenbergite. Moreover, one sample also contains ~ 8 mol. % of vacancy-bearing CaEsk. The samples were heated with a graphite furnace. Temperature was controlled using a thermocouple, axially inserted into the octahedron. Pressure was determined using the equation of state of gold and MgO. Diffraction patterns were collected with a pinholed Bicron Tl:NaI scintillator coupled to adjustable collimating slits. The offset of the sample position was corrected with the lattice parameters of gold. Ultrasonic signals were generated using a $LiNbO_3$ piezoelectric transducer, which was mounted on a stress free polished corner truncation of one of the tungsten carbide (WC) cubes. A cylindrical buffer rod made of Al_2O_3 was used to acoustically couple the sample to the WC cube. The average round-trip travel time at each P-T step was calculated using the pulsed echo overlap method from the 40-55 MHz and 10-25 MHz region of the ultrasound signal. Two thin gold foils were placed as length markers above and below the sample. The sample length was monitored using high-resolution X-ray tomography. Figure 3.4-4 depicts the shear wave velocity measured for one of the samples up to 9 GPa and 1273 K. An increase of 1000 K in temperature is found to reduce the sound velocity by ~ 0.1 km/s.

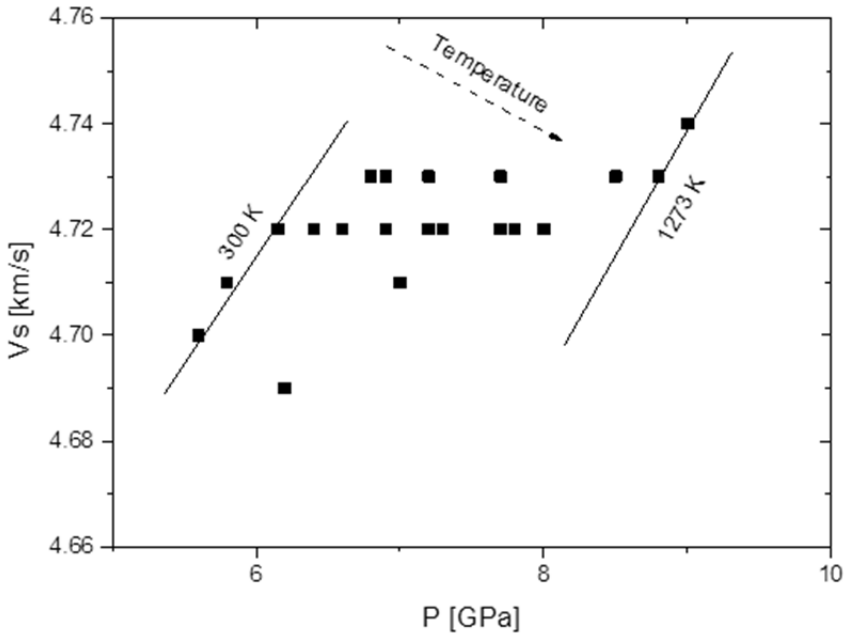

Fig. 3.4-4: Shear velocity as a function of pressure and temperature of sample RV03 containing equal amounts of CaTs and CaEsk.

e. *Single-crystal elasticity of majoritic garnets: stagnant slabs and thermal anomalies at the base of the transition zone (M.G. Pamato, A. Kurnosov, T. Boffa Ballaran, D.J. Frost, L. Ziberna/Bristol, M. Giannini and D.M. Trots, in collaboration with S.N. Tkachev, K.K. Zhuravlev and V.B. Prakapenka/Chicago, S. Speziale/Potsdam)*

The principal method for constraining the thermal and chemical structure of the Earth's mantle, and for tracing the chemical anomalies potentially caused by subduction, is the interpretation of seismic observations through phase equilibria and mineral physics models. In this context, knowledge of the elastic properties of garnet minerals as a function of pressure, temperature and composition is essential since they are major components of both mafic and ultramafic rocks in the upper mantle and transition zone. Moreover they are the main host minerals for Al_2O_3 and CaO throughout these regions. This study aimes to obtain, experimentally, the elastic properties of majoritic garnets and to use them to constrain the thermodynamic properties of garnets at the conditions of the Earth's upper mantle and transition zone.

The elastic properties of single crystals of majoritic garnet ($Mg_{3.24}Al_{1.53}Si_{3.23}O_{12}$ and $Mg_{3.01}Fe_{0.17}Al_{1.68}Si_{3.15}O_{12}$) have been determined by Brilluoin spectroscopy and X-ray diffraction up to ~ 30 GPa and ~ 600 K using an externally heated diamond anvil cell. The compressional, V_p, and shear, V_s, wave velocities obtained from the measurements have been fitted to a thermo-elastic, self-consistent model to constrain the thermodynamic properties of pyrope, almandine and a fictive cubic majorite garnet end-member. This enabled velocities and densities of garnet compositions in the system Fe-CMAS (CaO-MgO-Al_2O_3-SiO_2) to be calculated at mantle conditions according to the phase relations along a typical mantle

adiabat. These data were also used, together with additional literature data describing the elastic properties of wadsleyite, ringwoodite, stishovite, $CaSiO_3$ perovskite and bridgmanite, to calculate acoustic velocities of mafic, harzburgitic and lherzolitic bulk compositions in the Earth's transition zone and uppermost lower mantle between 480 and 780 km at 1673 K. A comparison between the calculated wave velocities and those obtained from seismic reference models is given in Fig. 3.4-5. Both V_s and in minor amount V_p for all three mantle lithologies appear lower than those obtained from the seismic reference models due to the presence of garnets. A better agreement between the thermodynamic and reference models is obtained by assuming temperatures lower than 1673 K at the base of the transition zone. In particular, for a pyrolitic composition, temperatures should be as low as 1073 K, whereas for harzburgitic composition temperatures should be just 200 K lower than the 1673 K adiabat. A plausible explanation for the presence of colder regions at the base of the transition zone may be the occurrence of large lateral cold anomalies resulting from the stagnation and flattening out of subducting slabs. The presence of these slabs, which have much lower temperatures than the surrounding mantle, might be able to lower the average mantle temperatures. The subduction anomalies would be expected to contain a large proportion of harzburgite in which, due to the lower temperatures, akimotoite should be present at the expense of garnet. Higher velocities expected for akimotoite would further help to explain the mismatch in calculated and observed V_s.

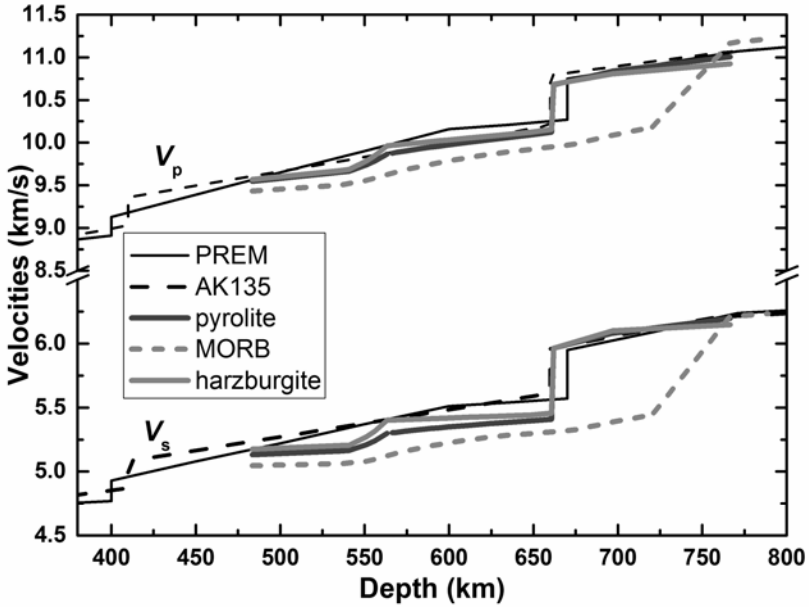

Fig. 3.4-5: Sound velocities for pyrolite (dark grey) harzburgite (grey) and MORB (dashed grey) compositions in the transition zone and uppermost lower mantle. The solid and dashed black curves show PREM and AK135 seismic reference models, respectively.

f. *Elastic properties of single crystal iron carbonate and implications for the deep Earth (C.A. McCammon, L.S. Dubrovinsky, V. Cerantola, I. Kupenko and R. Sinmyo; L.S. Ismailova/ Bayreuth; A. Kantor and A.I. Chumakov/Grenoble)*

The carbon cycle takes place not only on the Earth's surface, but also deep in its interior. But how much carbon gets subducted? Estimates suggest there may be vastly more carbon inside

the Earth than on its surface. Carbon is not easily incorporated into mantle phases, but instead occurs as accessory phases, most likely as carbonates. How can the abundance of carbonates in subducting slabs be determined? One possibility is by comparison of seismic data with laboratory measurements. Up to now, however, no elastic wave velocities have been measured for carbonates at mantle conditions. In particular, the high-spin to low-spin transition of Fe^{2+} in carbonates may influence elastic properties. As a preliminary step in the investigation, we have undertaken a study to measure the effect of pressure on the sound velocity of $FeCO_3$.

We synthesised both powder and single crystal $^{57}FeCO_3$ that were loaded into diamond anvil cells. Debye sound velocities were determined from Nuclear Inelastic Scattering (NIS) data collected at beamline ID18 at ESRF. Measurements at low pressure established the consistency of our NIS-derived sound velocities with values reported in the literature from Brillouin scattering. We also demonstrated the possibility to measure sound velocity anisotropy from different orientations of single crystals. The most remarkable result, however, was the profound change in the NIS data of $FeCO_3$ through the high-spin to low-spin transition (Fig. 3.4-6a) that caused a 17 % increase in Debye sound velocity (Fig. 3.4-6b). Preliminary high-temperature measurements using a portable double-sided laser heating setup showed similar behaviour at mantle temperatures. While $FeCO_3$ is only one end-member of mantle carbonates, the profound change in sound velocity coupled with an expected increase in anisotropy based on observations of other spin transitions provide a promising direction for detecting the presence of carbonate in slabs subducted into the lower mantle.

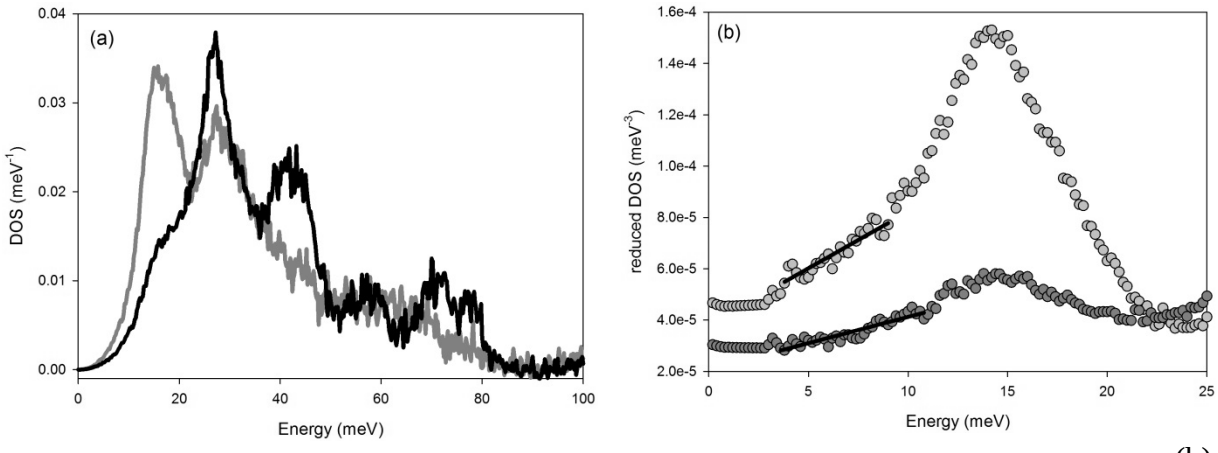

(a) (b)

Fig. 3.4-6: Effect of pressure on the properties of $FeCO_3$ derived from room temperature NIS data: (a) Partial density of states at 44 GPa (grey) (high-spin state) and 50 GPa (black) (low-spin state). (b) Reduced density of states of the high-spin state at 44 GPa (light grey, upper spectrum) and the low-spin state at 50 GPa (dark grey, lower spectrum). The zero intercepts of the solid lines are inversely proportional to the Debye sound velocities, indicating a 17 % increase from the high-spin to the low-spin state.

g. *Density of amorphous $MgSiO_3$ to lowermost mantle pressures (S. Petitgirard, R. Sinmyo, I. Kupenko and D.C. Rubie; W. Malfait/Zurich, L. Hennet/Orleans, D. Harries/Jena and M. Burghammer/Grenoble)*

Melting processes have been of crucial importance for the evolution and differentiation of the Earth throughout its history. Early in Earth's history, the formation of a magma ocean with depths of 1000 km or more facilitated the segregation of Earth's iron core. The possible concomitant formation of a deep Basal Magma Ocean (BMO) has been raised recently, and could have been caused by the accumulation of dense iron-rich silicate melt or by the melting at the base of the mantle due to the hot core. Tomographic images of the Earth reveal ultra-low velocity zones at the core-mantle boundary that could be attributed to dense melt pockets or remnant zones of the BMO. Unfortunately, measurements of amorphous silicate density over the entire pressure regime of the mantle are scarce and the density contrast between solid and liquid are difficult to assess due to the lack of such data.

Only few studies have reported density measurements of amorphous silicates at high pressures, and most limited to 60 GPa. High-pressure acoustic velocity measurements have been used to calculate the density of $MgSiO_3$ glass up to 30 GPa but exhibit a large discrepancy compared to recent calculations. SiO_2 glass was measured up to 55 GPa using the X-ray absorption method through the diamond anvils and very recently, X-ray diffraction has been used to infer the density of basaltic melt up to 60 GPa.

To improve upon these data, we have developed a new experimental setup that makes use of the absorption technique adapted to the confinement of the DAC to measure the density of $MgSiO_3$ glass up to 130 GPa. At ID13 beamline (ESRF, France), the sample contained in a beryllium gasket was irradiated with a micro-focus X-ray beam in two directions: perpendicular and parallel to the compression axis to obtain the absorption coefficient and density under pressure. Our data constrain the first experimental EoS for amorphous $MgSiO_3$ up to lowermost mantle pressures (Fig. 3.4-7a) and are in good agreement with a recent molecular dynamics (MD) simulation for the same system at ambient temperature (Fig. 3.4-7a). At 130 GPa, we found a density contrast of 1.8 % between the crystal and the amorphous phase of $MgSiO_3$, while according to Brillouin measurements the difference would be on the order of 25 to 30 %.

Our data can be split in two domains and constrained with two 3rd order Birch-Murnaghan EoS. At low pressure, below 30 GPa, the glass is extremely compressible with K_0 = 19 GPa, while at higher pressure the EoS gives a K_0 of 80 GPa, which is still three times lower than the value for $MgSiO_3$ bridgmanite. Using the thermal expansion coefficient and bulk isothermal modulus we can determine the density of amorphous $MgSiO_3$, and potentially melts, for different isotherms (Fig. 3.4-7b). Our results show that amorphous $MgSiO_3$ at high pressure is very dense with density values very close to its crystalline phase.

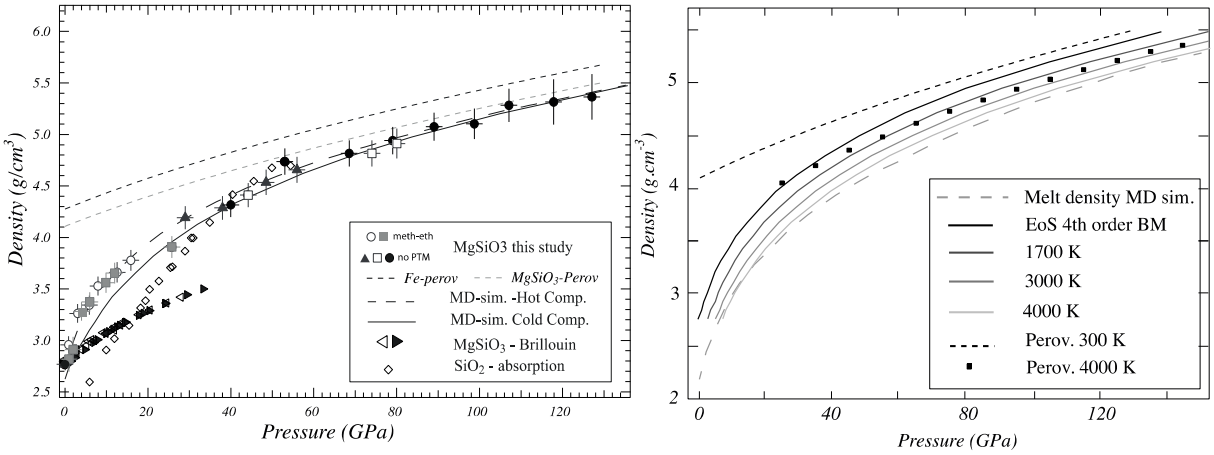

Fig. 3.4-7: a) Pressure-density results from 5 different runs and compared with other literature data based on MD-simulation for $MgSiO_3$ glass (black curve and long-dashed black curve), Brillouin data for $MgSiO_3$ glass (triangles) and SiO_2 glass using absorption technique (diamonds). b) Calculations of density of amorphous $MgSiO_3$ along different isotherms from 300 K (continuous black curve) to 4000 K (continuous light grey) and compared with MD-simulation results for melt densities at 4000 K (long-dashed grey curve). For comparison, the density of crystalline $MgSiO_3$ perovskite at 300 K (doted black curve) and 4000 K (squares) are also reported.

h. *Change of electrical and elastic properties of metals upon melting (F. Wagle, G. Steinle-Neumann and V. Vlček)*

Electrical and thermal conductivities are important parameters for the Earth's core in determining fundamental timescales for diffusion of heat and the Earth's magnetic field. Several numerical geodynamo models predict a strong influence of the magnetic diffusion timescales in both inner and outer core on the field reversal frequency and on the degree of stability the inner core imparts on the geodynamo. Ambient pressure studies reveal a discontinuous increase in both electrical resistivity, ρ_{el}, and isothermal compressibility, β_T, upon melting, which can have important implications for electronic transport quantities at the inner core boundary (ICB) of differentiated bodies. According to Ziman's theory, resistivity in a metal is mainly caused by scattering of quasi-free electrons by ionic (pseudo-)potentials $\mathcal{U}_k$ and can be computed via:

$$\rho_{el} = \frac{3\pi m^* n}{\hbar^3 e^2 {k_F}^2} \langle S(k)|\mathcal{U}_k|^2\rangle, \quad (1)$$

with

$$\langle S(k)|\mathcal{U}_k|^2\rangle = \frac{1}{4k_F}\int_0^{2k_F} S(k)|\mathcal{U}_k|^2 k^3 \,\mathrm{d}k. \quad (2)$$

where m^* is the effective electron mass, n the density of ions, e the elementary charge, k_F the Fermi wavenumber and $S(k)$ the static ion-ion structure factor. Thus, the increase of electrical resistivity upon melting occurs due to a sharp transition from an ordered to a disordered

structure, which is reflected by a change in the shape of $S(k)$. Assuming that values in the long wavelength limit are predominant to first order, Ziman related the resistivity jump to the change in $S(0)$ upon the solid-liquid phase transition:

$$\frac{\rho_{el}^{liq}}{\rho_{el}^{sol}} \simeq \frac{S(0)^{liq}}{S(0)^{sol}}. \tag{3}$$

The compressibility, β_T is related to the thermodynamic limit of the structure factor based on fluctuation theory

$$\lim_{k\to 0} S(k) = \rho k_B T \beta_T, \tag{4}$$

with density ρ and Boltzmann constant k_B; consequently:

$$\frac{\beta_T^{liq}}{\beta_T^{sol}} \simeq \frac{S(0)^{liq}}{S(0)^{sol}} \quad \rightarrow \quad \frac{\beta_T^{liq}}{\beta_T^{sol}} \simeq \frac{\rho_{el}^{liq}}{\rho_{el}^{sol}} \rightarrow \left(\frac{\beta_T^{liq}}{\beta_T^{sol}}\right) \Big/ \left(\frac{\rho_{el}^{liq}}{\rho_{el}^{sol}}\right) \simeq 1 \tag{5}$$

Here, we present a survey of experimental data reported in the literature for the quantities ρ_{el} and β_T of different metals just above and below their melting point to assess whether their ratio is close to unity (Eq. 5) and therefore examine to which degree Ziman approximation holds.

The approximation used in Eq. (3) is fairly crude, since the reciprocal space integral (Eq. 2) has been approximated by the integrand value at $k \rightarrow 0$. Nevertheless, the experimental values for most metals yield a ratio reasonably close to the theoretically expected unity, as illustrated in Fig. 3.4-8. We observe agreement for the alkaline and the alkaline earth metals, as well as for Al, which is the prototype of a simple metal. The theory also works well for some free-electron-like metals (*e.g.*, Cu, Ag and Au in group 11), while it fails completely to represent other metals, such as Hg, Sb and Bi. A striking feature is that Ziman's approach holds very well for iron. Since all data points are all taken at ambient pressure, we must assume at this point that Eq. (5) remains valid at high *P* and *T* in order to apply it to planetary interiors. This assumption is justified, if ρ_{el} and β_T in both the solid and the liquid phase decrease by the same factor with increasing pressure. This appears to be the case for iron up to 5 GPa, as measured in previous experiments. Assuming that it continues to do so up to the pressures of the Earth's core, we can use the change of β_T at the ICB known from seismic reference models – such as PREM –, on the one hand, and the estimate $\rho_{el}^{liq} \approx 61\,\mu\Omega \cdot \mathrm{cm}$ from computational studies, on the other hand, to infer the resistivity in the solid inner core. Our value of $\rho_{el}^{sol} \approx 59\,\mu\Omega \cdot \mathrm{cm}$ is consistent with previously reported results from a computational study on the resistivity of ε-iron at conditions of the ICB ($\approx 57\,\mu\Omega \cdot \mathrm{cm}$). By way of applying a Bloch-Grüneisen model to our approach, we can determine the *P*-*T* dependence of ρ_{el} along the melting curve of iron and use this to infer resistivities for both the solid and liquid portions in the iron cores of other planets.

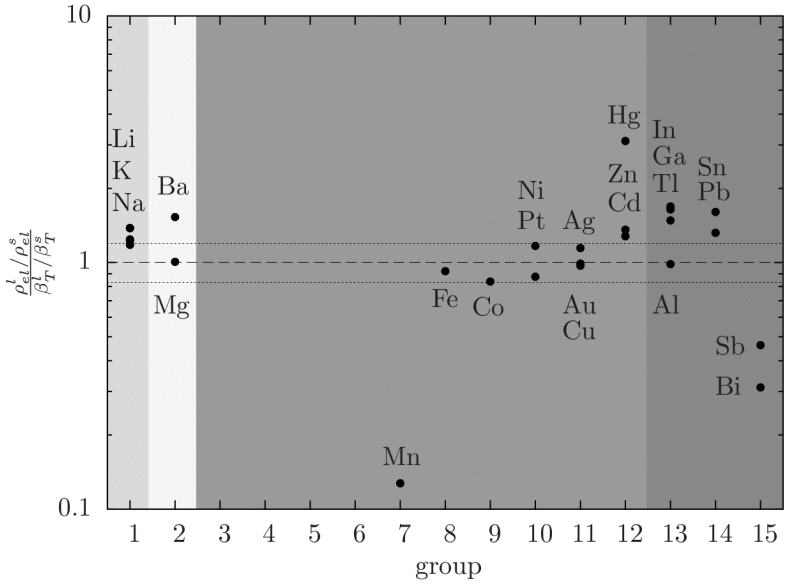

Fig. 3.4-8: Dimensionless ratio of electrical resistivity and β_T for a number of metals, as a function of their group in the periodic table. Measurements are taken from the literature at ambient pressure slightly above and below the melting point. Eq. (5) implies a ratio of 1 (dashed line).

i. *Valence state of Ti in natural hibonite: Implications for the oxygen fugacity in the Solar Nebula (M. Giannini and T. Boffa Ballaran, in collaboration with F. Langenhorst/Jena)*

To understand the evolution of our Solar System, the physical and chemical conditions at the beginning of its history need to be known. It is therefore not surprising that major efforts are underway to analyse meteorites, the oldest objects in our hands. In particular, carbonaceous chondrites are of interest because they represent the most primitive and pristine class of meteorites. Among the various components of chondrites CAIs (Calcium-Aluminium-rich inclusions) are considered the oldest. They contain high-temperature condensates such as hibonite ($Ca[Al,Ti,Mg,Si]_{12}O_{19}$) and Ti-rich clinopyroxene ($Ca[Mg,Al,Ti][Si,Al]_2O_6$). The Ti^{3+} content of these minerals has been correlated with the oxygen fugacity (fO_2) at the time of their formation, and represents the best estimate of the oxygen fugacity conditions at the early stages of the Solar Nebula. However, these previous spectroscopic and chemical studies reported quite discordant results with hibonite suggesting much higher oxygen fugacity conditions than those obtained from clinopyrones. Since the oxidation state of any cation in a mineral depends not only on temperature, pressure and oxygen fugacity but also on the phase assemblage (*i.e.*, the activities of all components) and the crystal structure, we have undertaken a careful study to correctly determine the cation distribution of Ti in synthetic and meteoritic samples to be used to quantify their Ti^{3+}/Ti_{tot} ratios from spectroscopic data.

We have developed a novel sol-gel synthesis procedure for obtaining single-crystals as well as polycrystalline samples of hibonite containing Ti in different oxidation states. These samples were characterised by X-ray diffraction (XRD), microprobe analysis and Energy Electron

Loss Spectroscopy (EELS) in order to obtain a specific calibration for quantifying the amount of Ti^{3+} in hibonite. This calibration has now been used to constrain the Ti^{3+}/Ti^{4+} ratio of grains of natural hibonites found in seven different CAIs of several carbonaceous chondrites having low degree of alteration.

Natural hibonite grains have been extracted from their host meteorites and thinned down to electron transparency for TEM observation using the Focused Ion Beam (FIB) technique. EEL spectra have been then collected on these lamellae of natural hibonite and the Ti^{3+}/Ti^{4+} ratio has been determined according to the method developed at BGI (see annual report 2013). The results are shown in Fig. 3.4-9 on the appropriate Ti^{3+}-fO_2 relationship which takes into account the Ti^{tot}/Mg content of these crystals. The corresponding oxygen fugacities obtained from these natural hibonites cover a wide range between log fO_2 = -14 and log fO_2 = -0.5, thus suggesting that these materials have been exposed during their formation to oxygen fugacities several orders of magnitude more oxidising than expected for the Solar Nebula. Transient

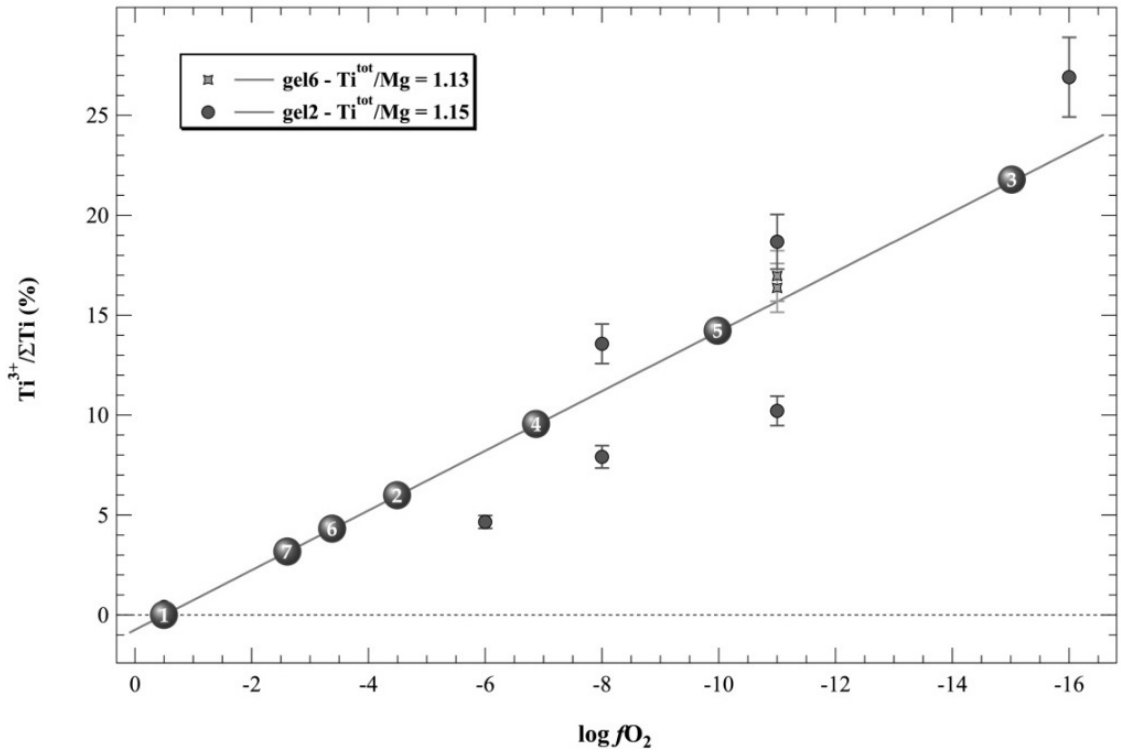

Fig. 3.4-9: Ti^{3+}-fO_2 relationship for synthetic hibonite samples (full symbols and solid line) together with the measurements carried out on natural hibonites (numbered bullet points). 1 = Dar al Gani 203 (CO3), 2 = Acfer 182 (CH3), 3 = Acfer 182 (CH3), 4 = El Djouf 001 (CR2), 5 = Acfer 059 (CR2), 6 = Acfer 094 (C-unique), 7 = Acfer 094 (C-unique).

heating events that triggered the formation of CAIs were likely associated with locally oxidising environments due to low-pressure vaporisation and dissociation of lithophile elements oxides (*e.g.*, MgO and SiO_2). The oxygen fugacity recorded by a refractory phase

like hibonite likely reflects these transient heating events. Clinopyrones, on the other hand, condensed at lower temperatures than hibonite and therefore were not exposed to the transient high-temperature events but likely have recorded the reducing conditions predicted by thermodynamic calculations of Solar Nebula condensationat. A re-equilibration of hibonite to the restored more reducing condition did not occur due to the strong effect of its crystal chemistry in stabilising the Ti^{4+} - Mg^{2+} couples.

j. *The most frequent interfaces in olivine aggregates (K. Marquardt, in collaboration with G.S. Rohrer and B. Lin/Pittsburgh; L. Morales and E. Rybacki/Potsdam)*

Many properties of rocks are controlled by the network of their internal surfaces, the area distribution of grain boundaries and their properties. A major unknown parameter is the area formed by different grain surfaces and whether or not this can be approximated as being isotropic. The storage of incompatible elements on grain boundaries and their diffusion along them, which is order of magnitude faster compared to lattice diffusion, is a result of the strongly differing grain boundary structures that depend on their orientation and properties. Understanding the distribution of different grain boundaries can significantly enhance predictions of grain boundary controlled processes, for example melt propagation, wetting, segregation or retention. Here we investigated a synthetic hot isostatically pressed forsterite aggregate as a first approximation for dunites (Fig. 3.4-10a).

We used stereology analyses of electron backscatter diffraction (EBSD) maps (Fig. 3.4-10b) extracting grain boundary traces to measure the grain boundary plane area for our polycrystalline olivine aggregate. To apply stereology on 2D sections, samples with no or minor lattice preferred orientation (LPO) are needed to provide a sufficiently random distribution.

Our investigations of a hot isostatically pressed forsterite reveal an anisotropic area distribution of forsterite grain boundaries (Fig. 3.4-10c). The grain boundary plane distribution shows that grain boundary planes of high-angle grain boundaries are terminated by low-index planes (Fig. 3.4-10c). The {100} surfaces occur more frequently than {010}, whereas {001} displays a normal distribution. No preference for special grain boundaries of any type is observed. Low index grain boundary planes occur more frequently than random grain boundary planes. Since the misorientation distribution between neighbouring crystals is random, the energy minimization is mainly related to reducing the surface energy of each individual crystal, thereby forming grain boundaries of low energy surfaces, rather than due to the rotation of the lattice of adjacent crystals to produce higher frequencies of special misorientations as suggested by the coincidence site lattice (CSL) theory.

Furthermore, energy minimization seems to occur by faceting the grain boundary planes into low-index surfaces that are also the low energy surfaces of single crystals.

In the future, the results of this work can lead to refined models of melt segregation, percolation and retention.

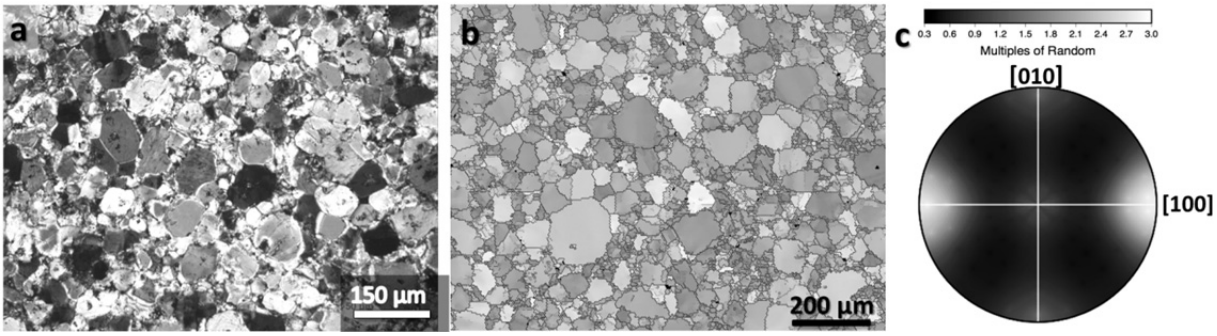

Fig. 3-4.10: Hot isostatically pressed forsterite. a) Micrograph of a thin section, using crossed Nichols. b) EBSD map. The gray level varies with crystal orientation. c) Distribution of grain-boundary planes averaged over all misorientations. Grain boundary planes with (100) surfaces occur nearly three times more than the area of random orientations. (010) surfaces are 1.5 times more frequent than random orientations and (001) surfaces display a random frequency.

3.5 Fluids, melts and their interaction with minerals

Volcanic eruptions release large amounts of water, carbon dioxide, hydrogen chloride and sulfur dioxide to the atmosphere. The total fluxes of HCl from volcanoes are so large that they could severely damage the stratospheric ozone layer. However, it is unclear how much of the HCl released by volcanoes actually reaches the stratosphere. The first contribution in this chapter shows that adsorption on the surface of volcanic ashes may under some circumstances remove most of the HCl from the eruption column. Interestingly, HCl adsorption increases with temperature, while it was previously found that SO_2 adsorption decreases with temperature. This means that HCl and SO_2 are fractionated during adsorption and the fractionation factor changes by five orders of magnitude over just 300 K. This effect needs to be taken into account when deriving volcanic gas compositions from analyses of adsorbates on ash surfaces. In 2014, the Bárðarbunga fissure eruption on Iceland received considerable media attention. A short contribution in this annual report describes the first measurements of the H_2O and CO_2 content of the magma before and after degassing; the fluid inclusion data show that degassing of the magma must have started at a depth of about 9 km and the magma can therefore not originate from a shallow upper crustal magma chamber, as has been proposed. A third contribution in this annual report attempts to quantify the amount of sulfur that may be released by subduction zone magmas. Here, anhydrite ($CaSO_4$) may lock up most of the sulfur and make it unavailable for rapid degassing. A new model of anhydrite solubility in magmas allows full quantification of this effect. Model calculations for the 1991 Pinatubo eruption show that sulfur degassing is enhanced by some depolymerization of the melt, which destabilizes anhydrite. A volcanic gas species that has received little attention so far is carbon monoxide, which is usually only a trace component in terrestrial volcanic gases. However, carbon monoxide may play an important role in planetary degassing under reduced conditions, *e.g.*, on the Moon. A contribution therefore looks in detail at the speciation of carbon monoxide in silicate melts and glasses; it is shown that there is no strong interaction of carbon monoxide with iron in the melt, as previously proposed.

Forecasting volcanic eruptions requires a detailed knowledge of the volume, location and water content of the magma in a reservoir below the surface. Since silicate melts are relatively good electrical conductors, and since their conductivity greatly increases with water content, magneto telluric methods that measure electrical conductivity in crust and upper mantle have become a standard tool for studying active volcanoes. These methods require experimental calibrations of melt conductivity as function of pressure, temperature and water content. Two contributions in this annual report therefore provide new data on the conductivity of rhyolitic and dacitic melts. The data are applied to constrain the magma storage conditions below three volcanoes, Uturuncu in Bolivia, Usu in Japan, and Mt. St. Helens in the USA.

Diffusion in silicate melts controls the timescales of many geologic processes. A contribution in this annual report studies the pressure dependence of diffusion coefficients in silicate melts and also in molten iron, in order to better understand the timescales and processes of core

formation in planets. A complex dependence of the Si self-diffusion coefficient on pressure is observed, which is likely related to coordination changes in the melt around 10 GPa.

The last two contributions in this section of the annual report look at the storage of water and hydrogen in the mantle. Usually, hydrogen is dissolved as OH groups in mantle minerals. However, under very reducing conditions molecular H_2 may become an important species in minerals. Indeed, it seems that H_2 has a detectable solubility in olivine and pyroxenes, although it is orders of magnitude below the water/OH solubility under more oxidizing conditions. These data suggest that hydrogen may only remain in the silicate portion of a planet, if rather oxidizing conditions prevailed during accretion. The last contribution in this chapter provides new data on water solubility in garnet, stishovite and in bridgmanite, the most important phase of the lower mantle.

a. *The adsorption of HCl on volcanic ashes (X. Gutierrez and H. Keppler)*

The destruction of ozone in the stratosphere is catalyzed by chlorine compounds. Since hydrogen chloride (HCl) is often a major component of volcanic gases, explosive volcanic eruptions could potentially affect stratospheric ozone. However, it is uncertain how important this effect is in reality because a number of processes could reduce the fraction of HCl in the eruption column that actually reaches the stratosphere. One of these processes is the adsorption of HCl on the surface of volcanic ashes.

In order to constrain the fate of HCl in a volcanic eruption column, we have therefore studied the adsorption of HCl on volcanic ashes over a temperature range from -76 to +150 °C, relevant for a dilute volcanic plume in some distance from the vent. As a proxy for volcanic ash, synthetic glass powders of rhyolitic, dacitic and andesitic composition were used. The specific surface of the glass powders was determined by measuring the BET adsorption isotherm of krypton and was found to be in the range of 1-2 m^2/g. HCl adsorption was measured by observing the decrease of HCl pressure due to adsorption in a system with known volume.

Figure 3.5-1 shows adsorption isotherms of HCl on dacite glass at different temperatures. Adsorption was found to be nearly completely irreversible, *i.e.*, HCl remained adsorbed on the surface when the pressure in the system was reduced to zero mbar. As is obvious from Fig. 3.5-1, adsorption strongly increases with temperature. This behaviour is unusual, but is has been observed before for chemisorption in some systems. Probably, adsorption of HCl on the glass requires some activation energy and at low temperatures, only sites with low activation energy are available for adsorption, while at higher temperatures, more sites become active. The dependence of HCl adsorption on HCl partial pressure and temperature can be described by the following equation:

$$\ln c_{HCl} = 1.26 - 75.28/T + 0.27 \ln p$$

where c_{HCl} is the equilibrium surface concentration in mg/m^2, T is temperature in Kelvin, and p is the partial pressure of HCl in mbar.

The extent of HCl adsorption in volcanic plumes depends mostly on the initial HCl concentration in the gas, the specific surface (or grain size) of the ash, and the temperature in the plume. The data presented here show that for a specific surface of the ash larger than 0.5 m^2/g, HCl will essentially be completely removed from the plume. For more coarse-grained ash, the process is less efficient, but HCl adsorption is still significant.

The analysis of volatiles adsorbed on ashes from volcanic eruptions is very often used to infer volcanic gas compositions. In relating measured concentration to gas phase compositions, it is usually assumed that that various gas species are equally strongly adsorbed. However, in this study we found that HCl adsorption increases with temperature, while the adsorption of SO_2 was previously observed to decrease with temperature. Therefore, adsorption should fractionate SO_2 from HCl, with the fractionation factor being strongly temperature dependent. In Fig. 3.5-2, we show the ratio of HCl and SO_2 adsorbed on dacitic ash in equilibrium with a gas phase containing equal molar fractions of both gases. Over a range of 300 °C, the fractionation factor varies by five orders (!) of magnitude. Obviously, many volcanic gas compositions derived from the analyses of adsorbates on ashes must be severely in error, since they did not take this effect into account.

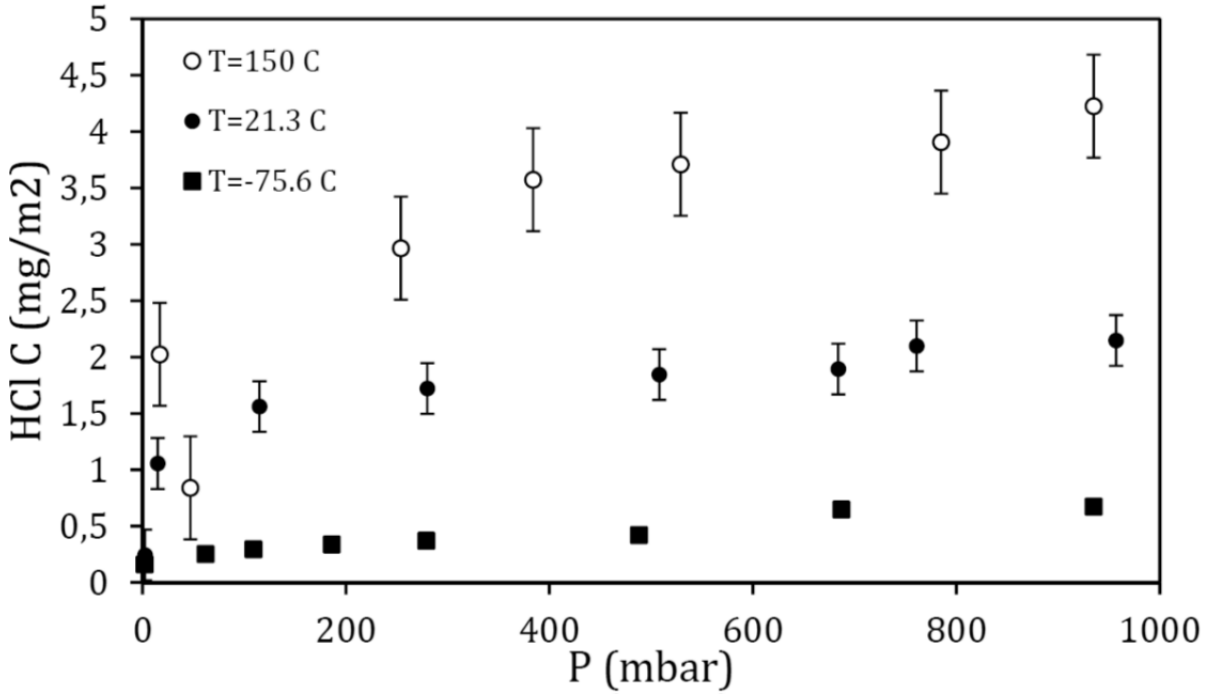

Fig. 3.5-1: Adsorption isotherms of HCl on dacitic glass powders at different temperatures.

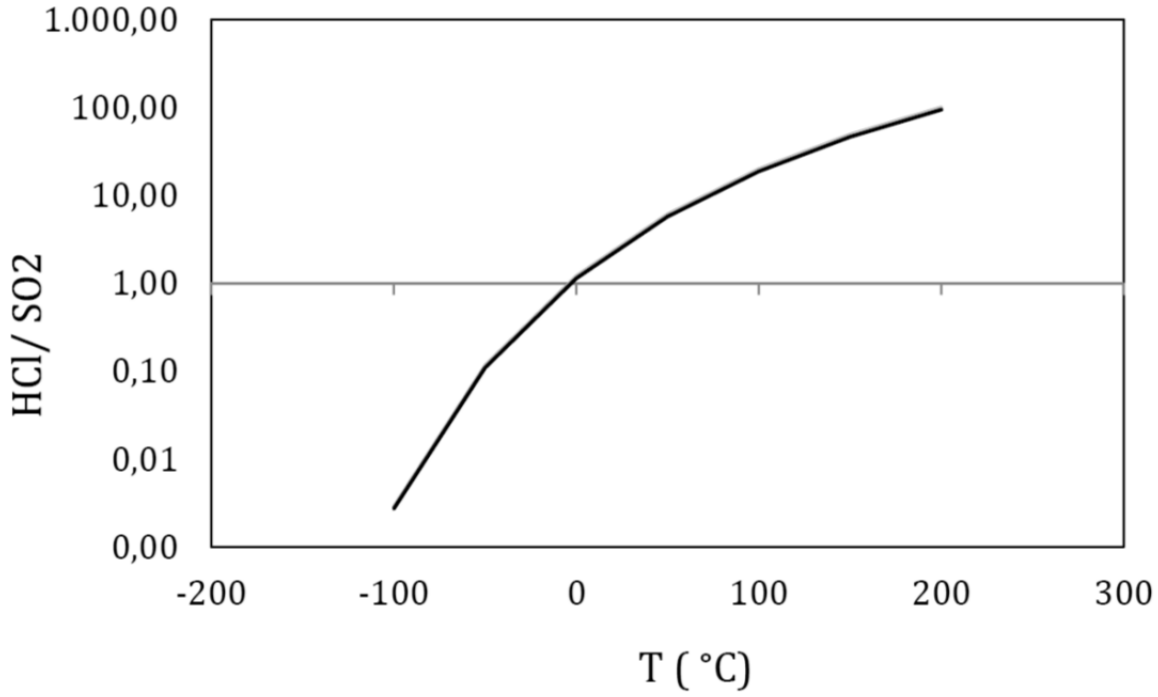

Fig. 3.5-2: Calculated ratio of HCl/SO_2 adsorbed on the surface of dacitic ash in equilibrium with a volcanic gas containing an equal molar fraction of HCl and SO_2.

b. *Volatile budget of the on-going Bárðarbunga fissure eruption on Iceland (E. Bali/Reykjavík and Bayreuth)*

Following two weeks after an intense earthquake swarm coupled with approximately 60 cm E-W extension across the volcanic zone north of Vatnajökull glacier, a fissure eruption started on 29th of August 2014 in the Bárðarbunga volcanic system. The area is the part of the Northern Volcanic Zone of Iceland and is characterized by eruptions of tholeiitic volcanic rocks. The continuing eruption produces lava fountains and a lava field associated with minor tephra fallout. The produced lava is almost aphyric, containing approximately 1 vol. % of plagioclase and minor olivine and clinopyroxene phenocrysts. Volumetric estimates suggest that more than 1 km^3 lava has been extruded, which makes this eruption the largest in Iceland in the last 150 years.

In order to constrain the volatile budget of the eruption, rapidly cooled tephra was collected on 31st of August and 4th and 8th of September from the vicinity of the fissure. Plagioclase and olivine phenocrysts were handpicked from these eruptive products and doubly polished. Phenocrysts contain glassy silicate melt inclusions with or without a fluid bubble as well as free fluid inclusions. H_2O and CO_2-contents of the glass were analyzed by FTIR spectroscopy whereas the fluid phase and the individual fluid inclusions were investigated by Raman spectroscopy. The H_2O-content of the studied melt inclusions varies between 0.1 and 0.5 wt. % whereas the CO_2-contents range from below detection limit to 900 ppm, indicating various

entrapment conditions after fluid saturation. Groundmass glass contains 0.1 wt. % of H_2O and no CO_2. According to the Raman spectra, individual fluid inclusions contained only CO_2. In these inclusions CO_2-density can be determined by the split of the CO_2 Fermi diad. The highest determined CO_2-density was 0.642 g/cm^3. At a temperature of 1170 °C, which is assumed to be the equilibrium temperature of the basalt based on various geothermometers, this CO_2-density corresponds to approximately 3 kbar entrapment pressure (~ 9 km entrapment depth). This means that the basalt became fluid saturated in mid-crustal levels, and it cannot be derived from a shallow crustal magma chamber (of 3 to 5 km depth) as suggested by some recent geophysical models. Taking into account the current estimation of extrusion rate (which seems to be constant after the first few days of the eruption) the estimated CO_2 output by this eruption is 500 kg/sec.

c. *Anhydrite solubility in differentiated arc magmas (M. Masotta and H. Keppler)*

Volcanic eruptions have a major effect on Earth's climate. Over long geologic timescales, climate is largely controlled by atmospheric CO_2 levels, which are maintained by the balance between CO_2 recycling in subduction zones and CO_2 release from volcanic activity. On short timescales, however, individual eruptions can cause distinct changes in surface temperature by injecting large amount of sulfur in the stratosphere. Sulfur species are photochemically oxidized to sulfate aerosols that backscatter the incoming solar radiation and therefore cool the Earth's surface. There appears to be a good correlation between the sulfur yield of major explosive eruptions and global surface temperatures for the last centuries. Global cooling has been observed in several years following major explosive eruptions in the historical record, the best-documented case probably being the 1991 Mt. Pinatubo eruption.

The behaviour of sulfur during an eruption is mainly controlled by two factors: (1) the partitioning of sulfur between the silicate melt and the fluid phase, and (2) the stability of sulfur-bearing minerals (mostly pyrrhotite FeS and anhydrite $CaSO_4$). These minerals may sequester considerable amounts of sulfur, making it unavailable to partition in the fluid phase at the eruptive timescale. Understanding the stability of these minerals has therefore important implication in determining the sulfur budget in magmas.

In this study, we investigated the stability of anhydrite in differentiated arc magmas. Anhydrite is commonly observed as accessory mineral in the eruptive products of sulfur-rich eruptions. The solubility product of anhydrite was examined in experiments using cold-seal pressure vessels at 2 kbar over a range of temperatures (800 to 1000 °C) and oxygen fugacities (0.5 log units above NNO to HM). The solubility product of anhydrite ($K_{SP} = X_{CaO}*X_{SO3}$) was found to increase with temperature and melt water content, whereas it decreases with the increasing degree of melt polymerization (decreasing nbo/t). Our new data as well as data from literature can be accurately described by the following regression equation (see Fig. 3.5-3a):

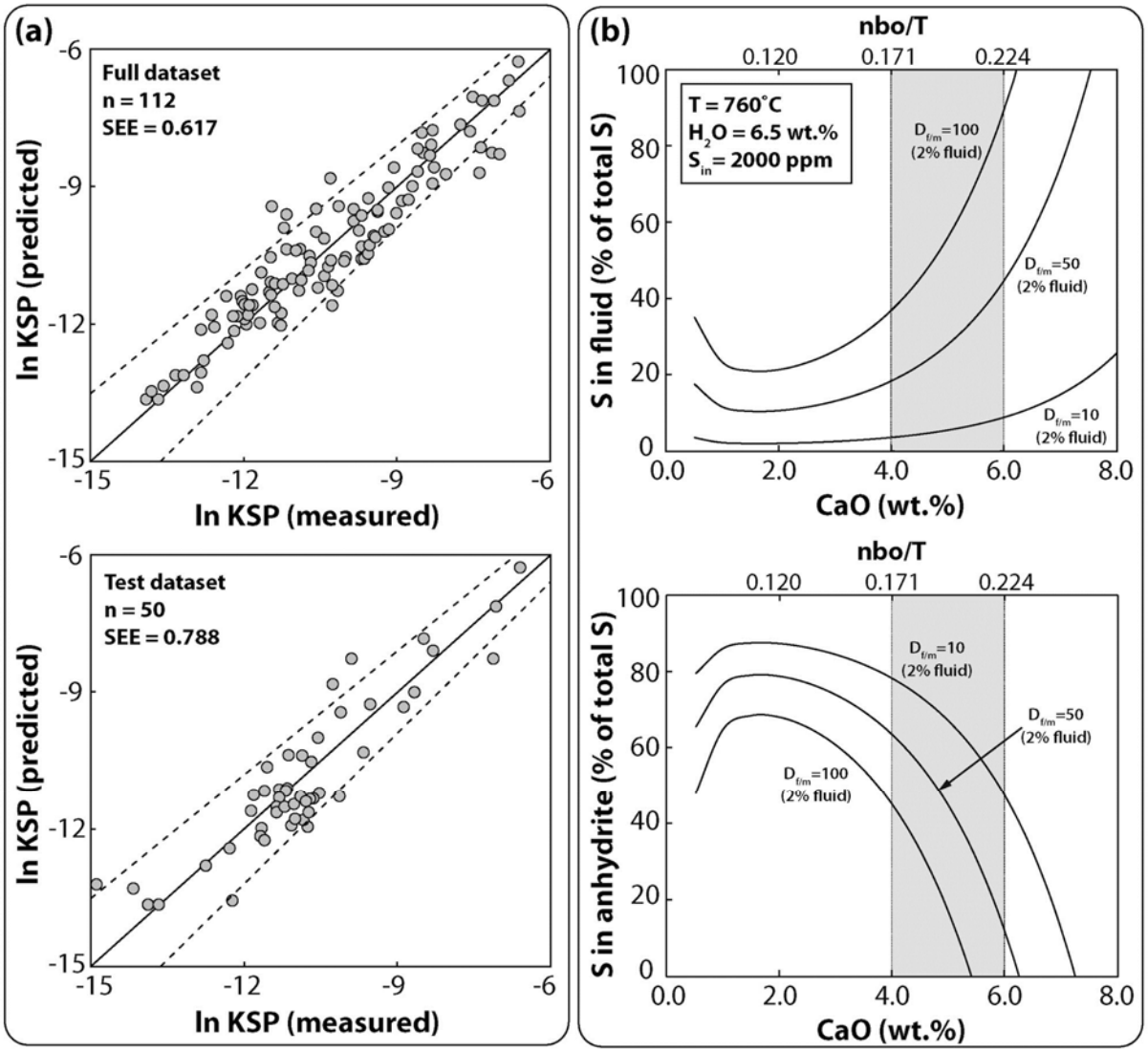

Fig. 3.5-3: (a) Calibration and test of the regression equation for the solubility product K_{SP} of anhydrite. (b) Calculation of the sulfur budget in Mt. Pinatubo dacite at 760 °C; the shaded area indicates the average CaO content of the Mt. Pinatubo dacite.

$$\ln K_{SP}^{Anhydrite} = 6.49 - 74.9\frac{nbo}{t} - 2.40\frac{10^4}{T(^\circ K)} + 10.2\frac{nbo}{t}\frac{10^5}{T(^\circ K)} + 0.39 \cdot H_2O(wt.\%)$$

We used our model to estimate the sulfur yield of some recent volcanic eruptions. The sulfur yield of the 1991 Mt. Pinatubo eruption was unusually large because of the high solubility of anhydrite (Fig. 3.5-3b). In general, high sulfur yields are expected when anhydrite solubility in the melt is high, *i.e.*, for somewhat depolymerized melts. For rhyolitic systems, most of the available sulfur will be locked up in anhydrite, so that even very large eruptions may only have a small effect on global surface temperatures. Our model therefore allows improved predictions of the environmental impact of explosive volcanic eruptions.

d. *The speciation of carbon monoxide in silicate melts and glasses (T. Yoshioka, C.A. McCammon, S. Shcheka, and H. Keppler)*

In terrestrial magmas, carbon is mostly dissolved as carbon dioxide and/or carbonate; as such, it plays an important role in melting processes in the mantle and in volcanic degassing. Carbon monoxide is usually only a trace species in volcanic gases and therefore, the solubility of carbon monoxide in silicate melts is poorly studied. However, under more reducing conditions than on the present-day Earth, *e.g.*, during magmatic activity on the Moon or in the very early, Hadean Earth, carbon monoxide may have been an important carbon species in magmas. Accordingly, the dissolution mechanism of carbon monoxide in silicate melts has recently received considerable attention and it has been suggested that a band seen near 2110 cm^{-1} in the Raman spectrum of some carbon-saturated glasses may be due to a distinct iron pentacarbonyl $Fe(CO)_5$ species. This could have very important geochemical consequences, as it would imply a strong coupling between the behaviour of iron and carbon under reducing conditions.

We have investigated the solubility mechanism of carbon monoxide in silicate melts by measuring the Raman, infrared, and ^{57}Fe Mossbauer spectra of carbon-saturated, reduced silicate glasses. We studied both Fe-bearing glasses with a composition close to a Lunar basalt, and otherwise identical glasses in which the FeO was completely replaced by a mixture of MgO and CaO. The Raman spectra of a Fe-bearing basaltic glass is shown in Fig. 3.5-4.

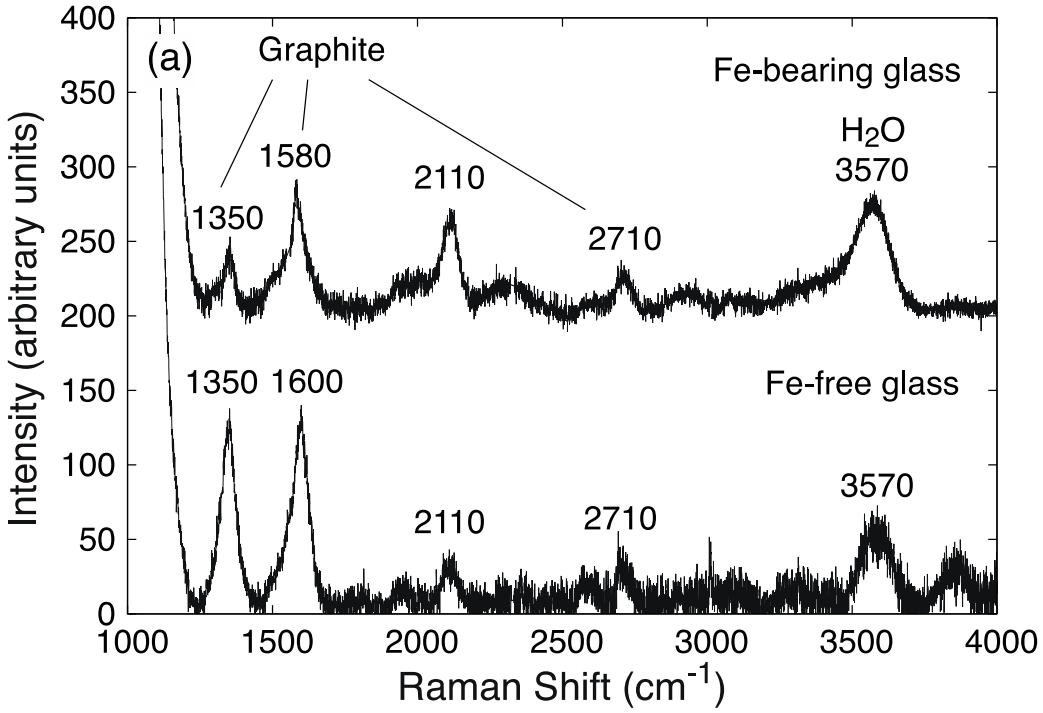

Fig. 3.5-4: Raman spectra of carbon-saturated, reduced glasses, with and without iron. Note that the band at 2110 cm^{-1}, assigned to some CO species, occurs in both spectra.

The glass does indeed show a prominent band at 2120 cm^{-1}, very close to the band that was previously assigned to the $Fe(CO)_5$ species. However, we observed the same band also in the Raman spectrum of the corresponding Fe-free glass. Similarly, a peak near 2210 cm^{-1} in the infrared spectrum, which was previously also assigned to some iron carbonyl species, is seen in both the Fe-bearing and Fe-free glass. Moreover, the ^{57}Fe Mössbauer spectra of the glasses do not show any component near zero isomer shift, as expected for carbonyls. These observations together rule out the presence of any iron carbonyl species in the glasses. However, the observed peak positions in the Raman and infrared spectra of the carbon-saturated glasses are clearly different from that of CO gas (2143 cm^{-1}), raising the question whether they can still be assigned to carbon monoxide or perhaps to some other species. A survey of the literature on CO absorption on various oxide surfaces shows that comparable shifts in infrared and Raman frequency are commonly observed and are likely caused by weak interactions between the CO dipole and the electrical fields induced by the host matrix. Accordingly, we conclude that all the bands in the 2100-2200 cm^{-1} range in both the Raman and infrared spectra are likely due to carbon monoxide molecules experiencing some weak interaction with the matrix. At high temperature in the melt, these interactions likely disappear and only one species of carbon monoxide is present. The solubility of reduced carbon in silicate melts is likely controlled by the overall degree of polymerization or the overall ionic porosity of the melt, not by specific interactions with iron.

e. *Electrical conductivity of hydrous rhyolitic melt (X. Guo and L. Zhang/Hefei, H. Keppler, H. Behrens/Hannover and H. Ni/Hefei)*

Volatile-rich rhyolitic magma can lead to explosive eruptions that pose a severe hazard to humans and the environment. Combined with magnetotelluric surveys, measurements of the electrical conductivity of hydrous rhyolitic melts play an important role in forecasting volcanic hazards, as they provide insights into the physicochemical state of magma chambers. So far, conductivity data for rhyolitic melts were limited to water contents up to 3 wt. % at pressures up to 0.4 GPa. In this study, we have investigated a wider range of water contents and pressures to more accurately constrain the influences of these parameters on the electrical conductivity of rhyolite melts.

Conductivity measurements were carried out for anhydrous and hydrous (2.2 - 6.0 wt. % H_2O) rhyolitic melts at 300-1200 °C and 0.5 - 1.0 GPa in a piston cylinder apparatus. The starting material for the anhydrous composition was a natural obsidian. Hydrous glasses were synthesized from melting the mixture of obsidian powder and water in a TZM vessel. A glass cylinder was prepared with a coaxial hole of 0.5 mm diameter to contain the inner platinum electrode; a $Pt_{95}Rh_5$ capsule was used as the outer electrode. Two platinum wires connected the electrodes to a Solartron 1260 impedance analyzer to measure electrical conductivity *in situ*. The assembly employed a molybdenum foil to suppress inductive interference from the heating circuit.

The measured electrical conductivity of rhyolitic melt increases with increasing temperature and decreases with pressure (Fig. 3.5-5). Furthermore, electrical conductivity is strongly enhanced by water. For anhydrous and hydrous samples, the temperature and pressure dependencies of electrical conductivity at 500 °C-1200 °C can be described by the Arrhenius law. The determined activation energy is 77.8 kJ/mol for the anhydrous sample, and 74.7 to 45.2 kJ/mol for the melts with 2.2 to 6.0 wt. % H_2O. Compared to previous measurements, our electrical conductivities of both anhydrous and hydrous rhyolitic melts are slightly higher, which can be attributed to the higher Na content in our samples as sodium is inferred to be the dominant charge carrier. Moreover, our results indicate that previous models significantly underestimate electrical conductivity for water content above 3.0 wt. %.

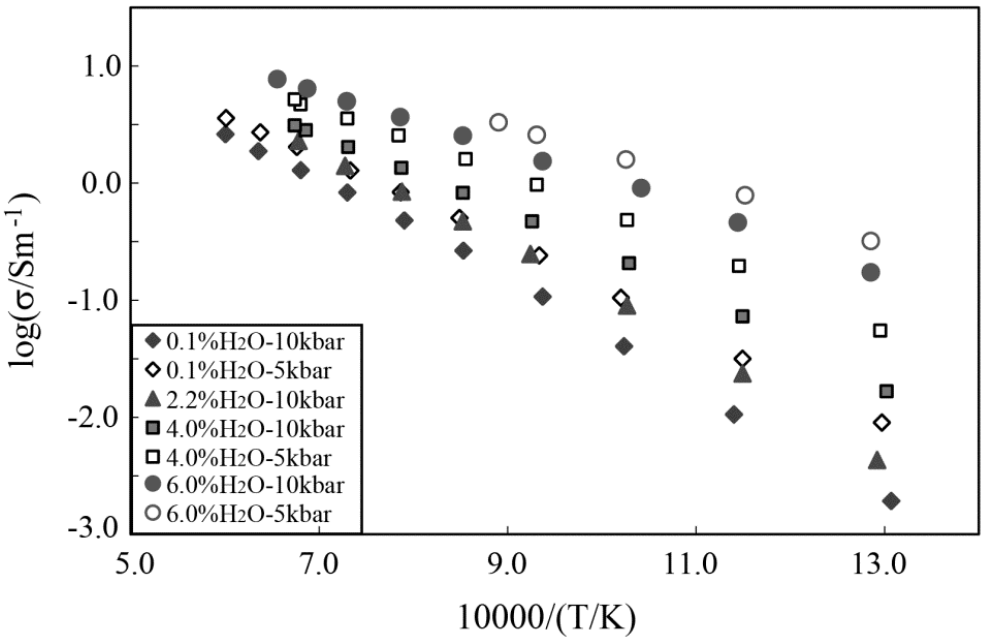

Fig. 3.5-5: Electrical conductivity of anhydrous and hydrous rhyolitic melts at 0.5 and 1.0 GPa

f. *The effect of water content, pressure and temperature on the electrical conductivity of silicate melts: implication for the Uturuncu magmatic system (South Bolivia) and magnetotelluric imaging in subduction areas (M. Laumonier; F. Gaillard and D. Sifré/ Orleans)*

In order to map and understand melting processes occurring at depth, geophysical remote sensing methods such as magnetotelluric surveys or seismic tomography have to be applied to the regions of interest. Recent magnetotelluric studies provide evidence for anomalously high electrical conductivity centered beneath Uturuncu Volcano (South Bolivia), which may be caused by the presence of silicate melt. Considering the combination of (i) the uplift of the

crust centered on Uturuncu volcano, (ii) the geothermal springs, and the (iii) dimension of the conductive body, a major replenishment has likely occurred and this requires the thorough appraisal of the storage conditions of melt at depth in the volcanic system. The quantitative interpretation of the magnetotelluric profiles requires a robust laboratory characterization of the electrical signature of silicate melts under controlled conditions of water content, pressure and temperature. So far, several studies have investigated the electrical conductivity of silicate melts, but few of them have addressed hydrous melts and the effect of pressure on melt conductivity remains unclear.

This study aims at conducting *in situ* electrical conductivity measurements of an andesite and a dacite from Uturuncu Volcano at various pressures, temperatures and water contents to develop a model integrating the effects of these three main variables. This model will help in the interpretation of the magnetotelluric surveys in areas above subduction zones, and in particular beneath Uturuncu volcano.

So far, we performed *in situ* electrical conductivity measurements on a dacitic melt using a 4-wire set up to ~ 1300 °C, 3.0 GPa and up to an H_2O content of 12 wt. %. Melt conductivity is strongly correlated with water content, and we observe a complex effect of pressure, which is relatively small at low water contents, but larger at high water contents. With increasing water content, the activation volume increases from 4 (dry) to 25 cm^3/mol (H_2O = 12 wt. %) and the activation energy decreases from 96 kJ (dry) to 62 kJ (12 wt. % H_2O). By comparison with diffusivity data, sodium appears to be the main charge carrier, even at high (12 wt. %) water content. From the data set, we have modeled the electrical conductivity of the dacite as a function of temperature, pressure and water content (Fig. 3.5-6). Water increases the conductivity by ~ 1.5 orders of magnitude, whereas pressure has a negative effect that is more important at higher water content. Using this model, the electrical conductivity of a dacite magma at relevant storage conditions beneath three volcanoes was calculated and compared with measured data (Fig. 3.5-7a). The high conductivity observed at shallow depths beneath Uturuncu volcano can be explained by the presence of a crystal-poor, water-saturated dacite. However, a water-saturated dacite would have a too high conductivity compared to the main structure observed deeper, and it is therefore not likely to be the main constituent of any reservoir at such depths. The electrical conductivity of andesites produced by the volcano will be investigated in further experiments to provide more constraints on the magmatic system beneath Uturuncu.

Usu volcano is one of the most active volcanos in Japan, with a SiO_2 content decreasing from 74 to 69 wt. % in the last eight eruptions since 1663, and with a low (< 14 % in volume) phenocryst content. A conductive body ($-0.12 < \text{Log } \sigma < -0.32$) is located at ~ 7 km below the surface. The conductivity of a water-saturated dacitic melt at such depth and 850 to 900 °C (determined from phase equilibrium experiments) would match the values obtained by magnetotelluric investigation if its crystal fraction is between 0.45 and 0.75 (Fig. 3.5-7b).

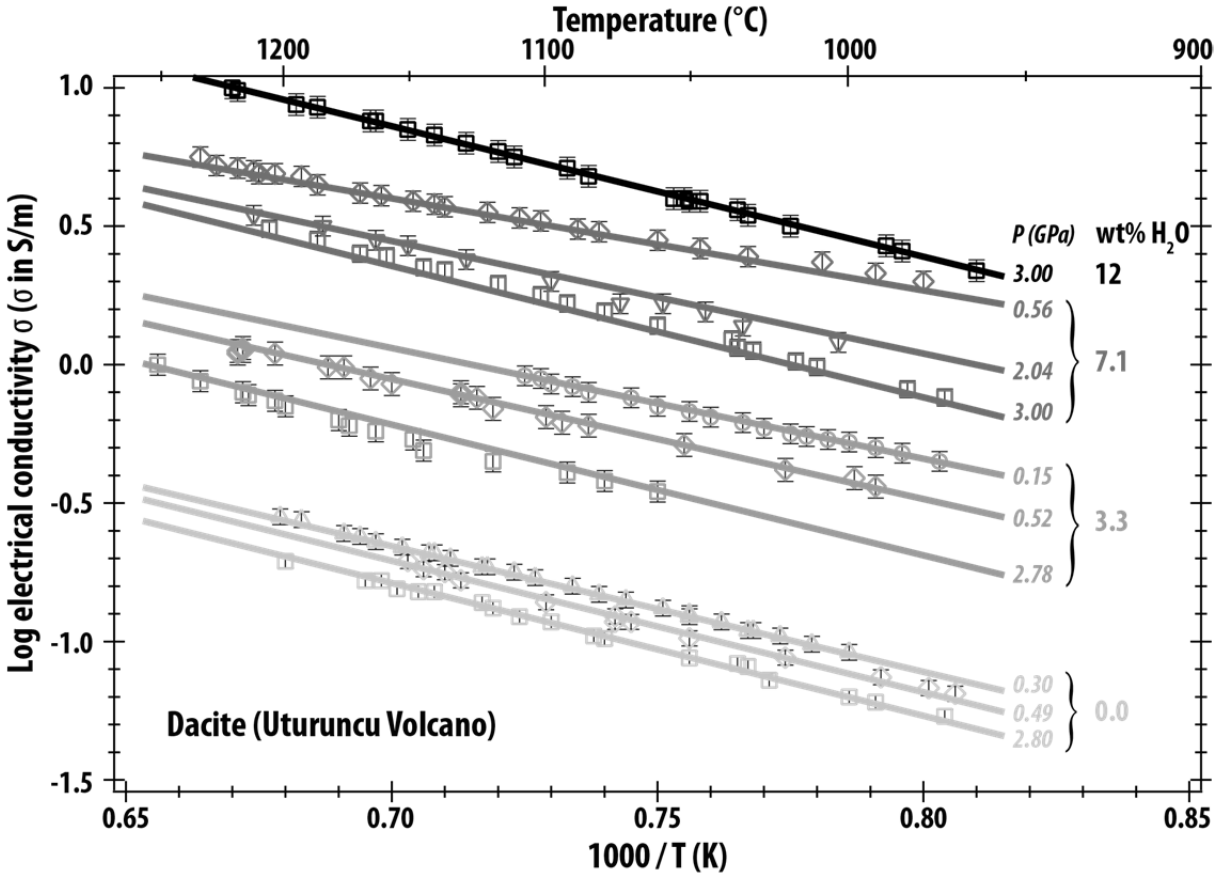

Fig. 3.5-6: Electrical conductivity of the Uturuncu dacite as a function of pressure, temperature, and water content.

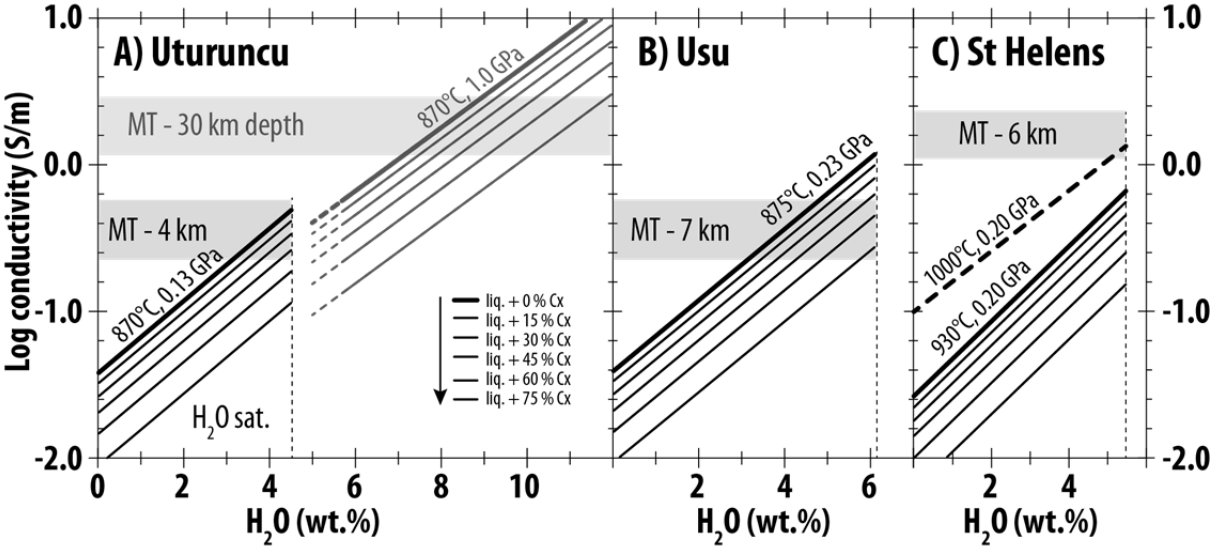

Fig. 3.5-7: A comparison between observed and predicted electrical conductivities for the crust below three volcanoes: (a) Uturuncu in Bolivia, (b) Usu in Japan, and (c) Mt. St. Helens in the USA.

Beneath Mt. St. Helens Volcano (Washington State, USA), a Log σ = 0.1 conductive body lies at ~ 6 km depth. The main eruptive products at Mt St Helens are dacitic in composition, but the model cannot explain such high conductive values by the presence of a water-saturated dacite, even under favorable conditions (Fig. 3.5-7c). Therefore, either the highly conductive body is not a magma (perhaps a brine or fluid) or the magma presently stored is not similar to the dacite from previous historical eruptions. The high conductivity, together with the observed zonation pattern in crystals and the presence of mafic inclusions, suggests that the dacite was formed by magma mixing between a deep mafic magma intruding a rhyolitic-like magma.

g. *Diffusion in liquid iron and silicate melt at high pressure (E.S. Posner, D.C. Rubie, D.J. Frost, B. Schmickler, V. Vlček and G. Steinle-Neumann)*

Diffusive transport properties of solute components in liquid iron and silicate melt at high pressures and temperatures have important implications for the time and length scales of metal-silicate equilibration during core formation, as well as for the chemical exchange across the core-mantle boundaries of differentiated planets during cooling. According to current models of the Earth's core-mantle segregation, substantial amounts of light elements (Si and/or O), as well as Cr, should have partitioned from a magma ocean into the metallic Fe-Ni cores of impacting bodies during accretion. Chemical and isotopic depletions of both Si and Cr in the Earth's mantle relative to chondrites and their increasingly siderophile (metal-loving) behaviour at elevated temperatures provide further support that these elements were, in fact, partitioned into the core during core formation.

In contrast to these predictions, however, the Si, O, and Cr contents of iron meteorites, which are derived from the metallic cores of early-formed planetesimals, are surprisingly low. The partitioning of Si, O, and Cr into liquid iron has been shown experimentally to increase with temperature so that their concentrations in a metallic core should decrease during cooling. We propose that molten planetesimal cores originally contained high concentrations of Si and/or O and Cr but that these elements became increasingly lithophile during cooling and were extracted from the core by reaction at the base of the overlying silicate mantle (magma ocean). Liquid planetesimal cores are predicted to convect, in which case the rate of Si, O, and Cr loss would be controlled by diffusion through a mechanical boundary layer at the top of the core. To test this hypothesis, we have conducted diffusion experiments on both Fe alloy and peridotite liquids over the *P-T* range of 3-24 GPa and 1915-2623 K in a multianvil apparatus. We have also performed first-principles molecular dynamic simulations to calculate diffusion coefficients over a much wider range of *P-T* conditions to extend our dataset to the Earth's outer core, where potential diffusive profiles of light elements and/or ongoing chemical exchange between metal-silicate have been used to model and interpret deviations from reference model seismic wave speeds in these respective regions.

Experimental samples for the liquid iron studies were diffusion-couples consisting of highly-polished cylindrical disks of (1) 99.97 % Fe and (2) metallic Fe alloy sintered from a mixture of metallic (Fe, Si, Cr) and/or FeO powders ($Fe_{85}Si_{14}Cr$, $Fe_{88}Si_7Cr$, $Fe_{92}Cr$, Fe_9O), contained in an MgO capsule. Experimental samples for the silicate melt studies were diffusion-couples consisting of sintered pellets of (1) isotopically natural peridotite powder enriched in 1 wt. % CoO and (2) isotopically enriched (^{30}Si, ^{18}O, ^{25}Mg, ^{44}Ca) peridotite powder with 1 wt. % NiO contained in a Re foil capsule. Due to rapid diffusion in small liquid samples, a series of experiments was conducted at each pressure, using variable heating rates, final quench temperatures (T_f), and run duration at T_f. To minimize the occurrence of diffusion prior to reaching the target temperature, a rapid heating rate between 20-50 K/sec was used to ramp the temperature to the required value. Experimental durations were very short (< 180 sec) and runs were terminated by quenching at ~ 500 K/sec by switching off the electrical power. Recovered capsules were cut and polished parallel to the axis of the cylindrical sample and profiles were measured by electron microprobe (EPMA) for Si and Cr in liquid metal, by secondary ion mass spectrometry (SIMS) for Si, O, Mg, Ca in silicate melt, by laser ablation inductively coupled plasma mass spectrometry (LA-ICP-MS) for Ni and Co in silicate melt, and by image analysis for O in liquid metal. All profiles from a particular pressure interval were fit simultaneously using a Crank-Nicolson finite difference approximation in order to refine the activation energy and pre-exponential diffusion coefficient. A typical diffusion profile and model fit to the data are shown in Fig. 3.5-8.

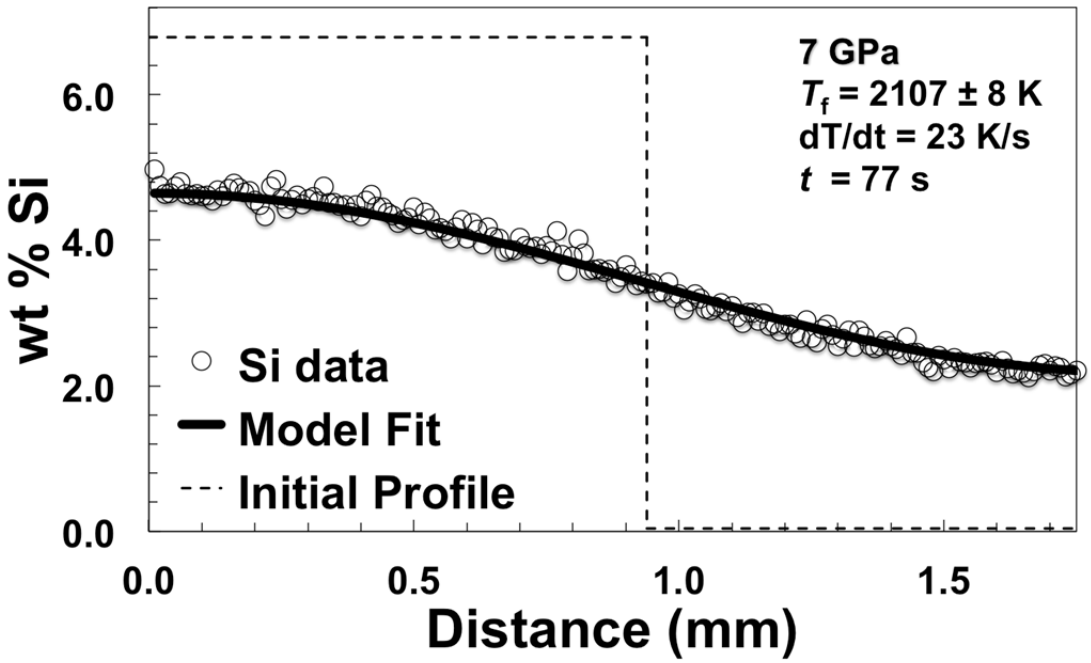

Fig. 3.5-8: Typical EPMA profile of Si diffusion in liquid iron at 7 GPa that was heated with a rate of 23 K/s to the final temperature (T_f) of 2107 ± 8 K and kept there for 77 s. Model fit to the data represents a global solution to all experiments conducted at 7 GPa. The pre-anneal profile is shown by dashed lines.

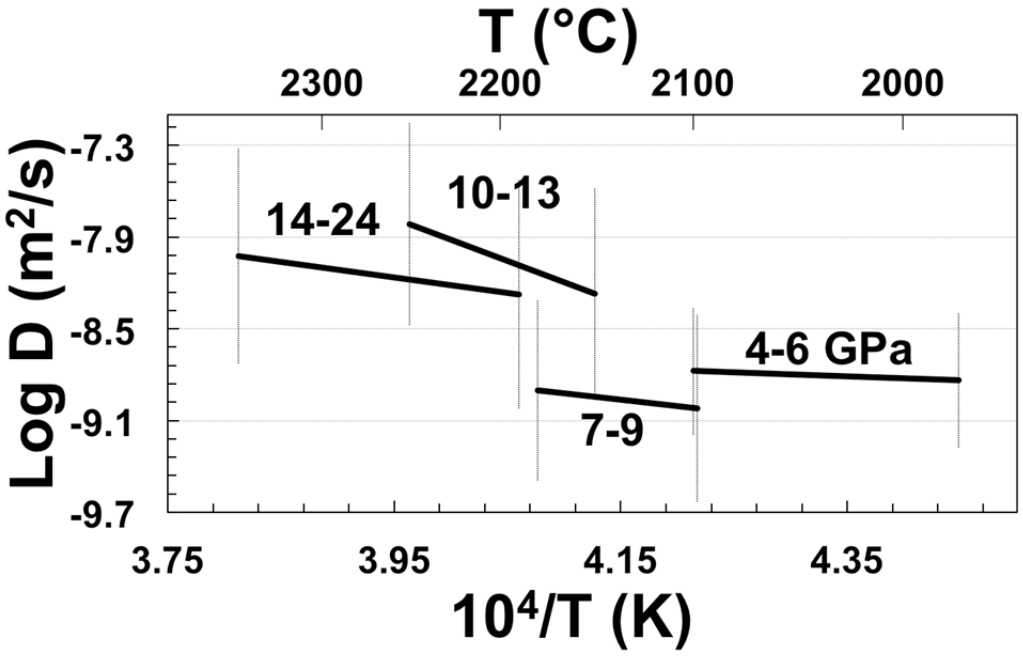

Fig. 3.5-9: Arrhenius relation for ^{30}Si self-diffusion in silicate melt for three pressure intervals (4-6, 7-9, 10-13, and 14-24 GPa). Si diffusion decreases with increasing pressure from 4-9 GPa and then abruptly increases between ~ 9-10 GPa by a factor of ~ 0.7 log units. Above ~ 10 GPa, Si diffusion decreases with increasing pressure. Error bars represent 1σ to the modeled activation energy.

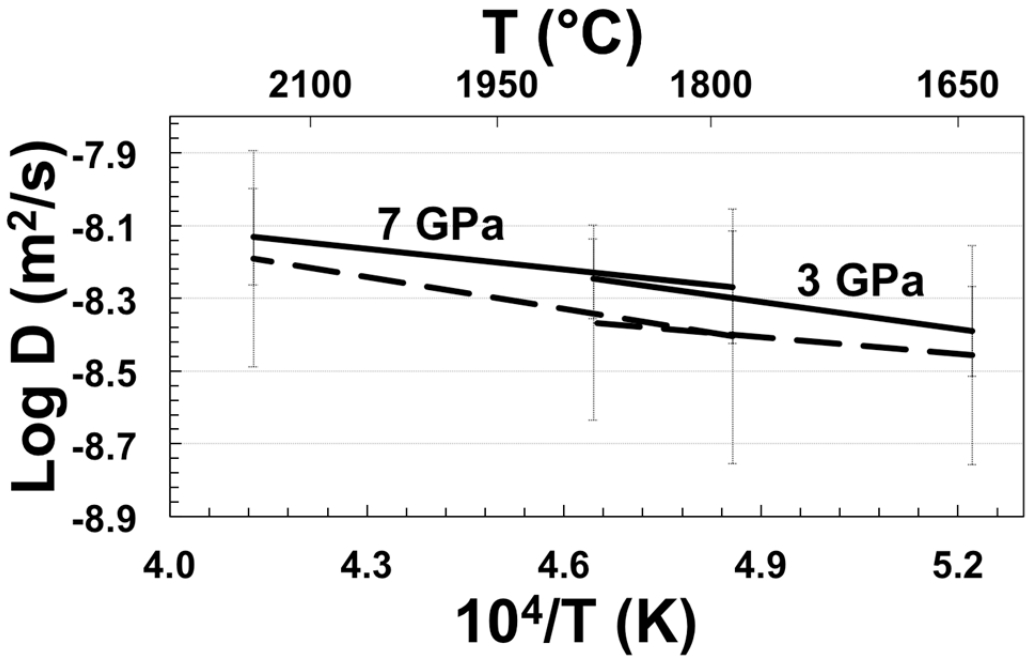

Fig. 3.5-10: Arrhenius relation for Si (solid lines) and Cr (dashed lines) diffusion in liquid iron as determined by simultaneous least-squares fit to all diffusion profiles conducted at 3 GPa (n = 8) and 7 GPa (n = 10). Error bars represent 1σ to the modeled activation energy.

The self-diffusivity of Si, Mg, Ca in silicate melt decreases with increasing pressure between 4 and 9 GPa. Between 9-10.5 GPa, there is a discontinuous increase in diffusivity by as much as ~ 0.7 log units for Si (Fig. 3.5-9) and ~ 0.5 and ~ 0.2 log units for Ca and Mg, respectively. Above 13 GPa, the diffusivity of Si, Mg, and Ca in silicate melt decreases with increasing pressure. It appears likely that the observed change in activation volume at ~ 9 GPa leading to the positive pressure effect is caused by a change in the melt structure such as the formation of higher coordination intermediate species. Our findings match well with previous studies, which have reported a positive-to-negative change in the pressure dependence on silicate melt viscosity between 8.5-13 GPa.

The Arrhenian relation for Si and Cr diffusion in liquid iron for experiments conducted using $Fe_{85}Si_{14}Cr$ alloy is shown in Fig. 3.5-10. At these concentrations, Si diffuses slightly (~ 0.06-0.14 log units) faster than Cr. Si diffuses approximately five times faster in liquid metal than in silicate melt at pressures below 7 GPa and temperatures above the peridotite liquidus. Liquid iron experiments at a third pressure interval (18 GPa) are in progress to allow for the calculation of the pressure dependence of diffusion (*i.e.*, activation volume). To assess the effect of solute concentration on the diffusion coefficient, we have designed a double chamber MgO capsule to allow for simultaneous annealing of diffusion couple alloys with variable solute concentrations.

h. *The solubility of molecular hydrogen in olivine and pyroxene (X. Yang/Nanjing and H. Keppler)*

Hydrogen may be stored as OH defects in the silicate minerals in the interior of a planet. This mechanism of hydrogen storage requires that oxygen fugacity is sufficiently high to allow the formation of water and OH groups. Planets may, however, also form under extremely reducing conditions, where hydrogen is not oxidized to H_2O, but present as molecular H_2. Retention of hydrogen inside the silicate mantle of a planet would then only be possible, if there were a significant solubility of H_2 in silicate minerals. From available data on He solubility, this does not appear implausible. We therefore studied the solubility of hydrogen in olivine and pyroxenes at 10-30 kbar and 1100 to 1300 °C.

Experiments were carried out in the piston cylinder apparatus with mixtures of natural olivine and pyroxene crystals and water sealed into thick-walled Fe capsules. Reaction of water with Fe during the experiments produces a fluid phase that consists of nearly 50 mol. % H_2. Run products were investigated by Raman spectroscopy. In order to detect traces of hydrogen, very high laser power (1 Watt of the 514 nm line of an argon laser) and long accumulation times (20 min) were used.

The spectra obtained showed a weak band of dissolved H_2 at 4123cm^{-1} in some of the olivine and pyroxene crystals. Notably, the position of this band is different from that of H_2 in fluid inclusions and it does not show the rotational fine structure of gaseous H_2. By comparison with the Raman spectra of H_2-containing glass standards, we could estimate that the content of molecular H_2 in these samples is in the order of a few ppm by weight.

Our data suggest that molecular hydrogen does indeed have a measurable solubility in upper mantle minerals; however, this solubility is orders of magnitude smaller than for H_2O. This implies that hydrogen may only be retained in the interior of a planet, if rather oxidizing conditions are already reached during the accretion.

i. *Water solubility in lower mantle phases (R. Myhill, L. Ziberna, D.J. Frost, T. Boffa Ballaran, H. Bureau/Paris, C. Raepsaet/Paris)*

The water storage capacity of upper mantle mineral assemblages generally increases with pressure. In the mantle transition zone, both wadsleyite and ringwoodite can hold on the order of 1 wt. % H_2O. In contrast, the lower mantle is apparently almost dry; some high-pressure experiments suggest that $MgSiO_3$ bridgmanite and MgO periclase hold only a few ppm H_2O. Nevertheless, these results are controversial, and few experiments have been performed on lower mantle minerals with more natural compositions.

In this study, we investigate the water solubility of Al-bearing lower mantle minerals, including bridgmanite, stishovite and garnet. Stishovite is a significant component of recycled oceanic crust, and can potentially hold significant amounts of water via the substitutions $Si^{4+} \leftrightarrow H^+ + Al^{3+}$ and $Si^{4+} \leftrightarrow 4H^+$. Garnet is stable within the uppermost ca. 100 km of the upper mantle, and could hold significantly more water than perovskite and periclase, at least partially decoupling water-driven melting from the upper-lower mantle boundary. Multianvil experiments were conducted at the BGI within 7/3 assemblies to simulate the conditions of the uppermost lower mantle.

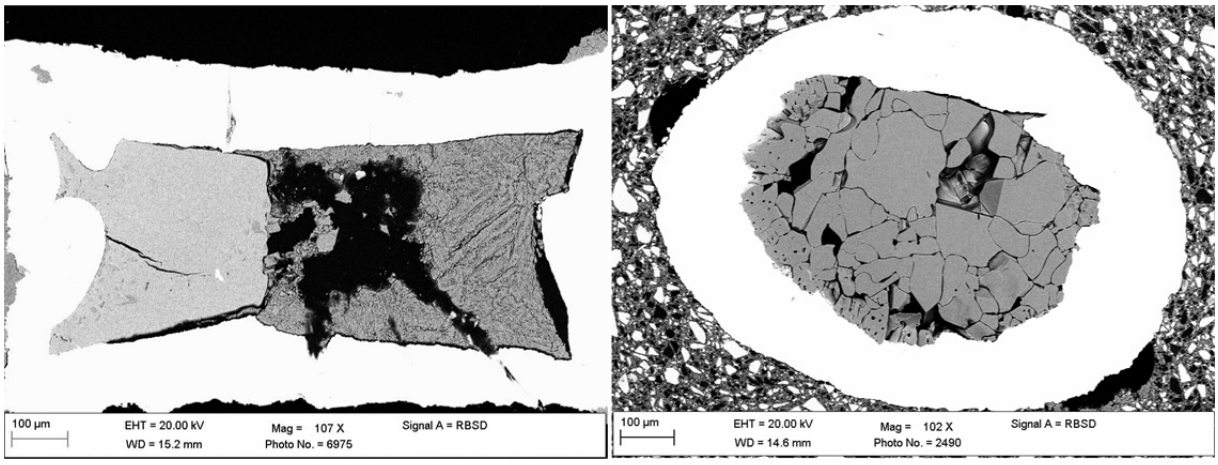

Fig. 3.5-11: SEM images of high pressure run products synthesized in hydrous environments at ~ 26 GPa. Left: A large equant aluminium-bearing perovskite (bridgmanite) mass within a quenched hydrous melt. The dendritic crystals in the melt are predominantly phase D. Right: Aluminous stishovite crystals. The capsule material is platinum.

Recovered sample microstructures and compositions were obtained with scanning electron microscopy and electron probe microanalysis. Large (> 100 micron) crystals (Fig. 3.5-11) were analyzed for water content using Elastic Recoil Detection Analysis (ERDA), at Saclay, France.

Preliminary results on bridgmanite indicate that significant water can be stored within the crystal structure. In Fe-free crystals with about 5 mol. % Al_2O_3, approximately 3000 ppm water is present. In Fe and Al-bearing samples the water concentrations are typically about 1000 ppm. We suggest that the high H_2O contents in Fe-free Al-bearing bridgmanite are a consequence of the large Al cation strongly preferring the B site. Accommodation of H on the smaller A site reduces distortion of the bridgmanite structure. Ferric iron also prefers the A site, such that the addition of iron reduces the water capacity of the structure.

3.6 Rheology

Understanding the dynamics and evolution of the Earth requires knowledge of rheological properties of the constituent minerals and mineral assemblages. Mineral phases and their properties change with increasing pressure and temperature in Earth's deep interior. The BGI utilizes and develops highly advanced methods to understand and quantify the rheological properties of Earth materials at these conditions. Results of rheological studies enable geophysical and geochemical observables to be interpreted and provide valuable input parameters for large-scale geodynamic modelling. The most common strain rates achieved in the laboratory are 10^{-4} to 10^{-5} s^{-1}, which are 7-8 orders of magnitude higher than natural strain rates of 10^{-12} s^{-1} or lower. However, deformation processes are controlled by various defects (point, line, and planar defects) whose behavior is relatively well understood. Therefore, identification and quantification of these defects enables laboratory rheological data to be used to understand deformation on geological time scales. Most contributions in this section describe deformation experiments on relevant minerals and rocks over a wide *P*-*T* range by using 6-axis multi-anvil presses and directed stress experiments in the diamond anvil cell.

The first contribution focuses on identifying mechanisms necessary to produce sufficient weakening of the lithosphere to allow tectonic plate motions. It shows that a mixture of enstatite and olivine results in rheological weakening compared to pure olivine aggregates. Deformation in multiphase materials also changes the reaction rate, shown in the second contribution where spinel-peridotite reacts to garnet-peridotite by producing more garnet under deformation conditions. Using the large-volume SAPHiR press at the neutron facility at the Forschungs-Neutronenquelle Heinz Maier-Leibnitz (FRM II) in Garching, crystallographic preferred orientation (CPO) formation in olivine at low strain rates of about 10^{-7} s^{-1} was investigated in the third contribution. No clear preservation of the A-type texture is found and B-type CPOs described in previous studies are observed also at low strain rates. Low seismic wave velocity layers (LVL) in the upper part of subducted slabs are interpreted as hydrated mafic rocks, partially caused by the presence of lawsonite. However, the fourth study finds that only weak crystallographic preferred orientation (CPO) develops in deformed lawsonite aggregates. The fifth contribution investigates the deformation mechanisms of high pressure subduction channels and finds that during subduction a transition from oblate to prolate strain occurs. The high pressure deformation studies using synchrotron radial x-ray diffraction of the next contribution show that ferropericlase strength increases at pressures of the upper part of the lower mantle. Resulting increase in mantle viscosity in high strain regions can eventually lead to stagnation of sinking slabs.

Deformation mechanisms at extreme *P* and *T* conditions corresponding to extrasolar planets are studied using a new single-crystal X-ray diffraction approach at high-pressures to study the strain-stress relationships in ice VI. The decrease of seismic wave velocity anisotropy observed at depths of 200 - 300 km is attributed to changes of olivine CPO. However a

pressure-induced slip-system transition of [100](010) to [001](010) dislocations is unlikely because they show a similar pressure dependence, as described in the eighth contribution.

The dislocation annihilation study of the final contribution yields dislocation mobilities at a temperature of 1500 K and a pressure of 3 GPa that are proportional to the water content raised to the power 1.2, which is in agreement with the results of deformation studies.

a. *Microstructural contrasts between a dunite and a two-phase harzburgite: Rock deformation at different temperatures, pressures, compositions and strain magnitudes (R.J.M. Farla)*

Models predicting the strength of the lithosphere fail to produce substantial weakening necessary for plate tectonic convection. Additional mechanisms are necessary that can lead to weakening, most likely in the form of localizing deformation as seen in nature. A recent experimental study in the literature by the same author reported tantalizing clues that a second phase (in this case orthopyroxene) can help localize deformation via dynamic recrystallization and phase mixing, thereby enhancing weakening. However, the study was limited to only one mode of deformation (nearly-simple shear), mixed pressure conditions, and one mixture of olivine plus enstatite. The role of water and aluminium content of enstatite on microstructural evolution and strength was not explored either.

In this study, we expand upon previous work by systematically exploring various conditions of temperature, pressure, and strain magnitude to investigate the microstructural evolution of olivine-enstatite mixtures. As before, the starting material is San Carlos peridotite olivine and enstatite-rich orthopyroxene, hand-picked for gem quality, crushed and sieved for grain size. We apply different modes of strain, such as plane strain and flattening strain on a stacked assembly of a pre-sintered olivine polycrystal and an olivine-enstatite polycrystal, for direct comparison. We also explore high-strain deformation in nearly-simple shear geometry. All experiments are carried out at a constant strain rate of 10^{-5} s^{-1}. We choose a temperature range between 1100 °C and 1400 °C, a pressure range between 2 and 6 GPa, and starting grain sizes > 10 µm to ensure initial deformation is controlled by power-law dislocation creep.

Preliminary results are presented in Fig. 3.6-1. After deformation, an olivine-enstatite mixture accumulated 34 % strain whereas the olivine sample accumulated 29 % strain. The most striking observation is the nearly complete recrystallization of enstatite grains in the mixture associated with recrystallization of some neighbouring olivine grains (d_{ol} = 7 µm and d_{en} = 5 µm). The shapes of the original enstatite grains are still apparent and the boundaries between the new grains share lower misorientation angles (10°-30°) than between large grains. This is suggestive of recrystallization by sub-grain rotation accompanied by grain boundary migration. In contrast, while some grain boundary bulging is apparent in the olivine sample as circled in Fig. 3.6-1, the average grain size has largely remained unchanged from the starting material (d_{ol} = 15 µm). Sub-grain rotation recrystallization therefore plays an important role in

enstatite, and clearly has an affect on olivine under these conditions. However, more strain is likely needed to localize deformation via subsequent phase-mixing of small grains into bands. The final differential stress in the mixture can be estimated as ~ 360 MPa using a recrystallized grain size piezometer, which must also apply to the olivine sample before quench. Stereographic projections along the main crystallographic directions [100], [010], and [001] show moderate crystallographic preferred orientation (CPO) in the olivine sample with maximum multiples of uniform distribution (MUD) of 4.2. The dominant slip system is A-type with [100] slip sub-parallel to the extension direction. A stronger CPO and more convincing demonstration of A-type slip in olivine is found in the mixture, as previously observed and may due to (sub)grain rotation with an anisotropic crystal growth component. In contrast, a weaker CPO is found in the recrystallized enstatite grains with typical [001] slip in the extension direction. Grain growth kinetics in enstatite is known to be more sluggish than in olivine.

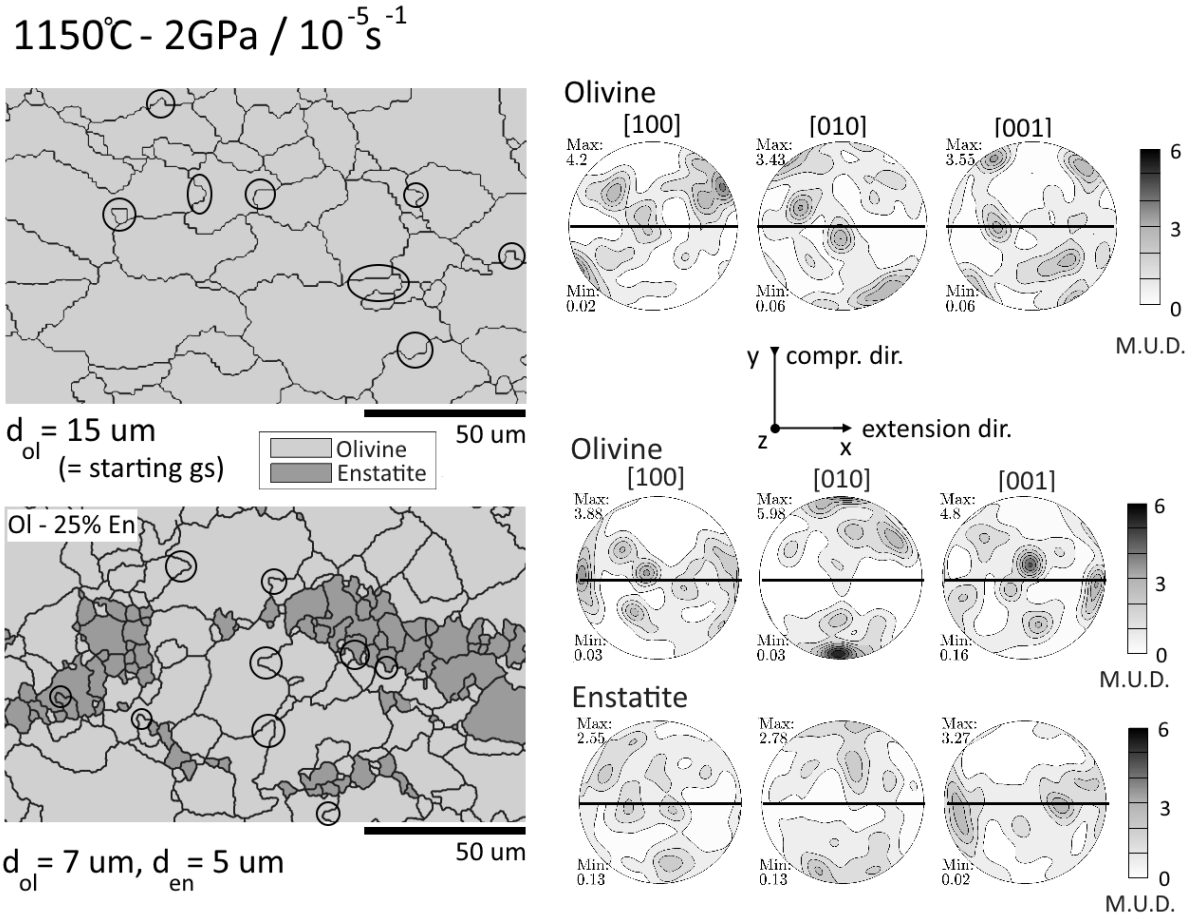

Fig. 3.6-1: Simultaneous pure shear deformation of an olivine polycrystal and olivine with 25 % enstatite at 1150 °C and 2 GPa. Starting grain size was 15 µm. On the left, the two EBSD maps show the grain shape, size and distribution of both phases. On the right, stereographic projections along [100], [010], and [001] are produced from the EBSD data with a half-width of 10° and maximum MUD of 6 for easy comparison. East-west is the extension direction (shear direction) and north-south the compression direction.

Despite having only described one experiment here, these preliminary results show that estimating the strength of the lithosphere using only olivine rheology may be inaccurate or in some regions where deformation is localized/localizing, entirely inappropriate.

b. *Correlation between strain rates and reaction rates at the transition from spinel to garnet lherzolite in the CMAS system (F. Heidelbach)*

Metamorphic rocks display abundant evidence of concurrent plastic deformation during mineral reactions. Here we investigate the reaction of clinopyroxene+orthopyroxene+spinel to garnet+olivine in the CMAS system under shear conditions and compare it with static phase transformation experiments. Starting materials were produced from glasses of an appropriate composition with up to 5 wt. % of water in a piston cylinder apparatus at a pressure of 1 GPa and a temperature of 1000 °C for up to 10 days in order to increase grain size. The resulting samples show grain sizes of 5-20 μm for all phases. Samples were then deformed in a 6-axis multianvil press in the garnet stability field at a temperature of 1100 °C and a pressure of 2.5 GPa to 30 % pure shear strain at strain rates from 5×10^{-4} to 5×10^{-6} sec^{-1}. Reference samples were kept for the same duration under static conditions.

Quantitative analysis of change in phase proportions was performed by using a SEM-EBSD, because it is difficult to separate phases by their chemistry because of the their compositional gradients due to the sluggish kinetics. Reactions proceed rather rapidly at the beginning (to about 50 % reaction progress after about 50 minutes) with a high nucleation rate due to the overstepping of the reaction boundary (Fig. 3.6-2), but slow down significantly since growth is impeded by phase boundaries. Apparently this effect cannot be balanced by the creation of new interphases due to deformation. Preliminary results show that the production of garnet is consistently higher in the deformed samples than in the statically annealed reference samples, indicating that deviatoric stresses enhance the reaction rates. The reaction rates appear to be coupled to the strain rates; they are however about two orders of magnitude faster both in the dynamic and the static experiments (Fig. 3.6-3) indicating that the reaction rate is not limited by the strain rate as has been suggested previously.

The deformed samples showed extremely homogeneous strain distribution and only weak development of CPO in olivine and clinopyoxene, indicating that deformation likely occurred by diffusion-assisted grain-boundary sliding. Newly formed garnet grains at the phase boundaries between spinel and pyroxene have a grain size up to 10 μm and form larger (> 200 μm) domains of equal orientation both in the statically and dynamically reacted samples. In the deformed samples, the orientation domains additionally show continuous orientation dispersion around the intermediate fabric axis (*i.e.*, the normal of the plane of maximum deformation), indicating that orientations change continuously with progressive deformation similar to the growth of porphyroblastic snowball garnets.

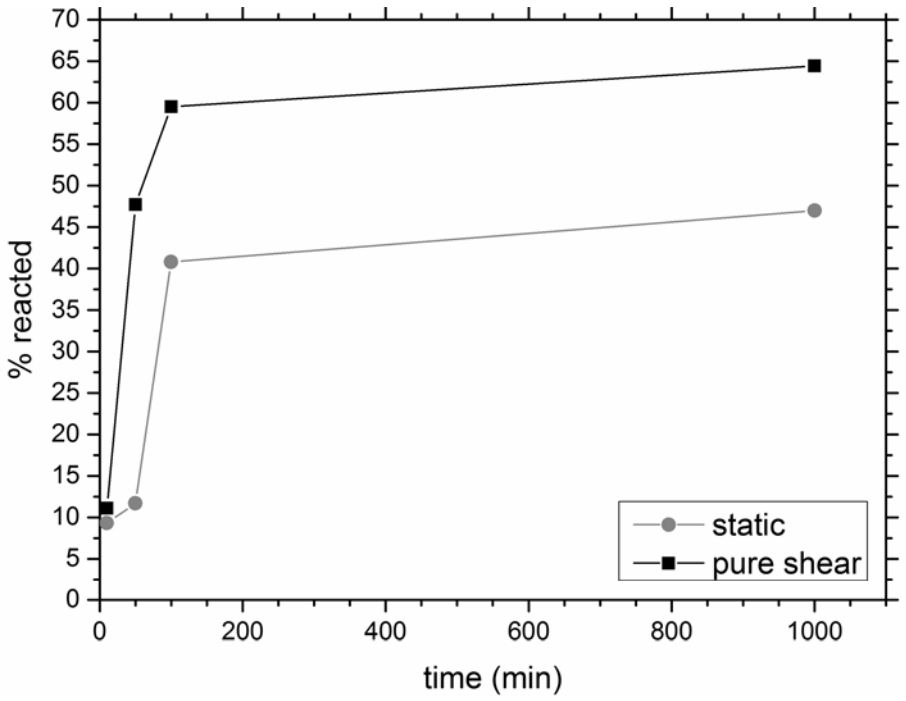

Fig. 3.6-2: Reaction progress vs time for deformed (pure shear) and statically reacted samples.

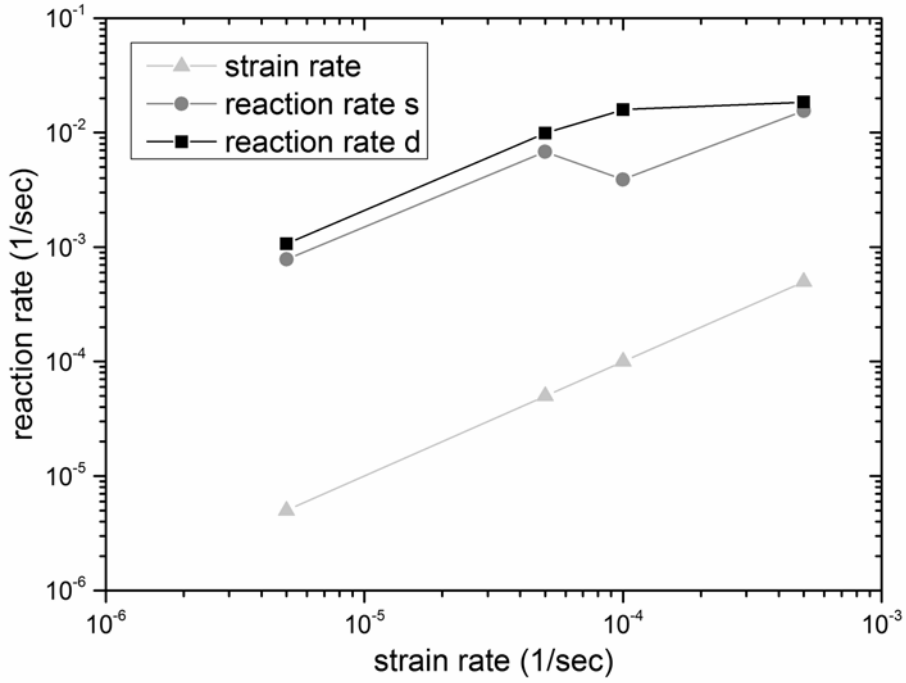

Fig. 3.6-3: Plot of reaction rates, *i. e*. reaction progress per time, (dynamic (d): solid squares, static (s): circles) versus strain rates, respectively run durations in the case of static experiments; for reference the strain rates are also drawn (triangles) in order to facilitate comparison between reaction rates and strain rates for different experiments.

c. *Texture development of olivine at high pressure and low strain rates (N. Walte, F. Heidelbach and D. Frost)*

The deformation behaviour of olivine, the dominant mineral phase of the upper mantle, has been intensely investigated by deformation experiments as well as by other more indirect methods to understand the nature of the weak asthenosphere, mantle flow, and seismic anisotropy in the upper mantle. Upper mantle seismic anisotropy has long been known and attributed to crystallographic preferred orientation (CPO) in olivine, a result of dislocation creep deformation. However, olivine shows a wide range of different CPOs depending on stress, water content, and confining pressure that hinders the direct inference of mantle flow directions from the measured seismic anisotropy. Over the last decade, CPO maps for olivine have been constructed over the whole pressure range of the upper mantle that predict a general switch form an A-type texture ([100](010) glide system) to a B- or C-type texture ([001](010) or [001](100), respectively) at a pressure of 6-8 GPa, which was connected to a change of seismic anisotropy in the deeper upper mantle. However, previous deformation studies have generally employed high strain rates of 10^{-5}-10^{-4} s^{-1}, which has led some authors to propose that the observed seismic transition with mantle depth in nature may be rather a result of a higher water content of olivine thereby implying that the experimental switch could be an artefact of an increased flow stress at high pressures.

The above results have been obtained by using a new generation of cubic multianvil devices allowing expanding the pressure range of controlled deformation experiments over the depth of the entire upper mantle including the transition zone of the Earth. However, strain rates that can be generated using this kind of devices are generally more than 10^{-6} s^{-1}, because their sample sizes and total time are currently limited to ~ 1 mm^3 and 1 day, respectively. For SAPHiR, the neutron instrument in construction at FRM II in Garching, new sample assemblies were developed that allow to subject larger sample volumes up to 20 mm^3 to high pressures for long periods of time to ensure good counting statistics with neutron diffraction.

Here, we use the large-volume SAPHiR assemblies for an offline deformation study of the texture development of olivine at a pressure of 8 GPa to demonstrate the experimental stability at high P and T for up to 5 days. Experiments were performed with 12/7 and 10/6 assemblies (cube length/anvil truncation length) with a sample capsule size of 3.5×3.0 and 2.2×2.5 mm (length × diameter), respectively. The assemblies contain a Re or Pt foil furnace for heating and the temperature is measured by a D-type thermocouple in contact with the top of the sample capsule. A test experiment with two thermocouples revealed a thermal difference of 100 °C between the center and top of the sample capsule at 1500 °C, which is due to the large sample length and the foil furnace. Samples for deformation experiments are polycrystalline San Carlos olivine that was ground and dried in a vacuum furnace at 200 °C for longer than 24 hours. The samples were compressed, heated and deformed by pure shear at low strain rates until total shortenings of 10-20 % were achieved (typically between 3 and 4 days). The samples were cut, polished and analyzed by SEM orientation contrast (OC) and electron back-scattered diffraction (EBSD).

Figure 3.6-4 displays two microstructures of runs that were deformed at 1300 °C and 1500 °C at strain rates of 8.4×10^{-7} and 7.6×10^{-7} s^{-1}, respectively, and at a pressure of 8 GPa. In the lower-temperature experiment, the grains have smoothly curved grain boundaries and 120° triple junctions close to an equilibrated foam texture. On the other hand, the higher-temperature sample is characterized by an uneven grain-size distribution with some very large grains (> 100 μm), irregular grain boundaries, and internal deformation features such as sub-grain boundaries and bending crystal lattices in the larger grains.

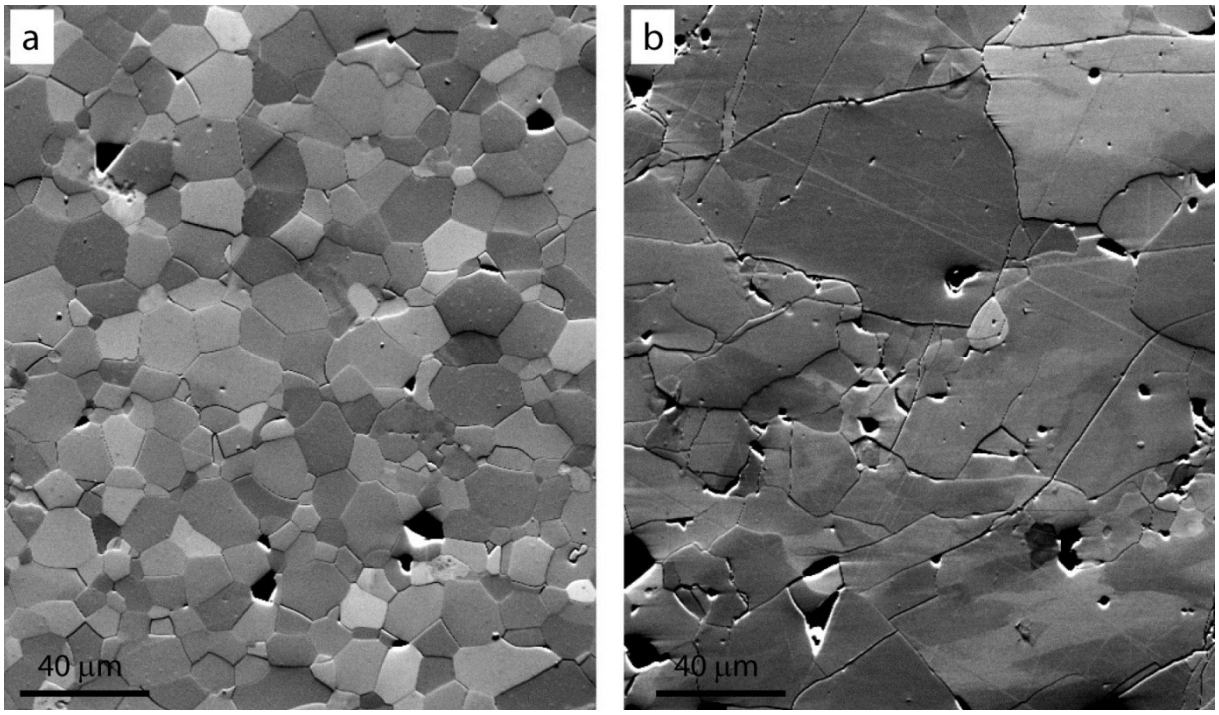

Fig. 3.6-4: Microstructure of single-phase olivine deformation at a strain-rate of 8×10^{-7} s^{-1}. (a) Experiment SA65 at a temperature of 1300 °C, the aggregate displays smoothly curved grain boundaries and little internal deformation features. (b) Experiment SA81 at a temperature of 1500 °C, the aggregate is dominated by large grains with internal deformation features. Axis of compression is vertical; axis of extension is horizontal.

The EBSD analysis for the lower-temperature experiment revealed that the [001] and [010] directions are concentrated in the directions of the greatest extension and the shortening, respectively, which indicates dislocation creep by the [001](010) slip system (B-type texture) (Fig. 3.6-5a). The CPO of the higher-temperature sample is strongly dominated by the largest crystals, which makes an interpretation difficult. However, when displaying the data with 1 point per grain (Fig. 3.6-5b-c), the resulting CPO is similar to the lower-temperature experiment with a [010] maximum parallel to the shortening direction. However, CPO in the shear direction is less clear, but a girdle of [001] in the pole figure and a weak maximum of [001] in the shear direction in the inverse pole figure (Fig. 3.6-5c) also indicates a B-type texture.

We have thus found no clear indication of a preservation of the A-type texture under lower strain rate conditions. The B-type CPOs found in our samples confirm previous results that were obtained at similar pressures and temperatures, but with two orders of magnitude higher strain rates. The unclear CPO and the uneven grain-sizes at 1500 °C suggest that the steady-state grain sizes were not obtained at the higher temperature, because the recrystallized grain size increases with decreasing flow stress and increasing temperature, and therefore grain-size sensitive creep (diffusion creep) may have contributed to deformation. The SAPHiR assemblies with large sample volumes are thus useful to investigate CPO of olivine in more realistic conditions for the upper mantle.

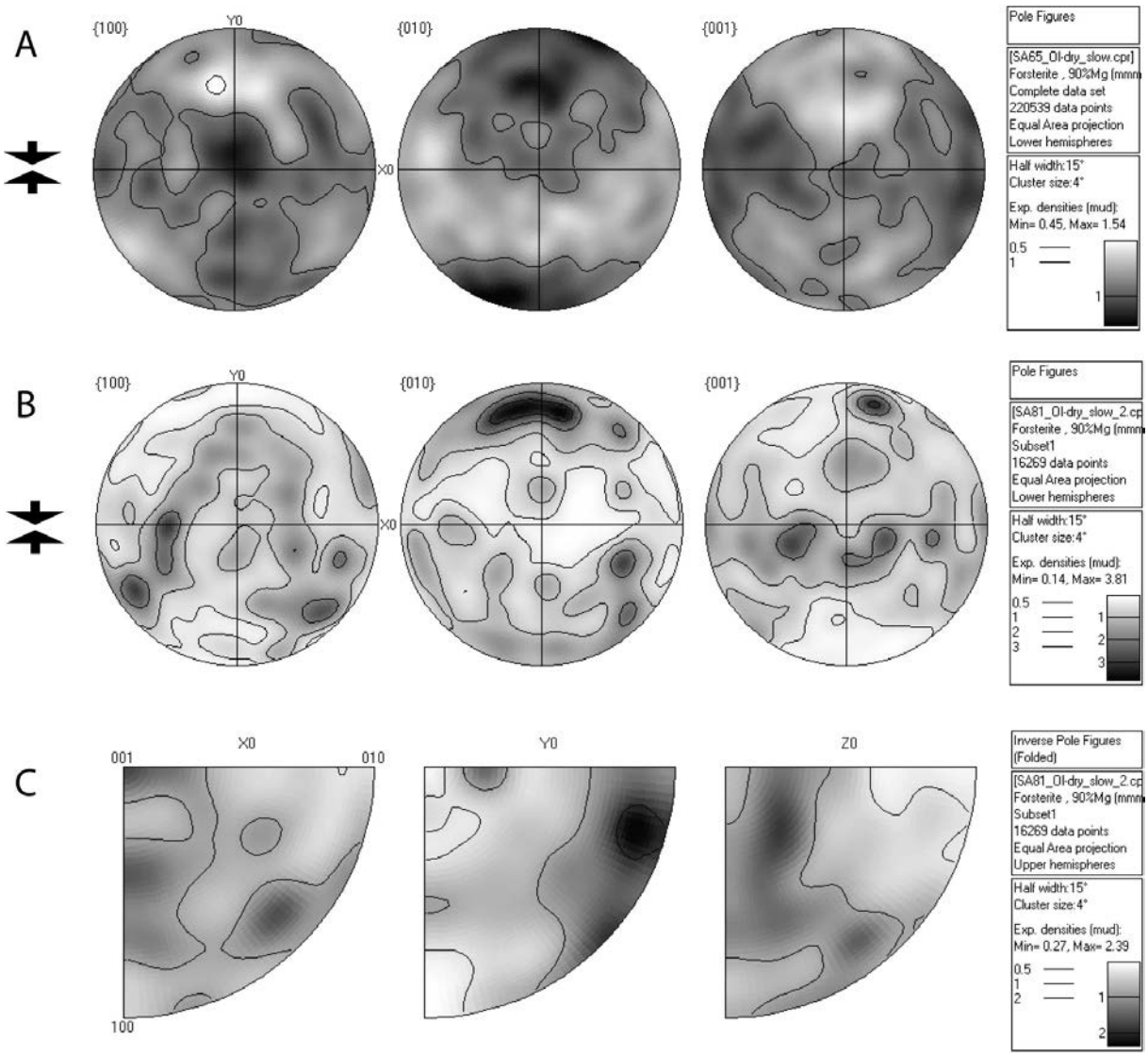

Fig. 3.6-5: Lower hemisphere pole figures for experiments SA65 (a) and SA81 (b) and inverse pole figure for SA 81 (c). Axis of compression is vertical; axis of extension is horizontal. The CPOs are compatible with a [001](010) glide system (B-type texture).

d. *Deformation mechanism of lawsonite in deep subducting slabs from high-pressure and high-temperature experiments (R. Iizuka/Matsuyama, N. Miyajima, V. Soustelle/Providence and D.J. Frost)*

Low-velocity layers (LVLs) are regions of low seismic wave velocity, which occur in the upper portions of subducting slabs and apparently persist to depths of 100−250 km. Hydrated mafic rocks provide a plausible explanation for the origin of LVL observations, because the hydrous minerals involved have intrinsic physical properties, which can influence seismic velocities and anisotropies along the slabs. Lawsonite ($CaAl_2Si_2O_7(OH)_2 \cdot H_2O$) is stable at depths greater than serpentine in subducting slabs and is considered to be one of the prime candidate hydrous minerals that may potentially be present in LVLs. Lawsonite single crystals have a high elastic anisotropy, suggesting that the development of its crystallographic preferred orientations (CPOs) might also assist in lowering seismic wave velocities. In our study, therefore, deformation experiments on lawsonite were conducted at high pressure and high temperature corresponding to 150 km depth in the subduction zone with the aim of investigating the dominant deformation mechanism.

Pure or simple shear deformation on a natural lawsonite powder with a fine grain size (< 25 μm) was performed at 5 GPa and 700 °C after annealing for ~ 20 h using a multianvil apparatus with 6 independently acting rams. Samples were deformed at strain rates of *ca*. 10^{-5} s^{-1} with a finite strain of 0.3~1.0 and analysed after recovery using a Scanning Electron Microscope (SEM) coupled with an Electron Backscatter Diffraction (EBSD) detector and a Transmission Electron Microscope (TEM).

The microstructure of deformed lawsonite from EBSD analysis displays a porphyroclastic texture with a bimodal grain size distribution. Porphyroclasts (20~50 μm in size) have undulose extinction, deformation lamellae, and irregular subgrain boundaries, implying the occurrence of dynamic recrystallization during the deformation. These porphyroclasts show a characteristic CPO pattern, in which the [100] axes form a girdle in the shear plane with a maximum concentration close to the shear direction. A maximum of the [010] axes occurs subnormal to the shear plane. This result indicates that the porphyroclasts were deformed in the dislocation creep regime.

Figure 3.6-6 displays representative weak-beam dark-field images obtained in the TEM. These images show that the deformed lawsonite has a high density of {110} twins and a variety of dislocations. Many wedge-shaped mechanical twins sharing the *c*-axis are observed and apparently induce lattice defects in the grains, although they do not lead to a major deformation mechanism. Some dislocation lines are relatively short and dense, often parallel to the [100] axis, and others are long and curved along the {110} plane. Due to the high concentration of water in lawsonite, severe damage from the electron beam could be easily seen, which causes dislocation lines to become blurred even when observed at low temperatures of -170 °C. Potential Burgers vectors seem to be not only 1/2<110> but also

[100], both of which are the shortest lattice distances in the crystal structure. Hydroxyl ions and H_2O molecules lie on both (110) and (010) planes, suggesting that these planes could be gliding planes accompanied by hydrolysis or dehydration reactions, but without breaking of strong Si−O−Si bonds. The dominant activation of 1/2<110>{110} slip system has been already proposed by a previous TEM study performed on a natural sample. However, the interplanar spacing d_{hkl} of the (010) slip plane is larger than that of (110). The combination of the short [100] Burgers vector $\boldsymbol{b}$ and the larger d_{010} results in a minimum in $|\boldsymbol{b}|/d_{hkl}$, a criterion often employed to identify the easiest slip system. Our study strongly supports the presence of numerous potential slip systems in lawsonite with [100](010) appearing to be the most dominant. The equivalent activation of multiple slip systems might, therefore, be responsible for the relatively weak CPO developed in the deformed lawsonite, which may be also caused by the effect of grain size reduction and the relatively low strain attained in the experiments.

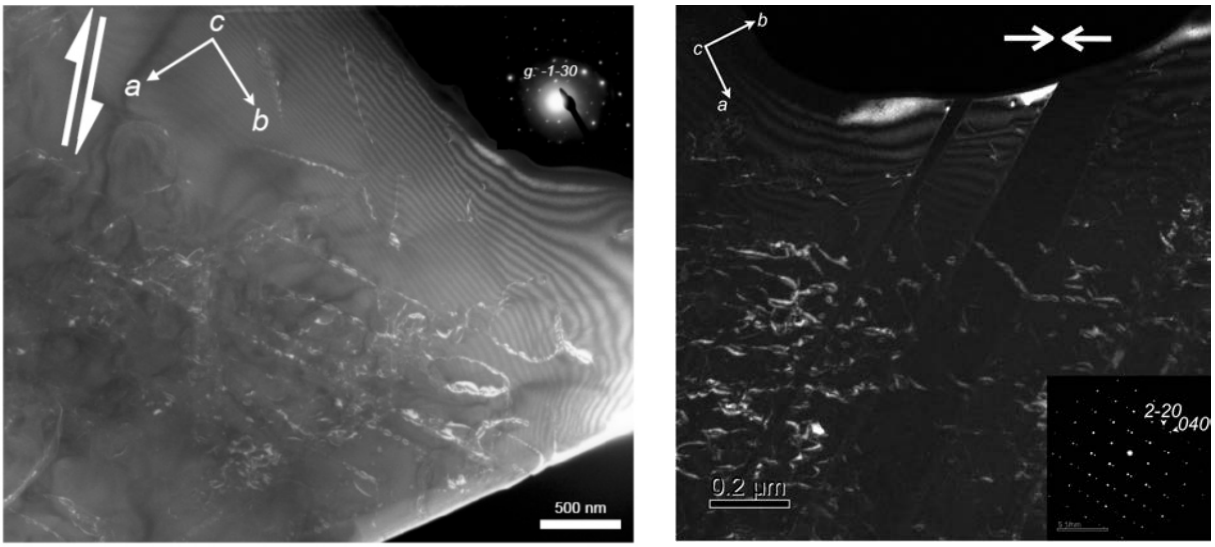

(a) (b)

Fig 3.6-6: Weak-beam dark-field TEM images of the dislocations and (110) twins in the deformed lawsonite. The insets are selected area electron diffraction patterns showing the nearest zone axis in the diffraction conditions containing the diffraction vectors of (a) g: -1-30, (b) g: 2-20 and 040 for respective twin domains.

e. *Deformation fabrics of high-pressure subduction channel rocks from the Eclogite Zone of the Tauern Window (Austria) (R. Keppler and M. Stipp/Kiel, F. Heidelbach)*

The Eclogite Zone (EZ) of the Tauern Window in Austria is a high-pressure metamorphic unit comprising lenses of eclogites in a matrix of gneisses and micaschist. The EZ, which originally formed in the Tertiary during subduction of the Penninic ocean beneath the Adriatic continent, was exposed to pressure-temperature conditions of 2.0-2.5 GPa and 600±30 °C and was exhumed in a very short time span of 1-2 Ma. During this fast exhumation, part of the rock was retrogressed to blueschist facies conditions. The exhumation likely took place in a

so-called subduction channel, a shear zone of a few km thickness above the subducting lithopheric slab. Although subduction channels are widely accepted as viable tectonic regime permitting exhumation of high-pressure rocks, the deformation mechanism within these mélange zones are not well understood.

To gain insights into the deformational processes taking place in subduction channels, two eclogite samples were collected in the EZ and investigated using EBSD analysis and EDX mapping in the SEM. One of the samples is a fresh eclogite (MS112), which still exhibits the high-pressure mineral assemblage and was not subjected to a retrogressive overprint. The other sample is a retrogressed eclogite (RK3), which was exposed to blueschist facies conditions during exhumation. The CPOs of omphacite in both samples, and retrogressive glaucophane were determined. Orientation maps of both samples showed large omphacite porphyroclasts with subgrains, as well as small recrystallized omphacite grains, indicating a dynamic recrystallization. The porphyroclasts in the fresh eclogite sample MS112 exhibit increasing jadeite component from core to rim, and the highest jadeit component is observed in the recrystallized grains. The jadeite components in omphacite primarily indicate pressures during its growth. The increasing jadeite component in the porphyrocrasts and the highest component in recrystallized grains suggest omphacite growth and dynamic recrystallization during subduction at increasing pressure. In the retrogressed sample, on the other hand, the porphyroclasts display decreasing jadeite component from core to rim and low jadeite component in the recrystallized grains, indicating omphacite growth and dynamic recrystallization at decreasing pressures during the exhumation of the rocks.

CPO of the omphacite porphyroclasts in the fresh eclogite MS112 exhibits a girdle distribution of (001) within the foliation plane and point maxima of (010) normal to the foliation (Fig. 3.6-7 top). This is a typical S-fabric of omphacite, indicating oblate strains. CPO of the recrystallized omphacites, on the other hand, displays (001) maxima in lineation direction and (010) girdles perpendicular to the lineation, which is a typical L-fabric of omphacite, indicating prolate strains (Fig. 3.6-7 bottom). This switch from an S-type fabric of the porphyroclasts to an L-type fabric of the recrystallized grains suggestsa transition from oblate to prolate strain during subduction.

CPO analysis of omphacite in the retrogressed eclogite RK3 shows an alignment of (001) in lineation direction and girdles of (010) perpendicular to the lineation, which is an L-fabric pointing to prolate strain, which is identical to the porphyroclasts in the fresh eclogite (Fig. 3.6-8 top). Glaucophane exhibits an alignment of (001) in lineation direction and girdles of (100) perpendicular to the lineation, which is a typical L-fabric of glaucophane and also suggests prolate strain (Fig. 3.6-8 bottom). The matching L-type fabric of omphacite and glaucophane shows that a similar strain regime persisted from the eclogite facies to the retrogressive blueschist facies. These findings yield important insights into the deformation processes within the EZ and subduction channels in general.

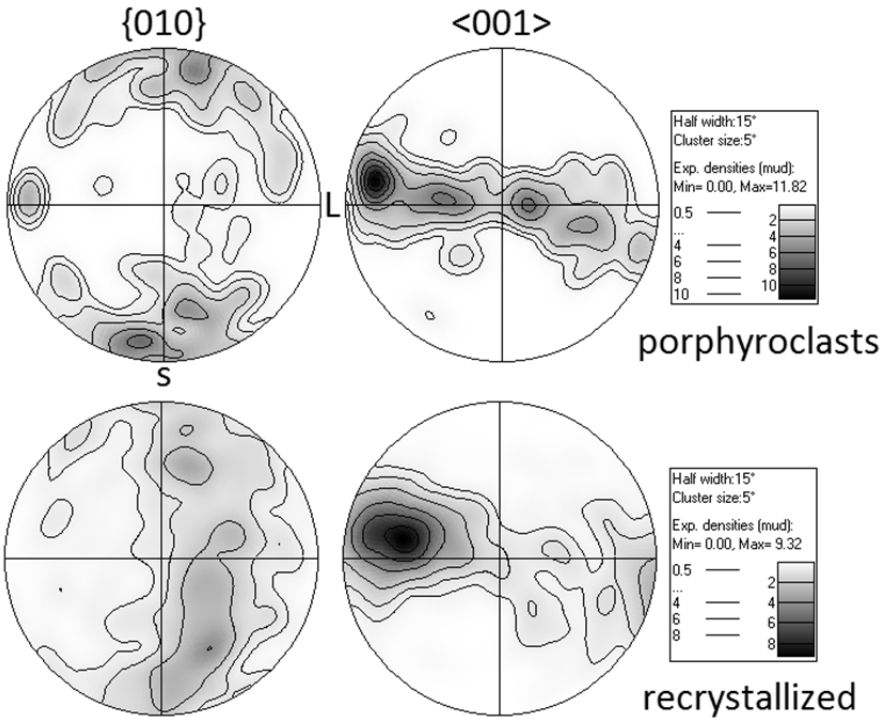

Fig. 3.6-7: CPOs of omphacite porphyroclasts (top) and recrystallized grains (bottom) in the fresh eclogite MS112; note the change from S to L-type CPO; equal area projections, lower hemisphere, foliation normal s is oriented NS, lineation L lies EW.

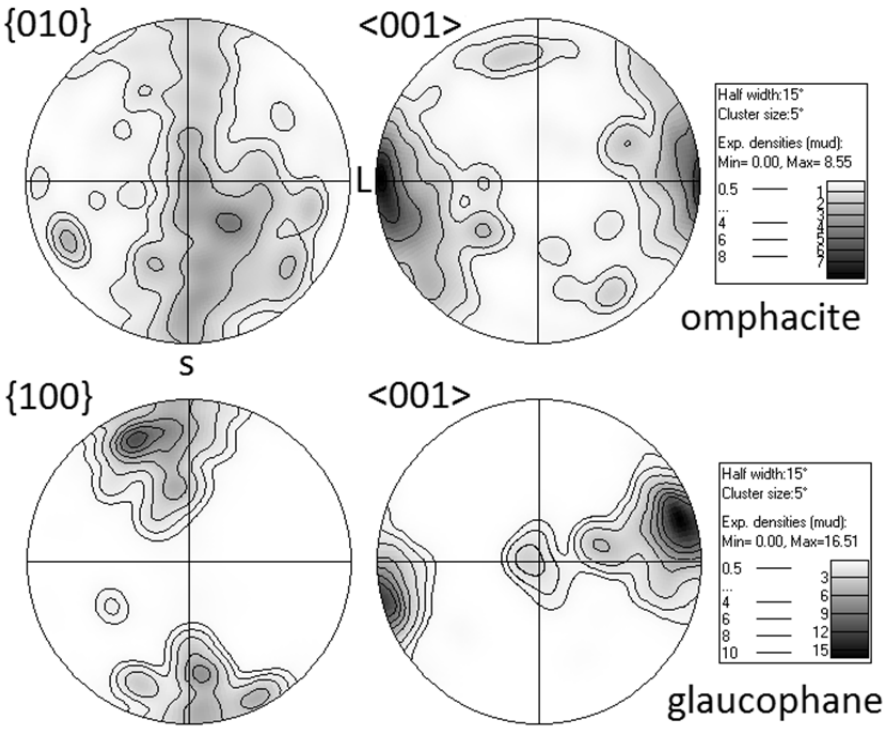

Fig. 3.6-8: CPO of omphacite (top) and glaucophane (bottom) of the retrogressed eclogite sample RK3; orientation of projections is the same as in Fig. 3.6-7.

f. *Deformation of (Mg,Fe)O ferropericlase at lower mantle pressures (H. Marquardt, in collaboration with L. Miyagi/Salt Lake City)*

The Earth's lower mantle, ranging from 660 to 2890 km depth, constitutes more than 50 % of Earth's volume and is the largest geochemical reservoir for many elements. Throughout Earth's history, substantial amounts of material have been exchanged between the deep mantle and Earth's surface and atmosphere. Subduction of oceanic lithosphere is the main process to recycle material from Earth's surface and atmosphere back into the deep mantle. Recent seismic tomography studies suggest that in many subduction systems, such as under South America and Indonesia, slabs broaden and stagnate in the upper 500-1000 km of the lower mantle.

In high strain regions of the lower mantle, such as near subducting slabs and in boundary layers, (Mg,Fe)O ferropericlase, which is the rheologically weakest lower mantle phase, is likely to form an interconnected network. Under these conditions, the overall deformation response will be dominated by ferropericlase even though $(Mg,Fe,Al)(Si,Al)O_3$ bridgmanite is volumetrically more abundant in the lower mantle.

In this project, we studied the deformation behaviour of (Mg,Fe)O ferropericlase to high pressures using synchrotron radial X-ray diffraction at Beamline 12.2.2 at the Advanced Light Source, Berkeley. We performed angle-dispersive, high-pressure radial X-ray diffraction (rXRD) on powders of $(Mg_{0.8}Fe_{0.2})O$. One run was performed in the diamond anvil cell (DAC) with a cubic boron nitride (cBN) gasket at pressures up to 80 GPa, whereas a second run was performed with a Be gasket to 96 GPa to verify that the choice of gasket material that may lead to different stress states does not affect the experimental results. All data were analyzed for unit-cell parameters, elastic strains, and lattice preferred orientation.

From our experiments, we estimated the flow strength, *i.e.*, a mesure of the resistance against plastic flow, of $(Mg_{0.8}Fe_{0.2})O$ at pressures of the lower mantle. We find that the flow strength increases by a factor of 3 at pressures from 20 to 65 GPa (Fig. 3.6-9). The discrepancy between our results and an earlier study on $(Mg_{0.83}Fe_{0.17})O$ is likely related to the experimental limitations in the previous study, which was performed in energy dispersive mode with a single element detector. We note that we observe highly consistent results in two different experimental runs using two different gasketing materials.

The observed increase in ferropericlase strength will generally increase mantle viscosity in high-strain regions, where ferropericlase forms an interconnected network. We used our experimental data for the strength of ferropericlase to calculate a viscosity profile using previously developed models that allow us to extrapolate room temperature, high-strain measurements to lower mantle conditions. Our model indicates a strong increase of lower mantle viscosity by 2.3±0.3 orders of magnitude in the upper 900 km of the lower mantle (Fig. 3.6-10). Such a strong viscosity increase can lead to stagnation of sinking slabs in the shallow lower mantle. At depths > 1500 km, the change of viscosity with depth becomes smaller. Below 1800 km depth, the iron spin crossover in ferropericlase may lead to a reduction in mantle viscosity because of enhanced element diffusion rates.

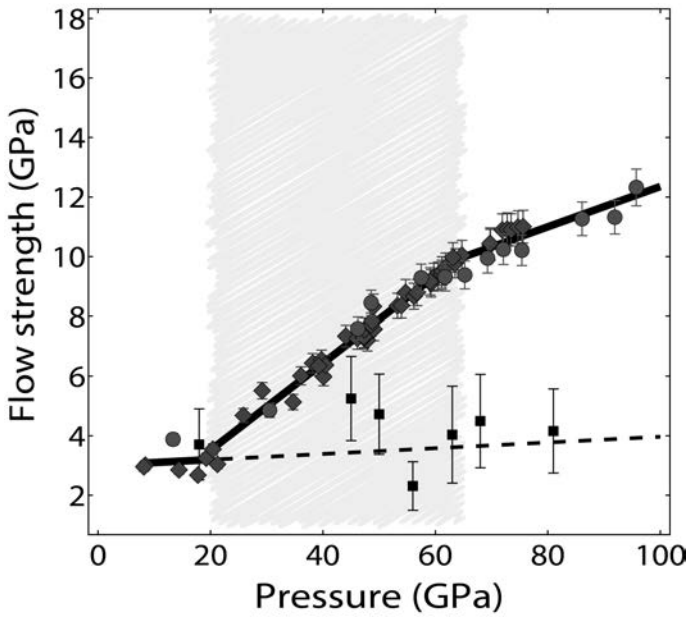

Fig. 3.6-9: Flow strength of lower mantle $(Mg_{0.8}Fe_{0.2})O$ ferropericlase measured in a Be-gasket (circles) and in a cBN gasket (diamonds). Solid lines are linear fits to data in the pressure ranges < 20 GPa, 20-65 GPa, and > 65 GPa. The dashed line is a linear extrapolation of our data collected at pressures < 20 GPa. Literature radial X-ray diffraction data on $(Mg_{0.83}Fe_{0.17})O$ are shown as squares for comparison (Lin *et al.*, 2009, PCM, 36, 585-592).

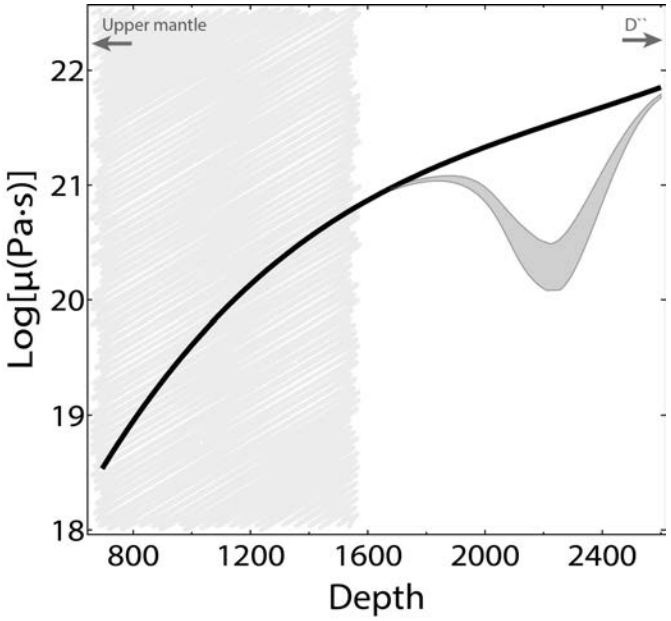

Fig. 3.6-10: Calculated viscosity profile for the lower mantle near subducting slabs. The viscosity calculation is performed assuming a simplified lower mantle assemblage with 80 vol. % bridgmanite and 20 vol. % of ferropericlase. The hatched region corresponds to the pressure range where the increase in flow strength was observed in our experiments. The shaded region illustrates a potential decrease of viscosities related to enhanced element diffusion rates caused by the iron spin crossover in ferropericlase.

The increase of viscosity in the shallow lower mantle is presumably reversible upon changes in pressure and thus unrelated to the past history of mantle convection. It can, therefore, provide a mechanism that leads to broadening and stagnation (or at least long residence time) of slabs in the shallow lower mantle and can help to produce distinct geochemical reservoirs in the Earth's lower mantle that are stable over geological time.

g. *The influence of the elastic properties of ices on the early differentiation of ice satellites (A.S. Pakhomova, T. Boffa Ballaran, A. Kurnosov and D.J. Frost, in collaboration with M. Leoni/Trento)*

Icy compounds of water, ammonia and methane, together with hydrogen and helium are the major constituents of planets and their satellites in the outer solar system. They comprise the bulk of Uranus and Neptune, and also form significant portions of the 22 major satellites orbiting the giant planets. These satellites, which are believed to have been accreted mainly before the dissipation of the solar nebula, are of particular interest to planetary science because they show a wide range of geological features including evidence for liquid oceans, active plate tectonics and volcanism. These extraterrestrial bodies have followed quite different processes of accretion, differentiation and early evolution. For example, among Galilean moons, Ganymede is fully differentiated with a metallic core, a rocky mantle, and an overlaying icy mantle and crust, whereas Callisto reveals an undifferentiated interior. The same applies to Saturn's satellites: Rhea's interior consists mostly of homogeneous mixture of ices and rocks, whereas Titan is likely differentiated with evidence of current cryovolcanic activity. In order to explore early dynamic processes that have led to varying degrees of differentiation of the interiors of different satellites, constraints on the viscosity of ice materials are required. Mechanical properties of materials are usually obtained in laboratories from polycrystalline aggregates deformation experiments. Our aim is to adopt a novel approach that makes use of high-pressure single-crystal X-ray diffraction to determine strain-stress relationships.

In order to fully benchmark this method, we have started a study of ice VI whose elastic properties and rheology are well known. A single crystal of ice VI (Fig. 3.6-11) has been grown *in situ* inside a four-screw DAC at room temperature. Firstly, water was loaded in the hole inside the indented rhenium gasket. Pressure was then increased to 1 GPa, where the formation of a number of ice VI crystals has been optically observed. At this point, the DAC was externally heated at 70 °C to melt all crystals except one which was left to grow at room temperature for a couple of days. Single-crystal X-ray diffraction experiments of ice VI were performed in the pressure range between 1.0 and 2.1 GPa with an average step size of 0.1 GPa. At every pressure step, the crystal was examined using a Huber 4-circle diffractometer to measure accurate unit-cell lattice parameters and to investigate broadening effects due to local stresses by analyzing θ- and ω-profiles of selected reflections. Data collections for structural refinements were performed by means of an Oxford XCalibur diffractometer with CCD detector at pressures of 1.0, 1.6 and 1.9 GPa. Above 1.1 GPa broadening of all reflections has been observed as well as appearance of extra peaks. Analysis of such complex

profiles and precise mapping of reflections in reciprocal space are at the moment under study in order to obtain insight on the possible mechanisms for accommodating local stresses during the compression of ice VI.

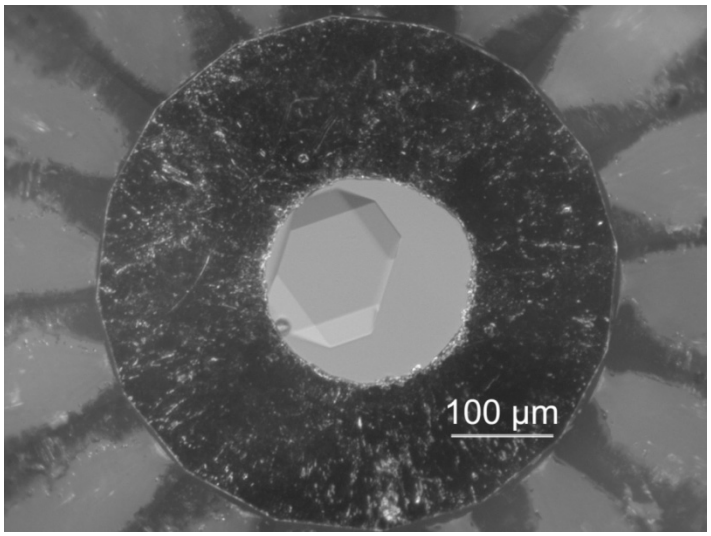

Fig. 3.6-11: Single crystal of ice VI grown inside the DAC.

h. *Pressure dependence of [100](010) and [001](010) dislocation mobility in natural olivine (L. Wang, Zs. Pintér, S. Blaha, R.J.M. Farla, T, Kawazoe and T. Katsura)*

Seismic studies show that, although the upper mantle down to 200 km depth has strong anisotropy in seismic wave velocities, this anisotropy rapidly decreases down to 300 km depth. Since olivine is the most abundant mineral in the upper mantle and it is elastically anisotropic, seismic anisotropy should be mainly caused by lattice preferred orientation (LPO) of olivine. Under this hypothesis, the decrease in anisotropy should be explained by change in olivine LPO with depth. Therefore, an open question is whether creep rates by different slip systems of olivine have different pressure dependences or not, because LPO should form by creep by a dominant slip system.

Change in slip systems with pressure was reported by studies based on deformation experiments. However, stresses and strain rates in the deformation experiments are by far higher than those in natural conditions. Therefore, deformation processes in the deformation experiments could be different from those in the Earth's mantle. To avoid this problem, we have adopted dislocation recovery experiment, in which dislocation annihilation rates, which are proportional to dislocation mobility, are measured under quasi-hydrostatic conditions. In this study, the annihilation rates of dislocations in the [100](010) and [001](010) systems (hereafter ***a***- and ***c***-dislocations, respectively) are measured under different pressures in the following way to investigate the pressure dependence of these two slip systems.

Oriented olivine single crystals were deformed at a pressure of 3 GPa and a temperature of 1600 K under simple shear geometry so that ***a***- or ***c***-dislocations were produced. The deformed crystals were annealed at 2, 7, and 12 GPa at 1650 K from 360 to 1426 min.

Dislocation densities before and after annealing were measured by the oxidation-decoration technique using an SEM. It was found that the majority of the ***a***-dislocations are edge dislocations with the Burgers vector of [100] and dislocation line elongated in the [001] direction, whereas those of the ***c***-dislocations are screw dislocations with the Burgers vector of [001] and dislocation line also elongated in the [001] direction. These results were confirmed by TEM observation. Based on these observations, densities of both dislocations were measured on the (001) planes. The dislocation annihilation rate (k) was obtained from the following equation, $k = (1/\rho_f - 1/\rho_i)/t$, where ρ_f and ρ_i are the dislocation densities after and before annealing respectively, and t is the annealing time.

Examples of changes in densities of ***a***- and ***c***-dislocations are shown in Fig. 3.6-12. Their dislocation annihilation rates are shown against pressure in Fig. 3.6-13. By fitting the data to the Arrhenius equation, the activation volumes for ***a***- and ***c***-dislocations, V_a and V_c, are found to be V_a= 2.7±0.2 and V_c = 2±1 cm^3/mol, respectively. Thus, the activation volumes of dislocation mobility in these two types of dislocations are identical within experimental errors. It is therefore concluded that the pressure-induced slip-system transition between these two slip systems is unlikely.

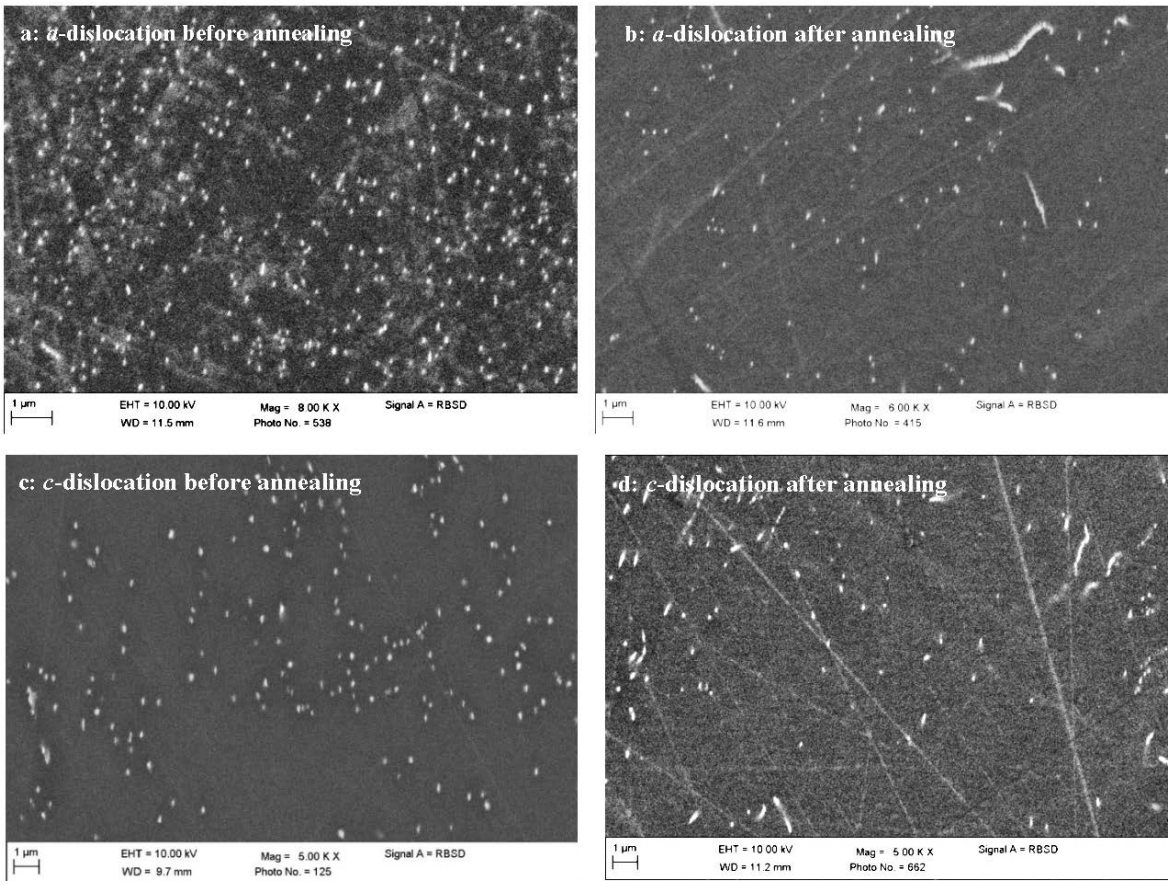

Fig: 3.6-12: BSE images showing the dislocation structures before and after annealing on the (010) planes. (a) and (b): ***a***-dislocations, (c) and (d): ***c***-dislocations. (a) and (c): before annealing, (b) and (d) after annealing The large decreases in dislocation density by the annealing are observed.

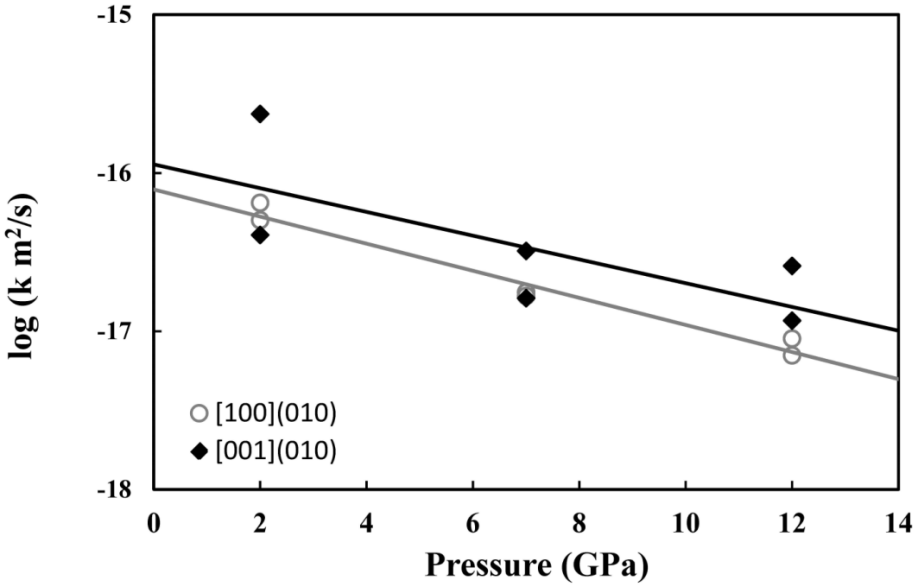

Fig: 3.6-13: Dislocation annihilation rate constants (*k*) in the [100](010) (open circle) and [001](010) (solid diamond) slip systems against pressure.

i. *Dislocation mobility of olivine as a function of water content (S. Blaha and T. Katsura)*

Plastic deformation is among transport mechanisms, which are controlled by the motion of defects such as point defects, dislocations, and grain boundaries. In the upper mantle, dislocation creep is considered to be the dominant mechanism, and driven by motion of dislocations. Understanding of dislocation mobility is therefore essential to investigate mantle dynamics.

Many deformation experiments have demonstrated that creep rates dramatically increase by incorporation of water, proportional to the water content raised to the power of 1.2. However, deviatoric stresses and strain rates in deformation experiments are far higher than those in upper mantle, and therefore previous results should be examined by an independent technique. In this study, water-content dependence of dislocation mobility is estimated by means of the dislocation-recovery technique. In this technique, olivine crystals are deformed to form dislocations, doped with water, and then annealed under quasi-hydrostatic conditions, as explained below.

The olivine crystals were deformed by simple shear in the [100] direction on the (010) plane at a temperature of 1600 K and a pressure of 3 GPa. These crystals were placed in graphite capsules surrounded by mixtures of talc and brucite, which are on one hand the water source and on the other hand controlling the silica activity, to dope with water at a temperature of 1500 K and a pressure of 3 GPa. This setup allowed recovery of an olivine single crystal without significant decompression cracks. The water-doped, deformed olivine crystals were annealed at a temperature of 1500 K and at a pressure of 3 GPa to annihilate dislocations by

adopting the same setup as for the hydration experiments, so that the chemical conditions (oxygen fugacity and silica activity) were similar to those of the water-doping experiment. FTIR-measurements of the recovered samples reproduce the features of FTIR spectra that are reported from olivine of mantle peridotite xenoliths.

Dislocation densities of the samples were obtained by the oxidation decoration technique (Fig. 3.6-14). The dislocation annihilation rates were obtained from the dislocation densities before and after the annealing and duration of the annealing by the following equation: $1/\rho_i - 1/\rho_f = kt$, where ρ_i is the dislocation density before the annealing, ρ_f is the dislocation density after the annealing, k is the dislocation annihilation rate, and t is the duration of the annealing. Figure 3.6-15 shows the water content dependence of the annihilation rate, which is considered proportional to the dislocation mobility, in this study. The annihilation rate (and mobility) is found to be proportional to the water content raised to the power of 1.2, which agrees to the results of the deformation experiments.

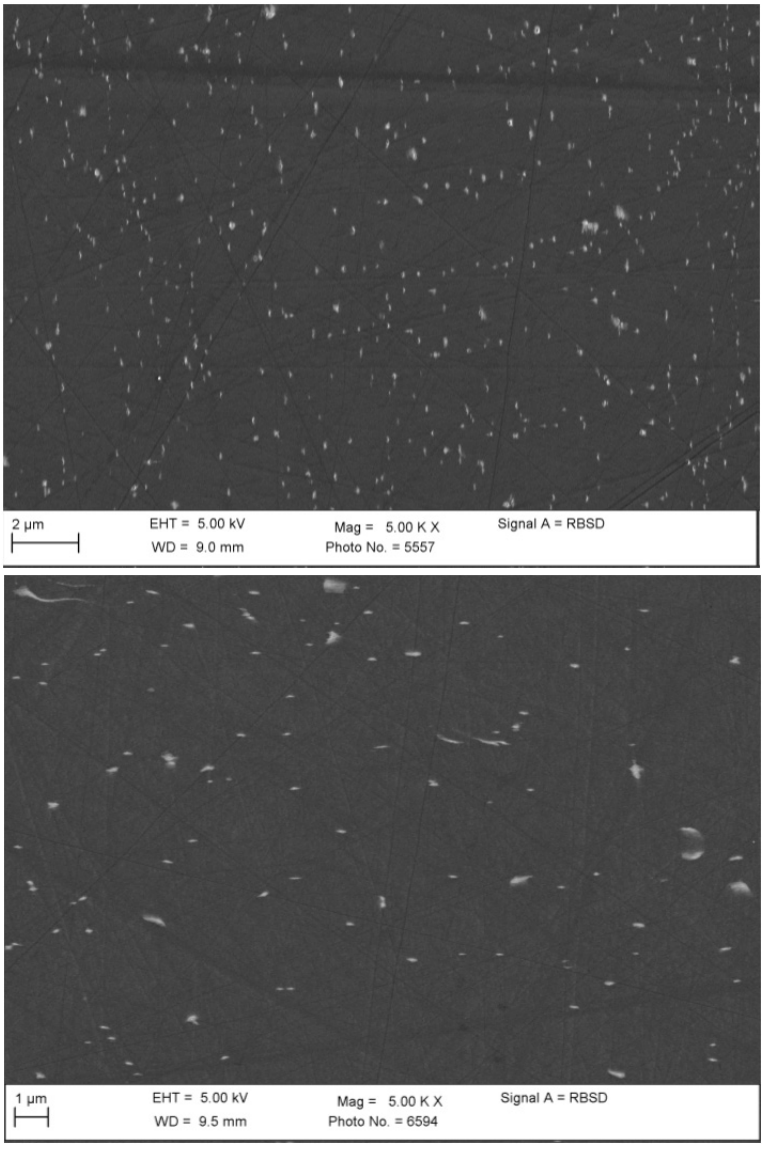

Fig. 3.6-14: BSE images of the oxidation-decorated dislocations before (a) and after (b) annealing at a temperature of 1200 K and a pressure of 3 GPa.

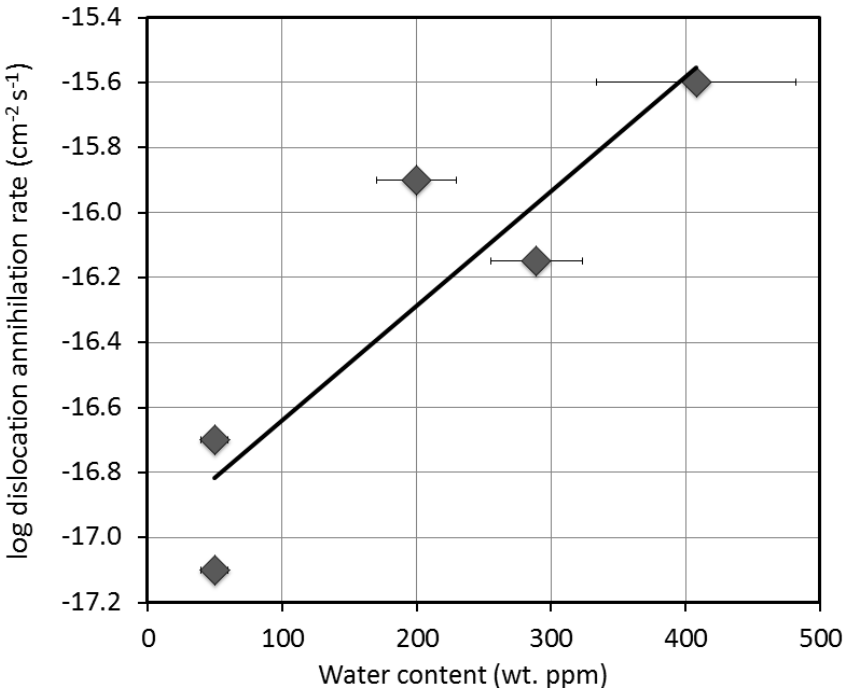

Fig. 3.6-15: Dislocation annihilation rate in the [100](010) slip system at a temperature of 1500 K and a pressure of 3 GPa as a function of water content.

3.7 Materials Science

Historically, experiments at high pressures and temperatures were first developed to investigate processes in the Earth's deep interior. The interpretation of such results and an interest in modeling the state of matter at very deep planetary interiors were among the reasons for advances of theoretical methods, including *ab initio* simulations. Subsequently physicists, chemists and material scientists started to use the methods developed by Earth scientists to study different classes of compounds at extreme conditions. At the Bayerisches Geoinstitut a combination of expertise in theoretical approaches, high-pressure equipment and analytical techniques is available making sophisticated and challenging research possible that addresses the physics and chemistry of materials at high pressure. In this chapter of the annual report, we present results of studies of various classes of solids: metallic, semi-conducting and insulating elements, oxides and manganites.

The first two contributions in the chapter present computational work, both at ambient pressure. In the first, a newly developed exchange potential is applied to a wide range of solids to explore the resulting changes in electronic structure, both directly in the band structure and more indirectly in the dielectric constant. A significant improvement in the description of Mott insulators in comparison to other semi-local exchange correlation functionals is found, opening a band gap for those materials investigated: Ge, α-Sn and CdO. The second contribution considers lattice vibrations in aluminium at high temperature, comparing trajectories of molecular dynamics simulations with the atomic displacements achieved in a newly developed self-consistent *ab initio* lattice dynamics (SCAILD) method. While the SCAILD method goes beyond the harmonic approximation, the displacements stay harmonic inherently, accessing significantly fewer states than molecular dynamics.

Controllable doping remains the main way to modify the electronic properties of materials, including silicon, one of the most important technological materials. Developing methods of silicon doping with boron may open new technological opportunities, and thus numerous studies were devoted to investigations of the solubility limits of boron in silicon at different conditions and physical properties of the resulting alloys. However, the solubility of boron atoms in the diamond-structured silicon matrix is surprisingly low, usually below 0.5 at. %: Creating $Si_{1-x}B_x$ alloys with a high boron content is technically challenging. The third contribution in the chapter demonstrates that synthesis at high pressure and high temperature allows the creation of silicon with 2.4 at. % of boron. Similarly important in the high-pressure/high-temperature synthesis of materials is the starting material, determining – among other things – the crystallinity of the synthesized material. This is well documented for diamond with different crystallinity being formed from a wide range of carbon allotropes. In the fourth contribution to this chapter glassy carbon balls are used to synthesize spherical nano-diamonds in a targeted way, tuning the synthesis conditions for optimal outcome. Further synthesis experiments and analysis of the created phases are reported in the following two contributions for two new high-pressure transition metal sesquioxide phases of Mn_2O_3 and In_2O_3. These materials combine relatively high hardness, interesting electronic and optical properties, making them potentially important for different applications.

Multiferroic materials have been at the focus of intensive scientific research in solid state physics and chemistry for a couple of years. Multiferroic materials demonstrate the coupling of electric and magnetic properties and are important for the development of new electronic devices in which optical properties or magnetism is controlled by an electric field. Manganites are important members of the multiferroic family, and in the final contribution the high-pressure phase stability and behaviour of YMn_2O_5 and $BiMnO_3$ are investigated.

a. *Improved description of the DFT eigenstates and dielectric constants with a semi-local exchange functional (V. Vlček and G. Steinle-Neumann; L. Leppert and S. Kümmel/Bayreuth; R. Armiento/Linköping)*

Density functional theory (DFT) provides an exact description of the ground state properties of matter. In the Kohn-Sham (KS) approach to it the many-body wave function is substituted with a set of eigenstates $|\psi_i\rangle$ with eigenenergies ϵ_i while the KS Hamiltonian is typically separated into four terms to form the KS equations:

$$\left(\hat{T} + \hat{V}_H + \hat{V}_{ext} + \hat{V}_{xc}\right)|\psi_i\rangle = \epsilon_i|\psi_i\rangle, \quad (1)$$

where $\hat{T}$ is kinetic energy operator, $\hat{V}_H$ is Hartree potential term, $\hat{V}_{ext}$ external potential term and $\hat{V}_{xc}$ exchange-correlation term (xc) that captures the mutual interactions among the electrons. The exact form of $\hat{V}_{xc}$ is not known in general and it has to be approximated in practice. In the KS approach, commonly used local and semi-local approximations are however unable to reproduce an important feature of the generally unknown exact xc functional: the derivative discontinuity Δ. This discontinuity is a constant jump in the potential upon variation in the number of electrons in the system. As such it represents a change in the chemical potential upon charge addition (or removal) and thus significantly contributes to the fundamental band gap

$$E_g = E_g^{KS} + \Delta, \quad (2)$$

where E_g^{KS} is the KS eigenvalue gap.

Recently, Armiento and Kümmel have proposed an energy functional for exchange only (AK13) that exhibits a derivative discontinuity for finite systems (atoms and molecules) but is semi-local in nature – *i.e.*, it stays fully within the KS framework. The functional was derived to reproduce some important exact properties of $\hat{V}_{xc}$. As a result, the description of the KS eigenstates is improved which in turn leads to a better description of the dielectric properties and qualitatively changes the band structures, *e.g.*, opening of a KS band gap E_g^{KS} for materials that are spuriously described as metallic by other (semi-)local functionals. The improved description of the band structures for solids can be illustrated on germanium, CdO and the α-polymorph of Sn; all the systems mentioned have small E_g and the effect of Δ is presumably substantial. Calculations with standard (semi-)local functionals predict zero (or

vanishing) E_g^{KS} for these three systems. Such functionals lack Δ by construction, *i.e.*, they fail to describe the qualitative nature of those systems. On the other hand, AK13 opens E_g^{KS}, as illustrated in Fig. 3.7-1, while still fulfilling the condition that $E_g^{KS} < E_g$ due to the lack Δ in periodic systems even with AK13.

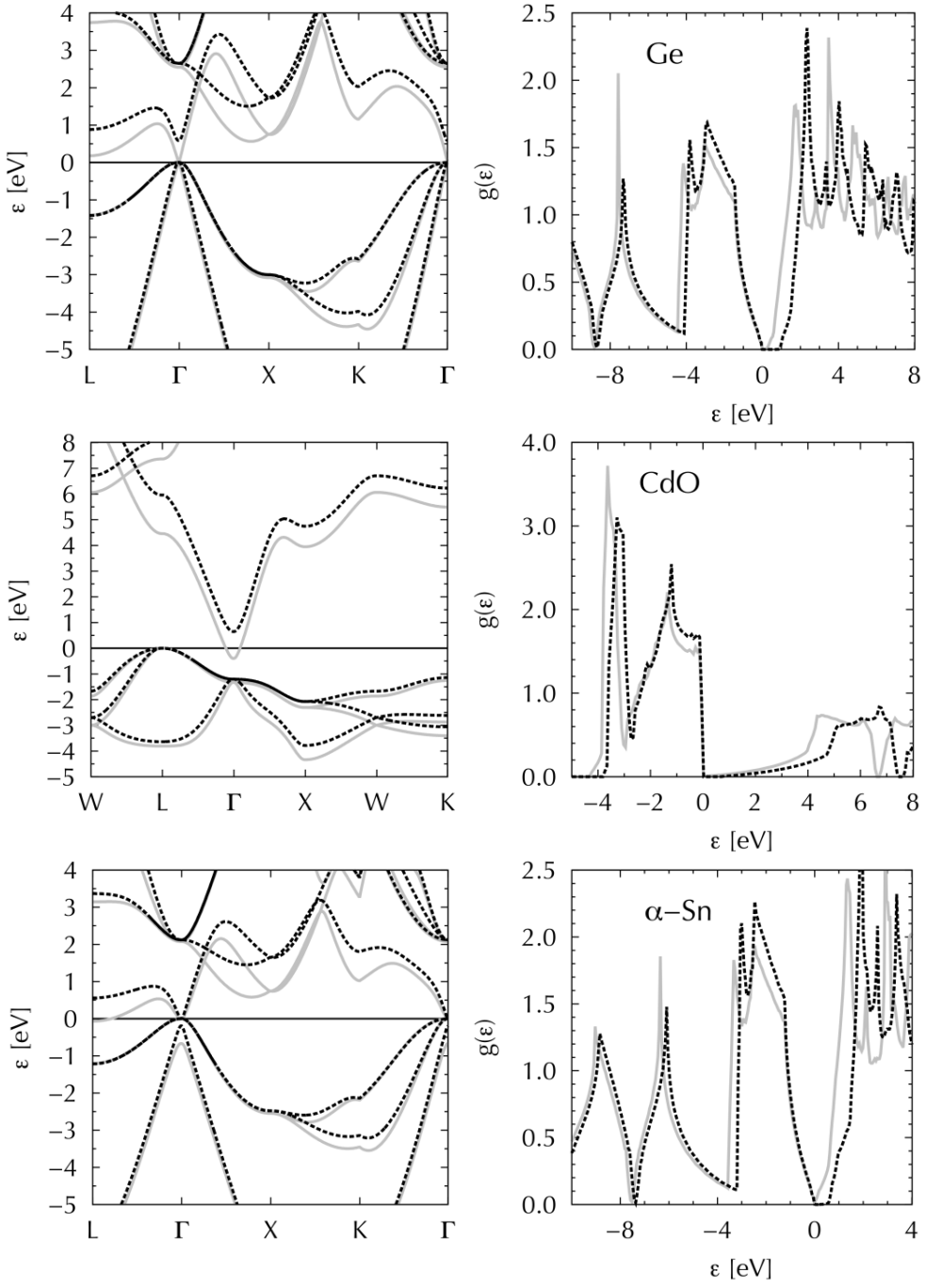

Fig. 3.7-1: Band structure (left) and the density of states (right) for Ge (top), α-Sn (middle) and CdO (bottom). Results of the calculations with the commonly used generalized gradient approximation to the xc energy functional are shown with a solid grey line, dashed black lines represent the AK13 results. The Fermi energy is chosen as the zero of energy, and is also indicated by the horizontal line for the band structure.

The improved description of the dielectric response is illustrated in Fig. 3.7-2 using a wider set of materials. It is worth noting that while for large E_g insulators (ionic crystals, for instance) standard semi-local xc energy functionals perform well, they fail for the small gap semiconductors. This failure is rectified by the AK13 functional, which gives excellent agreement between DFT and experimental values of the dielectric constant.

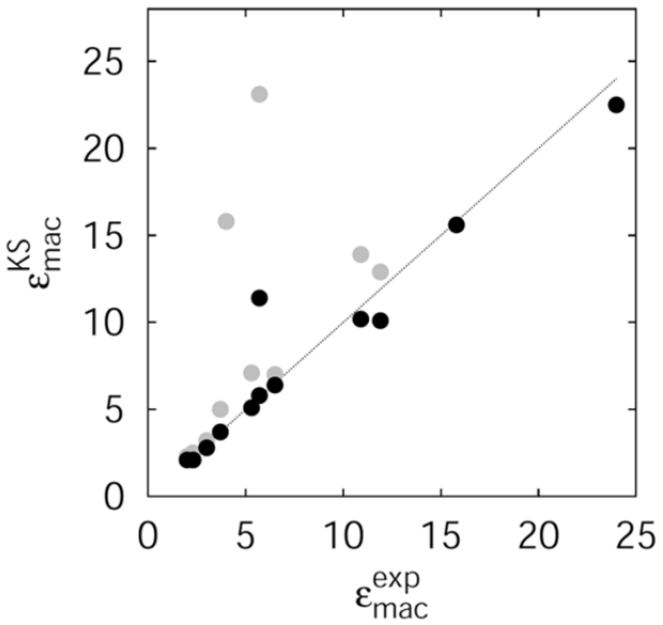

Fig. 3.7-2: Macroscopic dielectric constant for a wide set of materials from experiments (x-axis) and KS calculations (y-axis). Computational results of ε_{mac}^{KS} are obtained at the DFT level (*i.e.*, beyond the random-phase approximation) applying a commonly used generalized gradient approximation to the xc energy functional (grey circles) and the AK13 functional (black circles). The 1:1 correspondence is shown by the dotted line. The materials investigated include semiconductors, transition metal oxides and ionic crystals.

b. *Structure of aluminium at high temperature comparing molecular dynamics and self-consistent* ab initio *lattice dynamics results (L. Wang, G. Steinle-Neumann and V. Vlček)*

In computational solid state physics two different approaches to high-temperature properties are typically applied: molecular dynamics (MD) and lattice dynamics (LD). While both use supercells of the crystal structure studied and displace atoms from their equilibrium positions, the fundamental approach is quite different. In LD the displacement is that of individual atoms along crystallographically defined direction and the harmonic approximation is used to compute the dynamical matrix and consequently phonon frequencies and thermodynamic properties via the vibrational free energy. In MD, by contrast, all atoms are displaced according to the forces acting on them and thermodynamic properties are computed through ensemble averages. Due to their restrictions – harmonic and classical approximation, respectively – LD can be expected to give reliable results below the Debye temperature Θ_D, while MD performs well at higher temperatures. The association of computed eigenmodes with phonons and the shorter simulation time required make the extension of the LD approach to higher temperatures desirable, and recent methodological developments allow the inclusion of phonon-phonon interactions when computing the mode frequencies, allowing the displacement of all atoms in the supercell, similar to MD. This has been implemented in the self-consistent *ab initio* lattice dynamics (SCAILD) method, which has been successfully

applied to a number of problems in solid state physics. Here we evaluate the different simulation methods by looking in detail at the dynamics of atoms in solid (fcc) Al at ambient pressure as a function of temperature using both the SCAILD and MD methods.

As expected, differences in phonon frequencies between the quasi-harmonic lattice dynamics method and the SCAILD method increase with temperature, with the SCAILD frequencies showing significantly higher frequencies due to phonon-phonon coupling. When analyzing the displacement for SCAILD and MD simulations in detail through the radial distribution function (Fig. 3.7-3) – *i.e.*, the distance distribution between the atoms in the cell – differences become apparent. The displacements computed by the SCAILD method yields RDFs that are centered right on top of the equilibrium distances and symmetric around it, while the RDFs from the MD simulations show a nearest neighbor peak that is shifted to smaller distances and the RDF is asymmetric around the maximum, with more distances plotting at larger distances. Peak amplitudes of nearest and higher-order neighbor distances, however, are similar between the SCAILD and MD results. The SCAILD results reveal the inherent harmonic character of the method, even in the presence of phonon-phonon interactions. The asymmetry of the RDF in the MD runs is typical of MD results in that there is an increase in the background with growing distance.

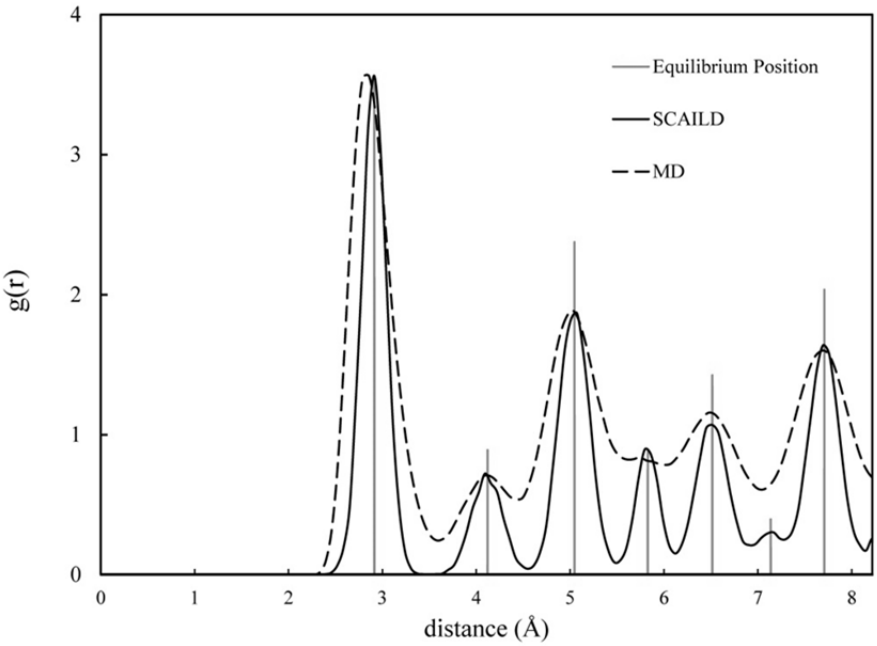

Fig. 3.7-3: Radial distribution function for the ideal crystal, MD and SCAILD methods at 900 K. Broadening of the peaks in the RDF from MD and SCAILD simulations is due to atomic displacements from the equilibrium positions.

When considering the mean square displacement (MSD) of the atoms from their equilibrium position (Fig. 3.7-4), a similar picture emerges: at high temperature the MSD from the MD simulations is significantly larger than that from the SCAILD method, while at 500 K both are

similar. It is remarkable though that the MSD computed from Debye-Waller factors is smaller yet than that of the SCAILD method, suggesting that phase space sampled in experiments is smaller than that in the simulations.

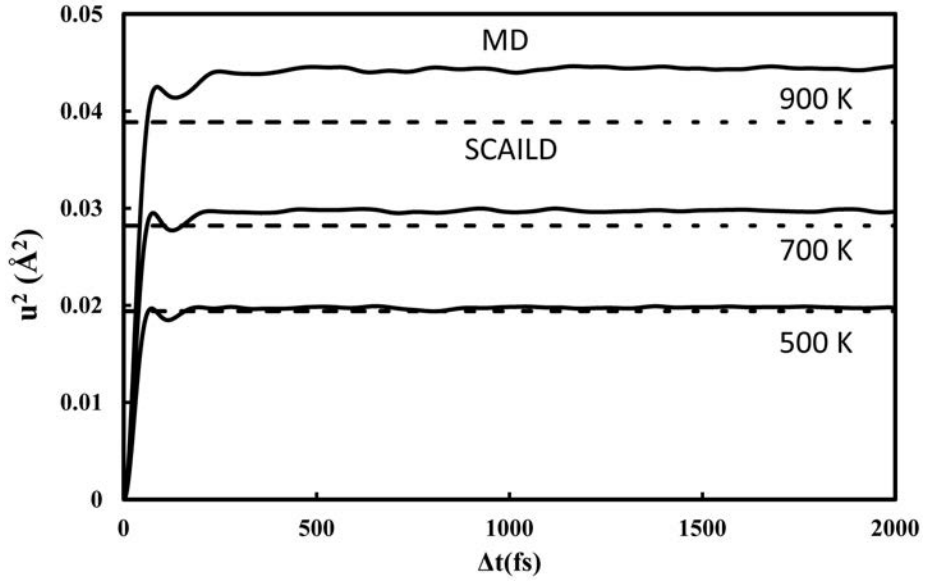

Fig. 3.7-4: Mean square displacement vs. time difference interval Δt at different temperatures in the MD and SCAILD simulations.

c. *Bulk silicon crystals with high boron content, $Si_{1-x}B_x$, and their metallic conductivity (S.V. Ovsyannikov, H. Gou, Y. Nakajima and L.S. Dubrovinsky; A.E. Karkin and V.V. Shchennikov/Yekaterinburg, R. Wirth/Potsdam, V. Dmitriev/Grenoble, N.A. Dubrovinskaia/ Bayreuth)*

Silicon remains an important technological material because of a combination of its unique and tunable semiconducting properties and low-cost methods of its production. Modifying the electronic properties of silicon is thus a potential route to new applications, *e.g.*, by controlled doping. Combining 'simple' silicon and 'enigmatic' boron for the creation of new advanced silicon-based materials with tunable optoelectronic properties was one of the early original strategies in the field. However, solubility of 'small' boron atoms in the silicon matrix is surprisingly low, usually below 0.5 at. %, and thus, creating $Si_{1-x}B_x$ alloys with high boron content adopting the diamond-type structure is technically challenging. In the current work we treated Si-B samples at high-pressure and high-temperature (HP-HT) conditions and found that we can prepare bulk $Si_{1-x}B_x$ alloys with x as high as 0.024 this way.

The samples of Si:B were prepared from silicon (Aldrich Chem. Corp. Inc., 99.9999 % purity) and β-boron crystals (Chempur Inc., 99.5 % purity) by HP-HT synthesis using both the piston-cylinder and multianvil press. We have performed more than a dozen of HP-HT synthesis runs at different HP-HT conditions below and above the melting curve of silicon.

We found that samples treated well above the melting point of Si at high pressures of several GPa demonstrate very unusual Raman spectra. At the same time, the samples treated at moderate high temperatures below the melting point of silicon, showed the conventional Raman spectra of crystalline Si.

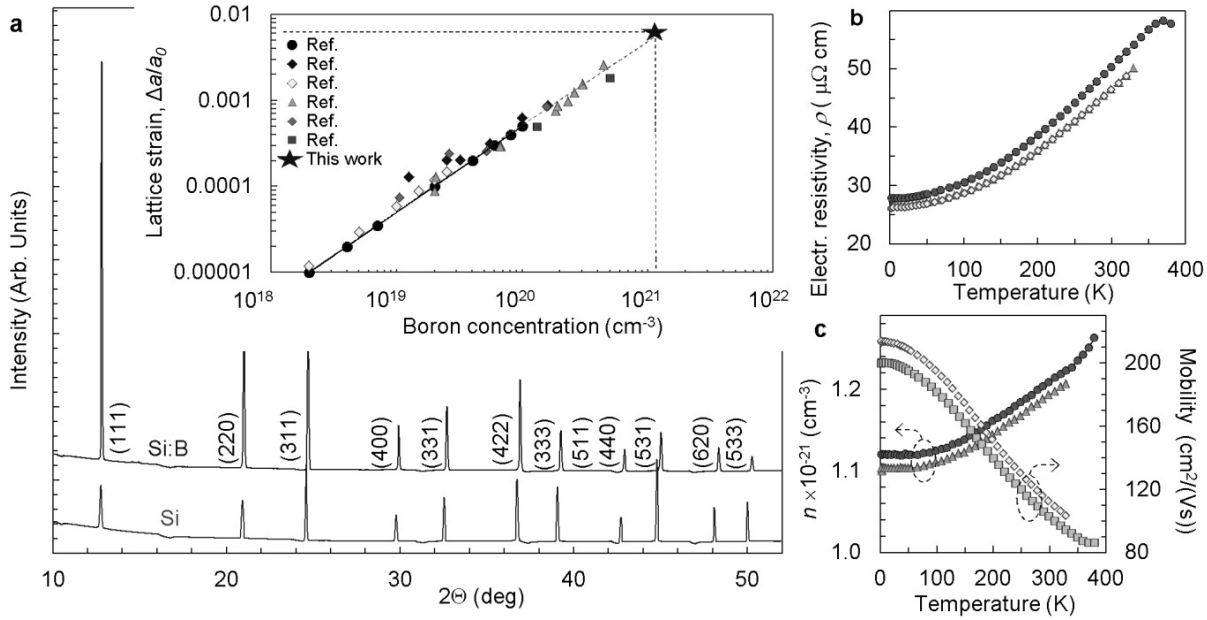

Fig. 3.7-5: Characterization of structural (*a*) and electronic transport properties (*b*, *c*) of boron-doped silicon. (*a*) Comparative X-ray diffraction patterns for two $Si_{1-x}B_x$ samples and a silicon standard collected at ambient conditions. The upper inset plots available literature data on lattice strain in Si:B induced by Si/B substitution. The temperature dependence of electrical resistivity (*b*), and carrier concentration and mobility (*c*) for $Si_{1-x}B_x$ samples. The carrier concentration data correspond approximately to the boron content in Si which weakly depends on temperature (*e.g.*, $x \sim 2.4$ at. % in $Si_{1-x}B_x$ at 300 K).

At the moment, there are three common experimental approaches to determine the composition of $Si_{1-x}B_x$ alloys with the diamond-type structure: (*i*) from Vegard's law (the linear dependence of the lattice parameter of $Si_{1-x}B_x$ vs boron concentration); (*ii*) from the Hall effect; (*iii*) from electrical resistivity values. We investigated structural and electronic transport properties of our $Si_{1-x}B_x$ samples, using all three methods. X-ray diffraction confirmed that the bulk samples of $Si_{1-x}B_x$ adopt the cubic diamond-type structure with a slightly reduced lattice constant (Fig. 3.7-5a). In the best samples we established the lattice parameter to be as low as 5.3967(1) Å *vs* 5.4305(3) Å in the undoped Si crystals. Vegard's law (inset in Fig. 3.7-5a) suggests that this lattice strain (~ 0.0063) corresponds to a boron concentration larger than ~ 10^{21} cm^{-3}. The temperature dependence of electrical resistivity and Hall effect in these samples confirm the metallic character of the electrical conduction (Fig. 3.7-5b,c). The positive sign of the Hall effect indicates *p*-type conductivity as expected for B-

doping. We determined the carrier concentration at ambient conditions as $n \sim 1.2 \times 10^{21}$ cm^{-3}, corresponding to 2.4 at. % of boron (Fig. 3.7-5d). Thus, we prepared the diamond-structured bulk $Si_{1-x}B_x$ alloys with the highest boron content ever achieved $x \sim 0.024$.

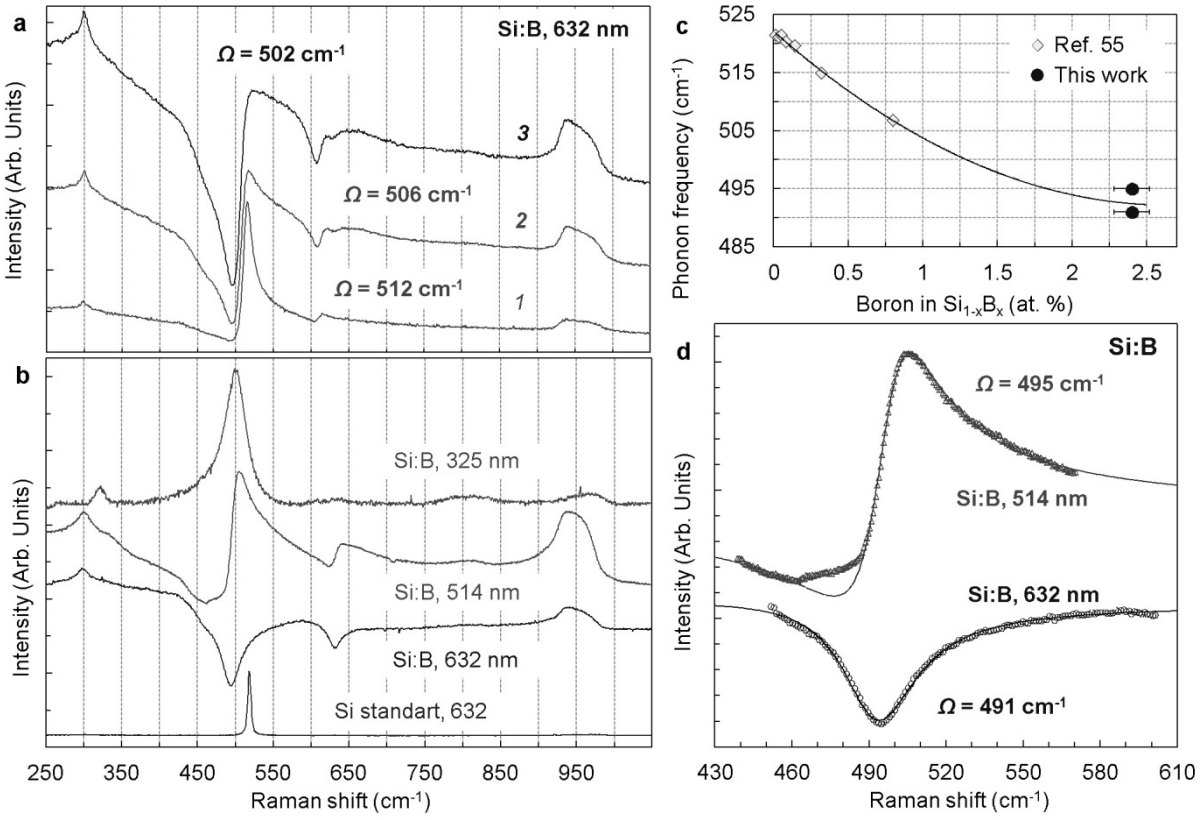

Fig. 3.7-6: Raman spectroscopy of $Si_{1-x}B_x$ at ambient conditions. (*a*) Samples with non-uniform boron distribution. This plot qualitatively shows that an increase in the boron content suppresses the main Si peak at ~ 521 cm^{-1} and enhances the background (from spectra 1 to 3). The inset shows an enlarged section of the spectrum *3* in the vicinity of peaks related to Si-B vibrations. (*b*) Sample with high and uniform boron distribution shows that parameters of the Fano interference strongly depend on the excitation energy. (*c*) The intrinsic phonon frequency (Ω) in $Si_{1-x}B_x$ *vs* B content. (*d*) Determination of the critical (intrinsic) frequency (Ω) in $Si_{1-x}B_x$ using Fano's theory.

We examine the optical properties of bulk $Si_{1-x}B_x$ alloys by means of Raman spectroscopy. The changes in the Raman spectra in the vicinity of the first-order Raman phonon mode of Si at 520 cm^{-1} (Fig. 3.7-6a,b) are related to a Fano-type interference between the discrete phonon line of Si and a continuum of electronic excitations related to the B dopants. Our samples show a distinct anti-resonance near 500 cm $^{-1}$ instead of the typical phonon peak (a spectrum excited with 632 nm in Fig. 3.7-6b). In our sample this interference resulted in a suppression of the Raman intensity for certain wave vectors. The $Si_{1-x}B_x$ alloys with moderate concentrations of B normally show weak peaks related to Si-B vibrations at 618 at 640 cm^{-1} for ^{11}B and ^{10}B isotopes, respectively. In our samples we can clearly see that both these peaks

also demonstrate the same anti-resonance effects (*e.g.*, doublets in Fig. 3.7-6a or one combined anti-resonant peak in Fig. 3.7-6b). The other peaks near 300 and 950 cm^{-1} are the known overtones of silicon assigned to 2TA and 2TO modes, respectively (Fig. 3.7-6b). In order to determine the intrinsic phonon frequency from the Raman spectra of the $Si_{1-x}B_x$ samples we used Fano's theory in which the Raman Intensity (I) in the vicinity of the resonance is determined as: $I \sim (q+\varepsilon)^2/(1+\varepsilon^2)$, where $\varepsilon=(\omega-\Omega)/\Gamma$, with ω the measured and Ω the critical (intrinsic) frequency. q and Γ are fitting parameters characterizing the transition probability (Γq^2) and real change in phonon self-energy from electron-phonon interactions (Γ) (Fig. 3.7-6d). We found the critical frequencies at $\Omega \sim 491$ and 495 cm^{-1} for the spectra excited with 632.5 and 514.5 nm laser lines, respectively. This minor divergence may potentially be related to small fluctuations in boron content. Thus, the frequency of the first-order Raman mode in $Si_{1-x}B_x$ was greatly softened compared to the peak of undoped single-crystalline silicon at ~ 521 cm^{-1} (Fig. 3.7-6c).

d. *Synthesis of nanocrystalline diamond from glassy carbon balls (N.A. Solopova and L.S. Dubrovinsky, N.A. Dubrovinskaia/Bayreuth)*

It is known that various carbon allotropes (graphite, glassy carbon, fullerite, carbon nanotubes, and others) can be directly transformed to poly- and nanocrystalline diamonds and diamond-like materials at high pressures and high temperatures (HP-HT). Recently, the synthesis of nanocrystalline diamond (NCD) balls was realized, when commercially available micron-size glassy carbon (GC) balls were used as precursor material. The NCD balls were found to possess exceptional mechanical strength and have been used as secondary anvils in the double-stage diamond anvil cell (ds-DAC) experiments for the generation of ultra-high pressures exceeding 600 GPa.

Motivated by these results, we conducted a series of experiments on the synthesis of NCDs from glassy carbon balls at variable high-pressure/high-temperature conditions. Synthesis of nanocrystalline diamond micro-balls was carried out at pressures of 9 to 18 GPa and temperatures of 1250 to 2000 °C using a multianvil apparatus. As a starting material we used commercially available glassy carbon balls (type 1, Alfa Aesar) with a size of 20-50 μm. Powders of sodium carbonate Na_2CO_3 (99.99 % purity), sodium chloride NaCl (99.99 % purity) or magnesium oxide MgO (99.99 % purity) were used as pressure media. Each powder was mixed with GC balls in the proportion 2:1 and placed into cylindrical capsules made of *h*-BN, Re, or Pt. The samples were gradually pressurized and then heated. The accuracy of the temperature measurements was ± 50 °C. Duration of heating was 1 or 5 min. The products of the synthesis, extracted from the capsules, were carefully washed in water (for Na_2CO_3 or NaCl pressure media) or in 1 M solution of HCl (for MgO) at 100 °C using an ultrasonic bath. A detailed characterization of the synthesis products was performed using an optical microscope, Raman spectroscopy and scanning electron microscopy (SEM).

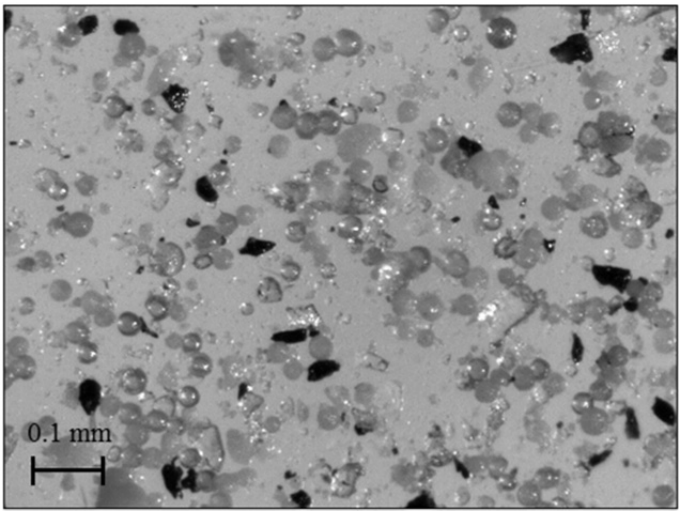

Fig. 3.7-7: Optical image of transparent nanocrystalline diamond balls synthesized from glassy carbon (experiment S5802, MgO pressure medium; 1850 °C, 18 GPa)

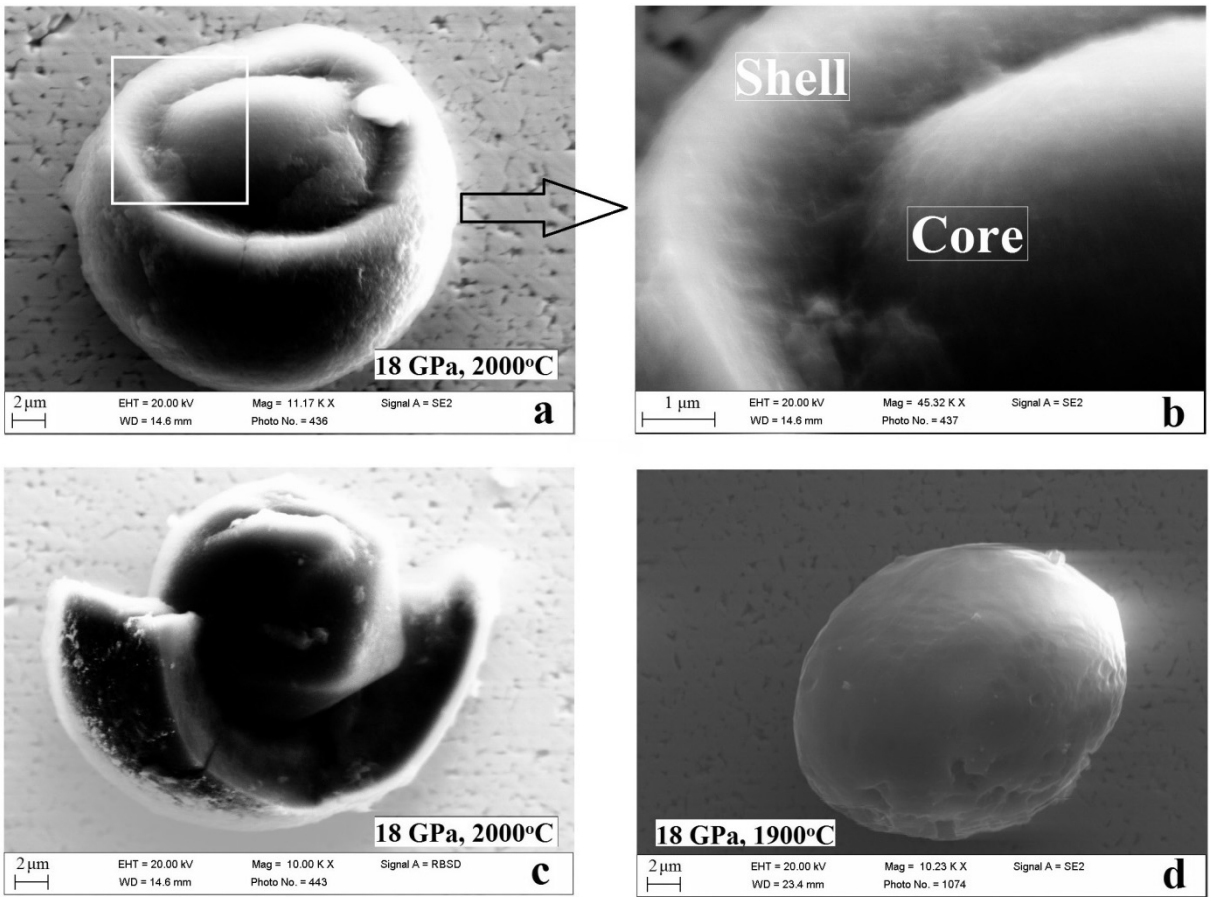

Fig. 3.7-8: SEM images of nanocrystalline diamond balls synthesized in an MgO pressure medium at 18 GPa and at various temperatures: (a-c) examples of the balls containing a nanocrystalline ‘core’ and a nanocrystalline ‘shell’ (experiment S5766; 2000 °C, 18 GPa); (d) lens-shaped nanocrystalline diamond ‘core’ (experiment S5845; 1900 °C, 18 GPa).

In a series of experiments we synthesized nanocrystalline diamond balls by direct transformation of glassy carbon precursors at pressures of 18 GPa and temperatures above 1500(±50) °C. We found that all external factors, such as pressure, temperature and synthesis medium, are interrelated and influence the quality of the synthetic diamond micro-balls. They determine the crystallinity, shape and transparancy of the balls and, consequently, their mechanical and optical properties. Optically transparent, homogeneous, well-consolidated nanocrystalline micro-balls, which do not fracture upon vibration, were obtained at pressures of 18 GPa and temperatures of 1850 - 2000 °C, with the MgO pressure medium remaining solid during the process of synthesis (Figs. 3.7-7 and 3.7-8). The use of pressure media which are liquid at synthesis conditions (NaCl, Na_2CO_3) yields the formation of opaque and microstructurally inhomogeneous balls which contain shells of different crystallinity, easily delaminating upon vibration. Thus, our results are important for constraining conditions for crystallization of nanodiamond aggregates with desired shapes and transparency from glassy carbon balls.

e. *A new hard oxide semiconductor with a direct and narrow band gap (S.V. Ovsyannikov, E. Bykova and L.S. Dubrovinsky; A.E. Karkin, N.V. Morozova and V.V. Shchennikov/Yekaterinburg, A.M. Abakumov/Antwerp, A.A. Tsirlin/Tallin and K.V. Glazyrin/Hamburg)*

Chemical bonding in inorganic solids partly predetermines and interconnects their elastic and electronic properties: metals are usually ductile, semiconductors are brittle, and insulating ceramics may be rather hard. The ability to combine these properties could greatly extend the applicability of materials for industrial use. High-pressure/high-temperature (HP-HT) synthesis is known to be a powerful tool for the preparation of new unique materials and phases of which properties can be very different from those of their ambient pressure analogues. We have examined the mechanical and physical properties of two high-pressure polymorphs prepared at HP-HT, namely, perovskite-type ζ-Mn_2O_3, and marokite-type Mn_3O_4 (labeled as γ-Mn_3O_4).

The temperature dependence of electrical resistivity were investigated in three bulk samples of pure ζ-Mn_2O_3 (Fig. 3.7-9a) synthesized in the stability field of this phase. Measurements unambiguously demonstrate an intrinsic semiconducting character of electrical conduction with activation energy E_a of ~ 0.27±0.02 eV (Fig. 3.7-9b). The Hall constant curves for these samples (Fig. 3.7-9c) show that slightly below room temperature ζ-Mn_2O_3 turns to *p*-type. At higher temperatures the hole and electron contributions to conductivity are almost equal. For an intrinsic semiconductor this means the equivalence of hole and electron mobilities, and hence, from these data we cannot determine the carrier concentration and mobility. The magnetoresistance (MR) effect in ζ-Mn_2O_3 appears as a conventional parabolic function of the magnetic field strength, B (Fig. 3.7-9d). From the MR effect we estimate the carrier mobility

to be $\mu_{n,p}$ ~ 123 cm^2/(Vs) at 309 K. Then, from the resistivity data we can estimate the intrinsic carrier concentration as n_i ~ 6×10^{14} cm^{-3} at 309 K. The electrical resistivity of γ-Mn_3O_4 was too high to be measured.

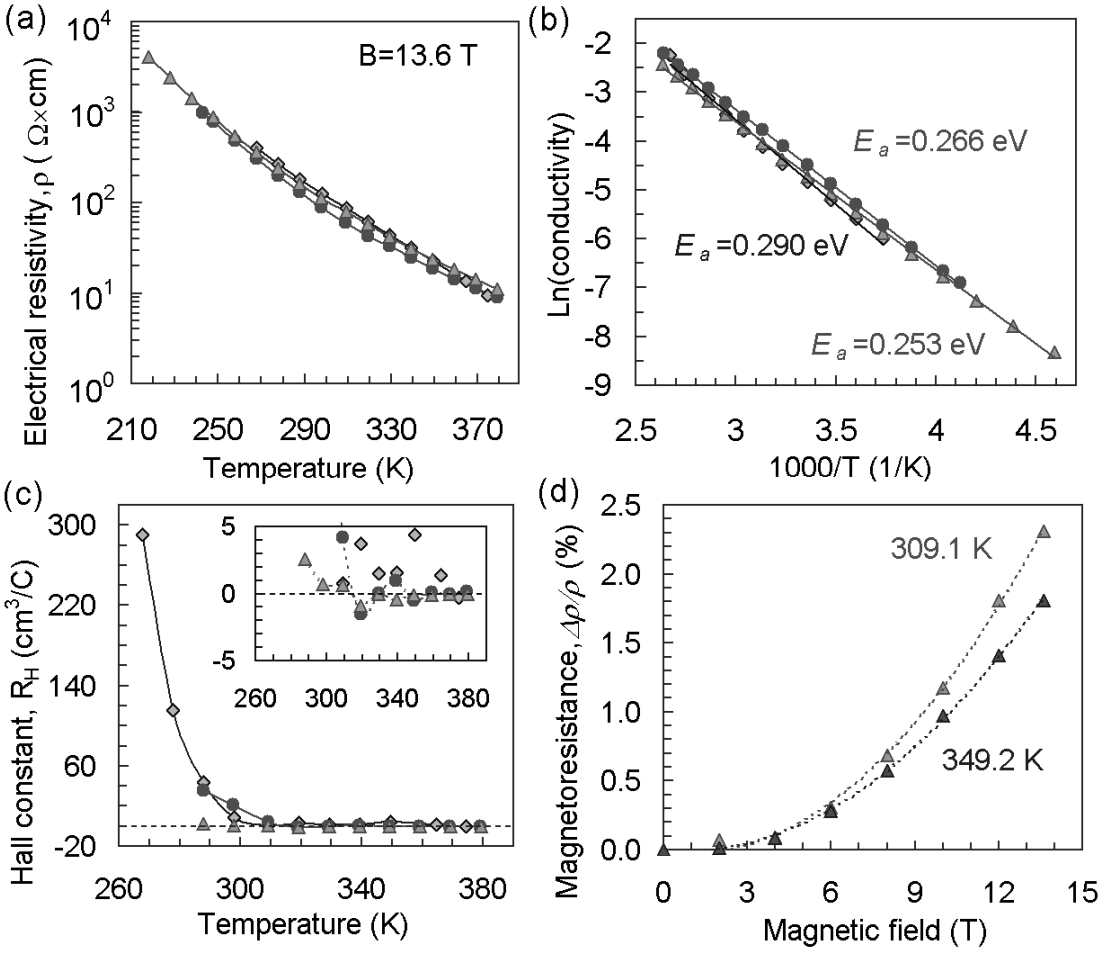

Fig. 3.7-9: Temperature dependence of (a) the electrical resistivity, (b) logarithm of conductivity, (c) the Hall constant, and (d) dependence of the MR effect on magnetic field strength for the perovskite-type ζ-Mn_2O_3 at ambient pressure. Three sets of the symbols correspond to three different samples investigated. The activation energies E_a for each of the samples are also provided.

We investigated the electronic band structure of both semiconductors by near-IR and optical absorption spectroscopy and distinctly detected the absorption edges (Fig. 3.7-10a). The edge profiles suggest a parabolic character of the energy bands. Hence, using the standard "parabolic" model we established that ζ-Mn_2O_3 has a direct fundamental band gap, E_g ~ 0.45 eV (Fig. 3.7-10b). Likewise, γ-Mn_3O_4 has an indirect fundamental band gap, E_g ~ 0.95 eV and a direct gap of ~ 1.3 eV (Fig. 3.7-10c). These E_g values are lower than those in the ambient-pressure polymorphs, *e.g.*, E_g ~ 1.3 eV in α-Mn_2O_3 and E_g ~ 2.5 eV in α-Mn_3O_4. The optical gap (Fig. 3.7-10b) and thermal band gap (E_g=2E_a ~ 0.54 eV, Fig. 3.7-9b) in ζ-Mn_2O_3 show a sizable difference of ~ 90 meV, thereby suggesting a large exciton binding energy.

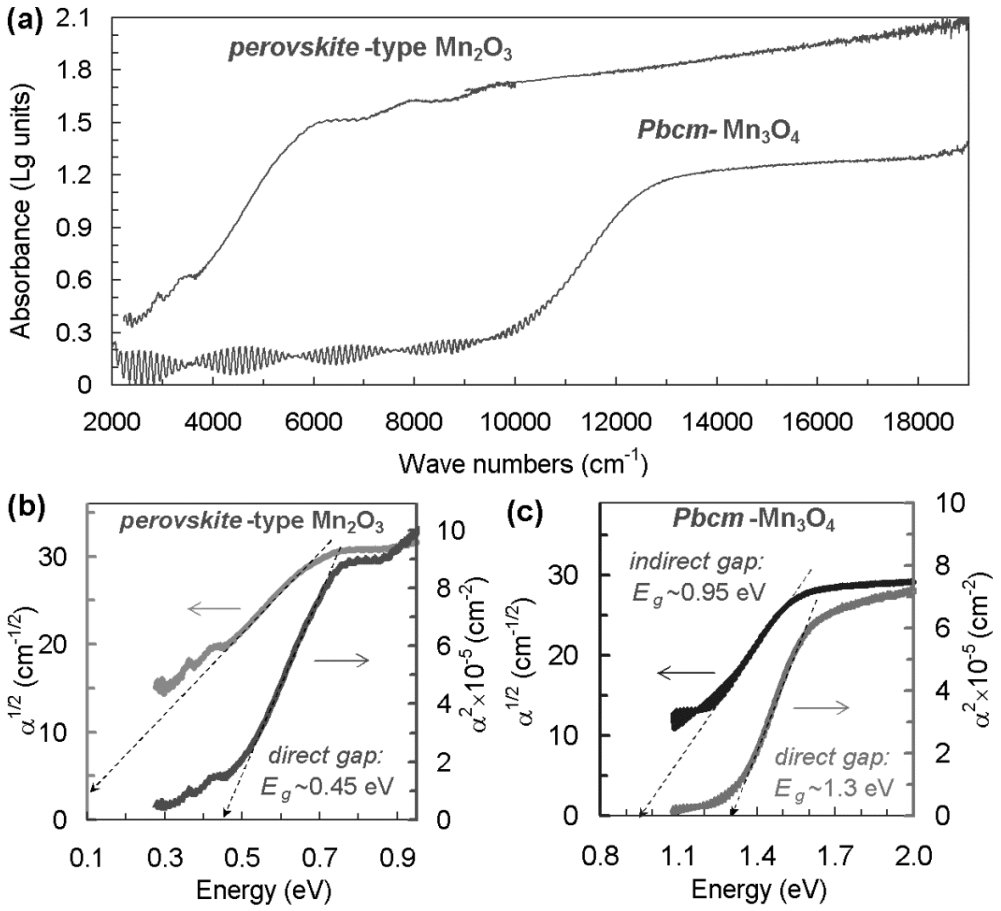

Fig. 3.7-10: Near-infrared and optical absorption α spectra of the perovskite-type ζ-Mn_2O_3 and marokite-type *Pbcm*-Mn_3O_4. (a) The original spectra in [cm^{-1}] units. (b) and (c) the same spectra replotted in '$\sqrt{\alpha}$ *vs E*' and 'α^2 *vs E*' representations (1 eV ≈ 8065 cm^{-1}) for determination of indirect and direct energy band gaps, respectively.

In direct examination of microhardness of the ζ-Mn_2O_3 at different loads ranging between 2 and 5 N we determine the Vickers hardness as H_V ~ 15(2) Gpa. This value is typical for nitride ceramics (*e.g.*, for Si_3N_4 H_V ~ 15.5 GPa). The known industrial semiconductors with similar band gaps are rather brittle and their H_V values are characteristic for soft materials (*e.g.*, InAs has H_V ~ 2.6 GPa, PbS has H_V ~ 0.8 GPa, and $Hg_{0.7}Cd_{0.3}Te$ has H_V ~ 0.7 GPa). ζ-Mn_2O_3 may hence provide an interesting alternative to such materials.

f. *High-pressure/high-temperature synthesis of In_2O_3 (B. García-Domene/Valencia; S.V. Ovsyannikov and L.S. Dubrovinsky)*

Indium oxide (In_2O_3) is a sesquioxide of the $A_2^{III}O_3$ family. As many other sesquioxides, In_2O_3 has caught the attention of the scientific community over the last years. It is an attractive material employed as a gas sensor, in thermoelectrics, and – in particular, when doped with Sn or F – as a transparent conductive oxide in many optoelectronics applications including solar cells, light-emitting diodes and liquid-crystal displays.

The synthesis of macroscopic quantities of In_2O_3 polymorphs as well as growth of their single crystals is of great interest for technology and fundamental science. On the one hand, the use of In_2O_3 single crystals as substrates for homo- and hetero-epitaxy still remain unexplored. On the other hand, In_2O_3 single crystals would allow the use of surface techniques (ARPES, UPS, XPS) that provide a direct determination of its electronic structure. Understanding the electronic structure in In_2O_3 polymorphs is required for guiding the synthesis towards transparent conductive oxides with improved optical and electronic properties.

In_2O_3 crystallizes at ambient conditions in the cubic bixbyite-type structure (c-In_2O_3, space group (SG) $Ia\bar{3}$, No. 206, Z=16), common to many rare-earth sesquioxides. At high pressures other phases are reported for this compound (Fig. 3.7-11), like the trigonal corundum-type structure (rh-In_2O_3, SG $R\bar{3}c$, Z=6), the orthorhombic Rh_2O_3-II structure (o´-In_2O_3, SG *Pbcn*, Z=4), and the orthorhombic α-Gd_2S_3 structure (o´´-In_2O_3, SG *Pnma*, Z=4). Recently, we discovered a new orthorhombic phase (SG *Pbca*, Nº 61, Z=8) of In_2O_3.

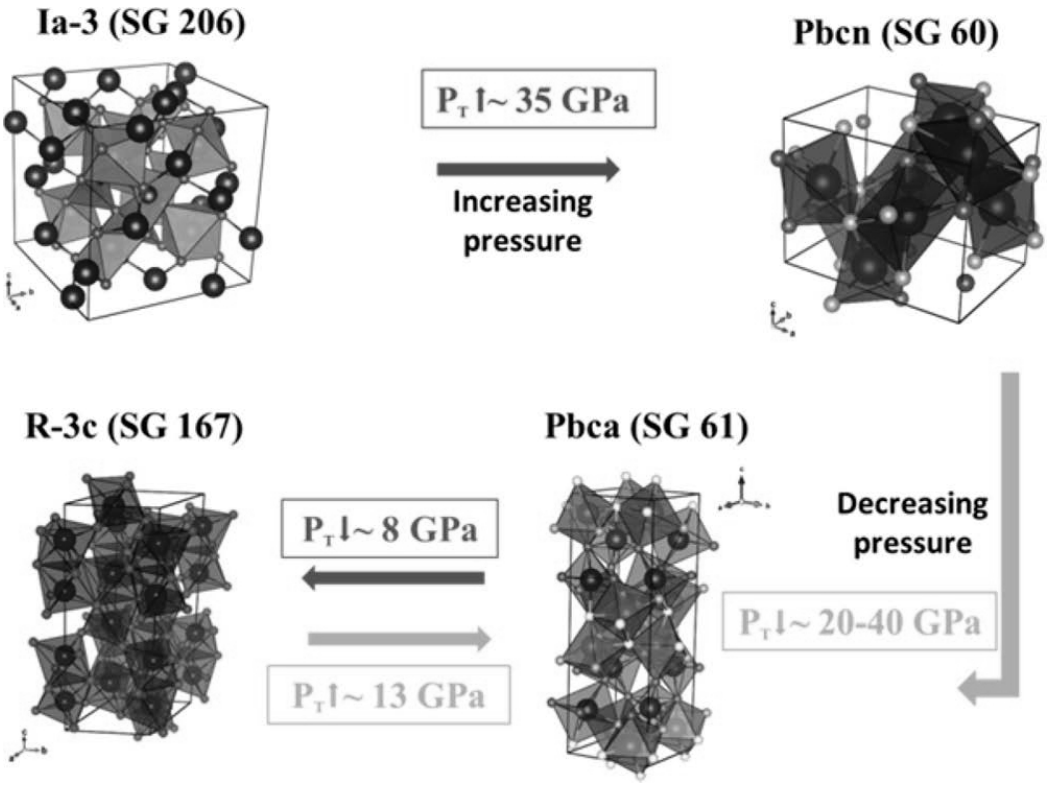

Fig. 3.7-11: Sequence of pressure-induced phase transitions in In_2O_3 up to 50 GPa at ambient temperature.

The aim of this project was to investigate the P-T phase diagram of In_2O_3 using the multianvil press (*ex situ* experiments) and to synthesize the corundum-type phase of Cr-doped In_2O_3. After treatment at different HP-HT conditions, the sample was thermally quenched before the

pressure was released. Recovered samples were characterized by X-ray diffraction, scanning electron microscopy, and Raman, near IR and visual spectroscopy. A precise determination of the phase boundaries for the different polymorphs is fundamental in order to evaluate its technological applicability.

Once the optimal conditions of pressure and temperature for the synthesis of the corundum phase were established (8 GPa and 1300 °C), we created a series of Cr-doped In_2O_3 oxides adopting the corundum-type structure with different dopant level, including $(In_{0.99}Cr_{0.01})_2O_3$, $(In_{0.95}Cr_{0.05})_2O_3$, and $(In_{0.90}Cr_{0.10})_2O_3$. We observed color changes in the synthesized samples from colorless and transparent In_2O_3 to red and green crystals in the Cr-doped samples and have started to investigate their properties.

g. *A structural phase transition in multiferroic YMn_2O_5 at high pressure (D.P. Kozlenko, S.H. Jabarov, E.V. Lukin and S.E. Kichanov/Dubna, L.S. Dubrovinsky)*

The multiferroic materials, demonstrating coupled electric and magnetic properties, are at the current focus of the extensive scientific research in the fields of condensed matter physics and materials science. Such materials could provide possibilities for controlling magnetic properties by electric field and vice versa, extremely important for the development of new electronic devices. YMn_2O_5 is an improper multiferroic, in which spontaneous electric polarization is induced by modulated magnetic ordering, breaking the inversion symmetry of the crystal structure.

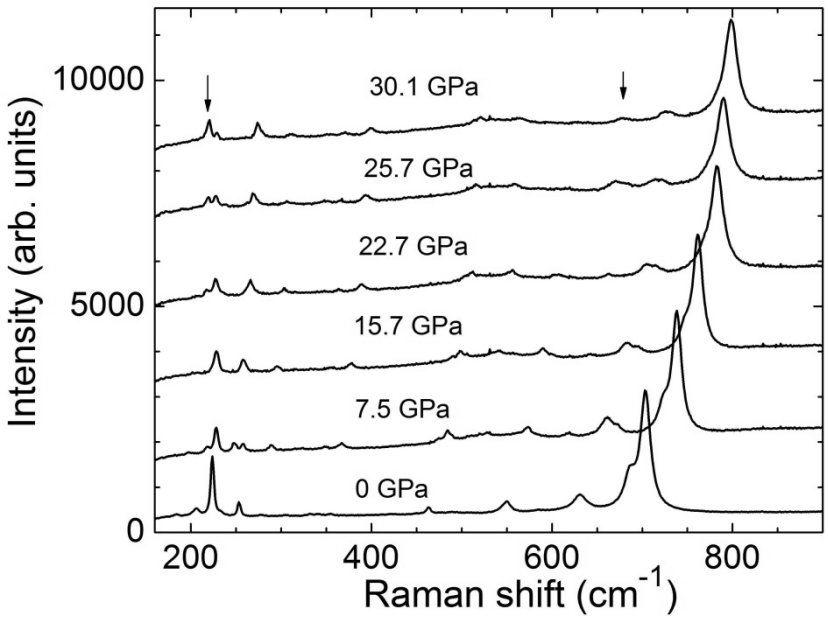

Fig. 3.7-12: Raman spectra of YMn_2O_5 obtained at various pressures.

Application of high pressure is a well-known route for stabilizing novel phases of materials. In order to determine the structural phase transitions in YMn_2O_5, Raman spectra were measured up to 30 GPa (Fig. 3.7-12). At pressures above 22 GPa, the appearance of additional modes at 220 and 675 cm^{-1} were observed (marked by arrows in Fig. 3.7-12), indicating a structural phase transition. For the structural analysis of the phase transformation in YMn_2O_5, the additional XRD experiments were performed at P02.2 beamline, Petra-III, DESY and data analysis is in progress.

h. *Structural studies of the P-T phase diagram of $BiMnO_3$ (S.H. Jabarov, D.P. Kozlenko, N.T. Dang, S.E. Kichanov, A.I. Mammadov, E.V. Lukin and B.N. Savenko/Dubna, L.S. Dubrovinsky)*

Structural phase transitions in $BiMnO_3$ were studied by means of energy-dispersive X-ray diffraction in the pressure range 0-4 GPa and temperature range 300-900 K, and by means of angle-dispersive X-ray diffraction and Raman spectroscopy at higher pressures up to 50 GPa and ambient temperature.

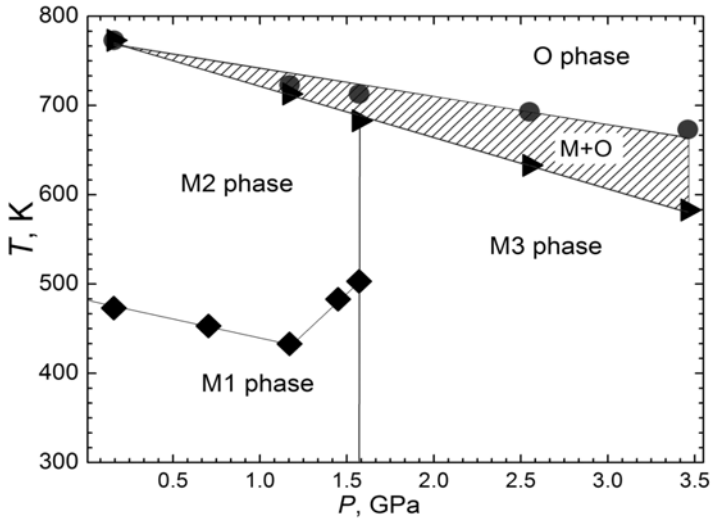

Fig. 3.7-13: The structural P-T phase diagram of $BiMnO_3$, obtained from the analysis of the energy dispersive XRD data.

At pressures $P < 1.6$ GPa on heating, two successive phase transformations from the initial monoclinic *C2/c* phase (M1) to monoclinic *C2/c* phase (M2) and further to the orthorhombic *Pnma* phase (O) were detected on the basis of the change of intensities and positions of the observed diffraction peaks, as well as calculated temperature dependencies of lattice parameters. The transformation temperatures at ambient pressure, $T_{M1\text{-}M2} = 490$ K and $T_{M2\text{-}O} = 773$ K are consistent with previous studies. At the monoclinic-monoclinic phase transformation, an abrupt increase of the a lattice parameter, as well as a decrease of the *b* and

c lattice parameters occurs, followed by a unit cell volume contraction of 0.2 %. Their characteristic values for $P \approx 0$ GPa are a = 9.559(4), b = 5.622(3), c = 9.861(4) Å, β = 110.6(1) at T = 295 K, and a = 9.615(4), b = 5.600(3), c = 9.786(4) Å, β = 108.7(1) at T = 573 K. At the monoclinic-orthorhombic phase transition, an abrupt decrease of all lattice parameters occurs, followed by a more pronounced unit cell volume reduction of 2.2 %. The lattice parameters have values a = 5.646(3), b = 7.886(4), c = 5.534(3) Å at T = 793 K.

Based on our data we established the P-T phase diagram of $BiMnO_3$ (Fig. 3.7-13). The transition temperature to the orthorhombic *Pnma* phase decreases rapidly with a pressure coefficient -56 K/GPa, reaching ambient temperature at $P \sim 8$ GPa and implying suppression of magnetoelectric properties. Lattice dynamics calculations have shown that in the Raman spectra of ambient and high-pressure monoclinic phases the “gerade” and “ungerade” vibrational modes of manganese octahedrons are present and their coupling leads to the appearance of complex mixed modes. The analysis of the pressure coefficients of the stretching and bending mode frequencies implies different compressibility mechanisms in the monoclinic and orthorhombic phases, characterized by larger contraction of average Mn-O bonds in the first case and Bi-O ones in the second case, respectively.

At $P \sim 20$ GPa, a structural phase transition to a new orthorhombic *Imma* phase of $BiMnO_3$ is found. This transition leads to a suppression of the long range $d(3y^2 - r^2)$ e_g orbital order in $BiMnO_3$, as evident from the rapid decrease of stretching modes intensity in Raman spectra.

3.8 Methodological Developments

An essential on-going goal in experimental and computational studies in the Earth sciences and material sciences is to improve existing techniques and to devise new ones. For example, such developments are applicable to (1) the generation of increasing high pressures and temperatures, as required to obtain a better understanding of the Earth's deep interior, (2) the generation of controlled non-hydrostatic stress as required in rheological studies, and (3) the characterization of the chemical composition of experimental samples. Of particular importance is the ability to measure, with increasing accuracy, important experimental parameters such as temperature, pressure, differential stress and oxygen fugacity. The contributions in this section cover many of these aspects of methodological developments.

A new multianvil system 'IRIS-15', that will be used to generate pressures of 60 GPa or more, was installed at BGI in 2014. This apparatus uses a set of six outer anvils to compress a cubic set of inner anvils. In order to generate extremely high pressures without breaking the inner anvils, it is essential that the volume compressed by the outer anvils preserves an exactly cubic geometry. The first contribution describes developments that have been performed in order to achieve this goal.

Three contributions present the results of developments in diamond anvil cell (DAC) experiments. In two of these, pressure and temperature conditions in DAC experiments are determined using florescence sensors. The first of these uses two different calibrants (ruby and Sm-YAG) simultaneously in order to determine both pressure and temperature. The following contribution describes the use of Sm-doped strontium tetraborate (Sm-STB) as a new pressure sensor which has been calibrated up to 60 GPa and, like Sm-YAG, is unaffected by temperature. The third contribution describes developments in achieving stable temperatures during laser-heating in the diamond anvil cell for studies involving nuclear resonance processes.

A major problem in performing rheological studies at high pressures in the multianvil apparatus is to be able to measure differential stress and conventional methods are often only possible when stresses are very high. An important development is the use of a piezoelectric sensor in the form of a single crystal of either quartz or $GaPO_4$. Measuring the electrical signal generated by such sensors enables stresses in the range 0-1 GPa to be measured at temperatures up to 600 K. Another problem in deformation studies is to determine the effect of H_2O on rheology: for example, OH dissolved in olivine has a strong weakening effect on rheology. In order to be able to deform samples at high pressures and temperatures to quantify the effects of dissolved OH on rheology and active slip systems, the sample needs to be contained in a metal capsule that inhibits the loss or gain of hydrogen. This creates a problem because such deformation experiments generally have to be performed using *in situ* X-ray diffraction in order to determine stress: for this, the sample cell needs to be transparent to X-rays and a metal capsule is therefore undesirable. Preliminary results in finding a solution to this problem are described in this section.

In many high-pressure experiments, oxygen fugacity must be determined quantitatively, in addition to temperature and pressure. The best method for doing this involves the use of a metal alloy redox sensor. For example, when a Fe-Pt alloy is contained in the sample during an experiment, the exact composition of the alloy is controlled by the oxygen fugacity. The results of a study in which three different alloy sensors are compared over a wide range of oxygen fugacities are described below.

In laser-heated DAC experiments, chemical reaction with the anvils can enrich the sample in carbon. This is a significant problem in liquid metal-silicate partitioning experiments because C dissolved in liquid Fe alloy can have a major effect on the partitioning of siderophile elements. In order to correct for this effect, the carbon content of quenched liquid iron must be measured. As described below, such measurements are very difficult and many precautions have to be taken to obtain the correct concentrations.

For measurements of physical properties, it is often desirable to use samples that are in the form of single crystals. The synthesis of very large single crystals of stishovite, a high-pressure SiO_2 polymorph is described below. Crystals with a size up to 1.7 × 1.5 × 1.0 mm have been synthesized in a multianvil apparatus for the purpose of equation of state and electrical conductivity measurements at conditions up to 500 GPa and 8000 K.

Fluid inclusions are studied in order to determine the compositions of ore-forming fluids. Because many ore minerals are opaque, this has previously been difficult, if not impossible. An important development described here involves the use of near-infrared (NIR) microscopy to study inclusions contained within opaque minerals.

In addition to the experimental developments presented so far the final contribution in this section presents advances in the understanding of theoretical aspects of computational chemistry. Within density functional theory the ionization potential, *i.e.*, the energy difference between a neutral molecule and its singly charged cation, is described well, but with increasing number of atoms in the cluster this agreement deteriorates for previously unknown reasons. By looking at the electrostatic energy in such a system this behaviour can be explained.

a. *Adjustment of the high-pressure volume in the new DIA-type multianvil apparatus 'IRIS-15' (L.-L. Shi, T. Katsura, T. Kawazoe and R.J.M. Farla, in collaboration with M. Petri/Mainleus)*

A new multianvil apparatus 'IRIS-15' was constructed by Max Voggenreiter GmbH, and installed at BGI in October 2014. This apparatus is designed for routinely generating pressures up to 60 GPa and temperatures up to 2300 K, which correspond to conditions in the upper region of the lower mantle. The apparatus is equipped with a DIA-type guide block

system. Six first-stage anvils made of hardened steel with a truncated edge length of 50 mm compress second-stage anvils consisting of tungsten carbide with an edge length of 26 mm. Second-stage anvils made of sintered diamond can be also compressed by placing tungsten carbide spacers on the first-stage anvils.

It is essential that the compressed volume formed by the six first-stage anvils should maintain a cubic shape in order to avoid breakage of the second-stage anvils and blow-out due to an imbalance of forces. However, the vertical and horizontal dimensions of the compressed volume tend to deviate as the press load is increased, because the structure of the guide block (Fig. 3.8.-1a) has not a cubic but a tetragonal symmetry. We found that the supports of the vertical anvils are stronger than those of the horizontal ones. As a result, the difference between the horizontal and vertical dimensions increases with increasing press load. Hence, the strength of the supports of the vertical anvils has to be adjusted to keep the difference constant (Fig. 3.8-1b-d). The dimensions were evaluated by compressing stainless steel blocks and measuring distances between opposite faces after decompression.

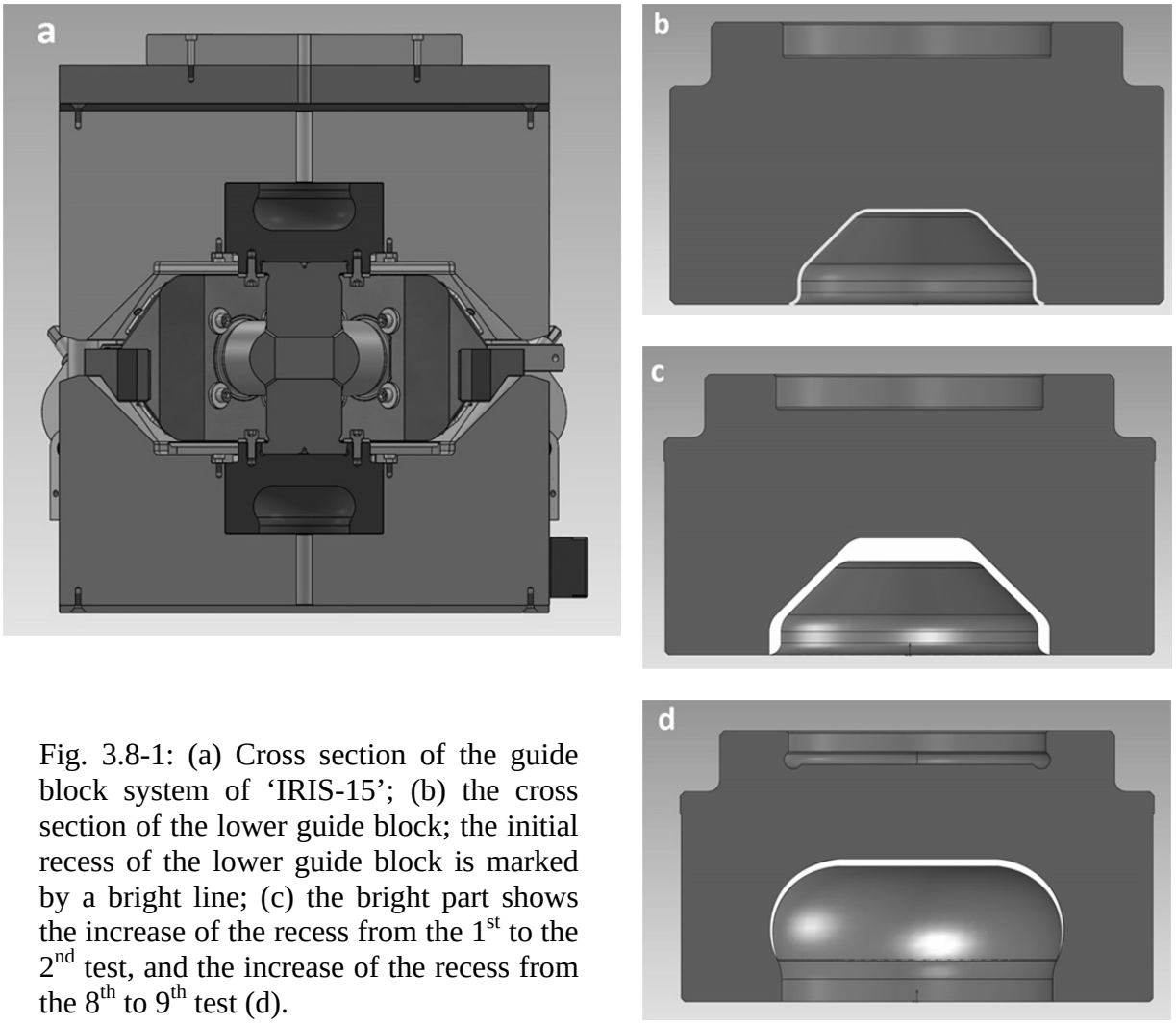

Fig. 3.8-1: (a) Cross section of the guide block system of ‘IRIS-15’; (b) the cross section of the lower guide block; the initial recess of the lower guide block is marked by a bright line; (c) the bright part shows the increase of the recess from the 1st to the 2nd test, and the increase of the recess from the 8th to 9th test (d).

We conducted 10 compressional tests during which the guide blocks were modified step by step (Fig. 3.8-2). Before adjustment, the horizontal dimension increases relative to the vertical dimension at a rate of 22 μm/MN. The deviation rate was reduced to 8 μm/MN after the first 3 adjustments, but it remained essentially constant thereafter in spite of further modification of the guide blocks. We assume that these phenomena are caused by friction between the guide blocks and the sliding wedges. In the 10th compression test, the lubrication between them was changed from Kapton sheets plus MoS_2 to Teflon sheets. Through this improvement, the deviation rate has become very small, -0.5 μm/MN, which is adequate for the generation of the ultrahigh pressures.

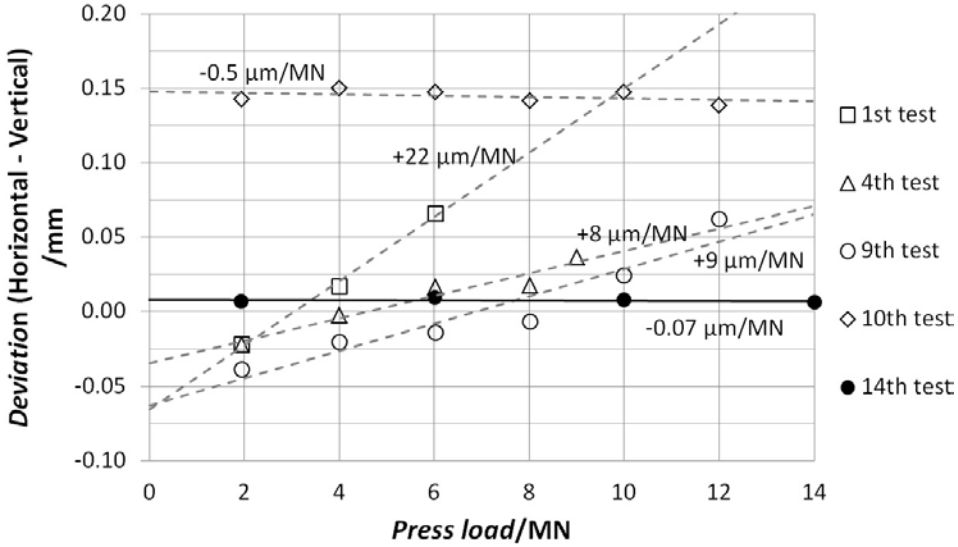

Fig. 3.8-2: The deviations of the horizontal dimensions from the vertical ones of the compressional space of 'IRIS-15'. The deviation increases with press load at an initial rate of 22 μm/MN (1st test, open squares). It is suppressed to 8 μm/MN after the first 3 adjustments (4th test, open triangles), but remains around this value by the later adjustments. By changing the lubrication, the rate was finally successfully suppressed to -0.07 μm/MN (14th test, solid circles).

b. *Calibration of the ruby pressure scale up to 800 K and 46 GPa under quasi-hydrostatic conditions (N. Siersch, A. Kurnosov and T. Boffa Ballaran)*

High-pressure and high-temperature experiments in the diamond anvil cell (DAC) require an accurate *in situ* pressure and temperature determination to obtain reproducible and reliable results. Major efforts have been spent by different groups for obtaining precise and accurate pressure calibrations using materials such as ruby, Sm-doped $Y_3Al_5O_{12}$ garnet (Sm:YAG), boron carbide etc., whose fluorescence or Raman signals can be easily measured during high-pressure experiments. However, less effort has been spent in obtaining *in situ* temperature calibrants, since usually one relies on the thermocouple reading. However, the position of the thermocouple can slightly change during loading of the DAC or during compression or decompression cycles giving rise to large uncertainties in temperature in spite of careful

preparation of the experiment and calibration of the thermocouple previous to the loading. Ideally, one should use two different reference materials in each experiment, one to determine pressure and one to determine temperature. Two very good candidates as reference materials are Sm:YAG whose fluorescence bands depend exclusively on pressure and appear to be independent of temperature and ruby whose fluorescence shows large variations both with temperature and pressure. Unfortunately, currently-published temperature calibrations of ruby give different results for a given fluorescence shift leading to the same large uncertainties which arise from reading temperature directly from a thermocouple.

In this study we have performed several high-pressure experiments at constant heating power which constrain the temperature in the diamond anvil cell and have used the pressure obtained from the fluorescence shift of Sm:YAG to calibrate the effect of temperature on the fluorescence shift of ruby. In the first experiment ruby fluorescence was measured with a micro-Raman with a red laser at room pressure in order to accurately define the ruby fluorescence shift with temperature. Four pieces of the metals indium, tin, zinc and aluminium with known melting temperatures were used to correctly assess the thermocouple temperature reading and two calibrations were obtained, one for temperatures lower than 450 °C where the ruby fluorescence lines R1 and R2 are still visible and one for higher temperatures where the broadening of the R1 and R2 peaks is so large that only one broad peak is visible.

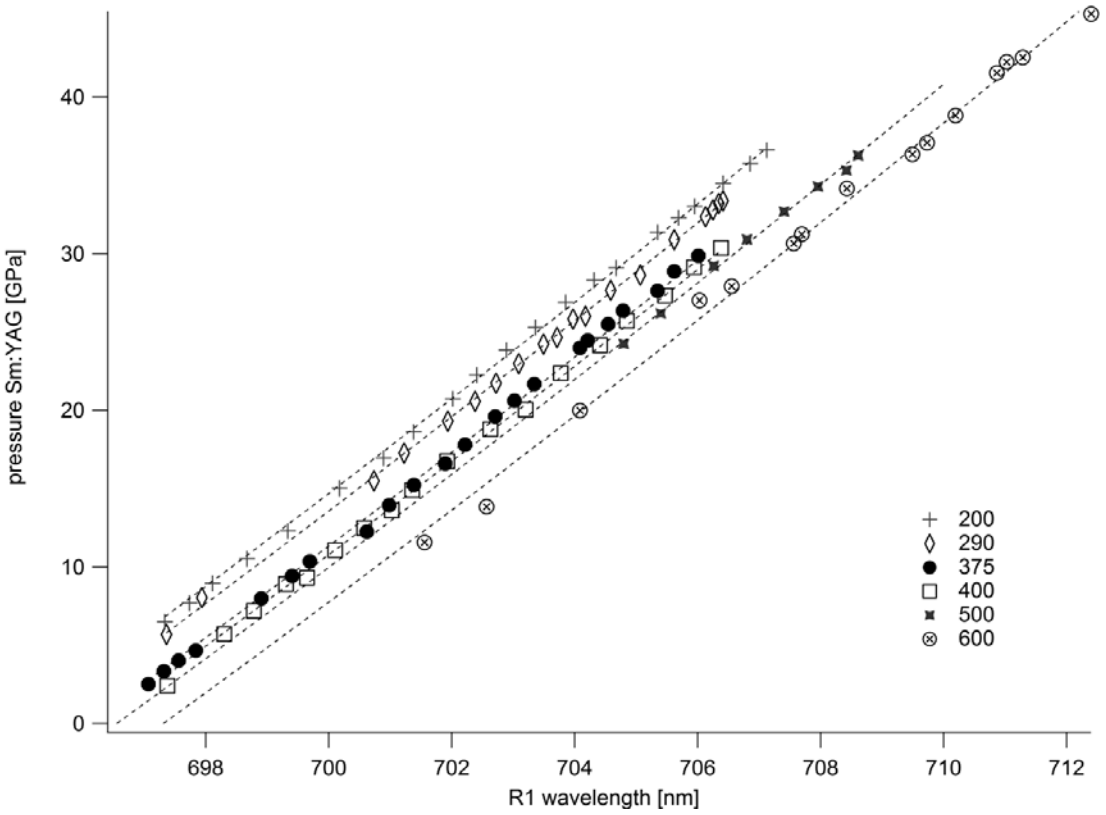

Fig. 3.8-3: The basic pressure equation was fitted to the R1 wavelength data points at different temperatures (K). The parameters A and B were kept fixed and fitting was performed by varying the value of λ.

We then conducted seven isothermal runs at temperatures ranging between 25 and 516 °C and at pressures up to 46 GPa using a micro-Raman spectrometer with a green laser. Since every experiment was conducted at constant temperature the ruby fluorescence shift with pressure was extrapolated to the room pressure value to determine accurately the temperature from the room pressure calibration of λ_0 of the first experiment. The temperature independent pressure calibration of a Sm:YAG single crystal performed by Trots *et al.* (2013) was used as a pressure reference. The ruby fluorescence shifts with pressure at different temperatures show the same behaviour (Fig. 3.8-3) and can be described according to the normally-used equation $P = \frac{A}{B} * [\left(1 + \left(\frac{\Delta\lambda}{\lambda 0}\right)\right)^{B} - 1]$ with the following parameters: A = 1982 and B = 7.665. The temperature dependence is described using a polynomial calculated from the room-pressure high-temperature experiments. We strongly recommend the use of two different calibrations depending on whether or not the R1 and R2 fluorescence peaks can be well resolved.

c. *Calibration of a Sm-STB fluorescence pressure sensor using Sm-YAG absolute pressure scale (S. Rashchenko/Novosibirsk, A. Kurnosov and L.S. Dubrovinsky)*

The most convenient way to measure pressure inside a diamond anvil cell (DAC) is to use fluorescence sensors which have a calibrated pressure-induced shift in fluorescence wavelength. The first proposed and the most widely used fluorescence sensor is ruby (Cr^{3+}-doped Al_2O_3). However, ruby is poorly suitable for high-temperature experiments because of its sensitivity to temperature, which introduces a lot of uncertainty into the pressure measurement at elevated temperatures. In addition, a range of differing calibrations have been proposed for the pressure shift of ruby fluorescence, causing discrepancies between studies in which different calibrations have been used.

Both of the above disadvantages could be avoided by using the *Sm-doped yttrium-aluminium garnet* (Sm-YAG) fluorescence pressure sensor which (1) demonstrates no temperature dependence of fluorescence wavelength, and (2) was recently calibrated using an absolute pressure scale. The fluorescence of Sm-YAG is represented by a doublet near 615 nm, which, unfortunately, broadens significantly as temperature is increased. As a result, the doublet cannot be deconvoluted into two peaks at temperatures above 250 °C, which strongly reduces the precision of pressure measurement even at moderate temperatures. Technically, additional disadvantages of Sm-YAG are low fluorescence intensity (compared with that of ruby), and fluorescence wavelength which cannot not be excited by typical red diode lasers.

A ‘next generation’ fluorescent pressure sensor is represented by *Sm-doped strontium tetraborate* (Sm-STB). This sensor also exhibits a negligible temperature influence on fluorescence wavelength. In contrast to Sm-YAG, it produces a single fluorescence line near 685 nm comparable in intensity with the ruby fluorescence (note that this wavelength could be excited even by a red diode laser). Another advantage of Sm-STB is a very simple

synthesis procedure. Recently the Sm-STB sensor was calibrated in quasi-hydrostatic (QH, Ar medium) and non-hydrostatic (NH, no pressure medium) conditions up to 50 GPa. The authors came to the conclusion that the level of hydrostaticity strongly influences the calibration curve of this sensor (Fig. 3.8-4). However, different standards were used for QH and NH calibrations, which were performed against the ruby fluorescence and Au equations of state, respectively. Herewith, the observed divergence of QH and NH calibration curves can easily be caused by inconsistency between these two pressure scales.

To solve this issue we recalibrate Sm-STB under quasi-hydrostatic conditions (He medium) up to 60 GPa using the recent Sm-YAG absolute pressure scale. As one can see, the resulting calibration is very close to previously reported NH curve calibrated against the Au equation of state (Fig. 3.8-4), indicating that the observed divergence of QH and NH calibration curves is due to inaccuracy in the used ruby scale, whereas hydrostaticity actually does not matter in the studied pressure range.

The resulting equation for pressure determination could now be written in the common form

$$P = \frac{A}{B}\left\{\left(1 + \frac{\Delta\lambda}{\lambda_0}\right)^B - 1\right\}$$

where A = 2822, B = -12.27, and λ_0 = 685.51.

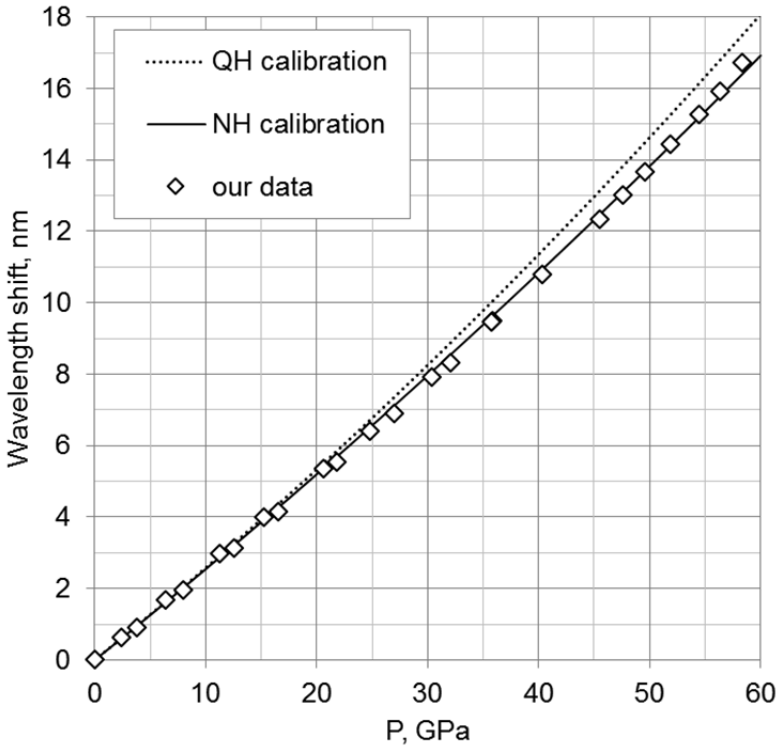

Fig. 3.8-4: Recent calibration curves for Sm-STB (dotted and solid lines) compared with our data (diamonds).

d. *Gated laser heating in diamond anvil cells for studies of nuclear resonance processes (I. Kupenko, C. Strohm, C.A. McCammon, V. Cerantola, S. Petitgirard and L.S. Dubrovinsky, in collaboration with K. Glazyrin/Hamburg; A.I. Chumakov and R. Rüffer/Grenoble)*

Laser heating in diamond anvil cells is a widely used method to generate extreme pressure and temperature conditions and to study the structure and properties of materials along planetary geotherms. However, continuous laser heating in DACs, especially at very high temperatures, is often complicated due to abrupt changes of a material's emissivity which lead to thermal runaway or flashes, hydrodynamic instability of thin very hot samples, problems with diffusion of a heated material into or out of a heated area, and possible chemical reactions between the sample and the thermal insulation and/or diamonds. Pulsed laser-heating may help to partially or fully overcome the problems listed above: delivery in short bursts of well-defined energy prevents uncontrolled changes in emissivity, suppresses diffusion and chemical reactions, and, due to low average power, keeps thermal insulating materials at a relatively low temperature which leads to more stable and better controllable heating. Here we demonstrate the coupling of the time resolved pulsed laser heating with Nuclear Forward Scattering (NFS) of synchrotron radiation. The experiment was carried out at the Nuclear Resonance beamline (ID 18) at the European Synchrotron Radiation Facility.

Laser heating was performed using a portable double-sided heating system for diamond anvil cells developed by our group. In our experiments we used single-sided laser heating, although switching to double-sided heating should be a straightforward development. For a pulsed operation a laser trigger signal was supplied to the trigger input of a delay generator. The generator was configured to supply two veto signals in order to acquire data during and in between laser pulses. Start and duration of the veto signals were adjusted according to a laser pulse profile (Fig. 3.8-5).

We show an example of the application of the setup to a NFS study of Fe_2O_3. Hematite Fe_2O_3 is a rhombohedrally structured wide gap insulator at ambient conditions with a Néel temperature (T_N) of 956 K. It is one of the major components in banded iron formations and studies of its properties at high pressure and high temperature are important for analysis of the subduction behaviour of slabs. The ambient temperature NFS spectrum of Fe_2O_3 (Fig. 3.8-6a) shows high-frequency quantum beats arising from magnetic hyperfine interactions and can be fitted with single component with magnetic hyperfine field (B_{hf}) 51.4(1) T in perfect agreement with previous studies. The high-temperature spectrum (Fig. 3.8-6b) shows a more complicated pattern that can be fitted by two magnetic components: one with B_{hf} equal to 51.7(2) T and the second with B_{hf} equal to 39.0(3) T. The component with high B_{hf} is exactly the same as is present in room temperature spectra and, therefore, should correspond to a material that remained unheated due to low power single-sided heating; whereas the second component corresponds to the hot material. Based on the difference of the centre shift between low-B_{hf} and high-B_{hf} components (0.83(4) mm/s) we obtained a temperature of 1400(50) K for the hot material. The high temperature component is still magnetically ordered, indicating that T_N of Fe_2O_3 increases with pressure to above 1400 K.

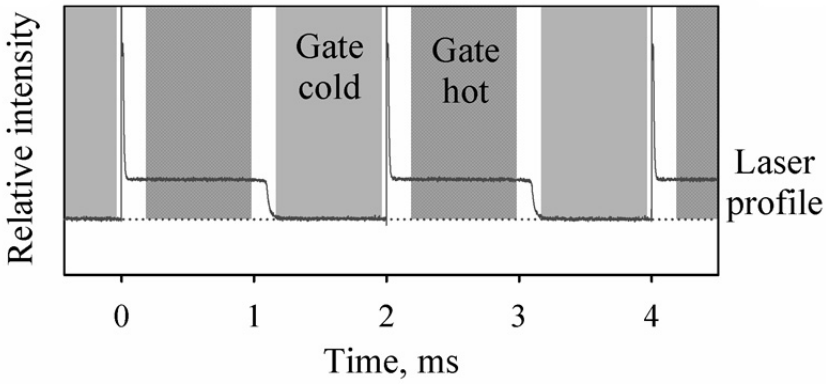

Fig. 3.8-5: Timing scheme of the experiment. Light grey filling and dark grey filling with diagonal crossing show time gates for collection of cold and hot data, respectively.

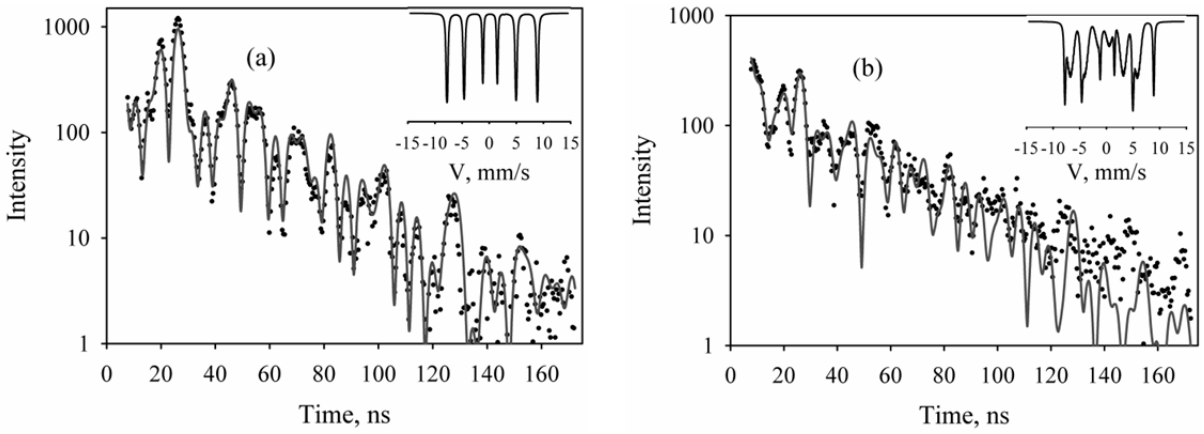

Fig. 3.8-6: High-pressure NFS spectra of Fe_2O_3 at 23(3) GPa and room temperature (a) and 1400(50) K (b). The temperature is determined from the shift of the centre shift values. The solid lines show the theoretical fits. The insets show corresponding energy spectra calculated from the fits.

e. *Use of piezoelectric sensors for* in situ *stress determinations at high pressure and temperature (M.A.G.M. Manthilake/Clermont-Ferrand, D.J. Frost and N. Walte)*

Knowledge of the rheological properties of rocks at conditions of the Earth's interior is essential for our understanding of plate tectonics. Although deformation experiments can now be performed at pressures greater than 3 GPa, a significant hurdle remains in terms of making accurate stress measurements. Currently the main method is to use *in situ* X-ray diffraction to examine the azimuthal dependence of lattice reflections relative to the principal stress direction. This method suffers from large uncertainties due to limited resolution and an incomplete understanding of the directional strength within a crystal. It also requires the experiment to be performed at a synchrotron X-ray facility. A long term project at BGI has been to examine the use of piezoelectric crystals as *in situ* stress transducers. Crystals such as

quartz develop an electrical charge in response to an applied stress. This response, although very weak, can be amplified and inverted to provide a voltage signal that is directly proportional to the applied stress. Previous reports have demonstrated that both quartz and isostructural $GaPO_4$ can be used in conjunction with the Mavo 6-ram multianvil press to measure stresses resulting from sample shortening with a resolution better than 10 MPa. Furthermore such experiments have been performed at nominal hydrostatic pressures up to 10 GPa.

Here we report results of experiments performed at high pressures with simultaneous heating up to 573 K. The high-pressure cubic cell assembly is shown in Fig. 3.8-7. A single crystal plate of either quartz or $GaPO_4$ is oriented along the X-axis and placed at the centre of the assembly. Gold foils are placed on each side of the crystal. Stress is transferred to the crystal through cylinders of dense alumina placed on each side. To minimize the stress on the sample during hydrostatic compression, crushable alumina is also employed in the sample column. The sample column is surrounded by boron nitride sleeves and a cylindrical molybdenum foil sleeve, which shields the sample from induced currents from the furnace. A Re foil furnace is employed and the cubic pressure assembly is made of MgO. The thermocouple is inserted to be nearly in contact with the outside of the furnace (Fig. 3.8-7). The assembled cube is then placed within the anvils of the 6-ram press. Pressure is applied by advancing all rams simultaneously, whereas pure shear sample shortening is achieved by advancing the rams along the sample axis. This can be achieved in steps on the order of 1 µm, but in general

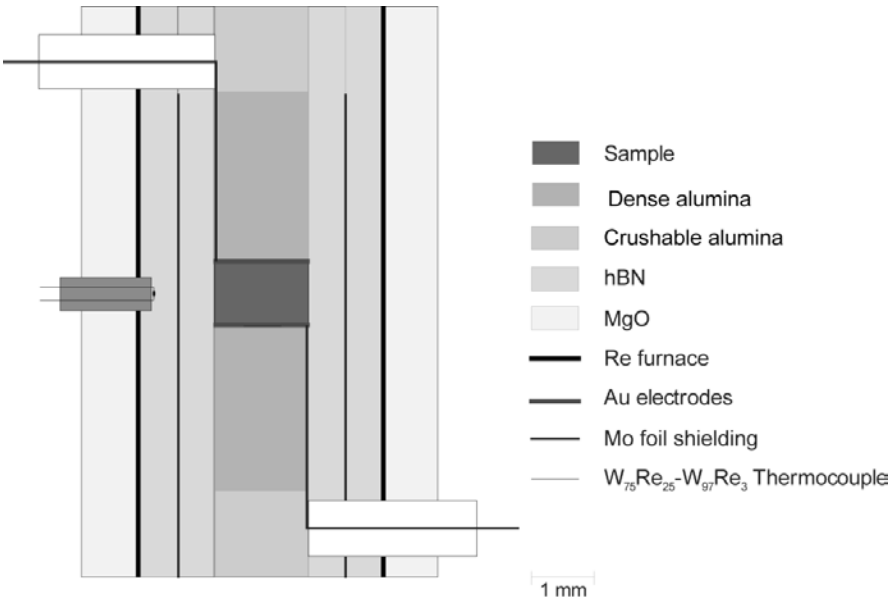

Fig. 3.8-7: The high pressure-cubic cell assembly of 6 mm edge length used for high pressure and temperature piezoelectric stress measurements.

each anvil was advanced in steps of 3-4 µm. Figure 3.8-8 shows the results of measurements made on quartz at 10 GPa. At each temperature the principal anvils compress the sample with

a combined displacement of 40 µm. The anvils are then retracted back to their initial hydrostatic position and the same procedure is followed by retracting the anvil further. This results in stresses that are reported as negative, due to the resulting negative slope in the amplifier voltage. Once temperature is applied the apparent response of the sample is to become immediately softer. This effect was found to be slightly greater for $GaPO_4$ crystals than for quartz. Due to a decrease in the impedance upon heating, likely of both the sample and assembly, the piezoelectric signal degrades with temperature, such that measurements significantly above 600 K would be impossible. However, it would still be possible to use such crystals as effective load cells within the sample column of a deformation experiment if they were placed outside of the hot spot of the assembly.

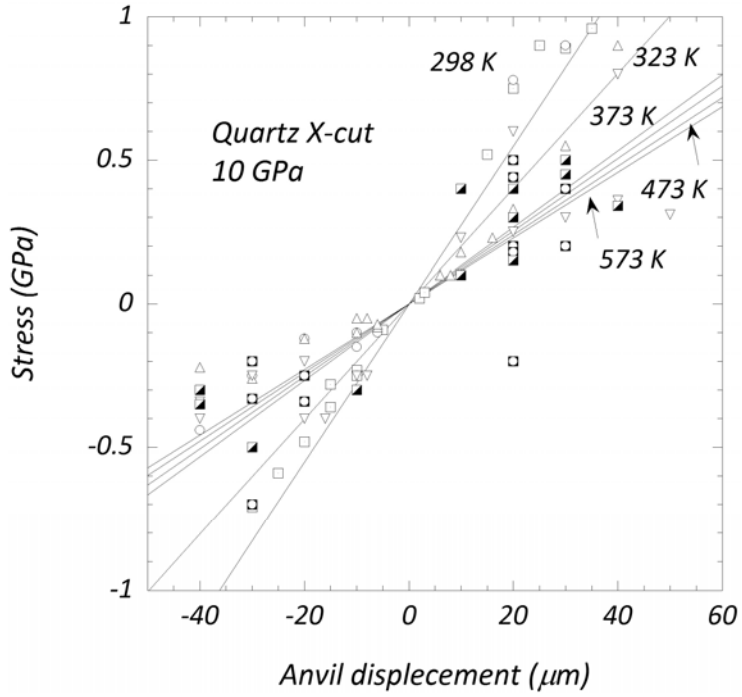

Fig. 3.8-8: Sample stress measurements versus anvil displacement measured on quartz at 10 GPa and up to 573 K. Measurements were made during both advancement and retraction of the principal anvils.

f. *Development of a new cell to investigate the effect of water on the rheology of olivine single crystals in the D-DIA multianvil apparatus coupled to synchrotron radiation (C. Bollinger, in collaboration with J. Chen/Miami)*

The rheology of olivine, the most abundant mineral in the Earth's upper mantle, is a critical physical property that controls the dynamical behaviour of this region of the Earth's interior. This parameter has therefore been the subject of numerous experimental studies for many years. The deformation of polycrystalline olivine is usually considered to be controlled by one or several dominant slip systems. Understanding the pressure-dependence of the activation of these slip systems enables the anisotropy of the upper mantle to be interpreted as a function of

depth. Moreover, previous studies have indicated that water can enter the olivine crystal lattice and significantly affect its physical properties. In particular, it has been shown that the dominant slip system in olivine changes at around 7 GPa from [100](010) to [001](010). In parallel, hydrogen fugacity influences the rheology by resulting in a hydrolytic weakening by a factor of about 1.5 to 2.5. Using multi-scale modeling with experimental and *ab initio* quantifications of slip-system critical resolved shear stresses (CRSS), we observed that even minor slip systems significantly influence aggregate lattice preferred orientations (LPOs). Hence, we also have to study the influence of pressure on the rheology of $[101]_c$ under hydrous conditions using oriented single crystals (*i.e.*, the dual system [100](001) and [001](100)).

In order to understand the effects of water on the dual [100](001) and [001](100) slip systems it is necessary to perform D-DIA deformation experiments coupled to synchrotron radiation on single crystals with fixed and controlled water contents. A necessity when using X-ray diffraction is to ensure the transparency of the diffracting material, including the metallic capsule that is necessary for retaining water. In D-DIA experiments, we commonly use boron-epoxy cubes or pyrophyllite cubes with a boron-epoxy window and strain markers to separate the different materials in the cell and to measure the shortening of the sample by X-ray radiography. Most studies have thus been performed in an open system, *i.e.*, without metallic capsules. Consequently, keeping a cell assembly dry to study the anhydrous behaviour of the olivine is problematic because both boron epoxy and pyrophyllite are known to dehydrate at high temperature, enriching the sample in H_2O. For hydrous studies, we need to use a talc sleeve close to the sample in order to hydrate it during the experiment. To avoid any contact with the surrounding materials, we have to isolate it with a metallic capsule. The challenge is to find a material that is sufficiently transparent to X-rays but not permeable to hydrogen diffusion. Vanadium or $Pd_{75}Ag_{25}$ seem to be good candidates and we now have to test the feasibility of the experiments at our conditions with this kind of metallic capsule in the cell assembly we commonly use at X17B2, NSLS, New York, US (Fig. 3.8-9).

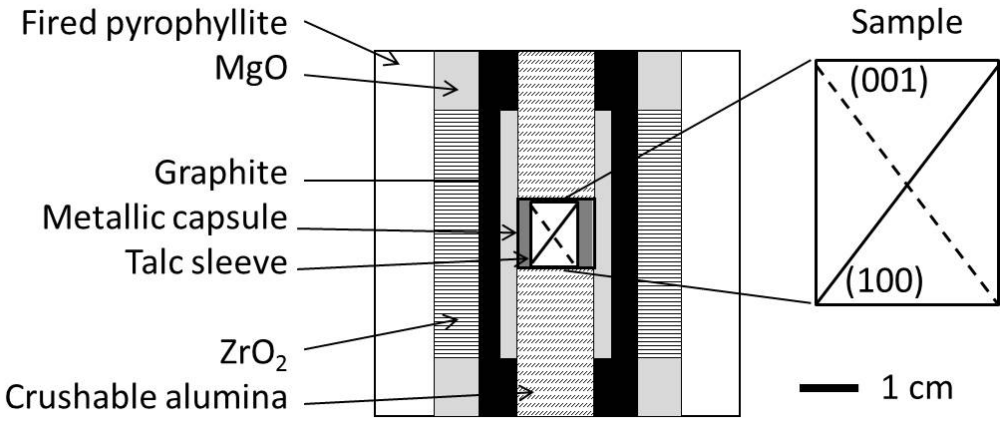

Fig. 3.8-9: HP-HT D-DIA deformation cell assembly. The pressure medium is fired pyrophyllite. The sample is a single crystal of olivine, orientated to activate the [100](001) and [001](100) slip systems during the deformation.

g. *Calibration of metal-alloy sliding redox sensors (H. Mohseni and D.J. Frost)*

Metal-alloy sliding redox sensors are increasingly being used to measure oxygen fugacities in experiments, such as those designed to calibrate mineral redox equilibria for use in oxy-thermobarometry. Different binary metal alloy systems have been proposed such as Fe-Ir, Fe-Pt and Fe-Pd for this purpose. To help evaluate the optimal system we have compared the oxygen fugacities measured using these 3 alloys when each is equilibrated at the same conditions in a CO/CO_2 gas mixing furnace.

Starting materials were dried, fine grained mixtures of Fe_3O_4 and MgO, in the appropriate proportions to obtain $(Mg_x,Fe_{1-x})O$ after reduction where x was either 0.1 or 0.25. Aliquots of these two mixtures were then combined with 5 wt. % of either Ir, Pd or Pt and each composition was pressed into a pellet. In most experiments 3 pellets containing the 3 different platinum group metals were run simultaneously within the gas mixing furnace. After equilibrating at a fixed fO_2 and 1200 °C for ~ 12 hours, the samples were drop quenched.

The quenched samples consisted of (Mg,Fe)O magnesiowustite, Fe-alloys and in some cases magnetite Fe_3O_4-$MgFe_2O_4$ solid solutions. Chemical compositions of individual phases were found to be homogeneous except for very large metal grains (> 20 microns). In most cases analyses were made on alloy grains < 5 microns in diameter. Based on the equilibrium,

$$2Fe_{\text{ metal}} + O_2 \leftrightarrow 2FeO_{\text{ oxide}} \quad (1)$$

the fO_2 can be calculated from,

$$\log fo_2 = \frac{\Delta_f G^0 + 2RT\left(\ln X_{FeO}^{fp} + \ln\gamma_{FeO}^{fp} - \ln X_{Fe}^{alloy} - \ln\gamma_{Fe}^{alloy}\right)}{RT\ln 10} \quad (2)$$

Where $\Delta_f G^0$ is the Gibbs free energy of formation of FeO, X and γ are respectively the mole fraction and activity coefficient of each component, R is the gas constant and T is temperature. Activity coefficients for both phases are calculated as a function of composition using Margules expressions taken from the literature. Due to the differences in activity-composition relations between the alloys, each contains a different mole fraction of Fe in the alloy at the same fO_2. At any set of conditions Pt contains the most Fe because it is the most non-ideal of the solid solutions, with the largest negative excess enthalpy of mixing and Ir alloys contain the least.

Figure 3.8-10 shows two comparisons between the fO_2 calculated using the Pt-Fe alloy sensor and both the Pd-Fe and Ir-Fe sensors. Pt-Fe and Pd-Fe fO_2 determinations are in very good agreement and the maximum deviation is < 0.3 log units. The agreement between Pt-Fe and Ir-Fe is also within 0.4 log units, except at the highest fO_2, where the Ir-Fe sensor deviates by over 4 log units.

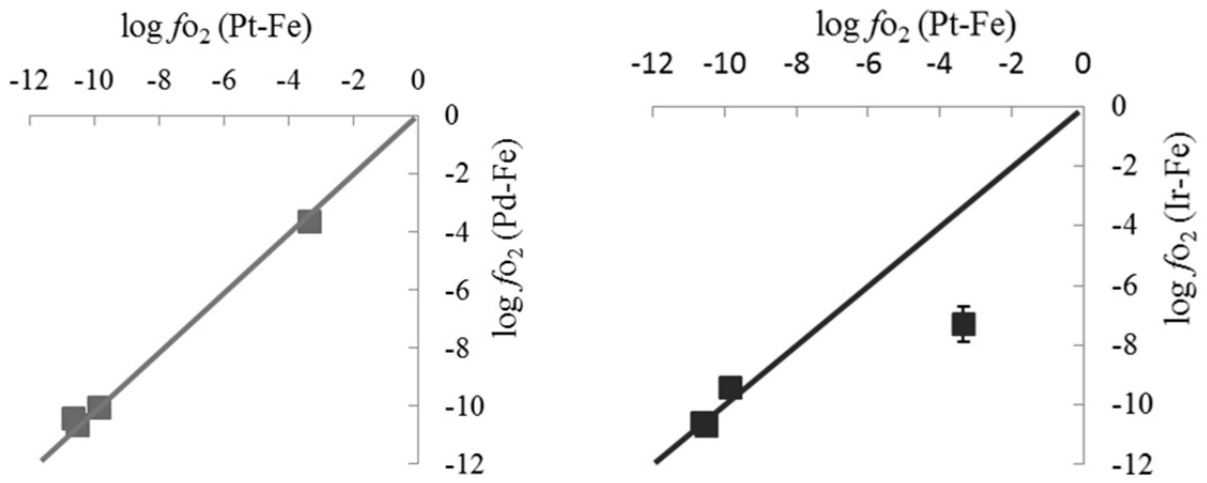

Fig. 3.8-10: Consistency between oxygen fugacities calculated using different alloy redox sensors at 3 sets of conditions. Whereas Pd-Fe and Pt-Fe sensors are in good agreement at all 3 conditions the Ir-Fe sensor deviates from the others at the highest oxygen fugacity.

With increasing fO_2 the Fe contents of all alloys drop. At the highest fO_2 the Fe concentration in the Ir metal alloy is 1.6 at. % or 0.5 wt. %. If the calculated fO_2 were to match that of the Pt-Fe alloy then the concentration would be ~ 0.05 wt. %. At this concentration level the alloy analyses may be susceptible to interference from secondary fluorescence. This occurs during electron microprobe analyses (EMPA) where electrons from the microprobe pass through the small metal alloy grains and excite iron atoms in the surrounding oxide material. X-rays are generated from Fe in the oxides, which appear in the metal analyses. Such secondary fluorescence contamination is likely small and only affects metal Fe concentrations when they are at or below ~ 0.5 wt. %. In Fig. 3.8-11 Ir-Fe activity coefficients (γ_{Fe}^{Ir-Fe}) have been back calculated using oxygen fugacities determined from the Pt-Fe sensor. As can be seen, the calculated activity coefficients are in very good agreement with the previous Ir-Fe measurements made in 1968. However, the data point from the highest fO_2 experiment falls well off the expected trend, most likely due to the effect of secondary fluorescence during EMPA analysis, as described above.

The alloy samples were also analysed using X-ray powder diffraction to determine the excess molar volumes ($\Delta_m\overline{V}^{ex}$), which are required in order to use these redox sensors at high pressure. The excess volumes are described with the equation $\Delta_m\overline{V}^{ex} = X_jX_iW_a{}^V$ where values for W^v of Ir, Pd and Pt alloys were found to be 0.07, 0.15 and 0.13 J/bar, respectively. As a result Ir activities will change the least with pressure and pressure will tend to make all solutions more ideal, such that their activity-composition relations will approach each other. However, along the Pt-Fe solution, for mid-range Fe concentrations, an intermediate $FePt_3$ structure is observed, which due to ordering of Fe onto the face centred site in each cell has the primitive cubic $Pm\overline{3}m$ space group, rather than the fully disordered FCC $Fm\overline{3}m$ unit cell. Some uncertainty remains as to the effect that this change in space group will have on $\Delta_m\overline{V}^{ex}$

for the Pt alloy and consequently on the oxygen fugacities calculated using the sensor at high pressures. Furthermore, electron microprobe analyses indicate significant carbon concentrations of the order of 1 wt. % in Pd-Fe alloys. None of the other alloys seem to be affected in this way. Although Figure 3.8-10 implies that carbon has little effect on the calculated fO_2, this might change at higher pressure and temperature if carbon solubility increases. In summary, although sliding redox sensors based on Ir-Fe alloy are limited at high oxygen fugacities by the resulting low Fe concentrations, the low carbon solubility and small excess volume of mixing probably makes them more reliable for use at high pressure compared to Pt or Pd alloys.

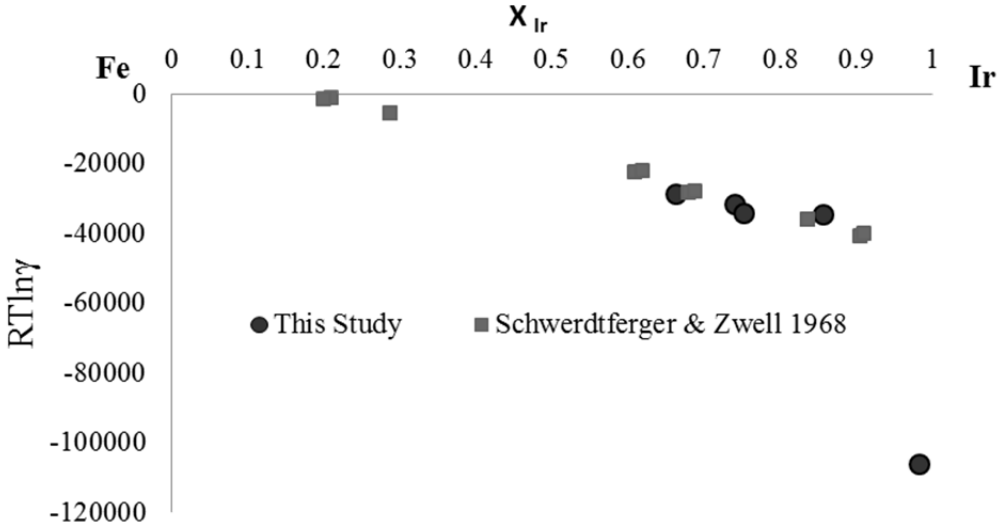

Fig. 3.8-11: Back calculated Ir-Fe activity coefficients, determined using the fO_2 determined from the Pt-Fe redox sensor. Data are compared with activity coefficients measured in the study of Schwerdtferger & Zwell (1968; Transactions of the Metallurgical Society of AIME, 242: 631). The data point for the lowest alloy Fe content falls significantly off the near linear trend. This is most likely due to erroneously high Fe content measurements from this sample, as a result of secondary Fe fluorescence from surrounding oxides during EMPA analysis.

h. *Quantitative chemical analysis of carbon and oxygen in molten Fe-rich alloy by analytical transmission electron microscopy (N. Miyajima; R.A. Fischer and A.J. Campbell/Chicago; D.J. Frost; D. Harries, F. Langenhorst and K. Pollok/Jena; S. Petitgirard and D.C. Rubie)*

Carbon dissolved in metal is likely to strongly affect metal-silicate partitioning of siderophile elements, such as Co, Ni, V, Cr, and light elements, such as Si and O, between molten Fe-rich alloy and silicate melt in a laser-heated diamond anvil cell (LHDAC). The source of such carbon is chemical reaction between the sample and the diamond anvils. In order to determine reliable metal-silicate partition coefficients, corrections must be made based on the concentration of carbon in the metal. Unfortunately carbon is extremely difficult to analyze quantitatively using transmission electron microscopy (TEM), due to various sources of

hydrocarbon contamination during sample preparation and in the TEM. The analysis of oxygen contents is also important for evaluating the metal-silicate partitioning of this element.

Here we report a procedure to evaluate carbon and oxygen contents in focused ion beam (FIB) prepared TEM lamellae from LHDAC samples (Fig. 3.8-12). The FIB lamellae were cleaned using a plasma cleaning system prior to TEM analysis. We calibrated ratios of partial cross-sections of carbon and oxygen against iron in electron energy-loss spectroscopy (EELS) analyses in a TEM operating at 200 kV under an oil-free vacuum system. The aim is to obtain a quantitative chemical analysis of carbon and oxygen dissolved in the molten Fe-rich alloy, combined with energy dispersive X-ray spectroscopy (EDXS) of the other heavier elements.

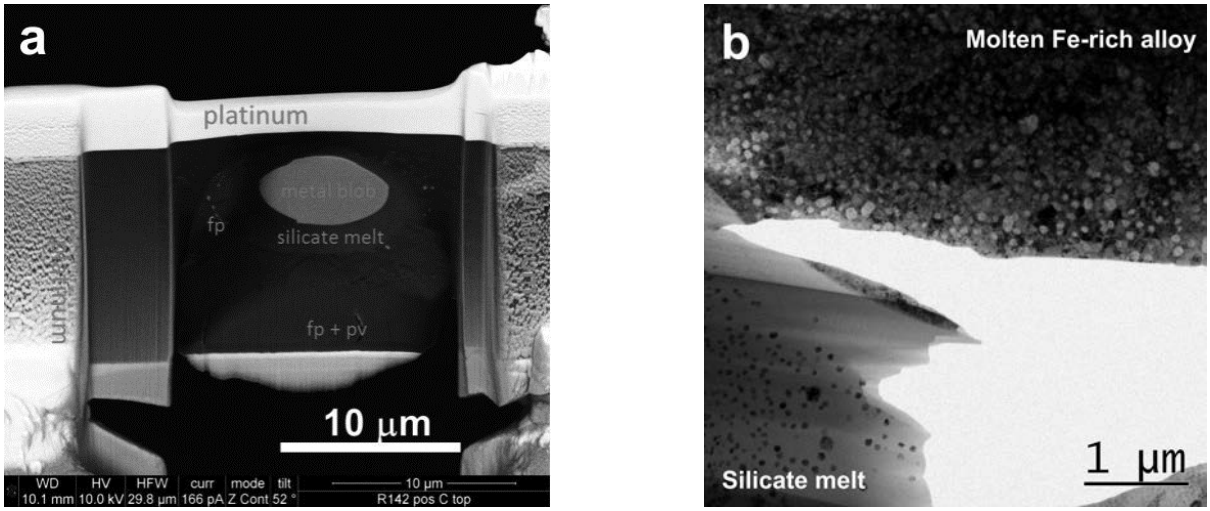

Fig. 3.8-12: (a) Secondary electron micrograph of an FIB lamella of quenched molten Fe-rich alloy and silicate melt in an LHDAC experiment. (b) Bright-field TEM micrograph of the boundary between molten Fe-rich alloy and silicate melt.

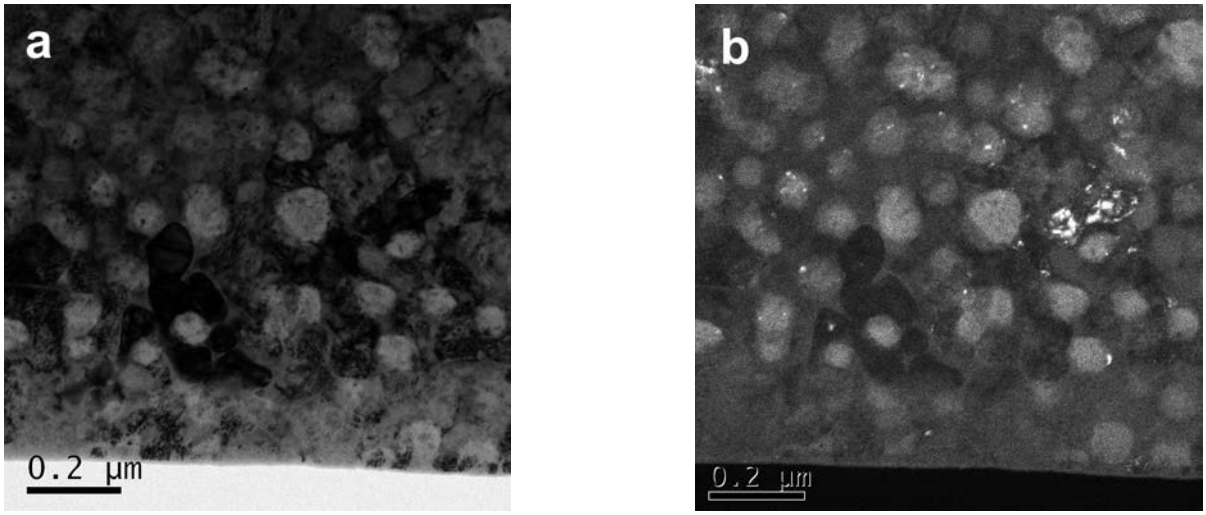

Fig. 3.8-13: (a) Bright field TEM micrograph of quench textures of the molten Fe-rich alloy. (b) Dark field TEM micrograph (with a d-spacing of 0.34 nm) of the same area, in which the iron carbide phase is visible with whitish contrast.

Preliminary results indicate 3-7 at. % carbon and 16-29 at. % oxygen in Fe-rich alloys recovered from 43-100 GPa and 3700-5500 K as evaluated by EELS, together with metal-silicate partitioning by EDXS. Also, in the TEM with diffraction contrast, the domains that contain the detected carbon, the iron carbide phase, are visible in a dark-field TEM image (Fig. 3.8-13). In the near future, we are planning to cross-check the obtained carbon contents with other established analytical techniques (*e.g.*, Nano-SIMS).

i. *Synthesis of large stishovite single crystals (A. Černok, S. Blaha and T. Boffa Ballaran; N.A. Dubrovinskaia/Bayreuth; L.S. Dubrovinsky)*

For many physical property measurements, it is desirable that samples are in the form of single crystals. Following the "thermal gradient method" of Shatskiy *et al.*, we synthesized single crystals of stishovite up to a maximum size of 1.7 × 1.5 × 1 mm (Fig. 3.8-14). The synthesis procedure follows two steps – we first synthesized polycrystalline stishovite from a quartz starting material using a standard multianvil assembly and then placed it in a second experiment, in which a thermal gradient across a capsule of a slightly modified assembly promotes the growth of large single crystals.

Coarse-grained, polycrystalline stishovite was synthesized starting from synthetic quartz. Trace element concentrations in the starting material are very low, as revealed by ICP-MS analyses: K (12 ppm), Al (7 ppm), P (4 ppm), Fe (3 ppm), Mg (2 ppm), Li, B, Na, Mn, Cu, Ga, Ge, Ag, and Sn (< 1 ppm), Ca, Ti and Au below detection limits. Samples and analyses were kindly provided by Andreas Audetat. The starting quartz was cut into 4.5 × 2.5 mm cylindrical rods from a very large single crystal from China. These single crystal rods fit precisely into a Pt capsule, with the *c* - crystallographic axis perpendicular to the bottom and the top. A welded Pt capsule (2.7 mm inner diameter, 6 mm height) was placed at the center of an 18 mm edge length Cr_2O_3-doped MgO octahedral multianvil pressure assembly (18M). A $W_{97}Re_3$-$W_{75}Re_{25}$ thermocouple was placed horizontally through the wall of the $LaCrO_3$ furnace and below the capsule, for monitoring the temperature. The octahedron was compressed using WC cubes with a truncation of 11 mm in the 5000t Kawai-type multianvil apparatus at BGI. The first synthesis experiment was carried out at 11 GPa and 1150 °C for 5 hours, but the experimental conditions at this stage are not crucial, as long as the run product consists of stishovite. We then placed this run product, which consisted of coarse grained stishovite and very small amount of fine grained coesite, into a Pt capsule of the same size as for the first experiment, together with 5 µl of distilled water. The sample was compressed to ~ 13.5 GPa and heated for 4 hours at ~ 1500 °C, using the temperature calibration of the previous run. In order to achieve a thermal gradient within the Pt capsule and improve the single crystal growth, we slightly modified the 18M assembly in this experiment: the zirconia disc on the bottom is 0.5mm longer and the zirconia disc on top is 0.5mm shorter, so that the capsule is not located exactly in the center of the heater. In one run, several large crystals of

stishovite, a few hundred μm up to 1 mm in size were contained in a fine-grained matrix of very fine-grained coesite and of needle-shaped crystals of stishovite. The c-axis of stishovite lies approximately along the longest dimension of the crystal. In another similar set of experiments we obtained large crystals, up to 1.7 mm in length (Fig. 3.8-14). In one experiment we could observe the crystallization of stishovite on the top lid of the capsule that was located furthest from the heater center, thus being exposed to a slightly lower temperature than the rest of the capsule (Fig. 3.8-14).

X-ray diffraction was performed on a relatively small crystal, 170 × 250 × 800 μm. Intensity data were collected at ambient conditions using an Xcalibur diffractometer with MoKα radiation operated at 40 kV and 30 mA, equipped with a CCD detector, a graphite monochromator and a 0.8 mm collimator. Omega scans were chosen to obtain coverage of 66 % of the full reciprocal sphere up to 2θmax = 70°, however a high redundancy collection was chosen in order to better constrain the absorption of this large crystal. Absorption corrections based on the crystal shape were taken into account for the correction of the reflection intensities using the CrysAlis package (Oxford Diffraction 2006). Optimization of a 3-D crystal shape model over X-ray diffraction data was based on a jpeg movie recorded every 2° during phi-rotation and resulted in a shape model that contains 10 faces. The rotational images confirmed good centering of the crystal. In spite of the relatively small absorption coefficient (*i.e.*, μ = 1.618 mm^{-1}) due to the large dimensions of the crystal we obtained transmission factor of 0.39/0.53 (min/max). However, the good shape analysis gave rise to an improvement of the R_{int} from 5 % to 2 %.

These single crystals of stishovite have been used to conduct laser-driven shock experiments yielding equation-of-state and electronic conductivity data at unprecedented conditions, at a pressure of 500 GPa and temperature above 8000 K, comparable to the core-mantle boundary conditions for a 5-Earth-mass super-Earth.

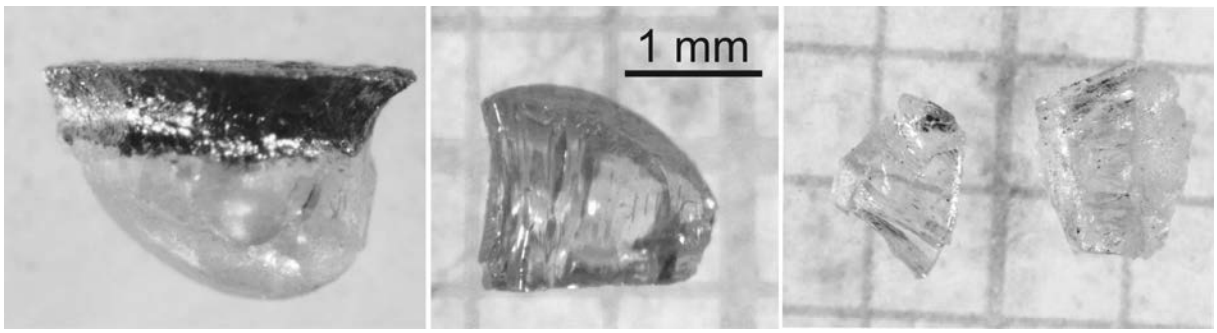

Fig. 3.8-14: Single crystals of stishovite from several experiments. Crystallization of stishovite occurred on the top lid of the capsule, that was located in the colder region of the asymmetrically modified 18M assembly (left). The largest single crystals synthesized in our experiments are shown (middle and right).

j. *First systematic study of synthetic fluid inclusions in opaque ore minerals: Method development (V. Casanova, K. Kouzmanov, N. Ubrig and L. Fontboté/Geneva; A. Audétat)*

Near-infrared (NIR) microscopy of ore minerals can be used to study internal textures of minerals that are opaque to the visible light, such as pyrite, enargite, wolframite, hematite and stibnite. It has also been successfully applied in studies of fluid inclusions (FI) hosted in opaque ore minerals, thus providing direct insights into P-T-X properties of ore-forming fluids. An earlier study performed on enargite-hosted FIs pointed out an important overestimation of fluid salinities and underestimation of homogenization temperatures owing to shifts in recorded phase transition temperatures as a function of the used light intensity. More recent work on FIs hosted in pyrite, found no significant impact of the light intensity on recorded phase change temperatures. It is critical to understand the processes behind light intensity-driven temperature shifts encountered in some NIR-transparent minerals in order to bring meaningful results to ore geology. Here we report results of the first systematic study of synthetic FIs in a variety of NIR-transparent ore minerals in an attempt to create standards for NIR-microthermometry.

Natural samples of enargite, pyrite, stibnite, hematite, Fe-rich, and Fe-poor sphalerite were selected on the basis of their transparency to NIR and their paucity in FIs. For each batch, an opaque mineral was loaded together with its powdered equivalent and synthetic quartz into a gold capsule to which an aqueous solution of known composition (5 wt. %, 10 wt. %, or 20 wt. % NaCl) spiked with Cs was added. After several days of equilibration in a cold-seal pressure vessel at fixed P-T conditions, the samples were cracked *in situ* and held at the same P-T conditions for several more days in order for the cracks to seal. The recovered samples were prepared as doubly-polished 120 µm-thick sections. Microthermometric measurements were performed using a Linkam stage FTIR-600 mounted on an Olympus BX51 microscope equipped with IR Olympus objectives. The microscope has been modified to accept a removable 1200 nm low-pass filter placed at the exit of the light source. NIR observations and image acquisition were done using an Olympus XM10 camera connected to the CellP® software. The 100 W Xe-halogen lamp intensity is controlled by an Olympus TH4-200 controller and recorded by a voltmeter mounted in parallel. Reflection and transmission Fourrier transform infrared (FTIR) spectra were acquired in the 800 - 3500 nm interval, using a Bruker 70v spectrometer coupled to a microscope. The intrinsic absorption of each mineral was then calculated.

Synthetic FIs (up to 70 µm in size) were obtained in enargite, pyrite, stibnite, Fe-rich, and Fe-poor sphalerite as well as in all quartz samples. Microthermometry performed under low light intensity yields similar apparent salinities for FIs trapped in quartz and NIR-transparent minerals from the same batch. With increasing light intensity, significantly underestimated final ice melting temperatures are recorded (Fig. 3.8-15). The correlation between light intensity and recorded temperatures is not linear but rather exponential (Fig. 3.8-15). It is important to stress that it is the intensity of light effectively reaching the sample that locally

overheats the sample. This overheating causes the recorded underestimation of temperatures (the thermocouple being shielded). The obtained correlation trends are therefore dependent on the light intensity and the microscope settings (diaphragms aperture, filters; Fig. 3.8-15) but also on the intrinsic absorption of each mineral. Indeed, results obtained for FI hosted in minerals with different absorption spectra show that if the shape of the correlation trends are similar, the span of recorded phase change temperatures is strongly dependant on the intrinsic absorption (Fig. 3.8-15). For a given microscope setting, the more absorbent a mineral, the larger the shift is between true and recorded phase change temperature.

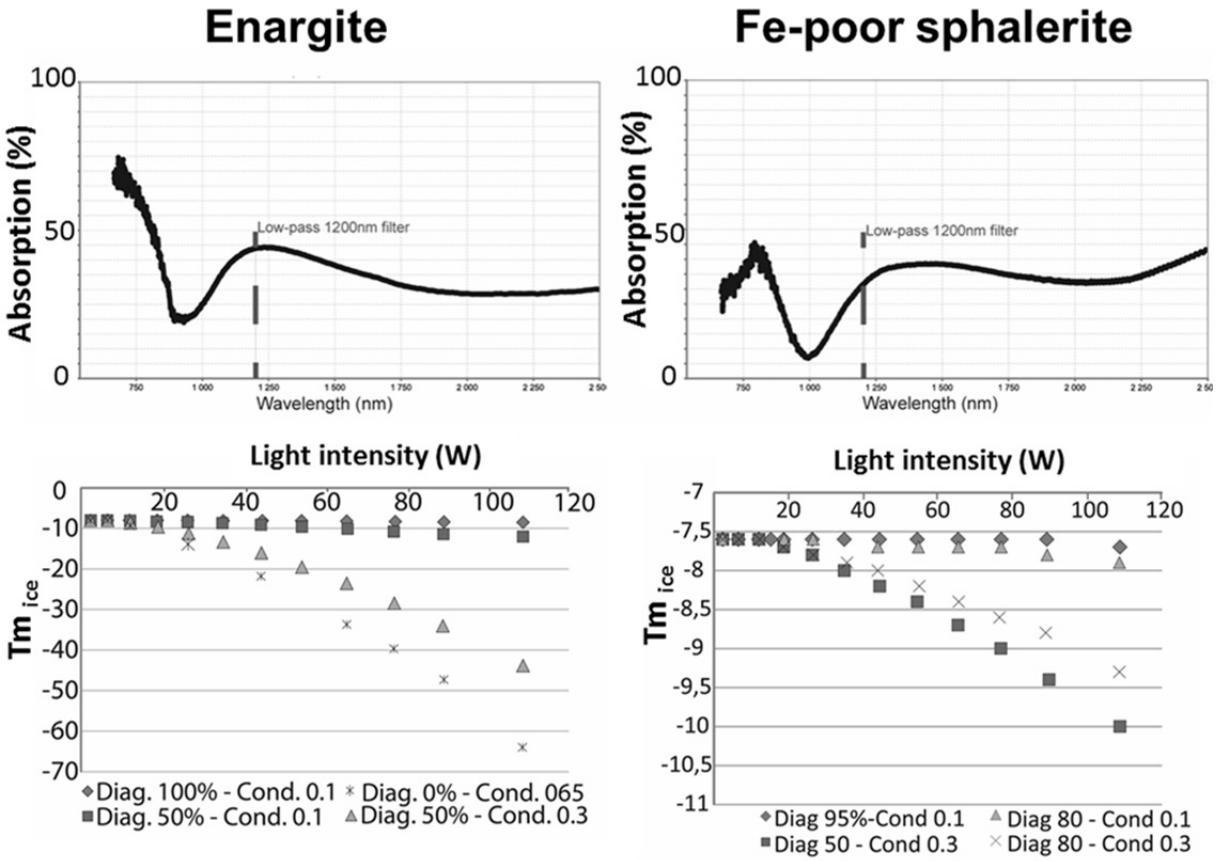

Fig. 3.8-15: Correlation curves between recorded final ice melting temperature (Tm_{ice}) of FI hosted in minerals with different intrinsic absorption (**left**: enargite; **right**: Fe-poor sphalerite) as a function of light source intensity for different microscope settings. Diag.: Diaphragm controlling the incoming beam width (0 %: fully open. 100 % nearly closed). Cond.: Aperture iris diaphragm positioned before the condenser lens.

This study shows that under the same conditions, cogenetic FIs in gangue and ore minerals trap the same fluid at least in terms of major elements. It also confirms that under poorly controlled light intensity and microscope settings during NIR-microthermometry, important underestimation of phase change temperatures can be recorded leading to overestimation of salinities (up to more than 100 %). This directly translates into important errors when

interpreting fluid origins or assessing the internal standard for LA-ICP-MS analyses. The shift spread recorded is a function of the intrinsic absorption of the host. For each NIR-transparent ore mineral, there is a range of light and microscope settings for which no shift is noticeable (Fig. 3.8-15).

k. *Ionizing finite systems – the role of electrostatics (V. Vlček and G. Steinle-Neumann, in collaboration with H.R. Eisenberg and R. Baer/Jerusalem)*

Over the past three decades density functional theory (DFT) and in particular the Kohn-Sham (KS) approach have become the basic tool in theoretical and computational material physics and quantum chemistry. While for the description of ground state properties the use of KS-DFT has rigorous theoretical foundations, there is no such basis for the description of excited states. Moreover, the fact that the generally unknown KS energy functional has to be approximated in practice leads to large errors in estimates for fundamental band gaps and ionization potentials (IP), *i.e.*, the energy difference between the neutral system and a cation with a single charge.

A prominent example for the failure of the approximate KS-DFT approach is the violation of the Perdew-Parr-Levy-Balduz condition for the total energy E_N of a system of N electrons

$$\left.\frac{\partial E_N}{\partial f_F}\right|_{N^-} = E_N - E_{N-1}, \qquad (1)$$

where f_F is the occupation of the frontier KS eigenstate and N^- indicates that the derivative is valuated for the electron deficient side. Noting that the left-hand side of the equation is equal to the highest occupied eigenvalue (Janak's theorem), we obtain the IP theorem

$$\epsilon_F = E_N - E_{N-1}, \qquad (2)$$

which thus provides a physical meaning to the eigenvalue of the KS eigenstate ϵ_F as the negative value of the first ionization energy.

In the approximate KS-DFT approach both conditions are violated: *For small systems*, the total energy difference between the N and $N-1$ particle system (ΔSCF), is known to agree well with the experimental IP, while the KS eigenstate ϵ_F generally provides a poor estimate of the IP. With increasing system size, however, the ΔSCF approach fails, providing the same poor estimates as those obtained from ϵ_F. It was argued for many years that this failure is related to the KS eigenstate relaxation that in general diminishes with system size; the actual size dependence is still in question, however.

We thoroughly analyze the departure from the Perdew-Parr-Levy-Balduz condition for a set of systems using the *energy curvature* C_{ij}, the second derivative of the total energy

$$C_{ij} = \left.\frac{\partial^2 E_N}{\partial f_i \partial f_j}\right|_{N^-}, \qquad (3)$$

which gauges the spurious dependence of ϵ_F on f_F (Eqs. 1 and 2). To first order, C_{ij} captures the difference between the estimate of the IP from ΔSCF and ϵ_F. Using the Hellmann-Feynman theorem we arrive at an expression for the energy curvature in a system of arbitrary shape and size, which is found to depend predominantly on the *Couloumb self-interaction energy* of the system. In the following we illustrate the limiting behaviour in two types of systems, by further approximating the electronic density of a system by a homogeneous electron gas (HEG) and calculating their Coulomb self-interaction energy:

(i) For 3-D nanocrystals with shape of a primitive cell of crystalline diamond the curvature is given by $C^{3D} \sim \frac{D}{\Omega^{1/3}}$ where D in HEG is 49 eV·bohr and Ω is the nanocrystal volume (Fig. 3.8-16).

(ii) For long 1-D alkane chains of length L and diameter d ($L \gg d$) (Fig. 3.8-17) the curvature is $C^{1D} \sim \frac{2}{L} \ln\left(2e^{-\frac{3}{4}\frac{L}{d}}\right)$.

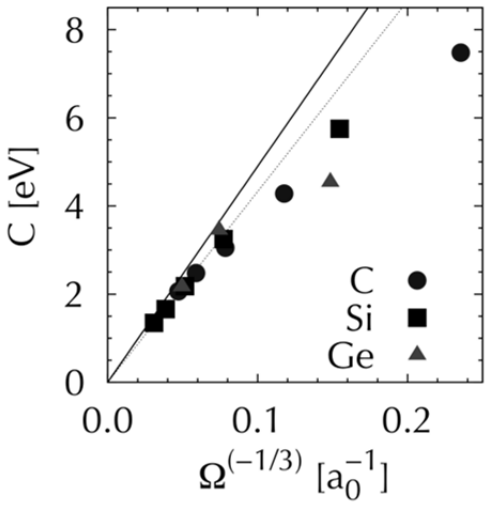

Fig. 3.8-16: Curvature C, obtained within the local density approximation for electron removal for diamond (circles), silicon (squares), and germanium (triangles) nanocrystals, as a function of $\Omega^{-1/3}$. The size of C captures the difference between the estimate of the IP from ΔSCF and ϵ_F. The dotted line represents a least-squares fit to the asymptotic dependence. The solid line represents the asymptotic dependence evaluated for HEG of the same size and shape as the nanocrystals using Eq. (3).

For both cases the energy curvature vanishes in the limit of infinite system size and the ΔSCF estimate of the IP approaches ϵ_F.

From Figure 3.8-16 it is clear that the main contribution to the ΔSCF-results stems from electrostatics, namely from the Coulomb self-interaction term that dominates the energy curvature. Even for 3-D systems with covalent bonding and significant localization of the electronic density, the HEG value for C^{3D} is very close to the actual results from first-principles calculations. The excellent agreement between the theoretical behaviour of C^{1D} and the actual results for the alkane chains (Fig. 3.8-17) further corroborates the validity of the theory.

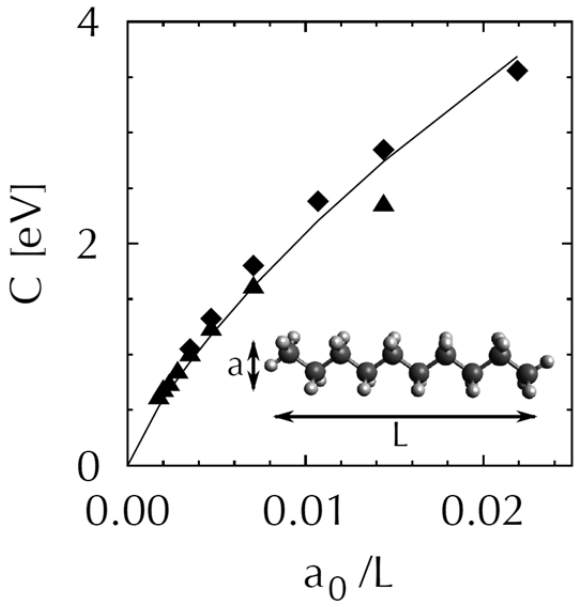

Fig. 3.8-17: Curvature C, obtained within the local density approximation for electron removal from alkane chains C_nH_{2n+2}, as a function of bohr/L. The line represents the asymptotic dependence expected from Eq. (3) for a unit-charge uniform electron gas of the same length as the chain and a radius of d = 2 bohr. Triangles and diamonds represent data obtained using the cc-PVDZ and STO-3G atomic basis sets, respectively. Inset: the hexane molecule C_6H_{10} as an example of an alkane chain, with d and L shown explicitly.

4. Publications, Conference Presentations, Seminars

4.1 Publications (published)

Supplement to **2013** (papers published at the end of 2013):

YAXLEY, G.M.; KAMENETSKY, V.S.; NICHOLS, G.T.; MAAS, R.; BELOUSOVA, E.; ROSENTHAL, A.; NORMAN, M. (2013): The discovery of kimberlites in Antarctica extends the vast Gondwanan Cretaceous province. Nature Communications 4, 2921, doi: 10.1038/ncomms3921

2014

a) Refereed international journals

AUDÉTAT, A.; GARBE-SCHÖNBERG, D.; KRONZ, A.; PETTKE, T.; RUSK, B.; DONOVAN, J.J.; LOWERS, H.A. (2014): Characterisation of a natural quartz crystal as a reference material for microanalytical determination of Ti, Al, Li, Fe, Mn, Ga and Ge. Journal of Geostandards and Geoanalytical Research, doi: 10.1111/j.1751-908X.2014. 00309.x

AUDÉTAT, A.; LOWENSTERN, J.B. (2014): Melt inclusions. – In: TUREKIAN, K.K.; HOLLAND, H.D. (Eds.): Geochemistry of mineral resources. Treatise on Geochemistry 13, 143-173

BOLLINGER, C.; RATERRON, P.; CORDIER, P.; MERKEL, S. (2014): Polycrystalline olivine rheology in dislocation creep: Revisiting experimental data to 8.1 GPa. Physics of the Earth and Planetary Interiors 228, 211-219

BYKOVA, E.A.; BOBROV, A.V.; SIROTKINA, E.A.; BINDI, L.; OVSYANNIKOV, S.V.; DUBROVINSKY, L.S.; LITVIN, Y.A. (2014): X-ray single-crystal and Raman study of knorringite, $Mg_3(Cr_{1.58}Mg_{0.21}Si_{0.21})Si_3O_{12}$, synthesized at 16 GPa and 1600 °C. Physics and Chemistry of Minerals 41, 267-272

BYKOVA, E.; TSIRLIN, A.A.; GOU, H.; DUBROVINSKY, L.; DUBROVINSKAIA, N. (2014): Novel non-magnetic hard boride Co_5B_{16} synthesized under high pressure. Journal of Alloys and Compounds 608, 69-72

CARLSON, R.W.; GARNERO, E.; HARRISON, T.M.; LI, J.; MANGA, M.; MCDONOUGH, W.F.; MUKHOPADHYAY, S.; ROMANOWICZ, B.; RUBIE, D.C.; WILLIAMS, Q.; ZHONG, S. (2014): How did early Earth become our modern world? Annual Review of Earth and Planetary Sciences 42, 151-178

ČERNOK A.; BOFFA BALLARAN, T.; CARACAS, R.; MIYAJIMA, N.; BYKOVA, E.; PRAKAPENKA, V.; LIERMANN, H.-P.; DUBROVINSKY, L. (2014): Pressure-induced phase transitions in coesite. American Mineralogist 99, 755-763

ČERNOK, A.; BYKOVA, E.; BOFFA BALLARAN, T.; LIERMANN, H.-P.; HANFLAND, M.; DUBROVINSKY, L.S. (2014): High-pressure crystal chemistry of coesite-I and its transition to coesite-II. Zeitschrift für Kristallographie – Crystalline Materials, 229 (11), 761-773

CHUKANOV, N.V.; KRIVOVICHEV, S.V.; PAKHOMOVA, A.S.; PEKOV, I.V.; SCHAFER, C.; VIGASINA, M.F.; VAN, K.V. (2014): Laachite, $(Ca,Mn)_2(Zr,Mn)_2Nb_2TiFeO_{14}$, a new zirconolite-related mineral from the Eifel volcanic region, Germany. European Journal of Mineralogy 26 (1), 103-111

CHUMAKOV, A.I.; MONACO, G.; FONTANA, A.; BOSAK, A.; HERMANN, R.; BESSAS, D.; WEHINGER, B.; CRICHTON, W.; KRISCH, M.; RUFFER, R.; BALDI, G.; CARINI JR., G.; CARINI, G.; D'ANGELO, G.; GILIOLI, E.; TRIPODO, G.; ZANATTA, M.; WINKLER, B.; MILMAN, V.; REFSON, K.; DOVE, M.; DUBROVINSKAIA, N.; DUBROVINSKY, L.; KEDING, R.; YUE, Y. (2014): Role of disorder in the thermodynamics and atomic dynamics of glasses. Physical Review Letters 112, 025502

DYADKIN, V.; GRIGORIEV, S.; OVSYANNIKOV, S.V.; BYKOVA, E.; DUBROVINSKY, L.; TSVYASHCHENKO, A.; FOMICHEVA, L.N.; CHERNYSHOV, D. (2014): Crystal structure and thermal expansion of $Mn_{1-x}Fe_xGe$. Acta Crystallographica Section B 70, 676-680

GIANNINI, M.; BOFFA BALLARAN, T.; LANGENHORST, F. (2014): Crystal chemistry of synthetic Ti-Mg bearing hibonites: A single crystal X-ray study. American Mineralogist 99, 2060-2067

GLAZYRIN, K.; BOFFA BALLARAN, T.; FROST, D.J.; MCCAMMON, C.; KANTOR, A.; MERLINI, M.; HANFLAND, M.; DUBROVINSKY, L. (2014): Magnesium silicate perovskite and effect of iron oxidation state on its bulk sound velocity at the conditions of the lower mantle. Earth and Planetary Science Letters 393, 182-186

GOU, H.; TSIRLIN, A.A.; BYKOVA, E.; ABAKUMOV, A.M.; VAN TENDELOO, G.; RICHTER, A.; OVSYANNIKOV, S.V.; KURNOSOV, A.V.; TROTS, D.M.; KONÔPKOVÁ, Z.; LIERMANN, H.-P.; DUBROVINSKY, L.; DUBROVINSKAIA, N. (2014): Peierls distortion, magnetism, and high hardness of manganese tetraboride. Physical Review B 89, 064108

GREEN, D.H.; HIBBERSON, W.O.; ROSENTHAL, A.; KOVACS, I.; YAXLEY, G.M.; BRINK, F. (2014): Experimental study of the influence of water on melting and phase assemblages in the upper mantle. Journal of Petrology 55, 10, 2067-2096

GREENBERG, E.; ROZENBERG, G.K.; XU, W.M.; PASTERNAK, M.P.; MCCAMMON, C.; GLAZYRIN, K.; DUBROVINSKY, L. (2014): Mott transition in $CaFe_2O_4$ at around 50 GPa. Physical Review B 88, 214109

JACOBSON, S.A.; MORBIDELLI, A.; RAYMOND, S.N.; O'BRIEN, D.P.; WALSH, K.J.; RUBIE, D.C. (2014): Highly siderophile elements in the Earth's mantle as a clock for the Moon-forming impact. Nature 508, 84-87

JACOBSON, S.A.; SCHEERES, D.J.; MCMAHON, J. (2014): The formation of the wide asynchronous binary asteroid population. Astrophysical Journal 780:1, 60-81

JACOBSON, S.A.; MARZARI, F.; ROSSI, A.; SCHEERES, D.J.; DAVIS, D.R. (2014): Effect of rotational disruption on the size-frequency distribution of the Main Belt asteroid population. Monthly Notices of the Royal Astronomical Society Letters 439, L95-L99

JACOBSON, S.A.; MORBIDELLI, A. (2014): Lunar and terrestrial planet formation in the Grand Tack scenario. Philosophical Transactions of the Royal Society A 372:2024, 0174

JACOBSON, S.A. (2014): Small asteroid system evolution. Proceedings of the International Astronomical Union 9, 108-117

KEPPLER, H. (2014): Earth's deep water reservoir. Nature 507, 174-175

KONSCHAK, A.; KEPPLER, H. (2014): The speciation of carbon dioxide in silicate melts. Contributions to Mineralogy and Petrology 167, 998

KOZLENKO, D.P.; KICHANOV, S.E.; LUKIN, E.V.; DANG, N.T.; DUBROVINSKY, L.S.; LIERMANN, H.-P.; MORGENROTH, W.; KAMYNIN, A.A.; GRIDNEV, S.A.; SAVENKO, B.N. (2014): Pressure-induced polar phases in relaxor multiferroic $PbFe_{0.5}Nb_{0.5}O_3$. Physical Review B 89, 174107

KOZLENKO, D.P.; DANG, N.T.; JABAROV, S.H.; BELIK, A.A.; KICHANOV, S.E.; LUKIN, E.V.; LATHE, C.; DUBROVINSKY, L.S.; KAZIMIROV, V.Yu.; SMIRNOV, M.B.; SAVENKO, B.N.; MAMMADOV, A.I.; TAKAYAMA-MUROMACHI, E.; KHIEM, L.H. (2014): Structural polymorphism in multiferroic $BiMnO_3$ at high pressures and temperatures. Journal of Alloys and Compounds 585, 741-747

KULARATNE, K.; AUDÉTAT, A. (2014): Rutile solubility in hydrous rhyolite melts at 750-900 °C and 2 kbar, with application to titanium-in-quartz (TitaniQ) thermobarometry. Geochimica et Cosmochimica Acta 125, 196-209

KUPENKO, I.; MCCAMMON, C.; SINMYO, R.; PRESCHER, C.; CHUMAKOV, A.I.; KANTOR, A.; RÜFFER, R.; DUBROVINSKY, L. (2014): Electronic spin state of Fe,Al-containing $MgSiO_3$ perovskite at lower mantle conditions. Lithos 189, 168-172

LAUMONIER, M.; SCAILLET, B.; ARBARET, L.; CHAMPALLIER, R. (2014): Experimental simulation of magma mixing at high pressure. Lithos 196, 281-300

LAUMONIER, M.; SCAILLET, B.; PICHAVANT, M.; CHAMPALLIER, R.; ANDUJAR, J.; ARBARET, L. (2014): On the conditions of magma mixing and its bearing on andesite production in the crust. Nature Communications 5, 5607

LITVIN, Yu.A.; SPIVAK, A.V.; SOLOPOVA, N.A.; DUBROVINSKY, L.S. (2014): On origin of lower-mantle diamonds and their primary inclusions. Physics of the Earth and Planetary Interiors 228, 176-185

LI, Y.; KEPPLER, H. (2014): Nitrogen speciation in mantle and crustal fluids. Geochimica et Cosmochimica Acta 129, 13-32

LIN, Y.; EL GORESY, A.; HU, S.; ZHANG, J.; GILLET, P.; XU, Y.; HAO, J.; MIYAHARA, M.; OUYANG, Z.; OHTANI, E.; XU, L.; YANG, W.; FENG, L.; ZHAO, X.; YANG, J.; OZAWA, S. (2014): NanoSIMS analysis of organic carbon from the Tissint Martian meteorite: Evidence for the past existence of subsurface organic-bearing fluids on Mars. Meteoritics & Planetary Science 49, 12, 2201-2218

LIU, X.; XIONG, X.; AUDÉTAT, A.; LI, Y.; SONG, M.; SUN, W.; DING, X. (2014): Partitioning of copper between olivine, orthopyroxene, clinopyroxene, spinel, garnet and silicate melts at upper mantle conditions. Geochimica et Cosmochimica Acta 125, 1-22

MARRA, F.; SOTTILI, G.; GAETA, M.; GIACCIO, B.; JICHA, B.; MASOTTA, M.; PALLADINO, D.M.; DEOCAMPO, D.M. (2014): Major explosive activity in the Monti Sabatini Volcanic District (central Italy) over the 800-390 ka interval: Geochronological-geochemical overview and tephrostratigraphic implications. Quaternary Science Reviews 94, 74-101

MASOTTA, M.; NI, H.; KEPPLER, H. (2014): *In situ* observations of bubble growth in basaltic, andesitic and rhyodacitic melts. Contributions to Mineralogy and Petrology 167, 976

MISITI, V.; VETERE, F.; HEIDELBACH, F. (2014): Crystallization from a melt and crystallization at subsolidus conditions: Comparison from crystal size distribution study on Gennargentu Rocks (Sardinia, Italy). Periodico di Mineralogia 83, 3, 401-418

MOLLO, S.; MASOTTA, M. (2014): Optimizing pre-eruptive temperature estimates in thermally and chemically zoned magma chambers. Chemical Geology 368, 97-103

MOOKHERJEE, M.; KEPPLER, H.; MANNING, C.E. (2014): Aluminum speciation in aqueous fluids at deep crustal pressure and temperature. Geochimica et Cosmochimica Acta 133, 128-141

MOROZOVA, N.V.; OVSYANNIKOV, S.V.; KOROBEINIKOV, I.V.; KARKIN, A.E.; TAKARABE, K.; MORI, Y.; NAKAMURA, S.; SHCHENNIKOV, V.V. (2014): Significant enhancement of thermoelectric properties and metallization of Al-doped Mg_2Si under pressure. Journal of Applied Physics 115, 213705

NI, H.; CHEN, Q.; KEPPLER, H. (2014): Electrical conductivity measurements of aqueous fluids under pressure with a hydrothermal diamond anvil cell. Reviews of Scientific Instruments 86, 115107

NI, H.; KEPPLER, H.; WALTE, N.; SCHIAVI, F.; CHEN, Y.; MASOTTA, M.; LI, Z. (2014): *In situ* observation of crystal growth in a basalt melt and the development of crystal size distribution in igneous rocks. Contributions to Mineralogy and Petrology 167, 1003

NISHIHARA, Y.; OHUCHI, T.; KAWAZOE, T.; SPENGLER, D.; TASAKA, M.; KIKEGAWA, T.; SUZUKI, A.; OHTANI, E. (2014): Rheology of fine-grained forsterite aggregate at deep upper mantle conditions. Journal of Geophysical Research 119, 253-273

NOVELLA, D.; KESHAV, S.; GUDFINSSON, G.H.; GHOSH, S. (2014): Melting phase relations of model carbonated peridotite from 2 to 3 GPa in the system CaO-MgO-Al_2O_3-SiO_2-CO_2 and further indication of possible unmixing between carbonatite and silicate liquids. Journal of Geophysical Research: Solid Earth 119, 2780-2800

NOVELLA, D., FROST, D.J. (2014): The composition of hydrous partial melts of garnet peridotite at 6 GPa: Implications for the origin of group II kimberlites. Journal of Petrology 55, 2097-2123

NOVELLA, D.; FROST, D.J.; HAURI, E.H.; BUREAU, H.; RAEPSAET, C.; ROBERGE, M. (2014): The distribution of H_2O between silicate melt and nominally anhydrous peridotite and the onset of hydrous melting in the deep upper mantle. Earth and Planetary Science Letters 400, 1-13

OHUCHI, T.; FUJINO, K.; KAWAZOE, T.; IRIFUNE, T. (2014): Crystallographic preferred orientation of wadsleyite and ringwoodite: effects of phase transformation and water on seismic anisotropy in the mantle transition zone. Earth and Planetary Science Letters 397, 133-144

OVSYANNIKOV, S.V.; GOU, H.; KARKIN, A.E.; SHCHENNIKOV, V.V.; WIRTH, R.; DMITRIEV, V.; NAKAJIMA, N.; DUBROVINSKAIA, N.; DUBROVINSKY, L. (2014): Bulk silicon crystals with the high boron content, $Si_{1-x}B_x$: Two semiconductors form an unusual metal. Chemistry of Materials 26, 5274-5281

PAKHOMOVA, A.S.; ARMBRUSTER, T.; KRIVOVICHEV, S.V.; YAKOVENCHUK, V.N. (2014): *In situ* temperature dependent dehydration of the zeolite merlinoite from the Khibiny massif, Russia: A single crystal X-ray study. European Journal of Mineralogy 26, 371-380

PAMATO, M.G.; KURNOSOV, A.; BOFFA BALLARAN, T.; TROTS, D.M.; CARACAS, R.; FROST, D.J. (2014): Hexagonal $Na_{0.41}[Na_{0.125}Mg_{0.79}Al_{0.085}]_2[Al_{0.79}Si_{0.21}]_6O_{12}$ (NAL phase): Crystal structure refinement and elasticity. American Mineralogist 99, 1562-1569

POSNER, E.S.; DERA, P.; DOWNS, R.T.; LAZARZ, J.D.; IRMEN, P. (2014): High-pressure single-crystal X-ray diffraction study of jadeite and kosmochlor. Physics and Chemistry of Minerals 41, 695-707

PRESCHER, C.; WEIGEL, C.; MCCAMMON, C.; NARYGINA, O.; POTAPKIN, V.; KUPENKO, I.; SINMYO, R.; CHUMAKOV, A.I.; DUBROVINSKY, L. (2014): Iron spin state in silicate glass at high pressure: Implications for melts in the Earth's lower mantle. Earth and Planetary Science Letters 385, 130-136

PRESCHER, C.; LANGENHORST, F.; DUBROVINSKY, L.S.; PRAKAPENKA, V.B.; MIYAJIMA, N. (2014): The effect of Fe spin crossovers on its partitioning behavior and oxidation state in a pyrolitic Earth's lower mantle system. Earth and Planetary Science Letters 399, 86-91

POLLOK, K.; HEIDELBACH, F.; JOHN, T.; LANGENHORST, F. (2014): Spherulitic omphacite in pseudotachylytes: Microstructures related to fast crystal growth from seismic melt at eclogite-facies conditions. Chemie der Erde – Geochemistry 74(3), 407-418

RATERRON, P.; DETREZ, F.; CASTELNAU, O.; BOLLINGER, C.; CORDIER, P.; MERKEL, S. (2014): Multiscale modeling of upper mantle plasticity: From single-crystal rheology to multiphase aggregate deformation. Physics of the Earth and Planetary Interiors 228, 232-243

ROBINSON, P.; LANGENHORST, F.; MCENROE, S.A.; FABIAN, K.; BOFFA BALLARAN, T. (2014): Ferroan geikielite and coupled spinel-rutile exsolution from titanohematite: Interface characterization and magnetic properties. American Mineralogist 99, 1694-1712

ROSENTHAL, A.; YAXLEY, G.M.; GREEN, D.H.; HERMANN, J.; KOVACS, I.; SPANDLER, C. (2014): Continuous eclogite melting and variable refertilisation in upwelling heterogeneous mantle. Scientific Reports 4, 6099, doi: 10.1038/srep06099

SAMUEL, H.; KING, S.D. (2014): Mixing at mid-ocean ridges controlled by small-scale convection and plate motion. Nature Geoscience 7, 602-605

SCHMAUSS, D.; KEPPLER, H. (2014): Adsorption of sulfur dioxide on volcanic ashes. American Mineralogist 99, 1085-1094

SCHMIDT, C.; WOHLERS, A.; MARQUARDT, K.; WATENPHUL, A. (2014): Experimental study on the pseudobinary H_2O+$NaAlSi_3O_8$ at 600-800 °C and 0.3-2.4 GPa. Chemical Geology 388, 40-47

SINMYO, R.; GLAZYRIN, K.; MCCAMMON, C.; KUPENKO, I.; KANTOR, A.; POTAPKIN, V.; CHUMAKOV, A.I.; RÜFFER, R.; DUBROVINSKY, L. (2014): The influence of solid solution on elastic wave velocity determination in (Mg, Fe)O using nuclear inelastic scattering. Physics of the Earth and Planetary Interiors 229, 16-23

SINMYO, R.; PESCE, G.; GREENBERG, E.; MCCAMMON, C.; DUBROVINSKY, L. (2014): Lower mantle electrical conductivity based on measurements of Al, Fe-bearing perovskite under lower mantle conditions. Earth and Planetary Science Letters 393, 165-172

SINMYO, R.; BYKOVA, E.; MCCAMMON, C.; KUPENKO, I.; POTAPKIN, V.; DUBROVINSKY, L. (2014): Crystal chemistry of Fe^{3+}-bearing (Mg, Fe)SiO_3 perovskite: a single-crystal X-ray diffraction study. Physics and Chemistry of Minerals 41, 409-417

SOLOPOVA, N.A.; DUBROVINSKY, L.; SPIVAK, A.V.; LITVIN, Yu.A.; DUBROVINSKAIA, N. (2014): Melting and decomposition of $MgCO_3$ at pressures up to 84 GPa. Physics and Chemistry of Minerals, doi: 10.1007/s00269-014-0701-1

SOLOZHENKO, V.L.; KURAKEVYCH, O.O.; LE GODEC, Y.; KURNOSOV, A.; OGANOV, A.R. (2014): Boron phosphide under pressure: *In situ* study by Raman scattering and X-ray diffraction. Journal of Applied Physics 116, 033501

SOUSTELLE, V.; WALTE, N.P.; MANTHILAKE, M.A.G.M.; FROST, D.J. (2014): Melt migration and melt-rock reactions in the deforming Earth's upper mantle: Experiments at high pressure and temperature. Geology 42, 83-86

SPEZIALE, S.; MARQUARDT, H.; DUFFY, T.S. (2014): Brillouin Scattering and its Application in Geosciences. – In: HENDERSON, G.S.; NEUVILLE, D.R.; DOWNS, T. (Eds.): Reviews in Mineralogy and Geochemistry: Spectroscopic Methods in Mineralogy and Materials Science. Mineralogical Society of America MSA 78, 543-603, Chapter 14

SPIVAK, A.; SOLOPOVA, N.; CERANTOLA, V.; BYKOVA, E.; ZAKHARCHENKO, E.; DUBROVINSKY, L.; LITVIN, Yu. (2014): Raman study of $MgCO_3$-$FeCO_3$ carbonate solid solution at high pressures up to 55 GPa. Physics and Chemistry of Minerals 41, 633-638

SUN, W.; AUDÉTAT, A.; DOLEJS, D. (2014): Solubility of molybdenite in hydrous granitic melts at 800 °C, 100-200 MPa. Geochimica et Cosmochimica Acta 131, 393-401

VERAS, D.; JACOBSON, S.A.; GÄNSICKE, B.T. (2014): Post-main-sequence debris from rotation-induced YORP break-up of small bodies. Monthly Notices of the Royal Astronomical Society 445:3, 2794-2799

YANG, X.; KEPPLER, H.; DUBROVINSKY, L.; KURNOSOV, A. (2014): *In situ* infrared spectra of hydroxyl in wadsleyite and ringwoodite at high pressure and high temperature. American Mineralogist 99, 724-729

YANG, X.; DINGDING, L.; QUNKE, X. (2014): CO_2-induced small water solubility in olivine and implications for properties of the shallow mantle. Earth and Planetary Science Letters 403, 37-47

b) Popular scientific magazines

MCCAMMON, C. (2014): Iron electronic state and the electrical conductivity of the Earth's lower mantle. ESRF Highlights 2013, 24-25 (*published in February 2014*)

4.2 Publications (submitted, in press)

AUDÉTAT, A.: Composition and formation conditions of magmas (melts, fluids and minerals) related to porphyry Mo mineralization at Climax, Colorado. Journal of Petrology (submitted)

AUZENDE, A.-l.; ESCARTIN, J.; WALTE, N.; GUILLOT, S.; HIRTH, G.; FROST, D.J.: Deformation mechanisms of antigorite serpentinite at subduction zone conditions determined from experimentally and naturally deformed rocks. Earth and Planetary Science Letters (submitted)

BEYER, C.; FROST, D.J.; MIYAJIMA, N.: Experimental calibration of a garnet-clinopyorxene geobarometer for mantle eclogites. Contributions to Mineralogy and Petrology (submitted)

BLYTHE, L.; DEEGAN, F.; FREDA, C.; JOLIS, E.M.; MASOTTA, M.; MISITI, V.; TADDEUCCI, J.; TROLL, V.: Rapid CO_2 bubble generation and migration during magma-carbonate interaction. Contributions to Mineralogy and Petrology (submitted)

BOLLINGER, C.; RATERRON, P.; CORDIER, P.; MERKEL, S.: Deformation of forsterite polycrystals at mantle pressure: Comparison with Fe-bearing olivine and the effect of iron on its plasticity. Physics of the Earth and Planetary Interiors (submitted)

BONS, P.; BAUR, A.; ELBURG, M.; LINDHUBER, M.J.; MARKS, M.A.W.; SOESOO, A.; VAN MILLIGEN, B.P.; WALTE, N.P.: Layered intrusions and traffic jams. Geology (accepted), doi: 10.1130/G36276.1

BYKOVA, E.; DUBROVINSKY, L.; DUBROVINSKAIA, N.; BYKOV, M.; MCCAMMON, C.; OVSYANNIKOV, S.V.; LIERMANN, H.-P.; KUPENKO, I.; CHUMAKOV, A.I.; RÜFFER, R.; HANFLAND, M.; PRAKAPENKA, V.: Fate of banded iron formations subducted into the lower mantle. Science (submitted)

CERANTOLA, V.; WALTE, N.; RUBIE, D.C.: Deformation of a crystalline system with two immiscible liquids: Implications for early core-mantle differentiation. Earth and Planetary Science Letters (submitted)

CHEMIA, Z.; DOLEJŠ, D.; STEINLE-NEUMANN, G.: Thermal effects of variable material properties and metamorphic reactions in a three-component subducting slab. Journal of Geophysical Research (submitted)

DUC-TIN, Q.; KEPPLER, H.: Monazite and xenotime solubility in granitic melts and the origin of the lanthanide tetrad effect. Contributions to Mineralogy and Petrology (submitted)

FARLA, R.J.M.; AMULELE, G.; GIRARD, J.; MIYAJIMA, N.; KARATO, S.: High pressure and temperature deformation experiments on polycrystalline wadsleyite using the rotational Drickamer apparatus. Physics and Chemistry of Minerals (submitted)

FISCHER, R.A.; NAKAJIMA, Y.; CAMPBELL, A.J.; FROST, D.J.; HARRIES, D.; LANGENHORST, F.; MIYAJIMA, N.; POLLOCK, K.; RUBIE, D.C.: High pressure metal-silicate partitioning of Ni, Co, V, Cr, Si and O. Geochimica et Cosmochimica Acta (submitted)

GENTILI, S.; BIAGIONI, C.; COMODI, P.; PASERO, M.; MCCAMMON, C.; BONADIMAN, C.: Ferri-kaersutite, $NaCa_2(Mg_3TiFe^{3+})(Si_6Al_2)O_{22}O_2$, a new anhydrous amphibole from Harrow Peaks, Northern Victoria Land, Antarctica. American Mineralogist (submitted)

HUANG, R.; KEPPLER, H.: Anhydrite stability and the effect of Ca on the behavior of sulfur in felsic magmas. American Mineralogist (in press)

HUMPHREYS, M.; BROOKER, R.; FRASER, D.; BURGISSER, A.; MANGAN, M.; MCCAMMON, C.: Iron oxidation state in hydrous rhyolites during magma ascent and degassing. Journal of Petrology (submitted)

JACOBSON, S.A.; WALSH, K.J.: Accretion of Earth. – In: BADRO, J.; WALTER, M.J. (Eds): Early Earth, AGU Geophysical Monograph Series, AGU/John Wiley & Sons, Inc., Washington, DC, USA (submitted)

JOACHIM, B.; PAWLEY, A.; MARQUARDT, K.; LYON, I.; HENKEL, T.; CLAY, P.; RUZIÉ, L.; BURGESS, R.; BALLENTINE, C.: Experimental partitioning of F, Cl and Br between forsterite, orthopyroxene and silicate melt at Earth's mantle conditions. Geochimica et Cosmochimica Acta (submitted)

KING, S.D.; FROST, D.J.; RUBIE, D.C.: Why cold slabs stagnate in the transition zone. Geology (submitted)

KUPENKO, I.; MCCAMMON, C.; SINMYO, R.; CERANTOLA, V.; POTAPKIN, V.; CHUMAKOV, A.I.; KANTOR, A.; RÜFFER, R.; DUBROVINSKY, L.: Oxidation state of the lower mantle: *In situ* observations of the iron electronic configuration in magnesium silicate perovskite at extreme conditions. Earth and Planetary Science Letters (submitted)

KUSIAK, M.; DUNKLEY, D.; WIRTH, R.; WHITEHOUSE, M.; WILDE, S.; MARQUARDT, K.: Metallic lead nanoparticles discovered in ancient zircons. Earth and Planetary Science Letters (submitted)

LAUMONIER, M.; GAILLARD, F.; SIFRÉ, D.: The effect of pressure and water concentration on the electrical conductivity of dacitic melts: implication for magnetotelluric imaging in subduction areas. Chemical Geology (in press). doi: 10.1016/j.chemgeo.2014.09.019

LAUMONIER, M.; SCAILLET, B.; ARBARET, L.; ANDUJAR, J.; CHAMPALLIER, R.: Experimental mixing of hydrous mafic-felsic crystal-bearing magmas. Chemical Geology (submitted)

LI, Y.; WIEDENBECK, M.; HUANG, R.; KEPPLER, H.: Nitrogen distribution between aqueous fluids and silicate melts. Earth and Planetary Science Letters (submitted)

LI, W.; AUDÉTAT, A.; ZHANG, J.: The role of evaporites in the formation of magnetite-apatite deposits along the Middle and Lower Yangtze River, China: evidence from LA-ICP-MS analysis of fluid inclusions. Ore Geology Reviews (submitted)

LIN, Y.; EL GORESY, A.; HU, S.; ZHANG, J.; GILLET, Ph.; XU, Y.; HAO, J.; MIYAHARA, M.; OUYANG, Z.; OHTANI, E.; XU, L.; YANG, W.; FENG, L.; ZHAO, X.; YANG, J.; OZAWA, Sh.: NanoSIMS analyses of organic carbon from the Tissint Martian meteorite: Evidence for past existence of subsurface organic-bearing fluids on Mars. Meteoritics and Planetary Sciences (in press)

LIU, X.; XIONG, X.; AUDÉTAT, A.; LI, Y.: Partitioning of Cu between mafic minerals, Fe-Ti oxides and intermediate to felsic melts. Geochimica et Cosmochimica Acta (submitted)

LITVIN, Yu.A.; SPIVAK, A.V.; DUBROVINSKY, L.S.: Evolution of the Earth's lower-mantle matter: stishovite paradox and origin of "super-deep" diamonds (experiments at 24 GPa). Lithos (submitted)

MARGOT, J.-L.; PRAVEC, P.; TAYLOR, P.A.; CARRY, B.; JACOBSON, S.A.: Properties of asteroid systems: binaries, triples, and pairs. – In: MICHEL, P.; DEMEO, F.E.; BOTTKE W.F. (Eds): Asteroids IV, U. Arizona-Press, Tucson, AZ, USA (submitted)

MARQUARDT, H.; MIYAGI, L.: Strength of ferropericlase and stagnation of slabs in Earth's shallow lower mantle. Nature Geoscience (submitted)

MARQUARDT, H.; SPEZIALE, S.; KOCH-MÜLLER, M.; MARQUARDT, K.; CAPITANI, G.: Structural insights and elasticity of single-crystal antigorite from high-pressure Raman and Brillouin spectroscopy measured in the (010) plane. American Mineralogist (submitted)

MARTIN, A.P.; PRICE, R.C.; COOPER, A.F.; MCCAMMON, C.A.: Petrogenesis of the rifting Southern Victoria Land lithospheric mantle, Antarctica, inferred from petrography, geochemistry, thermobarometry and oxybarometry of peridotite and pyroxenite xenoliths from Mount Morning. Journal of Petrology (submitted)

MASOTTA, M.; KEPPLER, H.: Anhydrite solubility in differentiated arc magmas. Geochmica et Cosmochimica Acta (submitted)

MCGOWAN, N.M.; GRIFFIN, W.L.; GONZÁLEZ-JIMÉNEZ, J.M.; BELOUSOVA, E.; AFONSO, J.C.; SHI, R.; MCCAMMON, C.A.; PEARSON, N.J.; O'REILLY, S.Y.: Tibetan chromitites: excavating the slab graveyard. Geology (submitted)

MILLOT, M.; DUBROVINSKAIA, N.; ČERNOK, A.; BLAHA, S.; DUBROVINSKY, L.; BRAUN, D.G.; CELLIERS, P.M.; COLLINS, G.W.; EGGERT, J.H.; JEANLOZ, R.: Melting of silica at planetary interior conditions using shock compression of stishovite. Science (submitted)

MIYAHARA, M.; OHTANI, E.; EL GORESY, A.; LIN, Y-T.; FENG, L.; ZHANG, J.-C.; GILLET, Ph.; NAGASE, T.; MUTO, J.; NISHIJIMA, M.: Unique large diamonds in a ureilite from Almahata Sitta 2008TC_3 asteroid. Geochimica et Cosmochimica Acta (submitted)

MOLLO, S.; MASOTTA, M.; FORNI, F.; BACHMANN, O.; DE ASTIS, G.; MOORE, G.; SCARLATO, P.: K-feldspar-liquid hygrometers specific to alkaline differentiated magmas. Chemical Geology (in press)

MOUSSALAM, Y.; MORIZET, Y.; MASSUYEAU, M.; LAUMONIER, M.; GAILLARD, F.: CO_2 solubility in kimberlite melts. Chemical Geology (in press)

MROSKO, M.; KOCH-MÜLLER, M.; MCCAMMON, C.; RHEDE, D.; SMYTH, J.; WIRTH, R.: Water, iron, redox environment: Effects on the wadsleyite - ringwoodite phase transition. Contributions to Mineralogy and Petrology (submitted)

NIMIS, P.; GONCHAROV, A.; IONOV, D.A.; MCCAMMON, C.: Fe^{3+} partitioning systematics between orthopyroxene and garnet in mantle peridotite xenoliths and implications for thermobarometry of oxidized and reduced mantle rocks. Contributions to Mineralogy and Petrology (submitted)

ORIOLO, S.; OYHANTÇABAL, P.; HEIDELBACH, F.; WEMMER, K.; SIEGESMUND, S.: Structural evolution of the Sarandí del Yí shear zone, Uruguay: Kinematics, deformation conditions and tectonic significance. International Journal of Earth Sciences (in press)

OVSYANNIKOV, S.V.; KARKIN, A.E.; MOROZOVA, N.V.; SHCHENNIKOV, V.V.; BYKOVA, E.; ABAKUMOV, A.M., TSIRLIN, A.A.; GLAZYRIN, K.; DUBROVINSKY, L. (2014): A hard oxide semiconductor with a direct and narrow bandgap and switchable *p-n* electrical conduction. Advanced Materials (in press)

PAMATO, M.G.; MYHILL, R.; BOFFA BALLARAN, T.; FROST, D.J.; HEIDELBACH, F.; MIYAJIMA, N.: Lower-mantle water reservoir implied by the extreme stability of a hydrous aluminosilicate. Nature Geoscience (accepted), doi: 10.1038/NGEO2306

PRESCHER, C.; DUBROVINSKY, L.; BYKOVA, E.; KUPENKO, I.; GLAZYRIN, K.; KANTOR, A.; MCCAMMON, C.; MOOKHERJEE, M.; MIYAJIMA, N.; CERANTOLA, V.; NAKAJIMA, Y.; DUBROVINSKAIA, N.; PRAKAPENKA, V.; RÜFFER, R.; CHUMAKOV, A.; HANFLAND, M.: Carbon in the Earth's core accounts for its high Poisson's ratio. Nature Geoscience (submitted)

REBECCA, A.F.; NAKAJIMAB, Y.; CAMPBELLA, A.J.; FROST, D.J.; HARRIES, D.; LANGENHORST, F.; MIYAJIMA, N.; POLLOK, K.; RUBIE, D. C. (2014): High pressure metal-silicate partitioning of Ni, Co, V, Cr, Si, and O. Geochimica et Cosmochimica Acta (submitted)

ROSENTHAL, A.; HAURI, E.H.; HIRSCHMANN, M.M.: Experimental determination of C, F, and H partitioning between upper minerals and carbonated basalt, CO_2/Ba and CO_2/Nb systematics of partial melting, and the CO_2 contents of basaltic source regions. Earth and Planetary Science Letters (accepted)

RUBIE, D.C.; JACOBSON, S.B.; MORBIDELLI, A.; O'BRIEN, D.P.; YOUNG, E.D.; DE VRIES, J.; NIMMO, F.; PALME, H.; FROST, D.J.: Accretion and differentiation of the terrestrial planets with implications for the compositions of early-formed Solar System bodies and accretion of water. Icarus (in press)

RUBIE, D.C.; NIMMO, F.; MELOSH, H.J.: Formation of the Earth's core. – In: Stevenson, D.J. (Ed.): Treatise on Geophysics 2nd Edition, Vol. 9: Evolution of the Earth. Elsevier, Amsterdam (in press)

RUBIE, D.C.; JACOBSON, S.A.: Mechanisms and geochemical models of core formation. – In: FISCHER, R.; TERASAKI, H. (Eds.): Deep Earth: Physics and Chemistry of the Lower Mantle and Core. AGU Monograph (submitted)

SPIVAK, A.V.; SOLOPOVA, N.A.; DUBROVINSKY, L.S.; LITVIN, Yu.A.: The $MgCO_3$-$FeCO_3$-$CaCO_3$-Na_2CO_3 system at 12-23 GPa: phase relations and significance for the genesis of super-deep diamonds. Doklady Earth Sciences (in press)

SPIVAK, A.V.; SOLOPOVA, N.A.; DUBROVINSKY, L.S.; LITVIN Yu.A.: Melting relations of multicompoment carbonate $MgCO_3$ – $FeCO_3$ – $CaCO_3$ – Na_2CO_3 system at 12-23 GPa: application to 'super-deep' diamond formation. American Mineralogist (submitted)

STAGNO, V.; FROST, D.J.; MCCAMMON, C.A.; FEI, Y.: The oxygen fugacity of graphite and diamond bearing eclogites in equilibrium with carbonate-rich melts. Implications for oxy-thermobarometry of eclogite rocks. Contributions to Mineralogy and Petrology (submitted)

THOMAS, S.-M.; WILSON, K.; KOCH-MÜLLER, M.; HAURI, E.; MCCAMMON, C.; JACOBSEN, S.D.; LAZARZ, J.; RHEDE, D.; REN, M.; BLAIR, N.; LENZ, S.: Quantification of water in majoritic garnet. American Mineralogist (submitted)

VLČEK, V.; STEINLE-NEUMANN, G.; LEPPERT, L.; ARMIENTO, R.; KÜMMEL, S.: Improved ground state electronic structure and optical dielectric constants with a semi-local exchange functional. Physical Review B (submitted)

VLČEK, V.; EISENBERG, H.; STEINLE-NEUMANN, G.; KRONIK, L.; BAER, R.: Deviations from piecewise linearity in the solid-state limit with approximate density functionals. Journal of Chemical Physics (submitted)

WALSH, K.J: JACOBSON, S.A.: Formation and dynamics of asteroid binaries. – In: MICHEL, P.; DEMEO, F.E.; BOTTKE W.F. (Eds): Asteroids IV, U. Arizona-Press, Tucson, AZ, USA (submitted)

4.3 Presentations at scientific institutions and at congresses

AUZENDE, A.-l.; ESCARDIN, J.; WALTE, N.; GUILLOT, S.; HIRTH, G.; FROST, D.: 15.-19.12.2014, AGU Fall Meeting, San Francisco, USA[*A]: "Deformation mechanisms of antigorite serpentinite at subduction zone conditions determined from experimentally and naturally deformed rocks", Abstract MR23C-4369, 2014

BALLHAUS, C.; HELMY, H.M.; FONSECA, R.O.C.; LAURENZ, V.; TREDOUX, M.: 11.-14.08.2014, 12th International Platinum Symposium, Yekaterinburg, Russia: "Metal-ligand associations of the PGE in magmatic liquids"

BIZIMIS, M.; PESLIER, A.; MCCAMMON, C.; KESHAV, S.; WILLIAMS, H.: 08.-13.06.2014, Goldschmidt 2014, Sacramento, USA: "Recycling of oceanic lithosphere: Water, fO_2 and Fe-isotope constraints"

BOFFA BALLARAN, T.; KULARATNE, K.; TRØNNES, R.G.: 05.08.-12.08.2014, 23th Congress and General Assembly of the International Union of Crystallography, Montreal, Canada: "High-pressure structural behaviour of $CaIrO_3$ polymorphs"

BUREAU, H.; FROST, D.; BOLFAN-CASANOVA, N.; LEROY, C.; ESTÈVE, I.: 15.-19.12.2014, AGU Fall Meeting, San Francisco, USA[*A]: "Diamond growth in the subduction factory", Abstract V11D-07, 2014

CERANTOLA, V.; KUPENKO, I.; MCCAMMON, C.; DUBROVINSKY, L.; KANTOR, I.; MARINI, C.; SOLOPOVA, N.; ISMAILOVA, L.; CHUMAKOV, A.; PASCARELLI, S.: 27.04.-02.05.2014, European Geosciences Union General Assembly, Vienna, Austria: "Fe-bearing carbonates in the lower mantle: an experimental approach", Geophysical Research Abstracts 16, EGU2014-3375, 2014

ČERNOK, A.; BYKOVA, E.; LIERMANN, H.-P.; DUBROVINSKY, L.: 27.04.-02.05.2014, European Geosciences Union General Assembly, Vienna, Austria: "High-pressure behavior of cristobalite under quasi-hydrostatic conditions", Geophysical Research Abstracts 16, EGU2014-10377-1, 2014

ČERNOK, A.; BYKOVA, E.; MARQUARDT, K.; HABLER, G.; LIERMANN, H.-P.; DUBROVINSKY, L.S.: 25.08.-03.09.2014, EMU School in Planetary Mineralogy, Glasgow, U.K.: "Cristobalite under high pressure"

CHANG, Y.-Y.; WU, Y.; LIN, J.-F.; MCCAMMON, C.; OKUCHI, T.; TOMIOKA, N.: 15.-19.12.2014, AGU Fall Meeting, San Francisco, USA[*A]: "Electronic spin and valence states of iron in the lower-mantle silicate perovskite", Abstract MR41B-4398, 2014

CHEN, J.; PAMATO, M.G.; INOUE, T.; KAKIZAWA, S.; YANG, B.; MA, C.; LIN, Y.; KATSURA, T.; KAWAZOE, T.; LIU, Z.: 15.-19.12.2014, AGU Fall Meeting, San Francisco, USA[*A]: "Effect of pressure on water solubility in aluminous magnesium silicate perovskite", Abstract MR21A-4306, 2014

DANNBERG, J.; EILON, Z.; GASSMOELLER, R.; ASIMOW, P.D.; FAUL, U.; MOULIK, P.; MYHILL, R.: 14.12.2014, Pre-AGU 2014 CIDER Workshop, Berkeley, USA: "Investigating mantle dynamics with grain size evolution"

DE VRIES, J.; NIMMO, F.; MELOSH, H.J.; JACOBSON, S.; MORBIDELLI, A.; RUBIE, D.C.: 17.-21.03.2014, 45th Lunar and Planetary Science Conference, The Woodlands, Houston, USA: "Melting due to impacts on frowing proto-planets"

DE VRIES, J.; NIMMO, F.; MELOSH, H.J.; JACOBSON, S.; MORBIDELLI, A., RUBIE, D.C.: 26.-30.05.2014, Meeting of the ERC Project ACCRETE (Accretion and Early Differentiation of the Terrestrial Planets), Nice, France: "Melting during planetary formation"

DORFMAN, S.; POTAPKIN, V.; KUPENKO, I.; CHUMAKOV, A.; NABIEI, F.; MAGREZ, A.; DUBROVINSKY, L.; MCCAMMON, C.; GILLET, P.: 15.-19.12.2014, AGU Fall Meeting, San Francisco, USA[*A]: "Complex effects of alumina/silica on ferric/ferrous iron in Earth's lower mantle", Abstract MR24A-01, 2014

EL GORESY, A.; GILLET, Ph.; NAKAMURA, T.; MIYAHARA, M.; OHTANI, E.; YOGO, K.; ISHIDA, M.H.; LIN, Y.; SCHULZE, H.: 08.-13.09.2014, 77th Annual Meeting of the Meteoritical Society, Casablanca, Morocco: "NWA7325: A highly reduced differentiated meteorite from an unknown parental planet in our solar system"

EL GORESY, A.; NAKAMURA, T.; MIYAHARA, M.; OHTANI, E.; GILLET, Ph.; JOGO, K.; YAMANOBE, M.; ISHIDA, H.: 08.-13.09.2014, 77th Annual Meeting of the Meteoritical Society, Casablanca, Morocco: "The unique differentiated meteorite NWA7325: Highly reduced, stark affinities to E-chondrites and unknown parental planet"

EL GORESY, A.; LIN, Y.; TRIELOFF, M.; BOYET, M.; GANNOUN, A.; SIMIONOVICI, A.; LEMELLE, L.: 02.-03.12.2014, 5th Annual Meeting of the SPP 1385, Universität Heidelberg, Institut für Geowissenschaften, Heidelberg, Germany: "Origin of EH3 and EL3 chondrites: Diverse source regions and first evidence for increase of C/O ratio during the course of condensation"

EVONUK, M.: 15.-19.12.2014, AGU Fall Meeting, San Francisco, USA[*A]: "Rotating convection in elliptical geometries", Abstract NG23A-3791, 2014

FARLA, R.J.M.; KARATO, S.; CAI, Z.: 27.04.-02.05.2014, European Geosciences Union General Assembly, Vienna, Austria: "Two-phase deformation of peridotite: recrystallization and phase-mixing", Geophysical Research Abstracts 16, EGU2014-5240, 2014

FARLA, R.J.M.; AMULELE, G.; GIRARD, J.; MIYAJIMA, N.; KARATO, S.: 21.-24.09.2014, GeoFrankfurt 'Earth System Dynamics", Frankfurt, Germany: "High pressure and temperature deformation experiments on polycrystalline wadsleyite using the rotational Drickamer apparatus"

FEI, H.; KOIZUMI, S.; SAKAMOTO, N.; HASHIGUCHI, M.; YURIMOTO, H.; MARQUARDT, K.; MIYAJIMA, N.; YAMAZAKI, D.; KATSURA, T.: 15.-19.12.2014, AGU Fall Meeting, San Francisco, USA[*A]: "Silicon grain boundary diffusion in forsterite and implications to upper mantle rheology", Abstract MR51A-03, 2014

FROST, D.J.: 28.-30.03.2014, 38. Edgar-Lüscher-Physikseminar 'Umwelt- und Geophysik', Zwiesel, Germany: "Hochdruckforschung – Struktur des Erdinnern"

FROST, D.J; KURNOSOV, A.; BOFFA BALLARAN, T.; PAMATO, M.; CHANTEL, J.: 08.-13.06.2014, Goldschmidt 2014, Sacramento, USA: "Elasticity measurements on magnesium silicate perovskite and the chemical composition of the lower mantle", Goldschmidt Abstracts, 2014, 742

FROST, D.J.: 03.-04.07.2014, DCO Workshop 'Diamonds and Mantle Geodynamics', Bristol, U.K.: "The chemical composition of the lower mantle based on laboratory elasticity measurements"

FROST, D.J.: 15.-16.09.2014, Geological Society of London colloquium 'Deep Earth Processes, windows on the workings of a planet', London, U.K.: "The chemical composition of the lower mantle based on laboratory elasticity measurements"

FROST, D.J.: 17.09.2014, ETH Zurich, Switzerland: "The chemical composition of the Earth’s lower mantle"

FROST, D.J.: 20.-21.11.2014, IPGP colloquium 'Structure and Dynamics of Earth-like Planets', Paris, France: "Planetary accretion models and the mineralogy of planetary interiors"

GENTILI, S.; BIAGIONI, C.; COMODI, P.; PASERO, M.; MCCAMMON, C.; BONADIMAN, C.: 10.-12.09.2014, 87° Congresso della Società Geologica Italiana e 90° Congresso della Società Italiana di Mineralogia e Petrologia, Milano, Italy: "Chemical, Mössbauer and structural data on a potentially new mineral from Harrow Peaks (Antarctica) in the oxo-amphibole group (amphibole supergroup)"

GIRARD, J.; AMULELE, G.; FARLA, R.J.M.; MOHIUDDIN, A.; KARATO, S.: 15.-19.12.2014, AGU Fall Meeting, San Francisco, USA[*A]: "Synchrotron *in situ* deformation experiments of bridgmanite + ferropericlase aggregates under the shallow lower mantle conditions”, Abstract MR51A-07, 2014

GU, T.; MCCAMMON, C.; LEE, K.: 15.-19.12.2014, AGU Fall Meeting, San Francisco, USA[*A]: "The effect of ferric iron concentration on lower mantle phase assemblage: Implications for mantle convection", Abstract MR41A-4370, 2014

HEIDELBACH, F.: 21.-24.09.2014, 92nd Annual Meeting Deutsche Mineralogische Gesellschaft, Jena, Germany: "Deformation fabrics at the transition from spinel to garnet lherzolite in the CMAS system"

HOPP, J.; STORK, J.-C.; TRIELOFF, M.; LUDWIG, T.; MEYER, H.-P.; MOSTEFAOUI, S.; EL GORESY, A.: 02.-03.12.2014, 5th Annual Meeting of the SPP 1385, Universität Heidelberg, Institut für Geowissenschaften, Heidelberg, Germany: "Short-lived nuclide dating of sulfides in enstatite chondrites"

HUMPHREYS, M.; BROOKER, R.; FRASER, D.; BURGISSER, A.; MANGAN, M.; MCCAMMON, C.; SMITH, V.: 08.-13.06.2014, Goldschmidt 2014, Sacramento, USA: "Fe oxidation state in hydrous magmas during ascent and degassing"

JACOBSON, S.A.; MORBIDELLI, A.; RUBIE, D.C.; O'BRIEN, D.P.; RAYMOND, R.N.; WALSH, K.J.; STEWART, S.; LOCK, S.: 17.-21.03.2014, 45th Lunar and Planetary Science Conference, The Woodlands, Houston, USA: "Planet formation within the Grand Tack model", Abstract 2274

JACOBSON, S.A.; SCHEERES, D.J.; ROSSI, A.; MARZARI, F.: 17.-21.03.2014, 45th Lunar and Planetary Science Conference, The Woodlands, Houston, USA: "The effects of rotational fission on the Main Belt asteroid population", Abstract 2363

JACOBSON, S.A.: 10.04.2014, Theory Group Seminar, Lund Observatory, University of Lund, Sweden: "Terrestrial planet formation in the age of the truncated disk"

JACOBSON, S.A.: 23.04.2014, Group Seminar, Westfälische Wilhelms-Universität Münster, Germany: "Terrestrial planet formation in the age of the truncated disk"

JACOBSON, S.A.; MORBIDELLI, A.: 28.04.-01.05.2014, American Astronomical Society, 2014 Meeting of the Division on Dynamical Astronomy, Philadelphia, USA: "Dynamical friction during planet formation in the Grand Tack scenario", Abstract 102.02

JACOBSON, S.A.: 06.06.2014, Eidgenössische Technische Hochschule (ETH), Department of Earth Sciences, Zurich, Switzerland: "Terrestrial planet formation in the age of the truncated disk"

JACOBSON, S.A.; SCHEERES, D.J.; MCMAHON, J.: 30.06.-04.07.2014, Asteroids, Comets & Meteors Meeting, Helsinki, Finland: "Forming the wide asynchronous binary asteroid population"

JACOBSON, S.A.; SCHEERES, D.J.; ROSSI, A.; MARZARI, F.; DAVIS, D.R.: 30.06.-04.07.2014, Asteroids, Comets & Meteors Meeting, Helsinki, Finland: "Both size-frequency distribution and sub-populations of the main belt asteroid population are consistent with YORP-induced rotational fission"

JACOBSON, S.A.: 07.-11.07.2014, IAU Symposium: Complex Planetary Systems, Namur, Belgium: "Small asteroid evolution"

JACOBSON, S.A.; RUBIE, D.C.; MORBIDELLI, A.; O'BRIEN, D.P.; YOUNG, E.D.; DE VRIES, J.; NIMMO, F.; PALME, H.; FROST, D.J.: 09.-14.11.2014, American Astronomical Society, 46th Annual Meeting of the Division for Planetary Sciences, Tucson, USA: "Accretion and core-mantle differentiation of the Earth and other terrestrial planets", Abstract 504.03

KATSURA, T.; WANG, L.; BLAHA, S.; PINTER, Z.; CHARITON, S.; FARLA, R.; KAWAZOE, T.; MIYAJIMA, N.: 15.-19.12.2014, AGU Fall Meeting, San Francisco, USA*A: "Pressure and temperature dependence of dislocation mobility in the [100](010) and [001](010) slip systems in olivine", Abstract MR51A-06, 2014

KAWAZOE, T.; MIYAJIMA, N.: 15.-19.12.2014, AGU Fall Meeting, San Francisco, USA*A: "Weak-beam dark-field TEM characterization of dislocations and slip systems in wadsleyite deformed in simple shear at pressure-temperature conditions of the mantle transition zone", Abstract MR23C-4372, 2014

KING, S.D.; FROST, D.J.; RUBIE, D.C.: 04.-07.05.2014, Annual Scientific Meeting of the Canadian Geophysical Union, Banff, Canada: "Subducted slab dynamics: Understanding the causes of slab stagnation"

KING, S.D.; FROST, D.J.; RUBIE, D.C.: 19.-22.10.2014, Annual Meeting of The Geological Society of America, Vancouver, Canada: "Subducted slab dynamics: Understanding the causes of slab stagnation"

KOROBEINIKOV, I.V.; OVSYANNIKOV, S.V.; SHCHENNIKOV, V.V.: 07.-12.09.2014, 52nd European High-Pressure Research Group Meeting (EHPRG), Lyon, France: "High pressure application for thermoelectricity"

KOROBEINIKOV, I.V.; MOROZOVA, N.V.; OVSYANNIKOV, S.V.; KARKIN, A.E.; TAKARABE, K.; MORI, Y.; NAKAMURA, S.; SHCHENNIKOV, V.V.: 07.-12.09.2014, 52nd European High-Pressure Research Group Meeting (EHPRG), Lyon, France: "Thermoelectric properties and metallization of Al-doped Mg_2Si under pressure"

LAUMONIER, M.; SCAILLET, B.; ARBARET, L.; PICHAVANT, M.; CHAMPALLIER, R.: 27.-31.10.2014, RST 2014, 24th Earth Sciences Meeting, Pau, France: "Magma mixing: Rheological and textural constraints from HP-HT experiments" id. 3-3-13 (Keynote communication)

LAURENZ, V.; RUBIE, D.C.; FROST, D. (2014): 26.-30.05.2014, Meeting of the ERC Project ACCRETE (Accretion and Early Differentiation of the Terrestrial Planets), Nice, France: "Metal-silicate partitioning of highly siderophile elements in S-bearing systems – Implications for the formation of Earth's core"

LAURENZ, V.; RUBIE, D.C.; FROST, D.: 08.-13.06.2014, Goldschmidt 2014, Sacramento, USA: "Metal-silicate partitioning of HSE in S-bearing systems – Implications for Earth's accretion and core formation"

LAURENZ, V.: 17.07.2014, Westfälische Wilhelms-Universität Münster, Institut für Mineralogie, Münster, Germany: "The geochemistry of HSE in space and time - What expeiments can tell us"

LAURENZ, V.; RUBIE, D.C.; FROST, D.J.: 21.-24.09.2014, 92nd Annual Meeting Deutsche Mineralogische Gesellschaft, Jena, Germany: "The importance of sulfur for the partitioning behaviour of the HSEs during Earth's accretion and differentiation"

LITVIN, Yu.A.; SPIVAK, A.V.; DUBROVINSKY, L.S.: 27.04.-02.05.2014, European Geosciences Union General Assembly, Vienna, Austria: "Melting phase relations and 'stishovite paradox' in lower-mantle system MgO – FeO – SiO_2 at 24 GPa", Geophysical Research Abstracts 16, EGU2014-9831-2, 2014

LITVIN, Yu.A.; SPIVAK, A.V.; DUBROVINSKY, L.S.: 07.-12.09.2014, 52nd European High-Pressure Research Group Meeting (EHPRG), Lyon, France: "Evolution of the Earth's lower-mantle matter: stishovite paradox and origin of 'super-deep' diamonds (experiments at 24 GPa)"

LIU, X.; XIONG, X.; AUDÉTAT, A.; LI, Y.: 08.-13.06.2014, Goldschmidt 2014, Sacramento, USA: "Partitioning of Cu between mafic minerals, magnetite and intermediate-felsic melts", Abstract 1489

MARQUARDT, H.: 03.03.2014, ETH Zurich, Switzerland: "The deep Earth in the laboratory: From diamond anvil cell experiments to global processes"

MARQUARDT, H.; MIYAGI, L.: 21.-24.09.2014, 92nd Annual Meeting Deutsche Mineralogische Gesellschaft, Jena, Germany (*invited*): "Strength of (Mg,Fe)O ferropericlase and the fate of slabs in Earth's lower mantle", Abstract PHY-T01

MARQUARDT, H.; MIYAGI, L.; MERKEL, S.; TOMÉ, C.; SPEZIALE, S.; LIERMANN, H.-P.: 15.-19.12.2014, AGU Fall Meeting, San Francisco, USA*A (*invited*): "High-pressure/high-temperature deformation of ferropericlase in the lower mantle", Abstract MR24A-08, 2014

MARQUARDT, K.; DOHMEN, R.; WAGNER, J.: 27.04.-02.05.2014, European Geosciences Union General Assembly, Vienna, Austria (*invited*): "Combined measurement of surface, grain boundary and lattice diffusion coefficients on olivine bi-crystals", Geophysical Research Abstracts 16, EGU2014- 10677-2, 2014

MARQUARDT, K.; ROHRER, G.S.; MORALES, L.F.G.; RYBACKI, E.: 21.-24.09.2014, 92nd Annual Meeting Deutsche Mineralogische Gesellschaft, Jena, Germany: "The most frequent interfaces between olivine crystals" pp. 232-233

MARQUARDT, K.: 24.11.2014, Carnegie Mellon University Pittsburgh, Department of Materials Science and Engineering (*invited*): "The grain boundary plane distribution of geomaterials: why it matters for (deep Earth) geosciences"

MASOTTA, M.; NI, H.; KEPPLER, H.: 21.-24.09.2014, 92nd Annual Meeting Deutsche Mineralogische Gesellschaft, Jena, Germany: "*In situ* observations of bubble growth in basaltic, andesitic and rhyodacitic melts"

MCCAMMON, C.: 20.-21.01.2014, The Fifth Meeting of Research Consortium on High-pressure Research and The Kumamoto International Symposium on Recent Advancements of Physics and Mineralogy VI, Kumamoto, Japan: "Probing the electronic structure and properties of minerals at extreme conditions using synchrotron radiation"

MCCAMMON, C.: 31.01.2014, 15th Solid State Day, Zentrum für Festkörperchemie und Neue Materialien, Hannover, Germany: "Iron matters: What we think we know about the Earth's interior"

MCCAMMON, C.; DUBROVINSKY, L.; CERANTOLA, V.; KUPENKO, I.; SINMYO, R.; PETITGIRARD, S.; ISMAILOVA, L.; KANTOR, A.; CHUMAKOV, A.: 27.04.-02.05.2014, European Geosciences Union General Assembly, Vienna, Austria: "Assessment of carbonate detectability in the lower mantle based on elastic wave velocity measurements of iron-bearing carbonates using nuclear inelastic scattering", Geophysical Research Abstracts 16, EGU2014-14308, 2014

MCCAMMON, C.; DUBROVINSKY, L.; CERANTOLA, V.; KUPENKO, I.; SINMYO, R.; PETITGIRARD, S.; ISMAILOVA, L.; KANTOR, A.; CHUMAKOV, A.: 27.04.-02.05.2014, 21st General Meeting of the International Mineralogical Association, Johannesburg, South Africa: "Elastic properties of iron-bearing carbonates and implications for the deep Earth"

MCCAMMON, C.A.; LESHER, C.; TSCHAUNER, O.: 22.-23.05.2014, 'Carbides, Nitrides and Related Materials in Earth, Planetary, and Materials Science' Workshop, Davis, USA: "Carbon and nitrogen recycling in stars and planets"

MCCAMMON, C.; CERANTOLA, V.; KUPENKO, I.; PRESCHER, C.; BYKOVA, E.; GLAZYRIN, K.; SINMYO, R.; KANTOR, A.; KANTOR, I.; PETITGIRARD, S.; ISMAILOVA, L.; MOOKHERJEE, M.; MIYAJIMA, N.; NAKAJIMA, Y.; PRAKAPENKA, V.; CHUMAKOV, A.; RÜFFER, R.; DUBROVINSKY, L.: 07.-12.09.2014, 52nd European High-Pressure Research Group Meeting (EHPRG), Lyon, France: "High pressure matters: The inside story of the Earth's deep carbon cycle"

MCCAMMON, C.: 18.09.2014, Structures, Properties and Reactions of Carbonates at High Pressures and Temperatures "CarboPaT" Review Panel Meeting, Frankfurt, Germany: "Elastic properties of carbonates at high pressures and temperatures"

MCCAMMON, C.; KUPENKO, I.; SINMYO, R.; CERANTOLA, V.; POTAPKIN, V.; CHUMAKOV, A.; KANTOR, A.; RÜFFER, R.; DUBROVINSKY, L.: 15.-19.12.2014, AGU Fall Meeting, San Francisco, USA[*A]: "Probing the oxidation state of iron in the deep mantle using high P,T Mössbauer spectroscopy", Abstract V52B-07, 2014

MCGOWAN, N.; GRIFFIN, W.; GONZÁLEZ-JIMÉNEZ, J.-M.; BELOUSOVA, E.; AFONSO, J.; SHI, R.; MCCAMMON, C.; PEARSON, N.; O'REILLY, S.: 08.-13.06.2014, Goldschmidt 2014, Sacramento, USA: "Tibetan chromitites: Digging in the slab graveyard"

MIYAJIMA, N.: 21.-23.05.2014, FEI European Titan User Club Meeting, European NanoPort, Eindhoven, The Netherlands: "Burgers vector determination in deformed minerals using thickness fringes in weak-beam dark-field TEM images"

MIYAJIMA, N.; FISCHER, R.A.; CAMPBELL, A.J.; FROST, D.J.; HARRIES, D.; LANGENHORST, F.; POLLOK, K.; PETITGIRARD, S.; RUBIE, D.C.: 21.-24.09.2014, 92nd Annual Meeting Deutsche Mineralogische Gesellschaft, Jena, Germany: "Quantitative chemical analysis of carbon and oxygen in molten Fe-rich alloy by analytical transmission electron microscopy"

MIYAJIMA, N.: 03.-07.11.2014, MinTEM 2014, Graduate and PhD Course, Villeneuve d'Ascq, France: Lecture and practical on "EELS for Mineralogy"

MIYAJIMA, N.: 07.11.2014, Université Lille 1, Unité Matériaux et Transformations, CNRS UMR 8207, Lille, France: "Mineralogical applications of the modern analytical TEM, FEI-Titan G2 80-200 S/TEM: a few evident progresses towards high pressure mineralogy"

MOOKHERJEE, M.; KEPPLER, H.; MANNING, C.: 15.-19.12.2014, AGU Fall Meeting, San Francisco, USA[*A]: "Alumino-silicate speciation in aqueous fluids at deep crustal conditions", Abstract V31D-4778, 2014

MOROZOVA, N.V.; OVSYANNIKOV, S.V.; VYSOCHANSKII, Y.; SHCHENNIKOV, V.V.: 06.-08.08.2014, 16th International Conference on High Pressure in Semiconductor Physics, Mexico City, Mexico: "Semiconductor – metal transition in a ferroelectric at high pressure"

MOROZOVA, N.V.; UMEROVA, Y.A.; KARKIN, A.E.; OVSYANNIKOV, S.V.; SHCHENNIKOV, V.V.: 07.-12.09.2014, 52nd European High-Pressure Research Group Meeting (EHPRG), Lyon, France: "High-pressure behavior of electronic transport properties of MFe$_2$As$_2$ (M – Eu, Sr, Ca) compounds"

MOUSSALLAM, Y.; MORIZET, Y.; FLORIAN, P.; LAUMONIER, M.; MASSUYEAU, M.; GAILLARD, F.: 27.04.-02.05.2014, European Geosciences Union General Assembly, Vienna, Austria: "The structure and CO_2 solubility of Kimberlite melts", Geophysical Research Abstracts 16, EGU2014-1766-1, 2014

MYHILL, R.; FROST, D.J.; SORBADERE, F.; MIYAJIMA, N.: 10.07.2014, CIDER Workshop, Santa Barbara, USA: "Melting of a partially oxidised upper mantle: an oxygen filter for the Earth?"

MYHILL, R.; SORBADERE, F.; FROST, D.J.; BOFFA BALLARAN, T.: 15.-16.09.2014, Geological Society of London colloquium 'Deep Earth Processes, windows on the workings of a planet', London, U.K.: "Ferric iron and its influence on Earth's deep structure"

MYHILL, R.; PAMATO, M.; ZIBERNA, L.; SORBADERE, F.; FROST, D.J.; BOFFA BALLARAN, T.: 04.12.2014, Saint Louis University, Earth Sciences Seminar, St. Louis, USA: "Volatile-driven melting in the deep mantle: an experimentalist's view on geochemical and seismological observations"

MYHILL, R.; DANNEBERG, J.; EILON, Z.; GASSMOELLER, R.; MOULIK, P.; FAUL, U.; ASIMOW, P.: 15.-19.12.2014, AGU Fall Meeting, San Francisco, USA[*A]: "Grain size evolution in the mantle and its effect on geodynamics and seismic observables", Abstract DI23A-4280, 2014

OVSYANNIKOV, S.V.; KARKIN, A.E.; MOROZOVA, N.V.; SHCHENNIKOV, V.V.; BYKOVA, E.; ABAKUMOV, A.M.; TSIRLIN, A.A.; GLAZYRIN, K.; DUBROVINSKY, L.: 06.-08.08.2014, 16th International Conference on High Pressure in Semiconductor Physics, Mexico City, Mexico: "Semiconducting properties of metastable manganese oxides"

OVSYANNIKOV, S.V.; KARKIN, A.E.; MOROZOVA, N.V.; SHCHENNIKOV, V.V.; BYKOVA, E.; ABAKUMOV, A.M.; TSIRLIN, A.A.; GLAZYRIN, K.; DUBROVINSKY, L.: 07.-12.09.2014, 52nd European High-Pressure Research Group Meeting (EHPRG), Lyon, France: "Electronic and optical properties of the high-pressure polymorphs of Mn_2O_3 and Mn_3O_4"

OVSYANNIKOV, S.V.; ZAINULIN, Y.G.; KADYROVA, N.I.; TYUTYUNNIK, A.P.; SEMENOVA, A.S.; KASINATHAN, D.; TSIRLIN, A.A.; MIYAJIMA, N.; KARKIN, A.E.: 07.-12.09.2014, 52nd European High-Pressure Research Group Meeting (EHPRG), Lyon, France: "HP-HT synthesis and properties of new double perovskite $CaCo_3V_4O_{12}$"

OVSYANNIKOV, S.V.; KARKIN, A.E.; MOROZOVA, N.V.; SHCHENNIKOV, V.V.; ABAKUMOV, A.M.; TSIRLIN, A.A.; DUBROVINSKY, L.: 24-26.09.2014, 3rd Workshop on High Pressure, Planetary, and Plasma Physics, Rostock, Germany: "Unusual properties of 'simple' oxides prepared at HP-HT conditions"

OVSYANNIKOV, S.V.; ZAINULIN, Y.G.; KADYROVA, N.I.; TYUTYUNNIK, A.P.; SEMENOVA, A.S.; KASINATHAN, D.; TSIRLIN, A.A.; MIYAJIMA, N.; KARKIN, A.E.: 24-26.09.2014, 3rd Workshop on High Pressure, Planetary, and Plasma Physics, Rostock, Germany: "HP-HT synthesis and properties of new unusual perovskite, $CaCo_3V_4O_{12}$"

OZAWA, S.; MARQUARDT, K.; MIYAHARA, M.; EL GORESY, A.; OHTANI, E.; MIYAJIMA, N.; GILLET, Ph.; BOUVIER, A.: 08.-13.09.2014, 77th Annual Meeting of the Meteoritical Society, Casablanca, Morocco: "Monoclinic baddeleyite in shergotty: TEM evidence of orthogonal domains induced by phase transformation from a dense polymorph and not by igneous origin"

PAMATO, M.G.; KURNOSOV, A.; TROTS, D.M.; BOFFA BALLARAN, T.; FROST, D.J.: 17.11.2014, University of Illinois at Urbana-Champaign, Champaign, USA: "Single-crystal elasticity of Al-rich phases in the Earth's transition zone and lower mantle"

PAMATO, M.G.; KURNOSOV, A.; BOFFA BALLARAN, T.; FROST, D.J; ZIBERNA, L.; GIANNINI, M.; TKACHEV, S.N.; ZHURAVLEV, K.K.; PRAKAPENKA, V.B.; SPEZIALE, S.: 15.-19.12.2014, AGU Fall Meeting, San Francisco, USA*A (*invited*): "Single crystal elasticity of majoritic garnets: stagnant slabs and thermal anomalies at the base of the transition zone", Abstract MR21B-04, 2014

PETITGIRARD, S.; MALFAIT, W.; SINMYO, R.; KUPENKO, I.; RUBIE, D.: 15.-19.12.2014, AGU Fall Meeting, San Francisco, USA*A: "Equation of state of amorphous $MgSiO_3$ and $(MgFe)SiO_3$ to lowermost mantle pressures", Abstract MR41A-4367, 2014

POSNER, E.S.; RUBIE, D.C.; FROST, D.J.; CARACAS, R.: 26.-30.05.2014, Meeting of the ERC Project ACCRETE (Accretion and Early Differentiation of the Terrestrial Planets), Nice, France: "Si and Cr diffusion in liquid iron: kinetic implications for the chemical evolution of planetesimal cores"

POSNER, E.S.; RUBIE, D.C.; FROST, D.J.; CARACAS, R.; STEINLE-NEUMANN, G.: 15.-16.09.2014, Geological Society of London colloquium 'Deep Earth Processes, windows on the workings of a planet', London, U.K.: "Si and Cr diffusion in liquid iron: kinetic implications for the basal region of a magma ocean and planetary core-mantle boundaries"

POSNER, E.S.; RUBIE, D.C.; FROST, D.J.; STEINLE-NEUMANN, G.; VLČEK, V.: 15.-19.12.2014, AGU Fall Meeting, San Francisco, USA*A: "High P-T experiments and first principles calculations of Si, O, and Cr diffusion in liquid iron", Abstract MR31A-4314, 2014

PRESCHER, C.; BYKOVA, E.; KUPENKO, L.; GLAZYRIN, K.; KANTOR, A.; MCCAMMON, C.A.; MOOKHERJEE, M.; MIYAJIMA, N.; CERANTOLA, V.; NAKAJIMA, Y.; PRAKAPENKA, V.; RÜFFER, R.; CHUMAKOV, A.; DUBROVINSKY, L.: 22.-23.05.2014, 'Carbides, Nitrides and Related Materials in Earth, Planetary, and Materials Science' Workshop, Davis, USA: "Nuclear inelastic scattering of Fe_7C_3 at high pressure and temperature"

ROSENTHAL, A.; HAURI, E.H.; HIRSCHMANN, M.M.: 18.-21.02.2014, Deep Carbon Observatory (DCO) Early Career Scientist Workshop, San Jose, Costa Rica: "High-pressure partitioning of C, H_2O and F between silicate minerals and carbonate-bearing silicate liquids"

ROSENTHAL, A.; HAURI, E.H.; HIRSCHMANN, M.M.: 18.-21.02.2014, Deep Carbon Observatory (DCO) Early Career Scientist Workshop, San Jose, Costa Rica: "Storage, partitioning and fluxes of carbon, water and fluorine in upwelling upper mantle"

ROSENTHAL, A.; FROST, D.J.: 27.04.-02.05.2014, European Geosciences Union General Assembly, Vienna, Austria: "High pressure experimental constraints on the fate of water during subduction of oceanic crustal material into the deep mantle", Geophysical Research Abstracts 16, EGU2014-16070, 2014

ROSENTHAL, A.; FROST, D.J.; PETITGIRARD, S.; YAXLEY, G.M.; BERRY, A.; WOODLAND, A.B.; PINTER, Z.; VASILYEV, P.; IONOV, D.A.; JACOB, D.E.; PEARSON, D.G.; KOVACS, I.; PADRON-NAVARTA, A.: 15.-19.12.2014, AGU Fall Meeting, San Francisco, USA[*A]: "High pressure experimental study of eclogite with varying H_2O contents", Abstract V13A-4744, 2014

RUBIE, D.C.; JACOBSON, S.A.; MORBIDELLI, A.; O'BRIEN, D.P.; YOUNG, E.D.: 17.-21.03.2014, 45th Lunar and Planetary Science Conference, The Woodlands, Houston, USA: "Accretion and differentiation of the terrestrial planets: implications for the compositions of early-formed solar system bodies", Abstract 1734

RUBIE, D.C.; JACOBSON, S.A.; MORBIDELLI, A.; O'BRIEN, D.P.; YOUNG, E.D.: 26.-30.05.2014, Meeting of the ERC Project ACCRETE (Accretion and Early Differentiation of the Terrestrial Planets), Nice, France: "Chemical constraints on the Grand Tack accretion model"

RUBIE, D.C.; HERNLUND, J.; JACOBSON, S.A.; MORBIDELLI, A.: 15.-16.09.2014, Geological Society of London colloquium 'Deep Earth Processes, windows on the workings of a planet', London, U.K.: "Development of an early density stratification in the Earth's core"

SIMIONOVICI, A.S.; LEMELLE, L.; BOYET, M.; GILLET, Ph.; RIVARD, C.; EL GORESY, A.: 08.-13.09.2014, 77th Annual Meeting of the Meteoritical Society, Casablanca, Morocco: "Nano-XRF study of earliest solar condensates in EL3 fragments from the Almahata Sitta TC_3 2008 asteroid"

SINMYO, R.; PESCE, G.; GREENBERG, E.; MCCAMMON, C.; DUBROVINSKY, L.: 15.-19.12.2014, AGU Fall Meeting, San Francisco, USA[*A]: "Lower mantle electrical conductivity based on measurements of Al, Fe-bearing perovskite under lower mantle conditions", Abstract MR22A-05, 2014

SPIVAK, A.V.; LITVIN, Yu.A.; DUBROVINSKY, L.S.; ZAKHARCHENKO, E.S.: 27.04.-02.05.2014, European Geosciences Union General Assembly, Vienna, Austria: "Melting relations of multicomponent carbonate system $MgCO_3$ – $FeCO_3$ – $CaCO_3$ – Na_2CO_3 at 12-23 GPa", Geophysical Research Abstracts 16, EGU2014-9941-1, 2014

STEINLE-NEUMANN, G.: 08.05.2014, The Hebrew University of Jerusalem, Department of Geology, Jerusalem, Israel: "Thermal effects of variable material properties and metamorphic reactions in a three-component subducting slab"

STEINLE-NEUMANN, G.; DOLEJŠ, D.: 24.-26.09.2014, 3rd Joint Workshop on High Pressure, Planetary, and Plasma Physics, Rostock, Germany: "Crystallizing the Hermean core – Thermodynamics of Fe melting"

STEINLE-NEUMANN, G.: 22.10.2014, ETH Zurich, Departement Erdwissenschaften, Zurich, Switzerland: "Crystallzing the inner core of Mercury, thermodynamic considerations from Fe melting"

UENVER-THIELE, L.; WOODLAND, A.; BOFFA BALLARAN, T.; FROST, D.J.: 01.-05.09.2014, 21st General Meeting of the Internation Mineralogical Association, Johannesburg, R.S.A.: "Experimental determination of the phase relations of $MgFe_2O_4$ at conditions of the deep upper mantle and transition zone: First results"

UENVER-THIELE, L.; WOODLAND, A.; BOFFA BALLARAN, T.; FROST, D.J.: 21.-24.09.2014, 92nd Annual Meeting Deutsche Mineralogische Gesellschaft, Jena, Germany: "Stability and structure of $Mg_2Fe_2O_5$ at high P-T conditions"

VLČEK, V.; EISENBERG, H.; STEINLE-NEUMANN, G.; KRONIK, L., BAER, R.: 30.03.-04.04.2014, DPG Frühjahrstagung der Sektion Kondensierte Materie, Dresden, Germany: "Energy curvature of solids with fractional charge in DFT"

VLČEK, V.; STEINLE-NEUMANN, G.; LEPPERT, L.; ARMIENTO, R.; KÜMMEL, S.: 23.-26.09.2014, 19th ETSF Workshop on Electronic Excitations, Zaragoza, Spain: "Ground state electronic structure and optical dielectric constants for solids with the s·ln(s) exchange functional"

WAGLE, F.; VLČEK, V.; STEINLE-NEUMANN, G.: 24.-26.09.2014, 3rd Joint Workshop on High Pressure, Planetary, and Plasma Physics, Rostock, Germany: "A systematic survey of electrical resistivity and compressibility data for metals near the melting point and implications on the Earth's core"

WENZ, M.; SORBADERE, F.; ROSENTHAL, A.; FROST, D.; MCCAMMON, C.: 15.-19.12.2014, AGU Fall Meeting, San Francisco, USA[*A]: "Experimental spinel standards for ferric iron (Fe^{3+}) determination during peridotite partial melting", Abstract V53B-4859, 2014

WU, X.; LIN, J.; LIU, J.; MAO, Z.; GUO, X.; TAKASHI, Y.; MCCAMMON, C.; XIAO, Y.; PRAKAPENKA, V.: 27.04.-02.05.2014, 21st General Meeting of the International Mineralogical Association, Johannesburg, South Africa: "Elasticity of single-crystal Phase D across the spin transitions of ferrous and ferric iron in the lower mantle"

WU, X.; LIN, J.-F.; LIU, J.; MAO, Z.; GUO, X.; YOSHINO, T.; MCCAMMON, C.; XIAO, Y.; PRAKAPENKA, V.: 15.-19.12.2014, AGU Fall Meeting, San Francisco, USA[*A]: "Elasticity of single-crystal Phase D across the spin transitions of ferrous and ferric iron in the lower mantle", Abstract MR41B-4392, 2014

WU, Y.; WU, X.; LIN, J.-F.; YOSHINO, T.; MCCAMMON, C.; XIAO, Y.; PRAKAPENKA, V.: 15.-19.12.2014, AGU Fall Meeting, San Francisco, USA[*A]: "Electronic spin and valence states of iron in the Al-rich NAL and CF phases in the subducted slabs", Abstract MR24A-04, 2014

YAMAZAKI, D.; FEI, H.; WIEDENBECK, M.; KATSURA, T.: 15.-19.12.2014, AGU Fall Meeting, San Francisco, USA[*A]: "Water has no effect on oxygen self-diffusion rate in forsterite", Abstract MR23C-4364, 2014

YAXLEY, G.M.; ROSENTHAL, A.: 27.04.-02.05.2014, European Geosciences Union General Assembly, Vienna, Austria: "Experimental study of the P-T stability of phlogopite in metasomatised peridotite with varying H_2O contents in the deep cratonic lithosphere", Geophysical Research Abstracts 16, EGU2014-4649, 2014

[*A] **AGU: American Geophysical Union Fall Meeting, 15.-19.12.2014, San Francisco, USA**

4.4 Lectures and seminars at Bayerisches Geoinstitut

ANTONANGELI, Daniele, Institut de Minéralogie et de Physique des Milieux Condensés, Paris, France: "Mineral-physics and geochemical constraints on the composition of the Earth's and Moon's core", 03.04.2014

ARMSTRONG, Katherine, Portland University, Department of Geology, Portland, USA: "A chemical and petrographic survey of large, igneous-textured inclusions in ordinary chondrites", 17.07.2014

BINA, Craig, Northwestern University, Department of Earth and Planetary Sciences, Evanston, USA: "Subduction dynamics in the mantle transition zone: Petrology, rheology, slab buckling, and trench migration", 08.12.2014

BOUVIER, Audrey, University of Western Ontario, Department of Earth Sciences, London, Canada: "Impact histories of Martian and lunar rocks", 20.03.2014

BYKOVA, Elena, Bayerisches Geoinstitut, Bayreuth, Germany: "Fate of iron oxides in subducted banded iron formations", 06.11.2014

CLARK, Alisha, University of California at Davis, Geological Department, Davis, USA: "Density and elasticity of amorphous silicates at high pressure: Anomalous behavior, network collapse, and implications for mantle melts", 11.11.2014

CONSTABLE, Steven, "Water, water, water, everywhere: Studies of mantle electrical conductivity", 03.06.2014

CORDIER, Patrick, Université Lille 1, UMET - Unité Matériaux et Transformation, CNRS, Villeneuve d'Ascq, France: "Rheology of mantle minerals: what's going on (down there)", 08.05.2014

DOBSON, David, University College London, Department of Earth Sciences, London, U.K.: "Textured rocks in the lowermost mantle", 10.07.2014

DUAN, Xianzhe, Chinese Academy of Sciences, Institute of Geology & Geophysics, Beijing, P.R. China: "Physical and chemical properties of fluids/melts in the deep Earth and their geological significances: Theoretical and experimental studies", 05.06.2014

FOLEY, Stephen F., Macquarie University, Department of Earth and Planetary Sciences, Sydney, Australia: "Trace elements in olivine and magma source regions in the Mediterranean", 27.05.2014

GIANNINI, Mattia, Bayerisches Geoinstitut, Bayreuth, Germany: "Ti^{3+} in hibonite: fO_2 vs crystal chemistry", 13.03.2014

GOZZI, Fernando, Università degli Studi di Roma "La Sapienza", Dipartimento di Scienze della Terra, Roma, Italy: "Primary magmatic calcite reveals origin from crustal carbonate", 06.03.2014

GUTIÉRREZ, Xochilt, Bayerisches Geoinstitut, Bayreuth, Germany: "The behavior of chlorine and sulfur during explosive volcanic eruptions", 21.08.2014

HERNLUND, John, Tokyo Institute of Technology, Earth-Life Science Institute, Tokyo, Japan: "Skeletons in Earth's closet: Relics of a violent youth", 10.09.2014

HIRAO, Naohisa, Japan Synchrotron Radiation Research Institute/SPring-8, Hyogo, Japan: "Recent synchrotron technical advances in high-pressure beamline BL10XU/SPring-8: Microbeam and integration of multiple techniques", 07.02.2014

IIZUKA, Riko, Ehime University, Geodynamics Research Center, Matsuyama, Japan: "Crystallographic preferred orientation of deformed lawsonite: Implications for low velocity layers in subduction zones", 11.12.2014

IRIFUNE, Tetsuo, Ehime University, Geodynamics Research Center, Matsuyama, Japan: "History of alphabet hydrous phases and discovery of phase H under the lower mantle", 04.09.2014

ISHII, Takayuki, Gakushuin University, Department of Chemistry, Tokyo, Japan: "High-pressure transitions of mantle rocks and minerals up to the uppermost lower mantle: Implications for material transportation processes in the mantle", 03.07.2014

JACOBSEN, Steven, Northwestern University, Department of Earth and Planetary Sciences, Evanston, USA: "Earth's deep water cycle: atomic to geophysical scales", 18.09.2014

JACOBSON, Seth, Bayerisches Geoinstitut, Bayreuth, Germany: "Terrestrial planet formation in a truncated disk", 09.09.2014

KING, Scott, Virginia Tech, Geosciences, Blacksburg, USA: "Slow diffusion in majoritic garnet and the dynamics of subduction", 12.06.2014

KUPENKO, Ilya, Bayerisches Geoinstitut, Bayreuth, Germany: "Portable laser-heating system for geo- and materials sciences", 02.10.2014

KUTCHEROV, Vladimir, Royal Institute of Technology, Department of Energy Technology, Stockholm, Sweden: "Experimental investigation of abiogenic synthesis of hydrocarbons under extreme thermobaric conditions: Main results and challenges", 27.03.2014

LAURENZ, Vera, Bayerisches Geoinstitut, Bayreuth, Germany: "The effect of sulfur on the metal-silicate partitioning of the highly siderophile elements – Implications for Earth's accretion and core formation", *Academy Commission Business Meeting*, 15.05.2014

LEONI, Matteo, Department of Materials Engineering and Industrial Technologies, Trento, Italy: "Beyond Scherrer formula and the Rietveld method for the analysis of structure and nanostructure of real materials", 12.12.2014

LI, Wanting, Bayerisches Geoinstitut, Bayreuth, Germany: "The role of evaporites in the formation of magnetite-apatite deposits along the Middle and Lower Yangtze River, China: Evidence from LA-ICP-MS analysis of fluid inclusions", 29.10.2014

LIU, Xiaobing, Northwestern University, Department of Earth and Planetary Sciences, Evanston, USA: "Hardness and elastic properties of boron-doped diamond", 20.11.2014

MALLIK, Ananya, Rice University, Department of Earth Science, Houston, USA: "Earth's upper mantle hybridization by chemical heterogeneity: Implications for genesis of ocean island basalts and ultra-potassic arc lavas", 27.05.2014

MARQUARDT, Hauke, Bayerisches Geoinstitut, Bayreuth, Germany: "Earth's mantle in the laboratory: From diamond anvil cell experiments to global processes", *Academy Commission Business Meeting*, 15.05.2014

MARQUARDT, Katharina, Bayerisches Geoinstitut, Bayreuth, Germany: "Anisotropic polycrystalline aggregates: Interaction of grain boundary, surface and volume diffusion", *Academy Commission Business Meeting*, 15.05.2014

MASOTTA, Matteo, Bayerisches Geoinstitut, Bayreuth, Germany: "Gas bubbles, eruption dynamics and sulfur release from volcanoes", 30.01.2014

MILANI, Sula, Università degli Studi di Padova, Dipartimento di Geoscienze, Padova, Italy: "Equation of state of garnets and implications for diamond geobarometry", 20.02.2014

MOHSENI, Hoda, Bayerisches Geoinstitut, Bayreuth, Germany: "Effective metal-alloy redox sensors and the oxygen fugacity of diamond formation", 03.03.2014

MOJZSIS, Stephen, University of Colorado at Boulder, Geological Sciences, Boulder, USA: "Early thermal events of the inner solar system from solid-state studies of asteroidal meteorites and lunar rocks", 17.07.2014

PAKHOMOVA, Anna, St. Petersburg State University, Crystallography Department, St. Petersburg, Russia: "X-ray single crystal diffraction studies of complex materials (molybdenum and titanium oxocompounds) and temperature induced processes (dehydration of zeolites)", 17.03.2014

PAMATO, Martha, Bayerisches Geoinstitut, Bayreuth, Germany: "Elasticity of mafic crust in the Earth's lower mantle", 24.07.2014

PETITGIRARD, Sylvain, "Density of amorphous $MgSiO_3$ to lowermost mantle pressure", 30.10.2014

REDMER, Ronald, Universität Rostock, Institut für Physik, Rostock, Germany: "Matter at deep planetary interior conditions", 26.06.2014

RUSHMER, Tracy, Macquarie University, Department of Earth and Planetary Sciences, Sydney, Australia: "Onset of subduction and the genesis of the continental crust in the earliest Earth", 04.12.2014

SINMYO, Ryosuke, Bayerisches Geoinstitut, Bayreuth, Germany: "The electrical conductivity measurements in Al, Fe-bearing perovskite under lower mantle condition", 23.01.2014

TAO, Renbiao, Beijing University, School of Earth and Space Sciences, Beijing, P.R. China: "Deep carbon cycle in southwestern Tianshan subduction zone: Petrological observation and experimental simulation", 19.05.2014

THOMAS, Christine, Universität Münster, Institut für Geophysik, Münster, Germany: "Are structures in D" due to a phase transition?", 25.07.2014

WAGLE, Fabian, Bayerisches Geoinstitut, Bayreuth, Germany: "Dynamic self-assembly of magnetic colloidal particles", 13.02.2014

WANG, Lin, Bayerisches Geoinstitut, Bayreuth, Germany: "The temperature and pressure dependence of [001](010) and [100](010) dislocation mobility in olivine", 20.08.2014

4.5 Conference organization

26.-30.05.2014, International Workshop on 'Accretion and Early Differentiation of the Terrestrial Planets' (ACCRETE), Nice, France (D.C. RUBIE; A. MORBIDELLI)

08.-13.06.2014, Goldschmidt 2014, Sacramento, USA: 'Deep Earth' Theme (Chairs: D.C. RUBIE; A.J. CAMPBELL; B. BUFFETT)

01.-05.09.2014, 21st General Meeting of the International Mineralogical Association, Johannesburg, South Africa: Parallel Session: Mineralogy in the Deep Earth (C. MCCAMMON; P. COMODI; T. INOUE; E. OHTANI)

24.-26.09.2014, Joint Workshop on High Pressure, Planetary, and Plasma Physics, University Rostock, Institute of Physics, Rostock, Germany (R. REDMER; H.-P. LIERMANN; G. STEINLE-NEUMANN; F. SOHL; T. TSCHENTSCHER; F.W. WAGNER; BECKER, A.)

15.-19.12.2014, American Geophysical Union Fall Meeting, San Francisco, USA: Session DI23A "Mantle Flow: Constraints from Mineral Physics, Geophysics and Modelling" (H. MARQUARDT; L. MIYAGI; A. NOWACKI)

15.-19.12.2014, American Geophysical Union Fall Meeting, San Francisco, USA: Session MR24A & MR41B: "The Role of Transition Elements in the Geophysical and Geochemical Processes in the Deep Earth" (J. LIN; C.A. MCCAMMON; R. WENTZCOVITCH)

15.-19.12.2014, American Geophysical Union Fall Meeting, San Francisco, USA: Session 3518 "Carbon: Storage, Migration, and Outgassing within Earth and Other Planetary Bodies" (V. STAGNO; T. LOPEZ; S. MIKHAIL; A. ROSENTHAL)

15.-19.12.2014, American Geophysical Union Fall Meeting, San Francisco, USA: Session MR41A "Physics and Chemistry of the Deep Earth" (T. KOMABAYASHI; J. ZHICHENG; B. CHEN; R. SINMYO)

5. Visiting scientists

5.1 Visiting scientists funded by the Bayerisches Geoinstitut

ANTONANGELI, Daniele, Institut de Minéralogie et de Physique des Milieux Condensés, Paris, France: 02.-04.04.2014

ARATO, Robert, Eötvös University, Budapest, Hungary: 21.-23.07.2014

ARMSTRONG, Katherine, Portland University, Department of Geology, Portland, U.K.: 15.-21.07.2014

BINA, Craig, Northwestern University, Department of Earth and Planetary Sciences, Evanston, USA: 05.-09.12.2014

BOUVIER, Audrey, University of Western Ontario, Department of Earth Sciences, London, Canada: 17.-21.03.2014

CLARK, Alisha, University of California at Davis, Geological Department, Davis, USA: 08.-13.11.2014

CONSTABLE, Steven, Scripps Institution of Oceanography, La Jolla, USA: 01.06.2014

CORDIER, Patrick, Université Lille 1, UMET - Unité Matériaux et Transformation, CNRS, Villeneuve d'Ascq, France: 08.-09.05.2014

DRUZHBIN, Dmitry, Novosibirsk State University, Department of Physics, Novosibirsk, Russia: 03.-07.08.2014

DUAN, Xianzhe, Chinese Academy of Sciences, Institute of Geology & Geophysics, Beijing, P.R. China: 03.-07.06.2014

FEDORTCHOUK, Yana, Dalhousie University, Department of Earth Sciences, Halifax, Canada: 01.04.-29.07.2014

FEI, Hongzhan, Okayama University, Institute for Study of the Earth's Interior, Okayama, Japan: 07.-30.06.2014, 14.11.-23.11.2014

FOLEY, Stephen F., Macquarie University, Department of Earth and Planetary Sciences, Sydney, Australia: 27.-29.05.2014

GOLABEK, Gregor, ETH Zurich, Institute of Geophysics, Zurich, Switzerland: 15.-18.01.2014, 13.-16.03.2014, 06.-07.04.2014

GOZZI, Fernando, Università degli Studi di Roma "La Sapienza", Dipartimento di Scienze della Terra, Roma, Italy: 05.03.-07.03.2014

HIRAO, Naohisa, Japan Synchrotron Radiation Research Institute/SPring-8, Hyogo, Japan: 06.-08.02.2014

HUANG, Rong, Beijing University, P.R. China: 12.-16.08.2014

IAFFALDANO, Giampiero, The Australian National University, Research School of Earth Sciences, Canberra, Australia: 15.-17.01.2014

ISHII, Takayuki, Gakushuin University, Department of Chemistry, Tokyo, Japan: 01.-25.07.2014

LIU, Xiaobing, Northwestern University, Department of Earth and Planetary Sciences, Evanston, USA: 14.10.-14.12.2014

MALLIK, Ananya, Rice University, Department of Earth Science, Houston, USA: 26.-28.05.2014

MELAI, Caterina, Università degli Studi di Padova, Dipartimento di Geoscienze, Padova, Italy: 01.09.-16.10.2014

MOJZSIS, Stephen, University of Colorado at Boulder, Geological Sciences, Boulder, USA: 16.-18.07.2014

NAKAGAWA, Takashi, Japan Agency for Marine-Earth Science and Technology, Institute for Research on Earth Evolution, Yokosuka, Japan: 15.-18.01.2014

PAKHOMOVA, Anna, St. Petersburg State University, Crystallography Department, St. Petersburg, Russia: 16.-19.03.2014

REDMER, Ronald, Universität Rostock, Institut für Physik, Rostock, Germany: 26.-27.06.2014

RUSHMER, Tracy, Macquarie University, Department of Earth and Planetary Sciences, Sydney, Australia: 03.-05.12.2014

SCHUBERTH, Bernhard, Ludwig-Maximilians-Universität München, Department für Geo- und Umweltwissenschaften, Geophysik, München, Germany: 15.-17.01.2014

STAGNO, Vincenzo, Carnegie Institution of Washington, Geophysical Laboratory, Washington, USA: 24.08.-07.09.2014

STEIN, Claudia, Westfälische Wilhelms-Universität Münster, Institut für Geophysik, Münster, Germany: 15.-18.01.2014

TAO, Renbiao, Beijing University, School of Earth and Space Sciences, Beijing, P.R. China: 18.-21.05.2014

TERMIN, Kathrin Anna, Universität Heidelberg, Germany: 03.07.2014

THIELEMANN, Marcel, ETH Zurich, Institute of Geophysics, Zurich, Switzerland: 21.-23.07.2014

5.2 Visiting scientists supported by other externally funded BGI projects

ANGEL, Ross, Università degli Studi di Padova, Dipartimento di Geoscienze, Padova, Italy: 19.-24.01.2014 (ERC ^{*A})

FISCHER, Rebecca, University of Chicago, Department of Geophysical Sciences, Chicago, USA: 20.-25.05.2014 (ERC ^{*A})

HERNLUND, John, Tokyo Institute of Technology, Earth-Life Science Institute, Tokyo, Japan: 08.-12.09.2014 (ERC ^{*A})

KLANG, Katharina, Universität Münster, Fachbereich Geowissenschaften, Münster, Germany: 26.-27.08.2014 (DFG ^{*B})

KULIK, Eleonora, National Research Center "Kurchatov Institute", Moscow, Russia: 16.-21.03.2014, 01.-02.07.2014 (DFG ^{*B})

RUMMEL, Lisa, Ruhr-Universität Bochum, Institut für Geologie, Mineralogie und Geophysik, Bochum, Germany: 20.05.2014 (DFG ^{*B})

SCHULZE, Kirsten, Christian-Albrechts-Universität zu Kiel, Germany: 26.-27.08.2014 (DFG ^{*B})

ZUCCHINI, Azzura, Università degli Studi di Perugia, Dipartimento di Scienze della Terra, Perugia, Italy: 17.-19.03.2014

[*A)] ERC: European Research Council

[*B)] DFG: Deutsche Forschungsgemeinschaft

5.3 Visiting scientists supported by the DFG Core Facility programme

ANZOLINI, Chiara, Università degli Studi di Padova, Dipartimento di Geoscienze, Padova, Italy: 22.02.-30.04.2014

BALI, Enikö, University of Iceland, Faculty of Earth Sciences, Reykjavík, Iceland: 12.-18.10.2014

BOLLINGER, Caroline, Université Lille 1, UMET - Unité Matériaux et Transformation, CNRS, Villeneuve d'Ascq, France: 07.01.-31.08.2014

CASANOVA, Vincent, University of Geneva, Earth and Environmental Sciences, Geneva, Switzerland: 24.06.-08.07.2014

CHRICHTON, Ewan, University of Edinburgh, School of Engineering, Edinburgh, U.K.: 03.-08.03.2014

FRACZEK, Elisabeth, University of Strathclyde, Institute of Photonics, Glasgow, U.K.: 12.-22.02.2014

GIEHL, Christopher, Universität Kiel, Institut für Geowissenschaften, Kiel, Germany: 02.-09.11.2014

GUIGNARD, Jeremy, European Synchrotron Radiation Facility, Grenoble, France: 11.-17.05.2014

HOLZHEID, Astrid, Universität Kiel, Institut für Geowissenschaften, Kiel, Germany: 02.-05.11.2014

KEMP, Alan, University of Strathclyde, Institute of Photonics, Glasgow, U.K.: 12.-15.02.2014

MALAVERGNE, Valerie, Université Paris-Est Marne-la-Vallée, Laboratoire Géomatériaux et Environnement, Marne-la-Vallée, France: 22.-26.09.2014

MANTHILAKE, Geeth, Université Blaise Pascal, Laboratoire Magmas et Volcans, Clermont-Ferrand, France: 31.07.-23.08.2014

NAMUR, Oliver, Leibniz Universität Hannover, Institut für Mineralogie, Hannover, Germany: 07.-25.04.2014

PONCET, Melissa, Université Paris-Est Marne-la-Vallée, Laboratoire Géomatériaux et Environnement, Marne-la-Vallée, France: 22.-30.09.2014

SANTANGELI, James, University College London, Department of Earth Sciences, London, U.K.: 19.-24.10.2014

UENVER-THIELE, Laura, Johann Wolfgang Goethe-Universität, Physikalisch-Chemische Mineralogie, Frankfurt/M., Germany: 02.-12.04.2014, 29.09.-07.10.2014

WOODLAND, Alan, Johann Wolfgang Goethe-Universität, Physikalisch-Chemische Mineralogie, Frankfurt/M., Germany: 02.-12.04.2014, 29.09.-07.10.2014

5.4 Visitors (externally funded)

BOBROV, Andrey, M.V. Lomonosov Moscow State University, Petrological Department, Moscow, Russia: 01.07.-31.08.2014

CEBULLA, Daniel, Universität Rostock, Institut für Physik, Rostock, Germany: 26.-27.06.2014

CHRISTENSEN, Ulrich, Max-Planck-Institut für Sonnensystemforschung, Katlenburg-Lindau, Germany: 16.-17.01.2014

DMITRIEV, Vladimir, European Synchrotron Radiation Facility, The Swiss-Norwegian Beamlines, Grenoble, France: 27.-31.01.2014

DOBSON, David, University College London, Department of Earth Sciences, London, U.K.: 19.-24.10.2014, 03.-04.11.2014

DOLEJŠ, David, Charles University, Institute of Petrology and Structural Geology, Prague, Czech Republic: 26.-28.05.2014, 23.-25.06.2014, 13.-15.07.2014, 30.11.-02.12.2014

FRENCH, Martin, Universität Rostock, Institut für Physik, Rostock, Germany: 26.-27.06.2014

GARCIA DOMEME, Braulio, Universitat de València, Department of Applied Physics, Spain: 01.09.-22.12.2014

IIZUKA, Riko, Ehime University, Geodynamics Research Center, Matsuyama, Japan: 01.01.-24.12.2014

IRIFUNE, Tetsuo, Ehime University, Geodynamics Research Center, Matsuyama, Japan: 04.-06.09.2014

KEPPLER, Ruth, GEOMAR, Forschungsbereich 4: Dynamik des Ozeanbodens, Kiel, Germany: 06.-10.04.2014

KING, Scott, Virginia Tech, Geosciences, Blacksburg, USA: 10.-18.06.2014

KOLESNIKOV, Anton, Russian State University of Oil and Gas, Moscow, Russia: 03.-15.11.2014

KOZLENKO, Denis, Frank Laboratory of Neutron Physics, Joint Institute for Nuclear Research, Dubna, Russia: 21.-31.07.2014

KREMSER, Victoria, Universität zu Köln, Geologie und Mineralogie, Köln, Germany: 25.09.2014

KRESSALL, Ryan, Dalhousie University, Department of Earth Sciences, Halifax, Canada: 01.-30.06.2014

KUTCHEROV, Vladimir, Royal Institute of Technology, Department of Energy Technology, Stockholm, Sweden: 26.-28.03.2014

LITVIN, Yury, Institute of Experimental Mineralogy, Chernogolovka, Moscow region, Russia: 14.-26.04.2014

NOACK, Nils, Universität zu Köln, Geowissenschaften, Köln, Germany: 29.-31.01.2014

RASHCHENKO, Sergey, Russian State University of Oil and Gas, Moscow, Russia: 12.09.-14.11.2014

RUMMEL, Reiner, TU München, Institut für Astronomische und Physikalische Geodäsie, München, Germany: 16.-17.01.2014

SECLAMAN, Alexandra, Ecole Normale Supérieure de Lyon, France: 26.02.-07.04.2014

SIMONOVA, Daria, Institute of Experimental Mineralogy, Chernogolovka, Moscow region, Russia: 24.01.-28.02.2014, 01.-31.08.2014

SMYTH, Joseph R., University of Colorado at Boulder, Department of Geological Sciences, Boulder, USA: 27.03.-07.04.2014, 21.-29.11.2014

SPIVAK, Anna, Institute of Experimental Mineralogy, Chernogolovka, Moscow region, Russia: 24.01.-28.02.2014, 01.-30.09.2014

SWAMY, Varghese, Monash University, Faculty of Engineering, Melbourne, Australia: 30.05.-09.06.2014

VASILYEV, Prokopiy, Australian National University, Research School of Earth Sciences, Canberra, Australia: 23.-24.09.2014

VASIUKOV, Denis, M.V. Lomonosov Moscow State University, Faculty of Physics, Russia: 25.06.-30.09.2014

YAGI, Takehiko, University of Tokyo, Institute for Solid State Physics, Tokyo, Japan: 08.-09.09.2014

YANG, Xiaozhi, Nanjing University, School of Earth Sciences and Engineering, Nanjing, P.R. China: 16.09.-14.10.2014

6. Additional scientific activities

6.1 Theses

Ph.D. theses

GIANNINI, Mattia: The crystal chemistry of hibonite: an indicator for oxygen fugacity during Solar nebula condensation?

KUPENKO, Ilya: Portable laser-heating system for experiments with diamond anvil cells and its application to studies of geophysically important materials.

PAMATO, Martha: Single crystal elasticity of transition zone and lower mantle phases.

M.Sc. theses

GUO, Haihao: Effect of dislocation on water solubility in olivine at 5 GPa and 1370-1410 K.

GUTIÉRREZ, Xochilt: The behavior of chlorine and sulfur during explosive volcanic eruptions.

MOHSENI AHOUEI, Hoda: Effective metal-alloy redox sensors and the oxygen fugacity of diamond formation

WANG, Lin: The temperature and pressure dependence of [001](010) and [100](010) dislocation mobility in olivine.

6.2 Honours and awards

AUDÉTAT, Andreas	Society of Economic Geologists International Exchange Lecturer 2015
BYKOVA, Elena	Poster Prize at the International Union of Crystallography in Montreal/Canada
CERANTOLA, Valerio	Student Poster Award at HERCULES School 2014 – **H**igher **E**uropean **R**esearch **C**ourse for **U**sers of **L**arge **E**xperimental **S**ystems
DUBROVINSKY, Leonid	Dr. h. c. University of Linköping/Sweden for research in crystallography and for the development of novel materials and long term collaboration with the Linköping University
FEI, Hongzhan	EON Kulturpreis Bayern 2014
NOVELLA, Davide	PhD thesis award 2014 from the Italian Mineralogical and Petrological Society (SIMP)
POSNER, Esther	European Association of Geochemistry, Student Travel Bursary

ROSENTHAL, Anja	Deep Carbon Observatory (DCO) Early Career Scientist Workshop Travel Award, 18.-21.02.2014, San Jose, Costa Rica Deep Carbon Observatory (DCO) Travel Award for leadership with the DCO Early Career Scientist Network, 15.-19.12.2014 AGU Meeting, San Francisco, USA
SORBADÈRE, Fanny	"Prix jeune chercheur" 2014 of the City of Clermont-Ferrand/France 2014 prize from "Comité National Français de Géodésie et Géophysique (CNFGG)" for her PhD thesis Price "Ami Boué" 2014 from the "Société Géologique de France" for her PhD thesis

6.3 Editorship of scientific journals

DUBROVINSKY, Leonid	Member, Editorial Board of the Journal of High Pressure Research
KATSURA, Tomoo	Associate Editor "Reviews of Geophysics"
KEPPLER, Hans	Editorial Board "Contributions to Mineralogy and Petrology"
MCCAMMON, Catherine	Chief Editor and Managing Editor "Physics and Chemistry of Minerals" Advisory Editor "Springer Briefs in Earth Sciences"
MIYAJIMA, Nobuyoshi	Associate Editor "European Journal of Mineralogy"
RUBIE, David	Editorial Board "Physics of the Earth and Planetary Interiors"

6.4 Membership of scientific advisory bodies

DUBROVINSKY, Leonid	Co-Chair of SIG "Crystallography at extreme conditions" of the European Crystallography Union Member, Review Panel for allocation of beam-time at ESRF Member, Review Panel of Canadian Light Source Member, Review Panel of SPRING8 Chair, Subcomission on Spectroscopy, Diffraction, and new Instrumentations in Mineral Physics of the International Mineralogical Association Member, Deep Carbon Observatory Scientific Steering Committee Member, Review Panel of PETRA III

FROST, Dan	Member of the council of the European Association of Geochemistry (EAG) - (Chair of the communications committee) Member, Geochemical Fellows Selection Committee (EAG-GSA) Member of the Scientific Committee for Goldschmidt 2015 Member of the Elements Executive Committee
KEPPLER, Hans	Member, Abraham Gottlob Werner Medal Committee, German Mineralogical Society (DMG) Chair, American Geophysical Union Fellow Committee (VGP section) Member, Commission for Research of Bayreuth University (Präsidialkommission für Forschung und wissenschaftlichen Nachwuchs) Member, German National Academy of Sciences (Leopoldina) Member, Bavarian Academy of Sciences Member, Deep Carbon Observatory Scientific Steering Committee Member, Alexander von Humboldt Foundation Selection Panel for Humboldt Awardees
MCCAMMON, Catherine	President, Volcanology, Geochemistry & Petrology Section of the American Geophysical Union Member, Council of the American Geophysical Union Member, Affiliation and Engagement Task Force of the American Geophysical Union Member, Bunsen Medal Committee, European Geosciences Union Chair, Sub-committee "Earth's Deep Interior" of the Commission of the Physics of Minerals, International Mineralogical Association IAVCEI representative, Inter-Association Commission for Physics and Chemistry of Earth Materials

7. Scientific and Technical Personnel

Name		Position	Duration in 2014	Funding source
ARATO, Robert	M.Sc.	Wiss. Mitarbeiter	from 15.10.	DFG
AUDÉTAT, Andreas	Dr.	Akad. Rat		BGI
BEYER, Christopher	M.Sc.	Wiss. Mitarbeiter		EU, DFG
BLAHA, Stephan	M.Sc.	Wiss. Mitarbeiter		DFG
BÖHM, Ulrich		Mechaniker		BGI
BOFFA BALLARAN, Tiziana	Dr.	Akad. Oberrätin		BGI
BOLLINGER, Caroline	Ph.D.	Wiss. Mitarbeiterin	from 15.09.	BGI/VP
BUCHEN, Johannes	Dipl.-Min.	Wiss. Mitarbeiter	from 01.05.	DFG
BUCHERT, Petra		Fremdsprachen-sekretärin		BGI
BYKOVA, Elena	Dipl. Chem.	Wiss. Mitarbeiter		BMBF
CERANTOLA, Valerio	M.Sc.	Stipendiat, Wiss. Hilfskraft		UB e.V. DFG
CERNOK, Ana	M.Sc.	Wiss. Mitarbeiterin	to 31.03. 01.06.-31.08.	BMBF UBT[2]
CHUST, Thomas	Dipl. Geophys.	Wiss. Mitarbeiter	from 01.06.	DFG
DE VRIES, Jellie	Dr.	Wiss. Mitarbeiterin		EU
DOBSON, David	Prof.	Forschungs-preisträger	01.07.-31.07.	AvH
DRUZHBIN, Dmitry	M.Sc.	Wiss. Mitarbeiter	from 01.11.	DFG
DUBROVINSKY, Leonid	Apl. Prof. Dr.	Akad. Direktor		BGI
EL GORESY, Ahmed	Prof. Dr.			BGI/VP[1]
EVONUK, Martha	Dr.	Wiss. Mitarbeiterin	to 04.12.	DFG
FARLA, Robert	Dr.	Wiss. Mitarbeiter Forschungsstipendiat	to 30.04. from 01.05.	BGI/VP AvH
FISCHER, Heinz		Mechaniker		BGI
FISCHER, Nicole	ROI	Verwalt. Beamtin		BGI
FROST, Daniel	Prof. Dr.	Stellvertr. Leiter		BGI
GOLLNER, Gertrud		Chem.-Techn. Assistentin		BGI
GUO, Haihao	M.Sc.	Stipendiat	from 01.10.	CSC
HEIDELBACH, Florian	Dr.	Wiss. Mitarbeiter		DFG
HUANG, Rong	M.Sc.	Wiss. Mitarbeiterin	from 20.11.	DFG
IIZUKA, Riko	Ph.D.	Stipendiatin	to 18.12.	JSPS
JABAROV, Sakin	Dr.	Stipendiat	from 01.07.	ANAS
JACOBSEN, Steven	Prof.	Forschungs-preisträger	from 08.07.	AvH

JACOBSON, Seth	Ph.D.	Wiss. Mitarbeiter		EU
KATSURA, Tomoo	Prof. Dr.	Leiter		BGI
KAWAZOE, Takaaki	Dr.	Akad. Rat		BGI
KEPPLER, Hans	Prof. Dr.	Professor		BGI
KEYSSNER, Stefan	Dr.	Akad. Oberrat		BGI
KISON-HERZING, Lydia		Sekretärin		BGI
KLASINSKI, Kurt	Dipl.-Ing. (FH)	Techn. Angestellter		BGI
KRAUßE, Detlef	Dipl.-Inform. (FH)	Techn. Angestellter		BGI
KRIEGL, Holger		Haustechniker		BGI
KULARATNE, Kanchana	M.Sc.	Wiss. Mitarbeiterin	to 24.03.	DFG
KULIK, Eleonora	Dipl.-Physik-ingenieurin	Wiss. Mitarbeiterin	from 03.07.	DFG
KUPENKO, Ilya	Dipl.-Physiker	Wiss. Mitarbeiter	from 15.02.	BMBF
KURNOSOV, Alexander	Dr.	Wiss. Mitarbeiter		EU
LAUMONIER, Mickaël	Dr.	Wiss. Mitarbeiter	01.03.-23.11.	BGI/VP
		Forschungsstipendiat	from 24.11.	AvH
LAURENZ, Vera	Dr. rer. nat.	Wiss. Mitarbeiterin	to 14.10.	EU
			from 15.10.	BGI/VP
LI, Wanting	M.Sc.	Stipendiatin	to 30.10.	CSC
LINHARDT, Sven		Elektrotechniker		BGI
MARQUARDT, Hauke	Dr.	Wiss. Mitarbeiter	from 01.04.	DFG
MARQUARDT, Katharina	Dr.	Akad. Rätin		BGI
MASOTTA, Matteo	Dr.	Forschungsstipendiat		AvH
MCCAMMON, Catherine	Dr.	Akad. Oberrätin		BGI
MIYAJIMA, Nobuyoshi	Dr.	Akad. Rat		BGI
MYHILL, Robert	Dr.	Forschungsstipendiat		AvH
NJUL, Raphael		Präparator		BGI
OVSYANNIKOV, Sergey	Dr.	Wiss. Mitarbeiter		DFG
PAKHOMOVA, Anna	Ph.D.	Wiss. Mitarbeiterin	03.06.-31.08.	BGI/VP
			01.09.-14.10.	DFG
			from 15.10.	BGI/VP
PAMATO, Martha	M.Sc.	Wiss. Mitarbeiterin	to 28.02.	DFG
			01.03.-31.07.	EU
PETIGIRARD, Sylvain	Ph.D.	Forschungsstipendiat		AvH
POSNER, Esther	M.Sc.	Wiss. Mitarbeiterin	to 28.02.	EU
			from 01.03.	DFG
POTZEL, Anke		Chem.-Techn. Assistentin		BGI
RAMMING, Gerd		Elektroniker		BGI

RAUSCH, Oliver		Mechaniker		BGI
ROSENTHAL, Anja	Dr.	Wiss. Mitarbeiterin		EU
RUBIE, David C.	Prof. Dr.	Professor		EU
SCHARFENBERG, Romina	B.Sc.	Sekretärin	from 18.08.	BGI
SCHULZE, Hubert		Präparator		BGI
SCHULZE, Kirsten	M.Sc.	Wiss. Mitarbeiterin	from 01.10.	DFG
SEROVAISKII, Aleksandr	M.Sc.	Stipendiat	from 01.09.	DAAD
SHCHEKA, Svyatoslav	Dr.	Wiss. Mitarbeiter		DFG
SHI, Lanlan	M.Sc.	Wiss. Mitarbeiterin	from 10.06.	DFG
SINMYO, Ryosuke	Dr.	Forschungsstipendiat	to 31.05.	AvH
		Wiss. Mitarbeiter	from 01.06.	DFG
SORBADERE, Fanny	Dr.	Wiss. Mitarbeiterin	to 31.08.	BGI/VP
		Forschungsstipendiat	from 01.09.	AvH
SOUSTELLE, Vincent	Dr.	Forschungsstipendiat	to 28.02.	AvH
STEINLE-NEUMANN, Gerd	Dr.	Akad. Oberrat	from 01.08.	BGI
STROHM, Cornelius	Dr.	Wiss. Mitarbeiter	to 14.04.	BMBF
TRENZ, Ulrike		Biol.-Techn. Assistentin		BGI
TROTS, Dmytro	Dr.	Wiss. Mitarbeiter	to 31.01.	BGI/VP
ÜBELHACK, Stefan		Mechaniker		BGI
VLCEK, Vojtech	M.Sc.	Wiss. Mitarbeiter		DFG
VOGEL, Antje	Dipl.-Min.	Wiss. Mitarbeiterin	to 30.06.	DFG
WAGLE, Fabian	M.Sc.	Wiss. Mitarbeiter	from 07.01.	DFG
WALTE, Nicolas	Dr.	Wiss. Mitarbeiter		BMBF
WANG, Lin	M.Sc.	Wiss. Mitarbeiter	from 01.10.	DFG
YOSHIOKA, Takahiro	M.Sc.	Wiss. Mitarbeiter	from 01.04.	DFG
ZHANG, Daohan	M.Sc.	Stipendiat	from 01.12.	CSC
ZIBERNA, Luca	Ph.D.	Wiss. Mitarbeiter	to 28.02.	EU

Abbreviations/explanations:

ANAS	Azerbaijan National Academy of Sciences
AvH	Alexander von Humboldt Foundation
BGI	Staff Position of Bayerisches Geoinstitut
BGI/VP	Visiting Scientists' Program of Bayerisches Geoinstitut
BMBF	Federal Ministry of Education and Research
CSC	Chinese Science Council
DAAD	German Academic Exchange Service
DFG	German Science Foundation
EU	European Union
JSPS	Japanese Society for the Promotion of Science
UB e.V.	Universität Bayern e.V.
UBT	Universität Bayreuth

[1] partially funded by the Visiting Scientists' Program of Bayerisches Geoinstitut

[2] Übergangsmittel für Doktoranden ("Feuerwehrfonds")

Index

Abakumov, A.M. 153
Aoki, T. 78
Armiento, R. 144
Audétat, A. 55, 58, 86, 178
Baer, R. 180
Bali, E. 109
Behrens, H. 113
Berry, A. 52
Beyer, C. 49, 95
Blaha, S. 138, 140, 176
Bobrov, A.V. 69, 71
Boffa Ballaran, T. 29, 65, 66, 76, 82, 90, 92, 93, 96, 102, 121, 137, 163, 176
Bollinger, C. 170
Bouvier, A. 79
Buchen, J. 90
Bureau, H. 121
Burghammer, M. 99
Buseck, P.R. 78
Bykov, M. 62, 69
Bykova, E. 62, 68, 69, 82, 153
Campbell, A.J. 174
Casanova, V. 178
Cerantola, V. 39, 69, 73, 97, 167
Černok, A. 82, 176
Chantel, J. 95
Chen, J. 170
Chumakov, A.I. 39, 62, 97, 167
Chust, T. 26
Crichton, W. 95
Dang, N.T. 158
de Vries, J. 22, 23
Dmitriev, V. 148
Donovan, J.J. 86
Dubrovinskaia, N.A. 62, 69, 78, 148, 151, 176
Dubrovinsky, L.S. 39, 46, 47, 54, 62, 68, 69, 71, 73, 78, 82, 97, 148, 151, 153, 155, 157, 158, 165, 167, 176
Eisenberg, H.R. 180
El Goresy, A. 33, 79
Farla, R.J.M. 124, 138, 161
Fischer, R.A. 174

Fontboté, L. 178
Frost, D.J. .....22, 29, 37, 41, 42, 45, 49, 51, 52, 65, 85, 93, 95, 96, 117, 121, 128, 131, ...137, 168, 172, 174
Gaillard, G. 114
Garbe-Schönberg, D. 86
García-Domene, B. 155
Garvie, L.A.J. 78
Giannini, M. 96, 102
Gillet, Ph. 33, 79
Glazyrin, K.V. 153, 167
Gou, H. 148
Grützner, T. 49
Guignard, J. 95
Guo, X. 113
Gutierrez, X. 107
Gutmann, M. 85
Hanfland, M. 62, 82
Harries, D. 99, 174
Heidelbach, F. 29, 126, 128, 132
Hennet, L. 99
Hernlund, J. 22, 34
Iizuka, R. 131
Ireland, T.R. 49
Ishida, M.H. 33
Ismailova, L.S. 68, 69, 71, 73, 97
Jabarov, S.H. 157, 158
Jacobsen, S.D. 76, 85
Jacobson, S.A. 22, 23, 34
Kantor, A. 39, 97
Kantor, I. 69, 73
Karkin, A.E. 148, 153
Katsura, T. 138, 140, 161
Kawazoe, T. 84, 90, 92, 138, 161
Keppler, H. 107, 110, 112, 113, 120, 132
Kichanov, S.E. 157, 158
Klemme, S. 49
Kolesnikov, A. 54
Kozlenko, D.P. 157, 158
Kronz, A. 86
Kümmel, S. 144
Kupenko, I. 39, 54, 62, 69, 73, 97, 99, 167
Kouzmanov, K. 178

Kurnosov, A. 76, 90, 92, 93, 96, 137, 163, 165
Kutcherov, V. 54
Langenhorst, F. 102, 174
Laumonier, M. 114
Laurenz, V. 37, 42
Leoni, M. 137
Leppert, L. 144
Li, W. 58
Liermann, H.-P. 62, 82
Lin, B. 104
Lin, Y. 33
Litvin, Y. 46, 47
Lowers, H.A. 86
Lukin, E.V. 157, 158
Magee, C. 49
Malfait, W. 99
Mammadov, A.I. 158
Manthilake, M.A.G.M. 168
Marquardt, H. 90, 92, 93, 135
Marquardt, K. 79, 104
Masotta, M. 110
McCammon, C.A. 39, 41, 42, 54, 62, 68, 69, 73, 74, 97, 112, 167
Melosh, H.J. 23
Miyagi, L. 135
Miyahara, M. 33, 79
Miyajima, N. 29, 79, 131, 174
Mohseni, H. 45, 172
Morales, L. 104
Morbidelli, A. 22, 23, 34
Morozova, N.V. 153
Myhill, R. 29, 41, 51, 121
Nakajima, Y. 41, 148
Nakamura, T. 33
Németh, P. 78
Ni, H. 113
Nimmo, F. 23
Ohtani, E. 33, 79
Ovsyannikov, S.V. 62, 68, 148, 153, 155
Ozawa, S. 79
Pakhomova, A.S. 137
Pamato, M.G. 29, 96
Petitgirard, S. 52, 99, 167, 174

Petri, M. 161
Pettke, T. 86
Pinter, Zs. 52, 74, 138
Pollok, K. 174
Posner, E.S. 117
Potapkin, V. 39
Prakapenka, V.B. 62, 96
Rashchenko, S. 165
Raepsaet, C. 121
Rohrer, G.S. 104
Rosenthal, A. 42, 52
Rubie, D.C. 22, 23, 34, 37, 99, 117, 174
Rusk, B. 86
Rüffer, R. 39, 62, 167
Rybacki, E. 104
Savenko, B.N. 158
Schmickler, B. 117
Schulze, H. 33
Schulze, K. 92
Serovaysky, A. 54
Shcheka, S. 112
Shchennikov, V.V. 148, 153
Shi, L.-L. 161
Siersch, N. 76, 163
Sifré, D. 114
Simonova, D. 46
Sinmyo, R. 39, 41, 68, 97, 99
Smyth, J.R. 85
Solopova, N.A. 151
Sorbadere, F. 42
Soustelle, V. 131
Speziale, S. 96
Spivak, A. 46, 47
Steinle-Neumann, G. 26, 100, 117, 144, 146, 180
Stipp, M. 132
Strohm, C. 167
Tkachev, S.N. 96
Trots, D.M. 96
Tsirlin, A.A. 153
Ubrig, N. 178
Uenver-Thiele, L. 65, 66
Vasiukov, D. 54

Vlček, V. 100, 117, 144, 146, 180
Wagle, F. 100
Walte, N. 128, 168
Wang, L. 138, 146
Wenz, M. 42
Wirth, R. 148
Woodland, A.B. 65, 66
Yang, X. 120
Yaxley, G.M. 52
Yogo, K. 33
Yoshioka, T. 112
Young, E.D. 34
Zhang, J. 58
Zhang, L. 113
Zhuravlev, K.K. 96
Ziberna, L. 96, 121